Thermolabile Protecting Groups in Metal-Organic Frameworks

A thesis presented in partial fulfilment of the requirements of the degree of

Doctor of Philosophy
in
Chemistry

at Massey University, Manawatu, New Zealand

Sebastian Blackwood
2016

For Meghan Blackwood

Abstract

Prior to the work carried out for this thesis, there were no publications in which bpy was used as a ligand backbone, or in which a carboxylate was incorporated into a MOF using a TPG. Also, to the best of our knowledge there are no examples in the literature of an ethyl carbamate TPG in MOFs.

In this thesis the range of TPG protected ligands has been expanded to include 1,4-bdc (Chapter 2) and bpy (Chapters 4 and 5). The bpy-NHBoc and bpy-TBE materials are the first examples of N-donor type ligands protected by TPGs. Furthermore, the bpy-TBE ligand is the first example of a TPG protected carboxylate in a MOF.

In Chapter 2, 1,4-bdc-NH_2 was protected as both the ethyl carbamate and the *tert*-butylcarbamate, giving 1,4-bdc-NHCOOEt and 1,4-bdc-NHBoc, which there then incorporated into a MOF-5-type framework. It was envisaged that thermolysis of the carbamate esters could generate an isocyanate group, though this was not expected for 1,4-bdc-NHBoc due to the tendency of *tert*-butylcarbamates to decompose to the amine. Despite thermolysis on the TGA apparatus only generating the amine, it was found that thermolysis under vacuum enabled not only enabled ~ 60 % conversion of the ethylcarbamate to 1,4-bdc-NCO, but also a ~20 % conversion of the *tert*-butylcarbamate to 1,4-bdc-NCO. The MOF-5 analogues in this work also proved sufficiently stable to survive the thermolysis conditions with little discernible effect on the porosity of the material.

In Chapter 3, 1,3-bdc-NH_2 was protected as both the ethyl carbamate and the *tert*-butylcarbamate, giving 1,3-bdc-NHCOOEt and 1,3-bdc-NHBoc, which there then incorporated into a lon-e-type framework. It became apparent the lon-e was a poor choice in MOF for use with TPGs as the framework was prone to collapse from desolvation, and it was not possible to thermolyse the materials without complete collapse of the MOFs.

In Chapter 4, bpy-NH_2 and bpy-CO_2H were protected with TPGs to give bpy-NHBoc and bpy-TBE respectively. The ligands were combined with bpdc and zinc to obtain the BMOF-1-bpdc analogues MUF20-Aβ and MUF20-Aγ. Whilst the thermolysed materials MUF20-$A\beta^t$ and MUF20-$A\gamma^t$ demonstrated significant gas uptakes compared to their protected counterparts, comparison of MUF20-$A\beta^t$ with the directly synthesised material MUF20-Aβ’ revealed significantly higher uptakes than the thermolysed materials. This discrepancy indicates that the BMOF-1-bpdc/MUF20 framework is partially degraded under thermolysis conditions. These results strongly imply that this framework is not compatible with TPGs. However, TPGs did allow for the installation of a carboxylate group into the

BMOF-1-bpdc/MUF20 framework which was not obtainable through direct synthesis methods.

In Chapter 5, bpy-TBE was combined with btb and Zn/Cu to obtain Zn-DUT-23-TBE and Cu-DUT-23-TBE. These materials were then thermolysed to produce Zn/Cu-DUT-23-CO_2H, materials that were not able to be directly synthesised using bpy-CO_2H. Unfortunately, the thermolysed materials demonstrated significant decreases in uptakes compared to their protected counterparts. However, the TPG containing materials also had markedly lower uptakes than the parent Zn-DUT-23 and Cu-DUT-23 materials, which has been attributed to pore collapse. This partial pore collapse may have sufficiently weakened the MOF framework to increase its sensitivity to the thermolysis conditions, resulting in a much larger decrease in uptake than would have been the case with a defect free material.

The results of this thesis revealed that MOF stability is a key factor in the compatibility of a material. Specifically, the MOF must be resistant to solvent removal and subsequent heating at elevated temperatures for extended periods. This is most clearly observed in Chapter 3, where the lon-e materials were very susceptible to solvent removal, and later were completely collapsed by thermolysis. These findings have led to the recommendations outlined in section 6.2 for the screening of MOFs for their compatibility with TPGs.

Contributions

All the work in this thesis was completed by Sebastian Blackwood

Except:

- Parallel syntheses of lon-e-NHBoc and lon-e-NHCOOEt for gas sorption were conducted by Yongchen Wang under supervision from Sebastian Blackwood.
- The MUF20 series was a collaborative effort between Sebastian Blackwood and Heather Jameson. As such, materials and data were freely shared. For the sake of clarity, I will be presenting the frameworks in Chapter 4, which includes experiments performed by Heather. Heather will present the rest of the MUF20 series in her thesis, which will include some of my data.

Acknowledgements

I would like to take the opportunity to thank the large number of people who have contributed to my PhD research and thesis. First, I would like to thank my supervisor Professor Shane Telfer for providing me this wonderful PhD opportunity and scholarship to carry out research in MOF chemistry. Thank you for your expert guidance on all matters throughout this PhD, from the big picture to the minutia. Thank you for providing funding for me to attend conferences and symposiums, and pushing me to be the best I can be.

I would also like to thank my co-supervisor, Associate Professor Gareth Rowlands, for his much-valued guidance during my first year when Shane was on sabbatical, as well as his expertise in organic chemistry that he generously provided throughout my PhD. I also thank Dr. Pat Edwards for assisting with specialized NMR experiments, Professor Geoff Jameson for discussions and advice on x-ray crystallography, and David Lun for his assistance and guidance in the lab. I also thank Heather Jameson, Dr. Lujia Liu, Yongchen Wang, Subo Lee, and all other current and past Telfer group members for scientific discussions and technical assistance.

I thank Dr. Marie Squire from University of Canterbury for some performing some ESI-MS experiments.

I would like to acknowledge the financial support from The MacDiarmid Institute for Advanced Materials and Nanotechnology for a Doctoral scholarship, and the Institute of Fundamental Sciences for my fourth year PhD funding. I also thank the IFS postgraduate travel fund for supporting me to attend a conference in Edinburgh. I greatly thank the MacDiarmid Institute for organizing and supporting annual student and postdoc symposiums and the AMN-7 conference in Nelson (special thanks to Professor Shane Telfer for organizing this conference).

I also thank IFS administration and technical staff for their great assistance during my PhD research and thesis writing.

I would like to take this opportunity to thanks all of my friends and family, whose encouragement and support have helped me throughout this PhD study. Finally, I would also like to thank my wife Meghan, whose love and strength have helped me every day.

Publications and thesis structure

Publications relevant to this thesis

None

Additional publications

1. A. Ferguson, L. Liu, **S. Blackwood** and S. G. Telfer, Recent Developments in Metal-Organic Framework (MOF) Chemistry, C*hemistry in New Zealand* **2014**, 78, 113-118.
2. P. Insiti, P. Jitthiang, K. Chainok, R. Chotima, J. Sirirak, **S**. **Blackwood**, A. Alkaş, S. G. Telfer, D. J. Harding, Substituent modulated packing in octahedral Ni(II) complexes, *Polyhedron* **2015**, 114, 242-248.

Table of Contents

Chapter 1 - Introduction

1.1 Metal-Organic Frameworks (MOFs)

Metal-organic frameworks (MOFs) are a comparatively new class of compound, first developed in the 1990s. These crystalline materials are highly porous and have large internal surface areas. This is largely due to their natural structure. By dissolving metal ions and divergent multi-dentate ligands together, it is possible for coordination complexes to form with uncapped binding sites on the ligands (Figure 1.1). These binding sites are directed away from the metal centre and allow for further metals to bind to the ligands. These metal ions in turn allow for the addition of more ligands to the structure, and this cycle repeats, building up the 3 D frameworks characteristic of MOF materials. Due to the inherent strength of metal-ligand bonds, MOFs are typically robust materials, capable of withstanding moderate heating and the desolvation of the framework. The ability to remove the solvent from the pores of MOFs allows for a wide number of uses for these materials which are covered later in this introduction (Section 1.2). The highly ordered nature of these materials allows for their structures to be elucidated using small molecule crystallographic techniques, rather than the larger molecule techniques required for materials such as proteins. This is highly beneficial as it is then possible to determine the exact nature of the pore environments using single crystal x-ray crystallography (SXRD). With this level of detailed analysis available, MOFs lend themselves to the study of how the nature of the pore environment affects the physical and chemical properties of the material. This chapter presents an

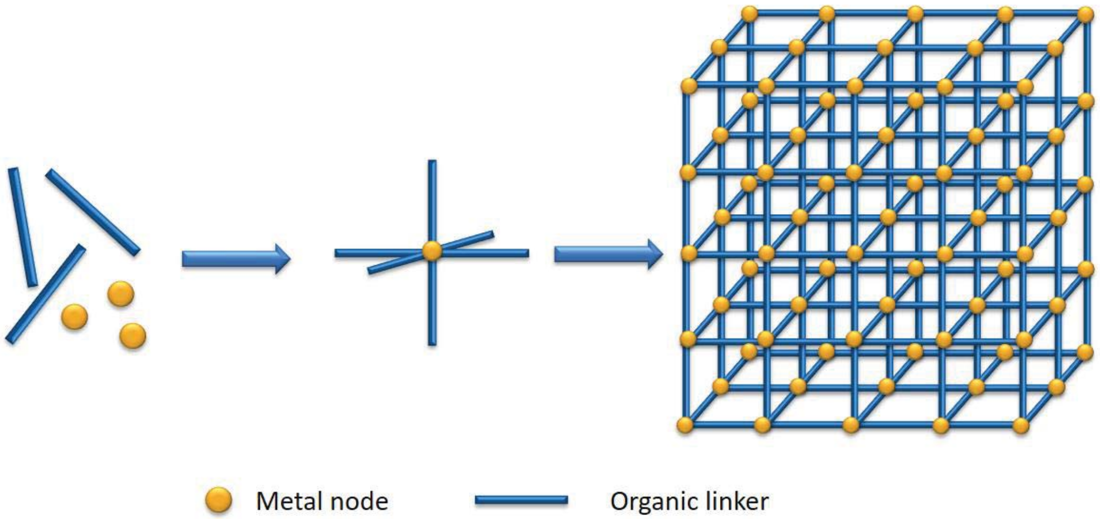

Figure 1.1 Scheme outlining the conceptual route to MOF synthesis. First organic linkers bind to metal nodes, then these complexes bind further linkers and nodes until a 3 D framework forms.

overview of MOFs, their various applications, the introduction of functionality into MOFs, and also an overview of thermolabile protecting groups (TPGs) and their use in MOFs and other materials.

1.1.1 Definitions & Terminology

First proposed in 1989 by Hoskins and Robson,[2,3] it was not until Yaghi's Nature paper in 1995[4] that the term "metal-organic framework" was coined, and with it a new field of chemistry exploded into being. With the appearance of this new field, there arose the need for a definition of what exactly a MOF is, and in 2012 a committee of MOF researchers defined MOFs as multi-dimensional co-ordination networks (a subset of coordination polymers), containing both inorganic and organic components, with at least the potential for porosity.[5] In 2013, the International Union of Pure and Applied Chemistry (IUPAC) published its recommendations for the definition of a MOF, stating that a MOF "is a coordination network with organic ligands containing potential voids."[6] The publication also defined its use of the term coordination network as a coordination polymer with cross-links between multiple chains such that it extends in 2 or 3 dimensions, and later emphasising that, "coordination network is in fact a subsection of coordination polymer."[6] This hierarchy of terms is illustrated in Figure 1.2, which shows that MOFs are a subset of coordination networks, which are in turn a subset of coordination polymers. Whilst this usage is what IUPAC recommends, this recommendation has come 14 years after Yaghi's

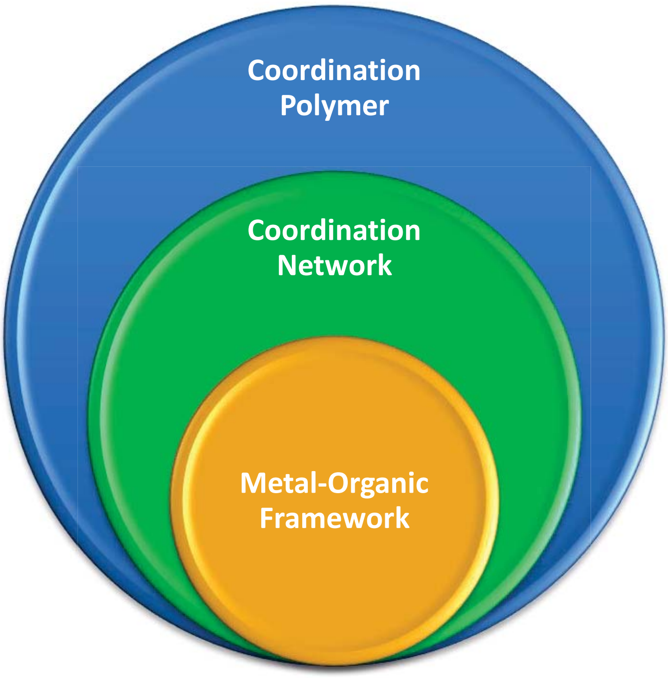

Figure 1.2 Schematic to illustrate the hierarchy of IUPAC terminology.

seminal paper, and the terms have become muddled to an extent where many groups have different terms for the same compounds. The term MOF, for instance, is not universally used, with groups around the world using terms such as metal organic materials (MOMs),[7] porous coordination polymers (PCPs),[8] and porous coordination networks (PCNs).[9] For the purposes of this thesis, the term MOF with be used as per the IUPAC recommendations, and any materials that fulfil the criteria will be referred to as MOFs regardless of the terms used in the cited literature.

There are no guidelines on how to name MOFs, and as such the naming of new materials has been largely left up to researchers. Typically, the name is comprised of an acronym in conjunction with a number. Sometimes the acronyms provide information about the material, such as isoreticular metal-organic frameworks (IRMOFs)[10] or zeolitic imidazolate frameworks (ZIFs).[11,12] Other acronyms are based on the place where the material was discovered, such as the University of Oslo (UiO),[13] the Hong Kong University of Science and Technology (HKUST),[14] and Matérial Institut Lavoisier (MIL).[15] The numbers assigned to individual materials usually hold little significance and are used as a means to differentiate materials made by the same group, though similar materials are often consecutively numbered. IRMOFs 2-7[10], for instance, are all functionalised analogues of IRMOF-1 (also known as MOF-5[16]), a MOF comprised of tetrahedral Zn_4O clusters joined in a cubic net by 1,4-benzenedicarboxylate (1,4-bdc, please refer to the back of this work for a fold out reference sheet of common ligands). As systematic nomenclature is impractical to use when conversing about MOF materials, researchers in the field of MOF chemistry usually refer to MOFs by the name given to them by the researchers who made them. Whilst it is possible to refer to MOFs by their unit cell formulae ($[Zn_4O(1,4\text{-bdc})_3]$ for IRMOF-1), these are not always unique to a single material, and as such can cause confusion during discussions.

1.1.2 Brief History of MOFs

Whilst MOFs are relatively new compounds, coordination networks have been in use for centuries. Prussian blue ($Fe_4[Fe(CN)_6]_3.XH_2O$), whose synthesis dates back as far as 1706, is possibly the first coordination network synthesised and has had many uses ranging from dyeing fabrics to curing heavy metal poisoning.[17] It was Robson's analysis of such coordination networks that led him to postulate that rational design of coordination networks could be achieved through analysis of the binding modes of metal ions and ligands.[2,3] Robson presented the rationale behind the logical steps that could be made to synthesise an infinite framework by replacing the acetonitrile ligands of $[Cu(CH_4CN)_4]^+$ with 4,4',4'',4'''-tetracyanotetraphenylmethane.

Though a revolutionary concept, the methodology of rational design and synthesis of coordination networks had not spread very far until Yaghi's 1999 Nature paper on MOF-5[16] galvanised the rapid widespread synthesis of MOFs by other groups. Whilst Yaghi had published a MOF paper in 1995 that used the same approach, the Co-1,3,5-benzenetricarboxylate (btc) paper[4] failed to generate the same magnitude of impact as the MOF-5 paper. This is because the MOF-5 paper demonstrated resistance to "activation" (the removal of occluded solvent molecules), as well as the highest recorded surface area at the time, with its Langmuir surface area calculated to be 2,900 m^2/g. MOF-5 is formed by combining zinc nitrate with 1,4-benzene dicarboxylate (1,4-bdc). As shown in Figure 1.3, the zinc(II) ions form a tetrahedral Zn_4O cluster around a central oxygen atom. Each Zn_4O cluster is able to accommodate six carboxylate groups in an octahedral geometry. The para positioning of the carboxylates in 1,4-bdc allows each ligand to bridge two Zn_4O clusters in a linear fashion. As more Zn_4O clusters and 1,4-bdc linkers accumulate the polymer expands in 3 dimensions, forming the infinite cubic lattice shown in Figure 1.3.

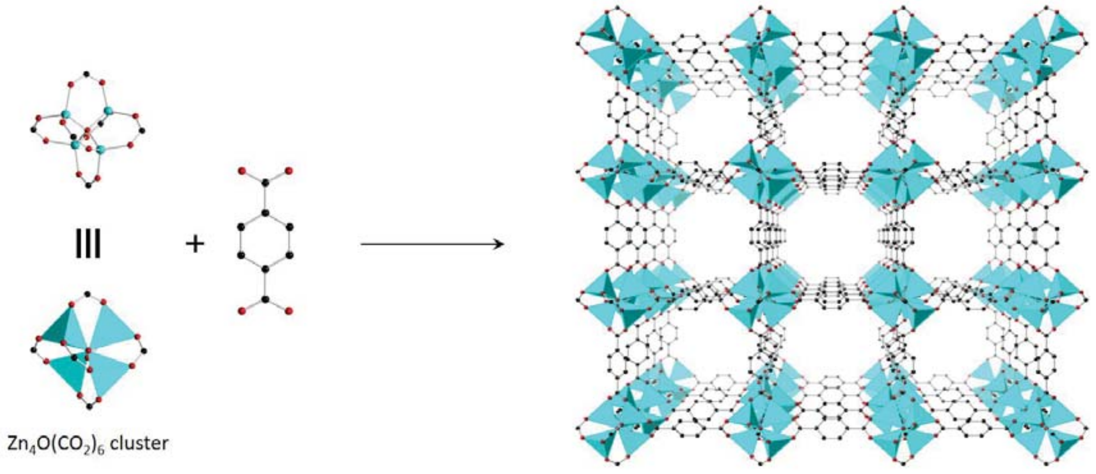

Figure 1.3 A scheme outlining the conceptual route to MOF-5 by linking 1,4-bdc with tetranuclear zinc(II) nodes. On the right is the MOF-5 structure determined by single crystal x-ray diffraction (SXRD). Atom colours: zinc = teal, carbon = black, oxygen = red (hydrogen atoms omitted for clarity).

Also in 1999, the Williams group published the structure of HKUST-1[14], which was synthesized by combining copper(II) nitrate with 1,3,5-benzenetricarboxylate (btc). HKUST-1 is built up from dinuclear copper nodes that are bonded to four carboxylate groups to generate paddlewheel clusters with open axial positions (Figure 1.4). Known as open metal sites, or exposed metal sites, these coordinatively unsaturated positions can allow for binding of guest molecules directly to the metal ions. In the as-synthesised material, these open metal sites are occupied by coordinated solvent molecules (water in the case of HKUST-1). However, they are often able to be removed to allow other molecules access to

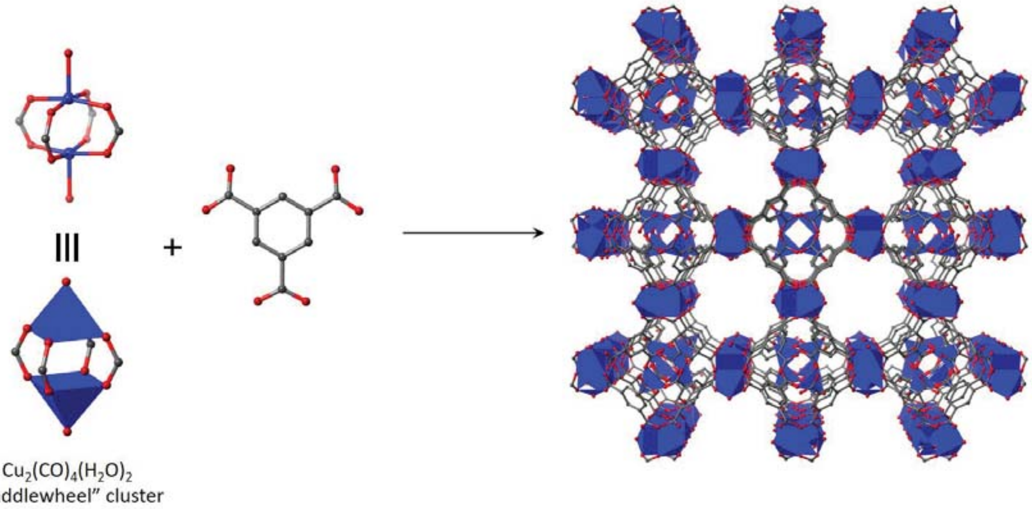

Figure 1.4 A scheme outlining the conceptual route to HKUST-1 by linking btc with dinuclear copper(II) paddlewheel nodes. On the right is the HKUST-1 structure determined by single crystal x-ray diffraction (SXRD). Atom colours: copper = blue, carbon = grey, oxygen = red (hydrogen atoms omitted for clarity).

the metal ions. The Williams group reports this in their paper, wherein the coordinated water molecules are replaced with pyridine by soaking HKUST-1 in dry pyridine. This is one of the very earliest examples of post-synthetic modification (PSM) of a MOF (see section 1.3.3 for more information regarding PSM).

As can be seen in Figure 1.5, the number of publications pertaining to MOFs per annum has increased exponentially, and since 2013 there have been more articles referencing MOFs per annum than coordination polymers. These numbers are actually understated as many groups still use terms other than MOF for these materials (*vide supra*). The explosion in

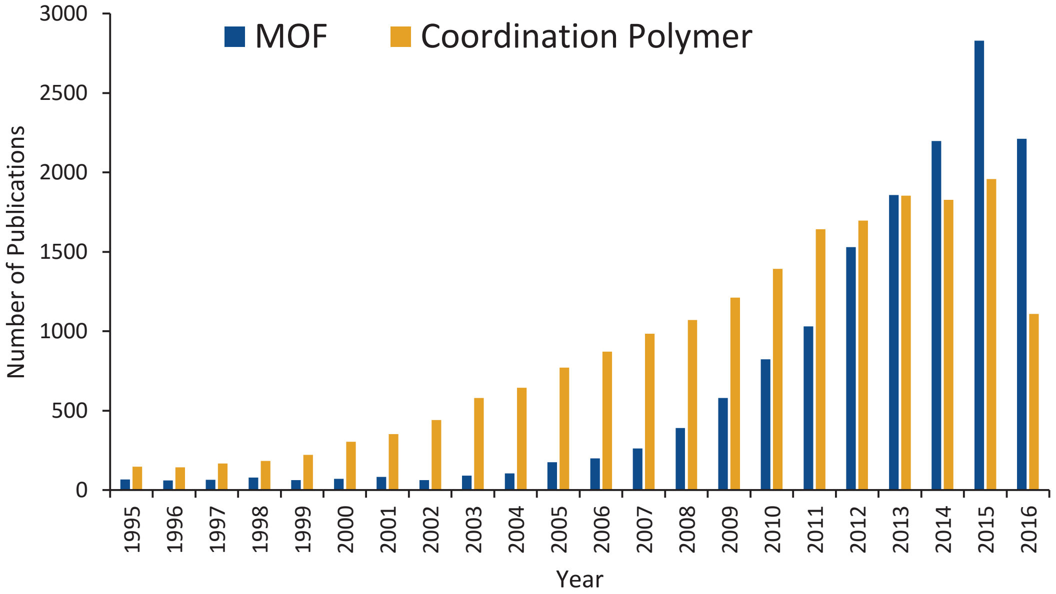

Figure 1.5 Number of publications with the topic coordination polymer (gold) and MOF (blue) since 1995 (source: SciFinder, 10/08/2016).

MOF articles is predominantly due to properties inherent to these materials that make MOFs highly desirable research targets. As Robson proposed in 1990,[3] MOFs have demonstrated: thermal, chemical, and mechanical stabilities; high crystallinity; high porosity with low density; the ability to uptake and separate guest molecules within pores; ability for PSM of the organic ligands; and catalytically active sites. It is these properties that have led to MOFs being developed for applications such as; gas storage, separation of gases and other compounds, catalysis, drug delivery, chemical sensing, and energy production.

1.1.3 Noteworthy examples of MOFs

A revolutionary material, MIL-101 (alongside the co-reported material MIL-100) was the first MOF to prove resistant to degradation by hydrolysis, which is a common problem for MOFs.[18-20] It was first reported by the Férey group in 2005. The original synthesis conditions involved mixing 1,4-bdc and chromium(III) nitrate in water with HF.[21] HF-free conditions have subsequently been developed.[22] In addition to its hydrolytic and chemical stability, MIL-101 set itself apart from other MOFs at the time by featuring large mesopores.

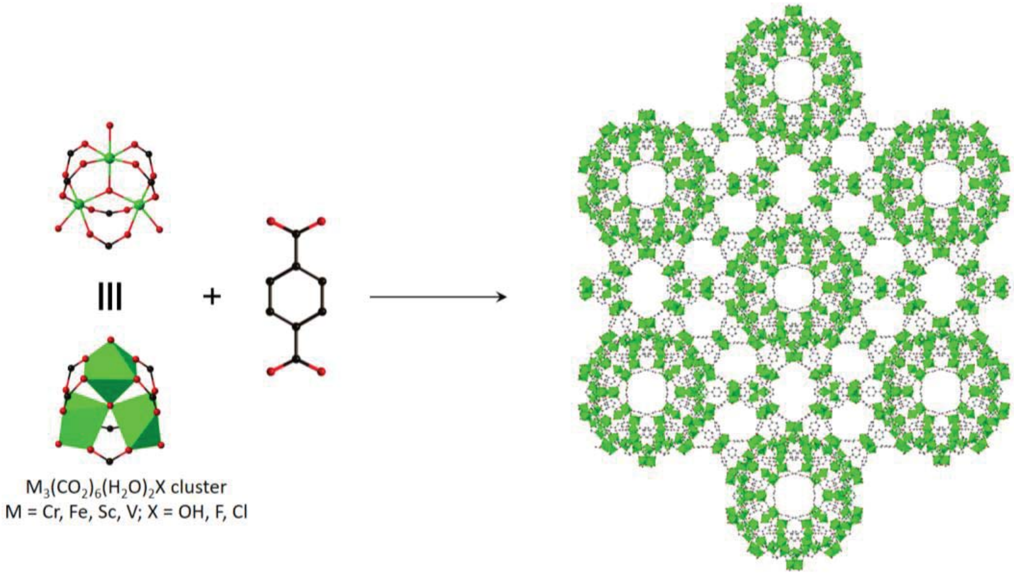

Figure 1.6 A scheme outlining the conceptual route to MIL-101 by linking $M_3(CO_2)_6(H_2O)_2X$ clusters with 1,4-bdc. On the right is the MIL-101-Fe structure determined by single crystal x-ray diffraction (SXRD). Atom colours: iron = green, carbon = black, oxygen = red (hydrogens omitted for clarity).

Its two types of mesopores have diameters of 29 Å and 34 Å. These pores have been demonstrated to encapsulate guest particles up to 13.1 Å in diameter.[21] These large pores are ideal for allowing the free passage of guest molecules throughout the framework. A number of MIL-101 analogues have been developed for various applications. A sulfonic acid functionalised MIL-101 material has been developed as a solid state Brønsted acid catalyst,[23,24] and MIL-101 materials activated by removal of water molecules coordinated to the metal clusters have been further functionalised for selective gas adsorption.[25,26]

ZIF-8 (ZIF = zeolitic imidazolate framework, Figure 1.7) is arguably the most well-studied MOF material. A Scifinder search reveals > 1,300 publications that feature this material. First reported by Chen's group in 2006,[11] it was reported later in the same year by Yaghi's group.[12] ZIF-8 is synthesised under solvothermal conditions from 2-methylimidazole and zinc nitrate in DMF or water. ZIF-8 is very stable in neutral and basic aqueous conditions. For example, it survives boiling aqueous 8 M NaOH. This stability is explained by the strong coordination bond between the nitrogen atoms of the imidazole ligand and the zinc cations. This bond is labile under acidic conditions, however. The remarkable stability of ZIF-8 is a contributing factor to the extensive research that has been carried out on this material.

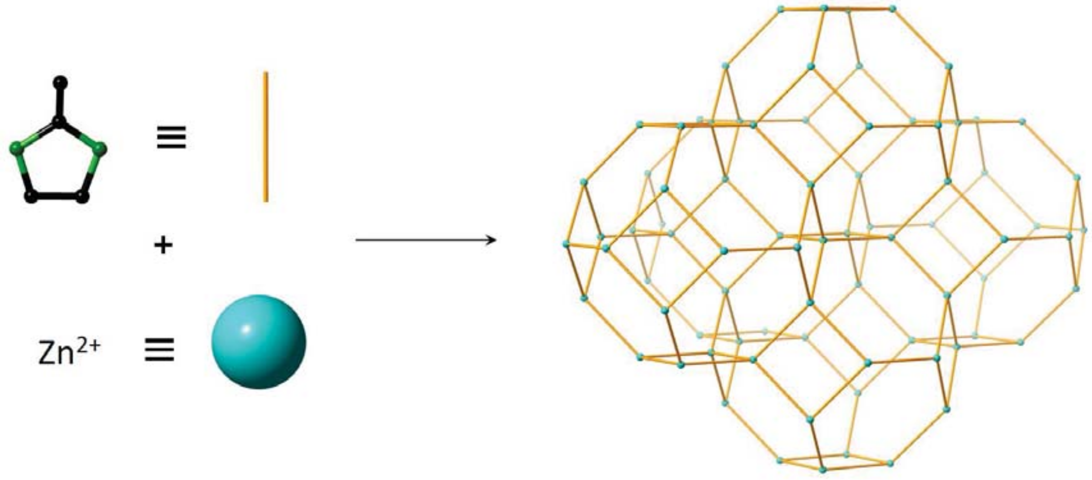

Figure 1.7 A scheme outlining the conceptual route to ZIF-8 by linking Zn^{2+} ions with 2-methylimidazolate. On the right is the ZIF-8 structure determined by single crystal x-ray diffraction (SXRD). Atom colours: zinc = teal, carbon = black, nitrogen = green. 2-methylimidazole rendered as gold rod for clarity.

First reported by Lillerud's group in 2008,[13] UiO-66 is another remarkably stable material. Stable in water, aqueous acid, base, and common organic solvents, it is synthesised by combining 1,4-bdc and zirconium(IV) chloride in DMF and heating at 120 °C. UiO-66's stability comes from the Zr(IV)-carboxylate bonds. Hydrolysis of the first carboxylate position around the metal cluster has an energy penalty of 38.2 kcal/mol.[27] Despite this remarkable stability, both the organic ligands and metal ions of UiO-66 can be post-synthetically exchanged to obtain stable derivatives that cannot be obtained through direct synthesis.[28,29] See section 1.3.3.2 for more information on post-synthetic exchange (PSE). The stability of the $Zr_6O_4(OH)_4(CO_2)_{12}$ secondary building unit (SBU) has been harnessed to produce other extraordinarily stable, highly porous MOFs utilizing alternative ligands.[30,31]

1.1.4 Synthesis of MOFs

Most contemporary MOF syntheses use solvothermal conditions. This differs from the first reported syntheses of MOFs, which typically used diffusion methods to induce framework crystallization. Yaghi's 1995 paper reported the diffusion of pyridine into a solution of btc and $Co(NO_3)_2$ in alcohol over three days to generate the reported material, and the MOF-5 synthesis reported in 1999 diffused triethylamine into a solution of $Zn(NO_3)_2$ and 1,4-bdc in DMF/chlorobenzene/H_2O_2. Both of these methods were conceived with the goal of slowly deprotonating the carboxylic acid moieties of the ligands through the diffusing of a base into the solution containing the MOF precursors. Within a few years, however, solvothermal synthesis had become the preferred method for the synthesis of many MOFs. It was found that using formamide solvents, such as DMF or DEF, in solvothermal syntheses resulted in deprotonation of carboxylate groups, removing the need for the addition of a base.[32,33] A paper by Hausdorf *et al.* revealed that it was the decomposition of diethylformamide at elevated temperatures in the presence of water that generated sufficient diethylamine to deprotonate the carboxylate groups and allow MOF-5 to form.[34] Since this discovery, the use of formamide solvents in solvothermal syntheses has become the preeminent method for obtaining MOFs with acidic binding groups. Water content of the reaction mixture also plays a key role in the synthesis of MOFs. In general, too little water reduces the rate of hydrolysis of the formamide solvent, which can inhibit MOF crystal

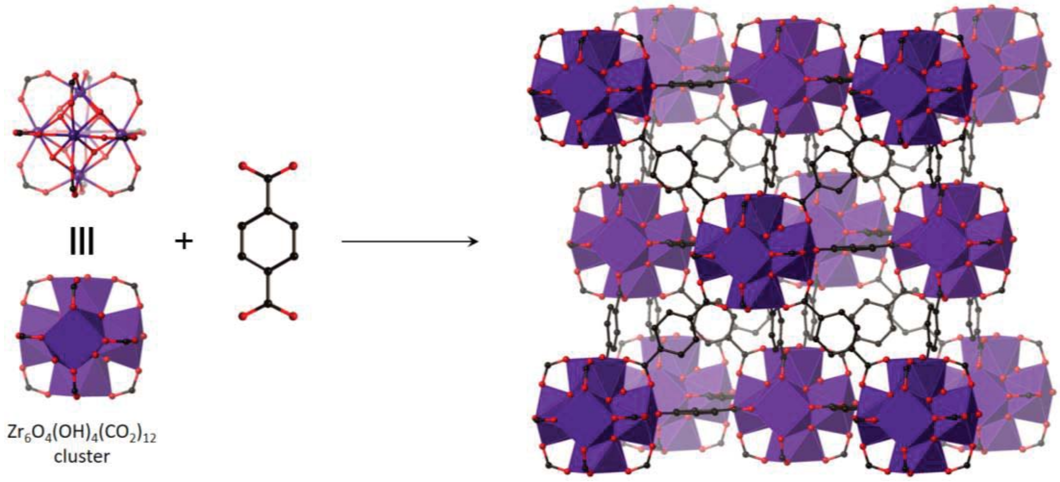

Figure 1.8 A scheme outlining the conceptual route to UiO-66 by linking $Zr_6O_4(OH)_2(CO_2)_{12}$ clusters with 1,4-bdc. On the right is the UiO-66 structure elucidated from powder x-ray diffraction (PXRD). Atom colours: zirconium = purple, carbon = black, oxygen = red (hydrogens omitted for clarity).

formation. Too much water, on the other hand, can prevent the formation of any solid material due to the coordination of H_2O to the metal ions. The water content of the solvent can also induce a different MOF phase to form.[34-36] In addition to solvothermal syntheses, MOFs have been reported to have been synthesised by microwave,[37,38] sonochemical,[39,40] electrochemical,[41] mechanochemical,[42,43] and hydrothermal[44-46] reaction methods. Where possible, syntheses are carried out in glass reaction vessels such as scintillation vials. This allows for easier monitoring of reactions compared to opaque reaction vessels such as autoclaves, and has the added advantages of being able to observe the materials without changing the reaction temperature and minimizing the amount of physical disruption to the syntheses.

It is not uncommon to find metal-ligand combinations that form MOFs so rapidly that only microcrystalline powders are obtained rather than large single crystals. This precludes structural characterisation by single-crystal X-ray diffraction. In these instances, modulators are often added to slow down crystal growth and allow for single crystals to form. Modulators function by competitively binding to the metal ions during synthesis, and must be displaced by the desired ligand to allow the MOF framework to form and propagate. Typically, non-divergent ligands such as benzoic acid (Figure 1.9) are used as modulators. While the foremost reason for using modulators is to produce large single crystals, modulators have also been used to enable the synthesis of kinetically disfavoured products.[47]

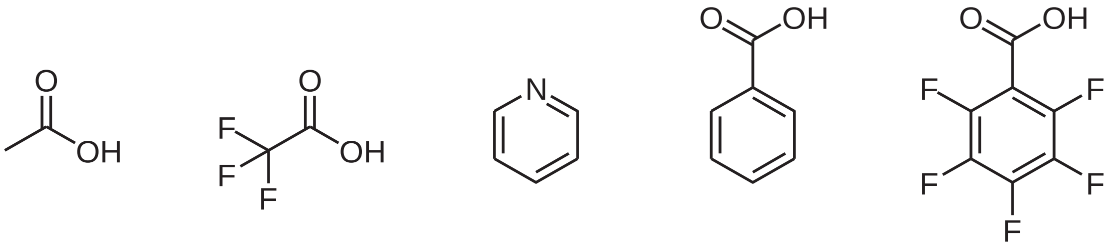

Figure 1.9 Examples of non-divergent modulators used in MOF syntheses.

1.2 Applications of MOFs

As Robson proposed in 1990,[3] MOFs have demonstrated thermal, chemical, and mechanical stabilities; high crystallinity; high porosity with low density; the ability to uptake and separate guest molecules within pores; resistance to post-synthetic modification (PSM) of the organic ligands; and catalytically active sites. It is these properties that have led to MOFs being developed for applications such as gas storage,[48-53] separation of gases and other compounds,[54-60] catalysis,[61-65] drug delivery,[66,67] chemical sensing,[68,69] photovoltaics,[70,71] biomedical imaging,[72]non-linear optics,[73,74] and semiconductors.[75,76] This is by no means a comprehensive list of potential MOF applications, and as more new MOFs are synthesised, an increasing number of applications are being found. A selection of noteworthy applications is introduced below.

1.2.1 Gas Storage and Separation

The resistance to the removal of solvent and high surface areas of MOFs predispose these materials to the adsorption of gas molecules, and thus their use in gas storage and separation. The first recorded instance of gas sorption in MOFs at low (sub-atmospheric) pressure was in Yaghi's 1998 paper, in which, after the removal of solvent molecules, MOF-2 demonstrated uptakes of ~120 cm^3/g (at STP) of N_2 at 77 K and ~80 cm^3/g (at STP) of CO_2 at 195 K.[77] From these humble beginnings, MOFs have since demonstrated dramatically higher uptakes, and various gas storage and gas separation application have been developed. This includes the use of a MOF as a hydrogen storage material in a hydrogen fuel cell powered car, the Mercedes Benz F125.[78] Many other practical applications for gas storage and separation by MOFs have shown great promise and many are undergoing the process of industrialisation and commercialisation.[79]

1.2.1.1 Natural gas storage

The primary component of natural gas is methane, which has the highest gravimetric energy density and lowest CO_2 emission per joule of energy produced of all fossil fuels. Methane is normally a gas at room temperature due to its low boiling point of 112 K. Furthermore, methane is impossible to liquefy at room temperature as its critical point is 190.6 K and 46 bar. This makes it challenging to increase methane's volumetric energy density to a point where it is useful for vehicular applications. Currently the most common technology compatible with the demands of vehicular applications is compressed natural gas (CNG). Whilst there are also liquefied natural gas (LNG) systems, these are operated at temperatures below the boiling point of methane, making them impractical for everyday vehicle use. CNG systems compress natural gas to 200-250 bar for use in on-board fuel tanks. Although this increases the volumetric energy density to over 2400 % of methane at atmospheric pressure, there are several drawbacks to this technology:

1. The high pressures of the system arouse safety concerns, especially in conjunction with the low flash point of methane.
2. Petroleum and diesel still have higher volumetric energy densities and use smaller fuel tanks.

3. CNG fuel tanks require thick walls in order to be safe, often negating any gravimetric energy density benefits.
4. CNG refuelling stations require very high operating pressures in order to pressurise the natural gas in the fuel tank. This is an expensive process, both in terms of the required infrastructure and in energy consumption.

Adsorbed natural gas (ANG) appears to be a promising alternative solution to overcoming the obstacles of methane's low volumetric energy density. ANG takes advantage of the greater concentration of gas molecules adsorbed to surfaces than that of gas molecules in the bulk gas phase by increasing the surface area present within a given volume. This is achieved by packing the gas tank with a porous material with a high internal surface area, and allows an ANG tank to store the same or greater amount of methane as a CNG system at much lower pressures. The reduced pressure of the system allows for thinner walled, and thus lighter, tanks to be used, often making ANG tanks lighter than CNG tanks despite the addition of the porous material. The lower pressure of ANG systems means that they are much safer and have lower operating costs than their CNG counterparts.

ANG tanks are already finding their way into vehicles. Though there are no commercially available ANG powered cars, Cenergy have demonstrated the ability to replace CNG tanks in multiple commercially available CNG vehicles at the 2016 ACT Expo, including a CNG dedicated Honda Civic GX.[80] Cenergy have used tanks packed with porous synthetic carbon to store concentrations of methane > 140 v/v at 298 K at 24 bar, and used these tanks to power vehicles, reporting that there was no observed difference in performance compared to petrol. Whilst the reported storage density is less than the target of 180 v/v at 298 K at 35 bar set by the United States Department of Energy,[81] it is occurring at just over ⅔ of the pressure. This potentially lowers the weight of the tank required and operation costs sufficiently to overcome the shortfall in volumetric storage. Though Cenergy do not state what form of synthesised carbon is used, their website mentions MOFs on their ANG technology page, strongly indicating that they are either using MOFs as the synthesised carbon (or the production thereof), or are developing technologies using MOFs. In terms of larger scale production, chemical giant BASF have developed ANG technology on an undisclosed MOF that is "ready to market",[79] however due to the lowering of the price of crude oil, these systems have not been released due to the lack of financial viability.

Due to the promise shown for ANG technology and its applications, MOFs are being developed for use in ANG and other gas storage applications. In order to determine if a MOF is suitable for gas storage, high pressure gas adsorption isotherms must be measured. In 1997, Kitagawa's group recorded the first high pressure isotherms for MOF materials, finding that the Co-bpy MOF synthesised had a volumetric methane uptake of 77 v/v STP at 30 bar (i.e. 77 mL of methane was taken up per mL of MOF).[82] Despite being lower than the target set by the US Department of Energy, the high uptake demonstrated indicated that MOFs have promise for gas storage applications. Whilst MOF-5 and MOF-177 demonstrated initial promise, it was not until 2007 that MOFs began to show their highest capacities. PCN-14, reported by Zhou's group, revealed a methane uptake of 230 v/v STP at 390 K and 35 bar.[83] Not only does this outperform the best known 200 v/v STP uptake for porous carbon, it is 28 % greater than the target set by the US Department of Energy. This is primarily achieved by the open metal sites revealed by the removal of coordinated water molecules. This has led to the investigation into the use of open metal sites in other MOFs to attain high gas storage capacities.[84,85]

Not only are new materials produced for novel applications, but old materials are examined using new techniques. This was how the Long and Hupp groups independently published their findings that HKUST-1 has the highest working capacity methane uptake among MOFs of 190 v/v STP, thanks to its high uptake of 227 v/v STP at 35 bar.[86,87] As with PCN-14 above, HKUST-1's high capacities are largely due to the open metal sites in the framework.

Despite apparently meeting the US Department of Energy targets, there are practical obstacles that need to be overcome if HKUST-1 is to be of use in gas storage applications. The first is that the packing efficiency of HKUST-1 is moderate at best, and would result in ~25 % of an ANG tank being unoccupied, effectively lowering the methane capacity to ~ 170 v/v, lower than the Department of Energy target. Secondly, other components of natural gas bind more strongly to open metal sites than methane which at the very least will decrease the uptake of the material or, in the case of water, destroy the MOF. Zr(IV) and Al(III) MOFs are being studied for gas storage applications as they are generally more resistant to hydrolysis than zinc(II) and copper(II) MOFs.

1.2.1.2 Gas separation

The predominant focus in the field of MOFs for gas separation is the selective adsorption of CO_2. CO_2 and water are the major exhaust components of the burning of organic compounds, such as fossil fuels. In order to match the increasing energy demands of today's society, the rate of burning of fossil fuels has increased, to the point where in 2014 global CO_2 emissions were at more than 35 Gton, nearly 60 % higher than in 1990.[88] Since CO_2 is a greenhouse gas, as the concentration of atmospheric CO_2 increases, so too will global temperatures. These elevated temperatures can lead to loss of habitats, rising water levels, and dramatic changes in global weather patterns. As such, it is highly desirable to reduce the amount of CO_2 present in the atmosphere. The main target of efforts to do so is to reduce the rate at which CO_2 is released into the atmosphere. The two main ways of achieving this are to either not generate CO_2 (through the use of nuclear power, hydroelectric power, wind power, solar power, electrochemical power, or through hydrogen combustion) or to prevent the CO_2 generated from escaping. It is for this latter purpose that MOFs with high selectivities for CO_2 are being developed.

The most practical and effective location to capture CO_2 released from the burning of fuels is in the exhaust pipe or flue. Flue gas is primarily comprised of N_2 (~70 %), with CO_2 comprising 10-15 % and water vapour at approximately 10-12 %, the remaining portion containing minor gases. Current technology for selectively removing CO_2 from flue gas involves the use of aqueous organic amine solutions. While this is highly effective in sequestering the CO_2, removal of CO_2 from a saturated solution is very energy intensive (taking ~30 % of the energy generated from burning coal[89]) due to the high temperatures required and the high thermal capacity of water. To circumvent this energy barrier to regeneration of the filtration material, MOFs are being investigated as porous adsorbents typically have lower CO_2 desorption energies than aqueous systems. MOFs are ideal candidates due to the tuneable nature of their pores and internal surface chemistries. Indeed, there are already examples of MOFs with better performance than current technologies.[90]

In order for a MOF to be suitable for CO_2 capture there are four key features that should be present:

1. The material should be highly selective for CO_2 over all other compounds likely to be present in flue gas (especially N_2 and water).
2. The MOF needs to be stable at the elevated temperatures and humidities of flue gas conditions. The material should be especially hydrolytically stable as the MOF is likely to become saturated by water vapour since it will be acting as a filter.

3. The working capacity (i.e. the range between the maximum uptake and the amount of CO_2 left after regeneration) should be as large as possible.
4. The energy required to regenerate the MOF should be as low as possible. Typically, this means as low a temperature as possible, and implies that the adsorption enthalpy should be as low as possible whilst still meeting all other criteria.

Researchers in the field of MOF chemistry have developed many ways to improve the selectivity of CO_2 over other adsorbates. Open metal sites have been shown to improve CO_2 selectivities,[91,92] however MOFs with open metal sites are often prone to hydrolysis (*vide supra*). It is possible to tune the window size of pores to allow CO_2 (kinetic diameter = 3.3 Å) to pass through but not N_2 (kinetic diameter = 3.64 Å),[93] however this can result in permeability issues and also does not prevent water (kinetic diameter = 2.68 Å) from passing through the pores. It is possible to introduce polar functional groups and/or tune pore size to enhance CO_2 adsorption,[25,94] however it is possible to make the interactions between the framework and CO_2 so strong that regenerating the MOF becomes energy intensive.

With so many properties that need to be balanced, it is sometimes necessary to approach the problem from a novel direction. Long's group did just that, and in 2015 they reported a series of "phase changing" MOF adsorbents.[90] In this work they reported the functionalization of an extended MOF-74-type (Zn_2(2,5-dihydroxy-1,4-bdc)) using 2,5-dihydroxy-4,4'-biphenyldicarboxylate through the coordination of N,N'-dimethylethylenediamine to the open metal sites of the MOF. This enables the insertion of CO_2 into the metal-nitrogen bond to form a carbamate bound to the metal ion. The spacing of these groups within the MOF promotes cooperative binding of CO_2 as the carbamates are stabilized through the interaction with the terminal nitrogen of an adjacent carbamate ligand. This is observed by the negligible low pressure CO_2 uptake of this material followed by a sharp increase in CO_2 uptake over a small pressure range. This material is remarkable in that, not only does it have an exceptional high working capacity due to the cooperative CO_2 binding, but it can do so at elevated temperatures and with little to no effect from saturated water vapour. Furthermore, the energy required to regenerate this system is low, thanks to the small temperature increase required to desorb the CO_2. This material is currently being developed for use in coal power plants by a company founded by the Long group for the purpose.

1.2.2 Catalysis

The highly tuneable and porous nature of MOFs makes them prime candidates for use as heterogeneous catalysts. Due to the ability to bring multiple functionalities together within a single MOF, MOFs have been investigated by many researchers for their future use as artificial enzymes.[95] Artificial enzymes are materials that have been developed to mimic enzyme activity. This can be desirable if the enzyme is unstable or expensive to extract, as well as offering the ability to improve/alter selectivity and/or reactivity. For example, due to the potential of H_2 as a fuel, hydrogenases are a target for artificial enzymes as they are able to produce H_2 through the reduction of water.[96] However, model systems of the hydrogenase active site are known to be unstable, especially when the process is driven photochemically.[97] In 2013, the groups of Cohen and Ott published their collaborative work on the incorporation of a 2,3-dithiolate-1,4-bdc-bound $[Fe-Fe](CO)_6$ complex into UiO-66 through PSE.[98] Not only was it found to be a functionally active catalyst, the functionalised MOF (UiO-66-[Fe-Fe]) was more catalytically active than the unbound catalyst. This was attributed to the stabilising effect of the framework as well as the framework restricting undesirable charge recombination of the reduced catalyst with oxidized ascorbate.

Another reaction of interest is the reduction of CO_2 to generate fuel as it would allow for the conversion of an undesirable waste product into a material of use.[99] In 2015, the Cohen and Kang groups presented their collaborative work on UiO-66 as a scaffold for CO_2 reduction catalysts. First, a functionalised UiO-66 analogue was obtained by combining $ZrCl_4$ with 1,4-bdc-NH_2 and *para*-1,4-bdc-$(NH_2)_2$ to obtain UiO-66-NH_2 with an approximately 6:1 ratio of 1,4-bdc-NH_2 to *para*-1,4-bdc-$(NH_2)_2$. The diamine species was included as it was found to improve the light absorption of the material, and thus enhance the photocatalytic activity. The material was then soaked in DMF solutions of $TiCl_4$ in order to PSE with Ti^{4+}, resulting in a 2.5:1 ratio of Zr^{4+} to Ti^{4+}. The Ti^{4+} was included to act as the catalytic active site of the MOF as it is able to accept electrons generated by the absorption of light by the ligands. This resulted in a robust photocatalytic MOF without the need for an external light sensitizer. The MOF demonstrated average turnover numbers of 6.27 with no discernible loss of catalytic activity after three cycles, more than four times greater than the turn over number of 1.52 for NH_2-MIL-125(Ti) reported by Horiuchi *et al* in 2012.[100]

1.3 Introduction of functionality into MOFs

1.3.1 Functional Groups in MOFs

The ability to incorporate functional groups into MOFs has long been known and is the subject of intense research efforts. Not only does this allow for an unprecedented degree of diversity amongst porous materials, the ability to tune the chemical nature of pore environments allows researchers to rationally design MOFs to have specific, and pre-determined properties. However, what can be formulated on paper and what is possible are not always the same, and as such researchers are constantly developing new methods of ligand and MOF synthesis to enable access to as many materials as possible. This section will outline various methods currently used to install functional groups into MOFs.

1.3.2 Direct incorporation

As with many things, the simplest solution to a given problem is the most desirable, which in this case means synthesis using a ligand containing an active functional group. Many MOFs, such as MOF-5 and UiO-66, are resistant to a wide variety of functional groups, and as such their functionalised analogues are able to be directly synthesised (i.e. without using protecting groups) with relative ease. This is not always the case, especially when the functional group in question is a strong metal binding group such as a carboxylic acid, as this allows for the functional group to compete with the binding groups for the metal ions. At best this will result in metal ions bound to the functional groups of the target MOF, though the more likely result is the synthesis of a different phase or no MOF at all.

Not only must the MOF be resistant to the presence of the functional group during synthesis, the functional group itself must be able to survive the synthesis conditions. This often affects thermally or hydrolytically unstable functional groups due to the presence of water and elevated temperatures in solvothermal syntheses. When encountering this problem, researcher will typically try modifying the reaction conditions, such as reducing the temperature or changing the solvents used, before abandoning the direct synthesis approach.

1.3.3 Post synthetic modification (PSM)

When incorporating the functional group during MOF synthesis is not possible, a common technique is to install the functionality after synthesis. Whilst PSM covers virtually anything that chemically alters the framework after synthesis, such as metal ion exchange and de-solvation of open metal sites, this section will focus on PSM techniques that install functional groups on the organic ligands. One of the most common PSM methods requires the use of a ligand containing a site that, whilst able to have a functional group affixed to it, is compatible with the synthesis of the desired framework. This ligand is then used in direct synthesis to obtain a MOF with the functional group precursor in the pores. After synthesis, the MOF is then treated with the appropriate reagent to generate the desired functional group *in situ*. Whilst there are numerous examples of this technique working, there are significant drawbacks to this method:

1. It requires a functional group precursor that is compatible with MOF synthesis
2. Conditions required to converted the precursor into the active functional group can be harsh and can lead to degradation of the MOF framework.
3. There is often <100% conversion to the active functional group due to the need for chemical species to penetrate deep into the MOF framework in order to access every site.

In short, whilst this method can be effective, it is by no means universally applicable, and as such has limited applications.

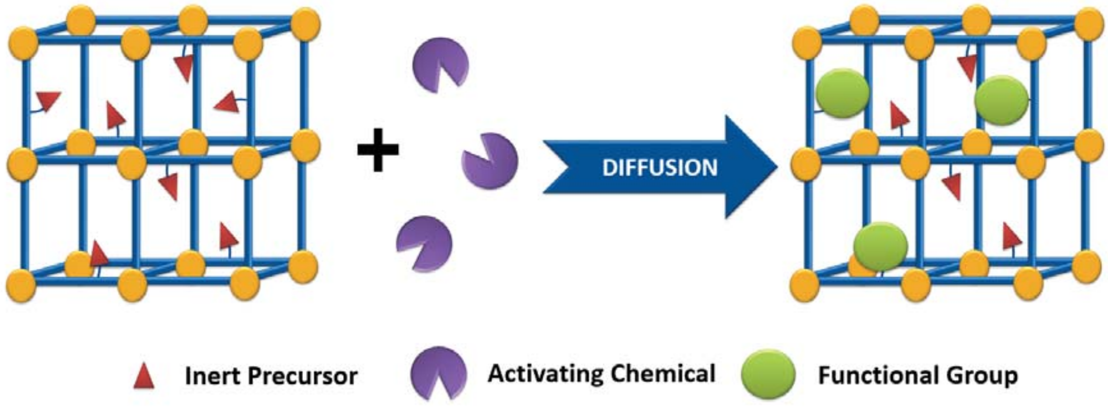

Figure 1.10 Schematic illustrating how in post synthetic modification not all inert precursors are necessarily converted to the active functional group.

1.3.3.2 Post-synthetic exchange (PSE)

PSE is a subsection of PSM, where instead of adding functionality to the ligands in the framework, ligands with the desired functional group are added to the synthesised framework. This typically happens in one of two ways; the functionalised ligand either displaces solvent molecules coordinated to the metal centre, or the functionalised ligand displaces its unfunctionalised analogue that was used in the MOF synthesis. Whilst typically gentler than the conditions required to covalently add the functional group (*vide supra*), this method has its own drawbacks:

1. It requires either that the MOF have open metal sites capable of ligand insertion, or that the ligands are sufficiently labile to allow for exchange.
2. As this method is diffusion and equilibrium driven, it is possible to have incomplete exchange, reducing the loading of functional group in the MOF.
3. This method can consume a large amount of functionalised ligand as high concentrations are required to maintain the concentration gradients to drive the

process. Also, the ligand solution may need to be exchanged multiple times if there is significant competition from the species being displaced.

4. This method often takes days-weeks to achieve complete ligand exchange.

Points 2 and 3 are the biggest drawbacks as reduced loading of functional groups is rarely desirable, and requiring large amounts of ligand can be problematic if the ligand is expensive and/or hard to synthesise. In addition, point 3 is a big drawback for industrial scale synthesis as, unless the ligand can be efficiently recovered, the process is very wasteful.

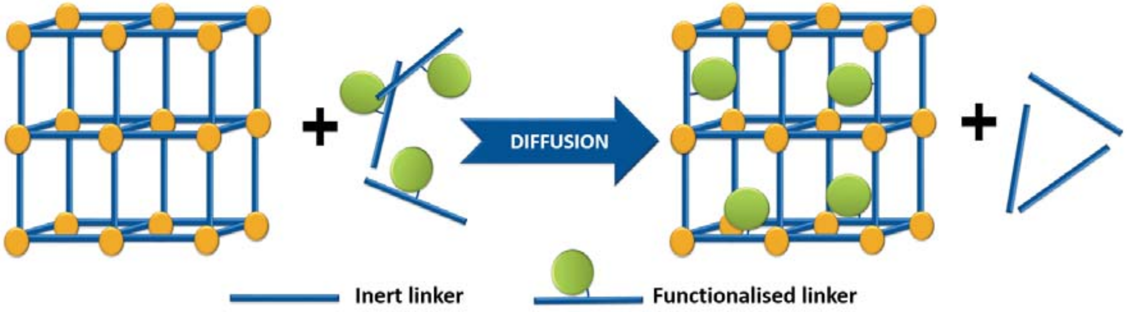

Figure 1.11 Schematic illustrating how in post synthetic exchange (PSE) not all inert linkers are necessarily exchanged with functionalised linkers.

1.3.3.3 Protecting Groups

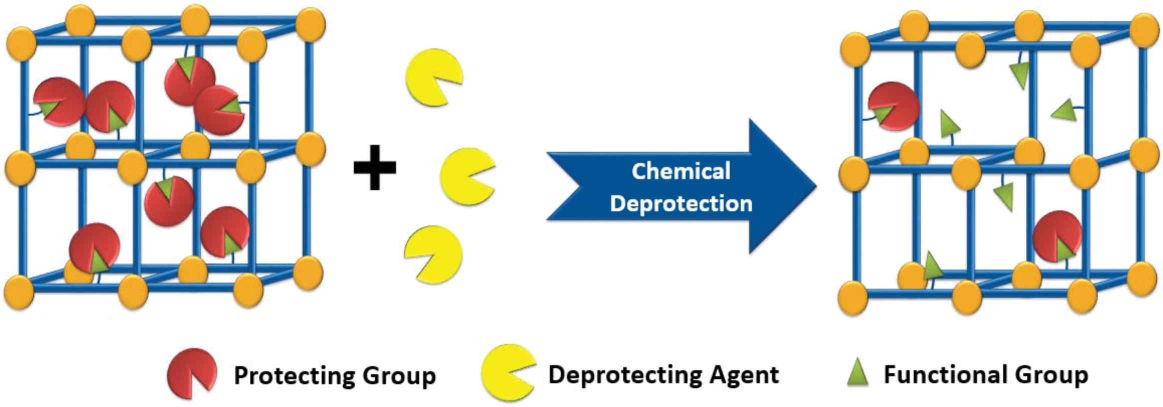

Figure 1.12 Schematic illustrating how chemical deprotection may leave some protecting groups intact and/or cause structural damage to the MOF as indicated by the defects.

An integral part of organic chemistry, protecting groups (PGs) are used to shield a functional group from conditions that would destroy the functional group, either through side reactions or degradation.[101] Many MOF synthesis conditions can also destroy functional groups, making PGs an obvious choice for incorporating functionality into MOFs. As such they have seen wide use in MOF synthesis. The ligand containing the functional group is protected with a PG, and then the ligand is used in MOF synthesis.[102-104] The MOF, now containing the protected functional group, is treated with a deprotecting agent to remove the PGs and reveal the active functional group. Whilst this method is more widely applicable than installing the functional groups after synthesis, it can still suffer from the same incomplete conversion and structural damage depending on the conditions required and the framework in question.

1.4 Thermolabile Protecting Groups (TPGs)

1.4.1 Overview

TPGs, as the name suggests, are a type of PGs whose deprotection can occur through solely the application of heat to the compound. These are ideal candidates for use in MOFs as, like regular PGs, they are able to ensure that a protected ligand is present with 100 % occupancy of protected functional group. At the deprotection step, TPGs have an advantage over conventional PGs in that the transfer of heat is more evenly distributed throughout the MOF than the chemical deprotecting agents typically are as heat does not need to navigate the pore like chemicals do. Furthermore, as MOFs typically demonstrate significant thermal stability (*vide supra*), the conditions required to thermolytically cleave the TPGs are often less destructive to the MOF framework than the chemical deprotection conditions required for PGs.

Due to the many names used to describe the process of thermolysis (such as thermal deblocking, pyrolysis, thermal degradation), a comprehensive literature analysis of TPG is difficult. For example, a literature search of SciFinder found only 35 references for the term ‘thermolabile protecting group’, and it should be noted that several of these did not actually refer to thermolabile protecting groups. In addition to the often multiple uses of these terms, the challenge is further compounded by the issue that the majority of these thermolyses occur in solvent, and often with the addition of a catalyst. These conditions are vastly different to the solvent-free environment of the desolvated MOF materials on which the thermolyses in this work were conducted. These factors have meant that an accurate overview of all TPG use is not possible, and as such important examples, such as the first use of TPGs or breakthroughs in TPG usage, may have been omitted. Furthermore, the term TPG itself is a potentially ambiguous term. For the sake of this work, a PG is only considered to be a TPG if thermolysis occurs solely as the result of elevated temperatures, and that the TPG is removed prior to any subsequent reactions. This does not exclude the thermolysis of TPGs in solvent, as it is often desirable to generate the functional groups *in situ* to prevent undesired reaction/degradation, though it should be possible for the thermolysis to be solvent-free. The use of a catalyst or activating agent precludes the term TPG as essentially the reaction is then a generic deprotection occurring at elevated temperatures. It is with the preceding caveats that the following overview of TPG use is presented.

1.4.2 Use of TPGs in organic compounds

It has been over 60 years since the first review on blocked isocyanates by Petersen.[105] Due to their use in polymer chemistry, the majority of subsequent publications relate to industrial applications, with a 1999 review paper by Wicks and Wicks stating that of their own literature search that more than 90% of the >2,600 publications found were patents.[106]

Chmielewski has published numerous publications and patents involving TPGs.[107-112] The majority of these are involved in DNA synthesis (see section 1.4.3), however some have broader applications, such as their 2015 paper demonstrating the use of the 2-pyridinyl-N-(2,4-difluorobenzyl)aminoethyl TPG to protect carboxylic acids.[111] This TPG is intriguing in that the deprotection is driven by a thermally induced cyclization within the TPG that ejects the carboxylic acid as a leaving group. Whilst the TPG did not perform uniformly well across all protected species, two of the protected species were fully deprotected after 2 hours at 90 °C, which shows there may be promise for this TPG for protecting carboxylates. Chmielewski's 2015 paper demonstrates the use of the 2-pyridinyl TPGs to protect nucleosides.[110] This class of TPG is intriguing in that the deprotection is driven by a thermally induced cyclization within the TPG that ejects a carboxylic acid as a leaving group. What is more impressive, however, is the ability to tune the thermostability of these TPGs. Figure 1.13 illustrates how pH can be used to alter the thermolability of the TPG. This property allows for greater control over when the thermolysis can occur, and as such is a highly desirable feature.

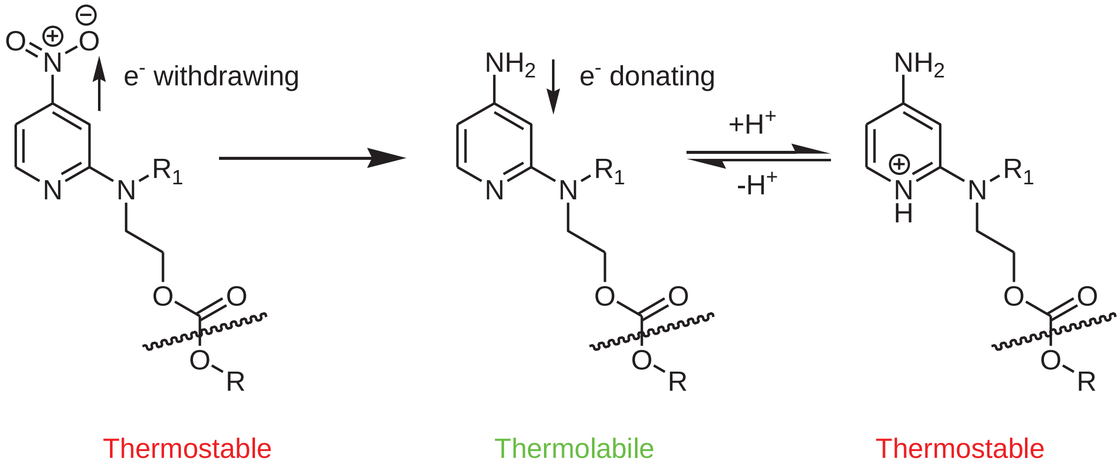

Figure 1.13 General scheme outlining the ability to tune the thermostability of 2-pyridyl TPGs.

1.4.3 Use of TPGs in DNA synthesis

Whilst the majority of naturally occurring DNA exists at or near room temperature, DNA artificially synthesised in a polymerase chain reaction (PCR) process will be typically heated to temperatures between 50-95 °C throughout various phases of the cycles. It is at these temperatures that *Taq* DNA polymerase will duplicate the desired DNA strands. As DNA nucleobases are expensive, it is desirable to protect the materials with PGs to prevent primer extension at ambient temperatures during sample preparation. Whilst in a DNA synthesiser these PGs are cleave chemically, this is not possible in PCR reactions as this can result in errors. TPGs are very useful here as they are stable at ambient temperatures, but labile at the elevated temperatures of the PCR process. In a 2009 paper[113], Koukhareva and Lebedev presented their findings that by reacting nucleosides with dihydrofuran they were able to protect nucleosides at the 3' position with a THF ester. They found that the THF TPG was stable at ambient temperatures, yet was readily and efficiently cleaved at the elevated temperatures of the PCR process. Furthermore, they found that the THF released, as well as any other thermal degradation products that may have formed, had no apparent effect on the accuracy of the PCR experiments.

1.4.4 Use of TPGs in polymers

Due to the prevalence and importance of polymers in today's society, there have been a great many publications on the various methods of polymer synthesis. These include the use of PGs (referred to as blocking groups by the field) to protect functional groups during synthesis, either to activate the functional groups post polymer synthesis, or to aid in multi-step syntheses where it is desirable to induce cross-linking in pre-formed polymers. Although there are many and varied methods of deprotecting PGs in polymers, this section will focus only on those relevant to TPGs.

A widely utilised method in polymer chemistry is to "block" isocyanates for use in cross-linking reactions, since it is often possible to both "deblock" and cross-link the polymers under the same conditions in a one-pot process. Not only does this simplify the cross-linking process, it allows for the production of simple one package (1K) coatings. 1K coatings have many advantages over two package (2K) coatings, such as the elimination of using improper ratios of the two components, reduction in waste and capital costs to the applicator, and are usually significantly less toxic.[114] 1K coatings also have their disadvantages, including that the temperatures required to cure 1K coatings are significantly higher than those required for 2K coatings, resulting in higher energy costs for the applicator as well as 1K coatings not being suitable for all surfaces. Isocyanates are a favoured blocking agent in 1K coatings as they able to be cleaved thermally without the presence of solvent or catalyst. A prime example of TPG use in powder coatings is the use of ε-caprolactam (CL) blocked isophorone diisocyanate (IPDI) and/or IPD isocyanurate (Figure 1.14) with polyols to form polyesters and acrylics that can later be induced to cross-link and form polyurethanes by heating. A 2001 review by Wicks and Wicks on the applications of blocked isocyanates,[114] and a great many patents involving CL blocked IPDI have been published, providing examples of patented processes[115] and materials.[116,117]

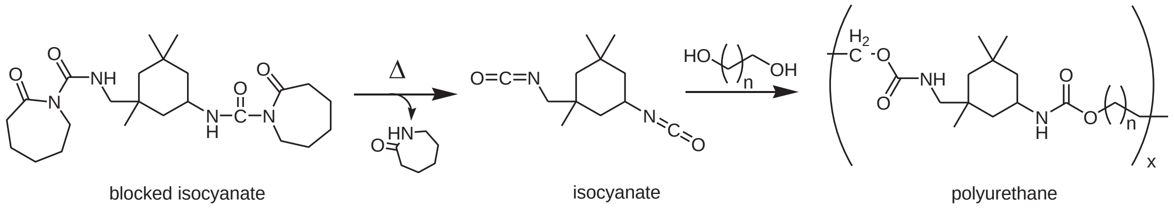

Figure 1.14 Thermolysis and subsequent polymerisation of CL blocked IPDI with an alkyl diol to produce a polyurethane.

Powder coatings are not the only uses for blocked isocyanates in polymers. TPG blocked isocyanates have also been used in coil coatings,[118,119] automotive coatings,[120,121] wire insulating coatings,[122] coatings for plastics,[123] adhesives,[124] sealants,[125] textiles,[126] and plastics.[127] For a more in-depth look at blocked isocyanates in polymers, the author recommends the two-part review series by Wicks and Wicks.[106,114]

1.4.5 Use of TPGs in MOFs

In order for a TPG to be suitable for use in MOFs it must be sufficiently stable to withstand the MOF synthesis, yet sufficiently labile to be thermally decomposed at temperatures below which MOF degradation can occur. As such thermogravimetric analysis (TGA) is a critical tool in the evaluation of TPGs for use in MOFs. However, the results can only ever be used as a guide since the conditions found in solvothermal syntheses are vastly different to those found inside a TGA instrument. Nonetheless, TGA is a useful screening tool, not only for TPGs in the free ligand, but also for the thermolysis conditions once the TPG is in the MOF as this has been observed to cause large changes in the thermal deprotection temperature (see Chapters 2 and 3).

To the best of our group's knowledge, the first published works involving thermolabile protecting groups and MOFs are the 2010[102] and 2011[103] papers published by the Telfer group. The 2010 paper investigated the installation of 2-*tert*-butoxycarbonylamino-4,4'-biphenyldicarboxylate (bpdc-NHBoc) into IRMOF-10[10], and its subsequent thermolysis to generate 2-amino-4,4'-biphenydicarboxylate (bpdc-NH_2). IRMOF-10, which is non-interpenetrated, typically requires dilute conditions to form as it is prone to interpenetration and instead forms IRMOF-9. However, the bulkiness of the TPGs in this instance suppressed the interpenetration. The 2011 paper also reported a non-interpenetrated framework, but this time with a proline functionalised bpdc protected by a Boc group. Direct synthesis of IRMOF-Pro without the use of the protected ligand was not possible. Furthermore, the proline moiety was shown to be catalytically active after thermolysis of the TPG. It is on these seminal works that this thesis builds on, expanding the library of ligand backbones beyond bpdc, utilizing TPGs other than Boc, and protecting non-amine species.

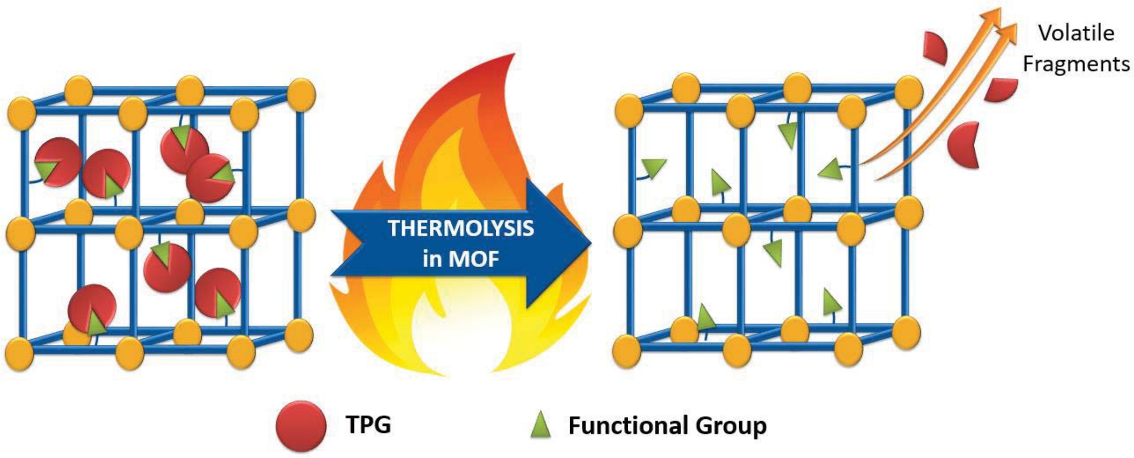

Figure 1.15 Schematic illustrating the general principles around TPGs in MOFs.

These seminal papers initiated the start of a new field of research, with many subsequent new papers reporting the use of TPGs in MOFs.[128-137] Typically they have been installed on ligands used directly in MOF synthesis, though there are examples of their use on ligands that bind to open metal sites after synthesis of the MOF. For example, the Feng group used ethylenediamine with one nitrogen protected as the *tert*-butyl carbamate (Figure 1.16) to bind to an open Cr site in MIL-101-Cr.[136] These works have also increased the variety of functional groups protected with TPGs. The Yaghi group have demonstrated the use of Boc to protect secondary amines[128], the Nguyen group has also used Boc to protect a hydroxyl moiety,[134] and the Kurmoo group have protected an terminal alkyne as a secondary alcohol.[131] These works have also expanded the library of ligand backbones to include nonlinear ditopic carboxylates,[132,133] tritopic carboxylates,[137] and mono[130,135] and ditopic[131,134] N-donor type ligands. Increasing the diversity of TPG-containing ligand backbones is essential if TPGs are to be more widely utilised. Not all of these results were successful, with the Fröba group finding that their diisophthalate based materials collapsed under the conditions required to remove the TPGs.[132]

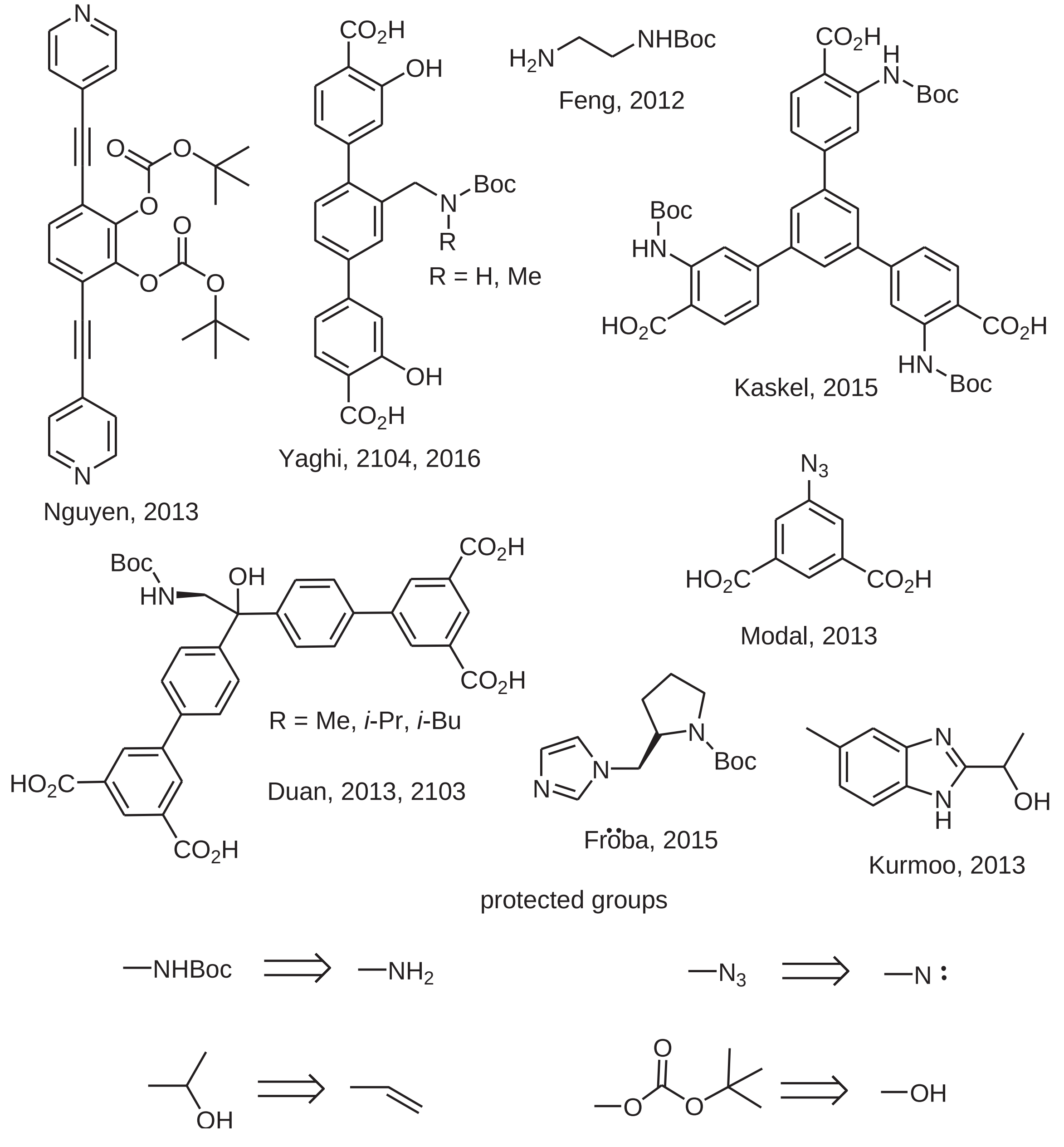

Figure 1.16 Examples of TPG-containing ligands from the literature.

1.5 Introduction to selected experimental techniques

1.5.1 Gas Adsorption

1.5.1.1 Process

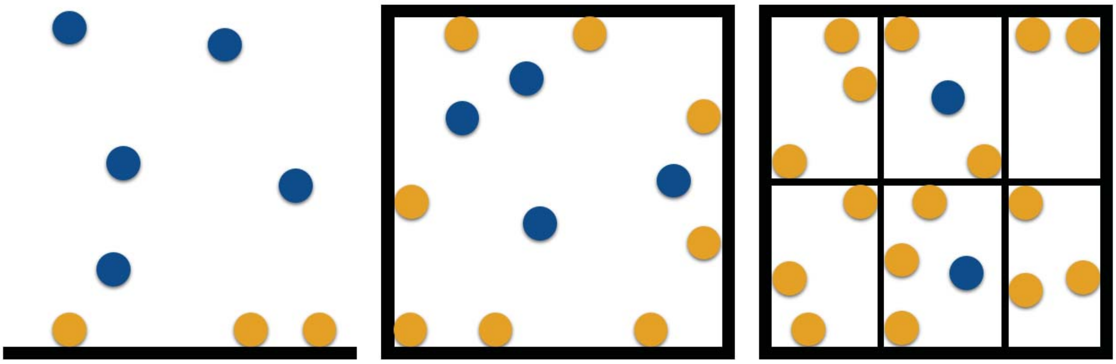

Figure 1.17 Schematic illustrating that as the surface in a given area increases, so does the amount of adsorbed gas. Gold spheres = adsorbed gas molecules, blue spheres = free gas molecules.

Gas adsorption is the process in which gaseous molecules adhere to the surface of a material. Adsorption differs from absorption in that adsorption is a strictly surface only phenomenon whereas absorption involves the entirety of the material. As such, as the surface area within a given volume increases, so too does the amount of adsorbed gas, as illustrated in Figure 1.17. Gas adsorption is typically physisorption as no formal bonds are formed, however there are rare examples where chemisorption has occurred.

Gas adsorption profiles are reported as adsorption isotherms, in which loading of a gas at a given temperature is recorded as a function of pressure of the system at a fixed temperature. This is necessary since as gas adsorption is highly dependent on the temperature of the system. Many theoretical models have been developed in order to describe gas sorption isotherms, and these include the Henry, Langmuir, and Brunauer-Emmett-Teller (BET) models.

1.5.1.2 BET surface area calculations

BET surface areas are the most widely accepted method for calculating and comparing a material’s apparent surface area. The values are usually calculated using the material’s nitrogen isotherm at 77 K, though there are instances of researchers using CO_2 isotherms measured at 195 K. Often the entire isotherm does not fit with the BET model, and researchers are forced to choose apparently linear regions in order to obtain a reportable value. Due to the nature of the BET calculation, the apparent surface areas calculated can vary tremendously depending on the region selected. This is why Walton and Snurr proposed the following procedure for deciding what range of data is appropriate for BET calculations[138]:

1. First, the isotherm region where $v(1 - P/P_0)$ increases with respect to P/P_0 (v is amount of N_2 adsorbed). P/P_0 is the ratio of P, the pressure of the system at each point in the measurement, and P_0 is the condensation pressure of the adsorbent at the temperature of the measurement.
2. Next, $\frac{P/P_0}{v(1-P/P_0)}$ was plotted against P/P_0 using sequential data point that led to a positive intercept b and a slope a. $\frac{1}{a+b}$ is equal to the number of gas molecules adsorbed in the initial monolayer (v_m).
3. The BET surface area (A_{BET}) was then calculated using the following equation:

$$A_{BET} = v_m \left(\frac{cm^3}{g}\right) * \frac{1\ (mol)}{22400\ (cm^3)} * \sigma_0\ (\text{Å}^2) * N_A\ (mol^{-1}) * 10^{-20}\ (\frac{m^2}{\text{Å}^2})$$

N_A is Avogadro’s constant and σ_0 is the cross-sectional area of a N_2 molecule (16.2 Å^2).

1.5.1.3 Gas sorption apparatus

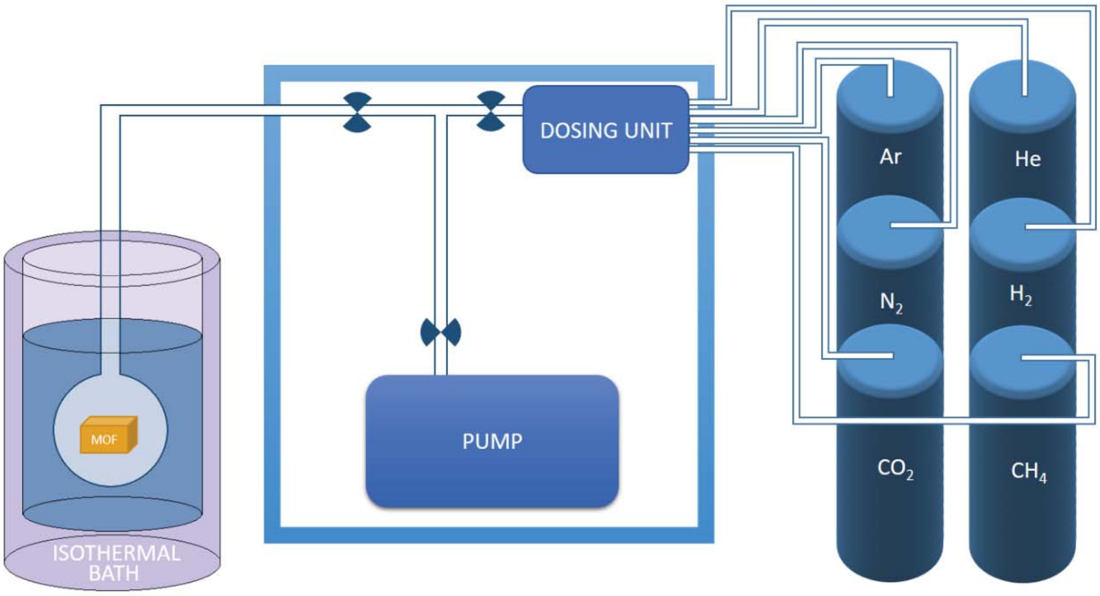

Figure 1.18 Schematic showing essential components of a gas sorption analyser.

Figure 1.18 illustrates the key components of a gas adsorption analyser. A glass sample tube containing the sample is evacuated under high vacuum and immersed in a bath with a constant temperature. The analyser then doses known amount of adsorbent into the sample tube, and reads the pressure frequently. Once the pressure reaches a constant value, equilibrium has been reached between the adsorbed and non-adsorbed molecules. The difference between the expected pressure calculated using the known dosage amount and the ideal gas law and the measured pressure is used to calculate the amount of adsorbed gas. This process is repeated for each data point in the instructions until a full isotherm has been recorded.

1.5.1.4 Reliability of measurements and calculations

The reliability of the gas adsorption measurements was investigated by a previous student, Lujia Liu. He found that with our Quantachrome Autosorb iQ2 instrument, the standard error was only 0.12 % of the mean value, meaning that the size of the symbols used on the isotherm plots were typically larger than the uncertainties for each data point. Sample preparation, activation, and handling all have significantly higher impacts on gas sorption measurements, and care must be taken to ensure proper sample protocol is followed. Using BET calculations, it is possible to compare with values previously obtained, either by our group or from the literature, to determine if the uptake has been impacted by how the sample was prepared/activated/handled. There is still the caveat that the choice of points used for BET calculations may lead to discrepancies. Linear regression using a least squares method produces standard deviations for the slope and intercept values, providing good estimate of the uncertainty of the BET surface area.

Chapter 2 -Thermolabile Protecting Groups in MOF-5

2.1 Introduction

As outlined in Chapter 1, the use of thermolabile protecting groups (TPGs) in MOFs, though a growing field, is not widespread. The aims of this work are to increase the diversity of ligands and MOFs that bear TPGs.

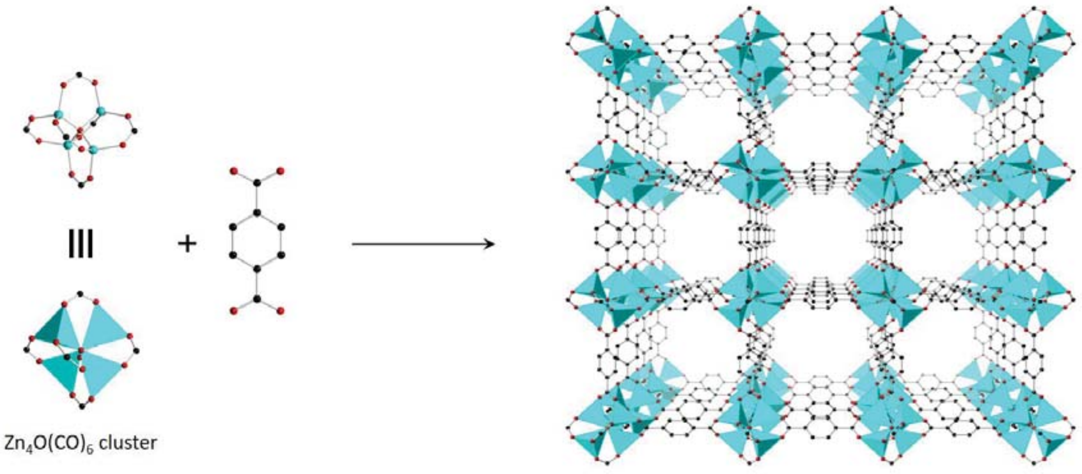

Figure 2.1 A scheme outlining the conceptual route to MOF-5 by linking 1,4-bdc with tetranuclear zinc(II) nodes. On the right is the MOF-5 structure determined by single crystal x-ray diffraction (SXRD). Atom colours: zinc = teal, carbon = black, oxygen = red (hydrogens omitted for clarity).

As a starting point, it was decided to first attempt the synthesis of MOF-5 analogues that bear TPGs, given that MOF-5 is the prototypical MOF.[35] MOF-5 is a cubic MOF, and is comprised of a Zn_4O cluster to which six 1,4-bdc ligands are bound, each through one of

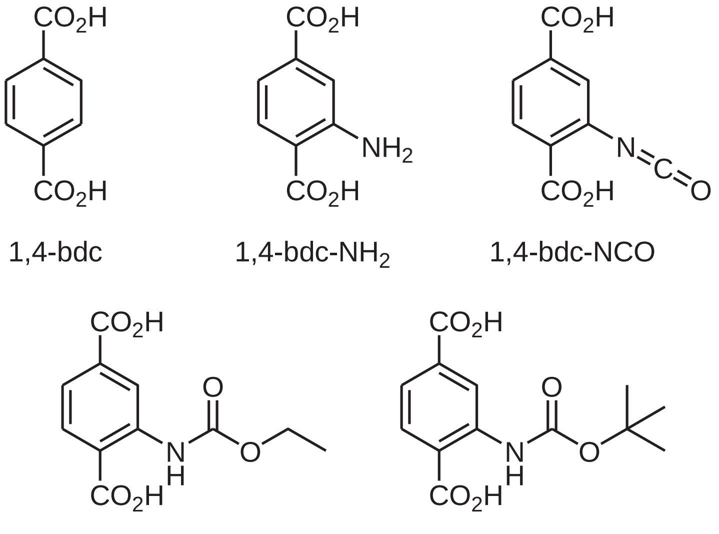
1,4-bdc

1,4-bdc-NH_2

1,4-bdc-NCO

1,4-bdc-NHCOOEt

1,4-bdc-NHBoc

Figure 2.2 Ligands involved in the synthesis of MOF-5 and its analogues relevant to this work.

their carboxylate groups. The free carboxylate groups of the 1,4-bdc ligands are then bound to successive Zn_4O clusters, which then bind more 1,4-bdc ligands, and this pattern continues, building up into the cubic network shown in Figure 2.1. Also known as IRMOF-1, it is part of a series of isoreticular MOFs (IRMOFs), where by increasing the length of the ligand, the Yaghi group were able to obtain extended materials with the same topologies.[10] Here, the term isoreticular means that the frameworks have the same topology despite being comprised of different ligands. MOF-5 has been used as a platform for catalysis,[139-142] a material for gas storage and separation,[143-145] and as a model system with which to perfect techniques to gain better insights on MOFs.[146-148] As the material is compatible with a wide range of ligand functionalities that do not impact MOF formation,[149] it was deemed an ideal framework on which to perform proof of concept work.

It was decided to protect 1,4-bdc-NH_2 with carbamate esters for several reasons: our group has successfully protected amines with carbamates in the past,[102] it was envisaged

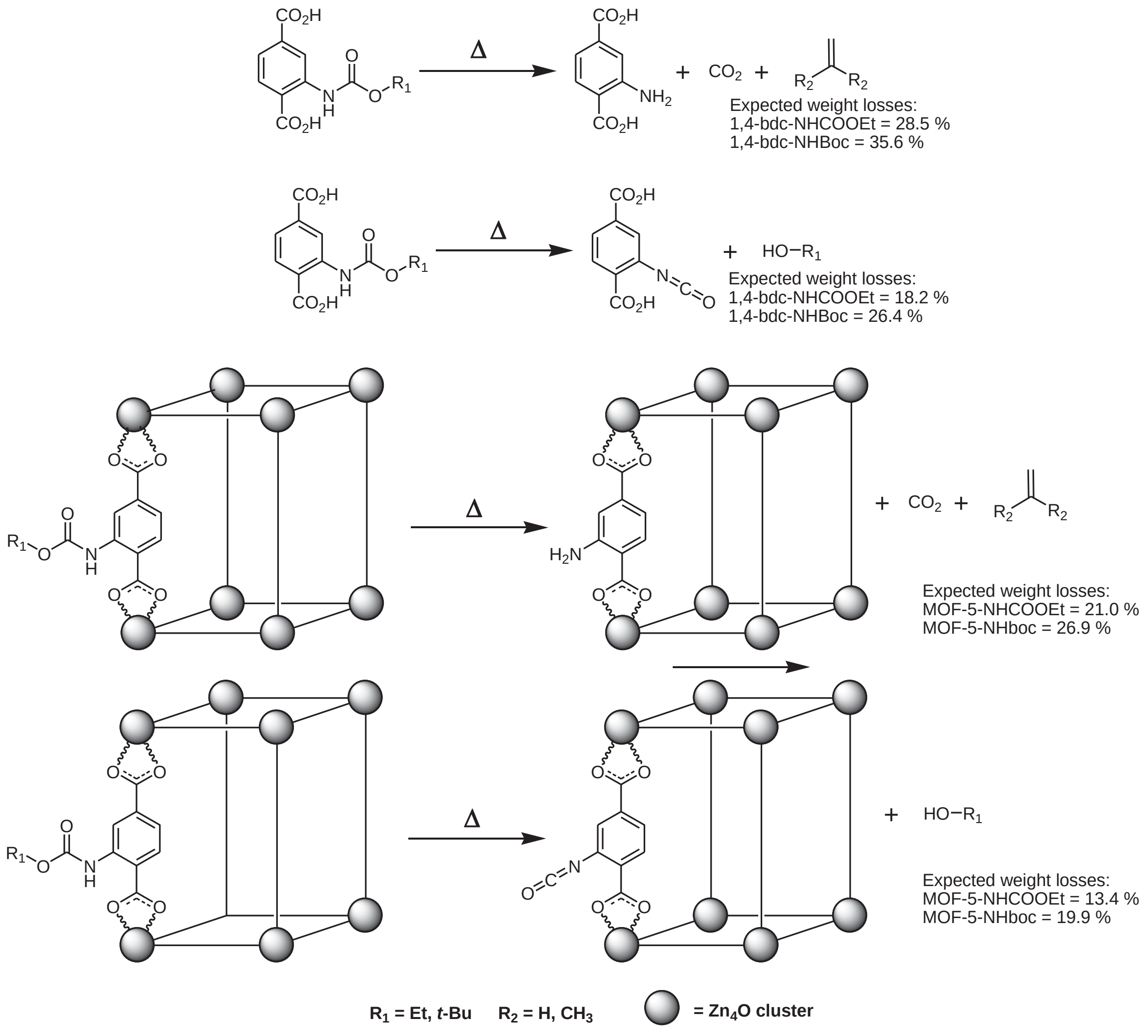

Expected weight losses:
1,4-bdc-NHCOOEt = 28.5 %
1,4-bdc-NHBoc = 35.6 %

Expected weight losses:
1,4-bdc-NHCOOEt = 18.2 %
1,4-bdc-NHBoc = 26.4 %

Expected weight losses:
MOF-5-NHCOOEt = 21.0 %
MOF-5-NHboc = 26.9 %

Expected weight losses:
MOF-5-NHCOOEt = 13.4 %
MOF-5-NHboc = 19.9 %

Figure 2.3 General schemes for thermal deprotection of carbamate esters depicting amine and isocyanate products for the free ligands (top) and MOFs (bottom), including expected weight loses.

that thermolysis of one or more of the TPGs could produce reactive functional groups (*vide infra*), and it was envisaged that the TPGs might impose ordering of the functional groups not seen in other MOF-5 analogues such as the amino functionalized IRMOF-3.[10] Thermolysis of the TPGs in Figure 2.2 can proceed to either the amine through loss of CO_2 and either ethene or isobutylene, or to the isocyanate (1,4-bdc-NCO) through loss of either EtOH or *t*-BuOH (Figure 2.3). According to a 1999 review paper by Wicks and Wicks on blocked isocyanates, alcohols are excellent PGs for isocyanates with the exception of tertiary alcohols, which instead form the amine upon deprotection.[106] This suggests that thermolysis of 1,4-bdc-NHCOOEt will generate 1,4-bdc-NCO, whereas 1,4-bdc-NHBoc is more likely be converted to 1,4-bdc-NH_2. When incorporated into a MOF-5 analogue this represents a new methodology for introducing isocyanate and amino groups into such frameworks.

2.2 Results and discussion

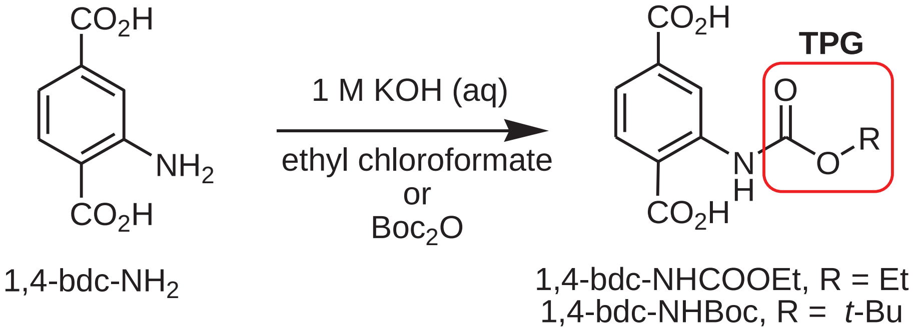

Figure 2.4 General synthetic route to 1,4-bdc-NHTPG ligands.

Ethyl chloroformate or Boc_2O was added dropwise to a solution of 1,4-bdc-NH_2 in aqueous KOH (1 M) to obtain 1,4-bdc-NHCOOEt and 1,4-bdc-NHBoc, respectively (Figure 2.4). A similar synthesis of 3-ethoxycarbonyl-benzoate was reported by Goswami *et al*. in 2001,[150] and a similar synthesis of 3-*tert*-butoxycarbonylaminobenzoate was reported by Khan *et al.* in 2012.[151] Interestingly, whilst there are no reported syntheses of 1,4-bdc-NHBoc, Volkringer and Cohen were able to post synthetically convert 1,4-bdc-NCO to 1,4-bdc-NHCOOEt by refluxing MIL-53(Al)-NCO in EtOH.[152] To our knowledge this is the first reported synthesis of 1,4-bdc-NHCOOEt as the free ligand. The ligand syntheses were facile with yields >90%, however there was difficulty in removing unreacted starting material (1,4-bdc-NH_2) from the products due to the similar solubility properties of the products and starting material. Eventually a recrystallization from hot methanol was settled upon that reduced the amount of 1,4-bdc-NH_2 remaining to $\leq$5%.

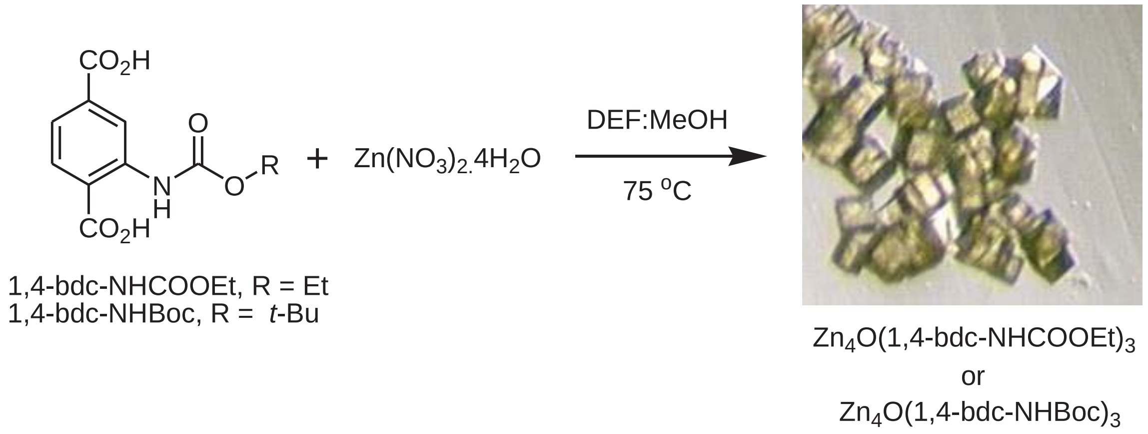

Figure 2.5 General synthetic route to MOF-5-NHCOOEt and MOF-5-NHBoc.

The ligands were then combined with five equivalents of $Zn(NO_3)_2.4H_2O$ in DEF:MeOH (1:2) and placed in a 75 °C oven for 24 hrs, affording transparent block shaped crystals (Figure 2.5). Powder X-ray diffraction (PXRD) of the synthesized materials revealed that the crystals are phase pure (only one species of crystalline material was present) and exhibit close similarities to the PXRD patterns of MOF-5 and IRMOF-3 ($[Zn_4O(1,4\text{-bdc-}NH_2)_3]$, Figure 2.7). These results indicate that the target materials MOF-5-NHCOOEt and MOF-5-NHBoc were successfully obtained. ^{1}H-NMR spectroscopic analysis of the digested MOFs was conducted to determine if the TPGs had survived the synthesis conditions. It was found

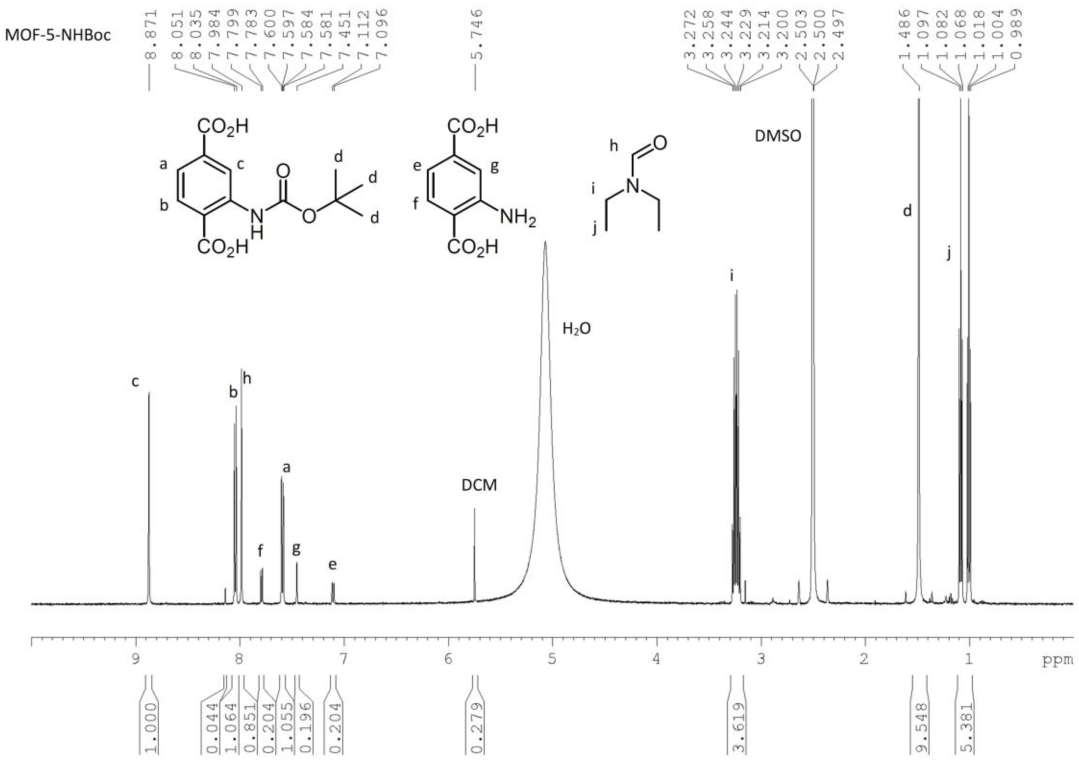

Figure 2.6 ^{1}H-NMR spectroscopic analysis of MOF-5-NHBoc in DMSO-d6/DCl (occluded DEF still present from synthesis).

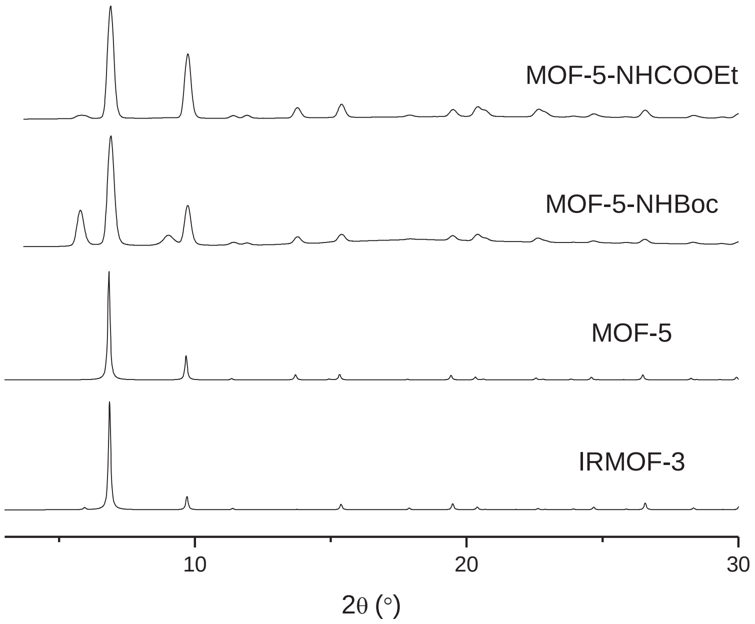

Figure 2.7 PXRD patterns of MOF-5-NHCOOEt and MOF-5-NHBoc (experimental), as well as MOF-5 and IRMOF-3 (calculated from literature cif files).

that the whilst the TPGs survived the synthesis of MOF-5-NHCOOEt (Figure 2.23), partial deprotection occurred during the MOF-5-NHBoc synthesis, with approximately 19% 1,4-bdc-NH_2 present in the MOF (Figure 2.6). Despite trialling numerous conditions, it was not possible to reduce the amount of 1,4-bdc-NH_2 forming, even with reduced temperatures and synthesis times. This indicates that the incorporation of 1,4-bdc-NH_2 into the material was necessary in order for the MOF to form. This is most likely occurring to reduce the steric hindrance in the pores caused by the bulky TPGs. Although it appears that there is sufficient pore volume to allow for all ligands to have an NHBoc TPG, it is possible that the motion of the TPG within the pores prevents the complete incorporation of NHBoc. If this is the case, then it would be necessary for either the 1,4-bdc-NH_2 present in the ligand material to be included as the MOF grows. This is supported by the reduced yield of MOF-5-NHBoc with respect to MOF-5-NHCOOEt, as the MOF-5-NHBoc synthesis is limited by the amount of 1,4-bdc-NH_2 present. It is further supported by the observation that the MOF-5-NHCOOEt crystals formed faster and grew quicker than the MOF-5-NHBoc crystals, as the presence of 1,4-bdc-NH_2 was not required in the case of MOF-5-NHCOOEt.

Single crystal X-ray diffraction (SCXD) of the MOFs revealed the same network topology as MOF-5 (Figure 2.8). As with MOF-5, the asymmetric units (ASUs) of MOF-5-NHCOOEt and MOF-5-NHBoc contain the central oxygen atom from the Zn_4O cluster, a zinc atom, a carbonyl oxygen atom, a carbonyl carbon atom, and two aromatic carbon atoms. Unfortunately, it was not possible to identify the carbamate group on the Fourier difference

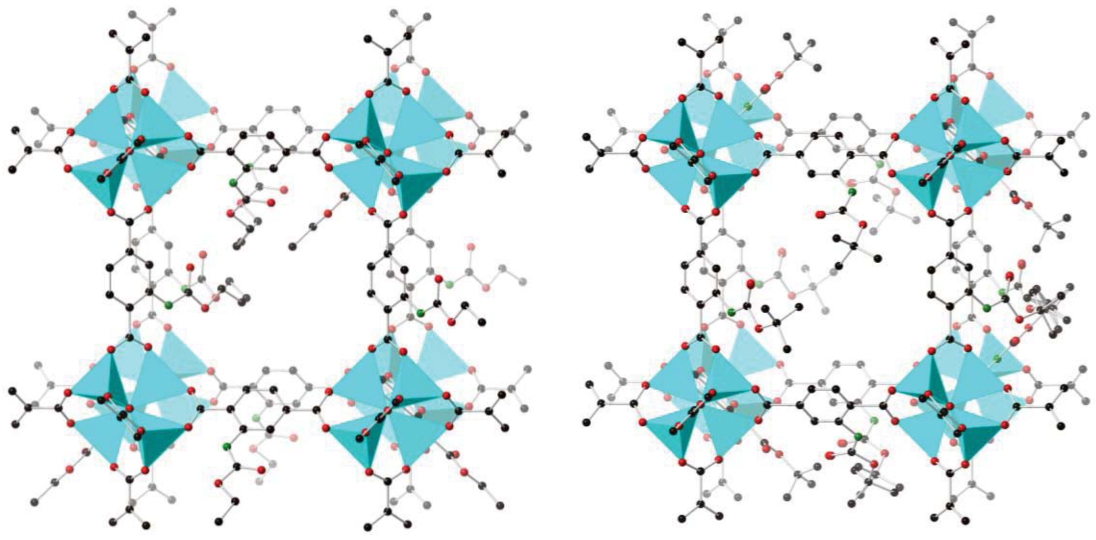

Figure 2.8 Structure determined by SXRD of MOF-5-NHCOOEt (left) and MOF-5-NHBoc (right). Disorder not shown for clarity.

map. This is due to the combination of two difference sources of disorder: first, since the four carbons of the bdc ring are crystallographically equivalent, the occupancy of the side group is quartered. Second, the side group is not fixed in position but is free to rotate about its bond. These two factors combined made the signals from the side chain atoms impossible to distinguish from the solvent occupying the pores. Due to the close proximity of the side chains on different ligands it is conceivable that they are able to interact and direct each other into an ordered arrangement. However, as the SXRD data revealed that the four equatorial carbons of the 1,4-bdc-TPG ligands are crystallographically equivalent, it can be concluded that there has been no ordering of the functional groups in MOF-5-NHCOOEt nor MOF-5-NHBoc.

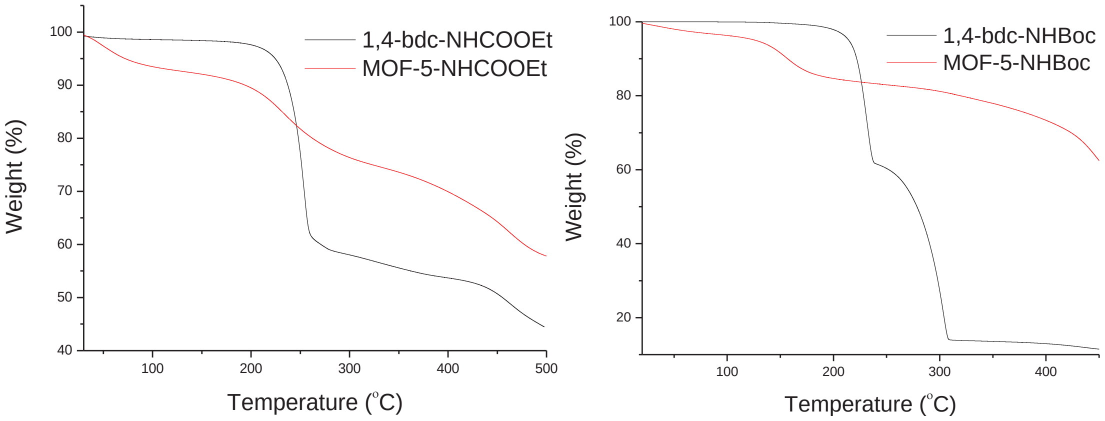

Figure 2.9 TGA traces of 1,4-bdc-NHCOOEt and MOF-5-NHCOOEt (left), and 1,4-bdc-NHBoc and MOF-5-NHBoc (right).

TGA of 1,4-bdc-NHBoc (Figure 2.9) revealed a weight loss of 38% at commencing at 210 °C, which agrees with the expected weight percent loss of 35.6% attributable to the loss of isobutylene and CO_2. Consistent with this, ^{1}H-NMR spectroscopic analysis of the material generated after this weight loss revealed complete conversion of the 1,4-bdc-NHBoc to 1,4-bdc-NH_2 (Figure 2.3). TGA of MOF-5-NHBoc (Figure 2.9) revealed a weight loss of 15.6% starting at 130 °C. After factoring in the amount of 1,4-bdc-NH_2 present in the MOF pre-thermolysis, the weight loss agrees with the 15.9% corresponding to *t*-BuOH (and thus the formation of an isocyanate group appended to the MOF) and not the 21.5% corresponding to CO_2H and isobutylene. However, ^{1}H-NMR spectroscopic analysis of the MOF digested after this weight loss showed only 1,4-bdc-NH_2. Whilst it is possible that the digest conditions required to dissolve the MOF could have converted 1,4-bdc-NCO to 1,4-bdc-NH_2, this is unlikely as elsewhere 1,4-bdc-NCO was able to be observed by ^{1}H-NMR spectroscopic analysis using the same digest conditions (*vide infra*). It is unknown why there is such a large decrease in the temperature required for thermal deprotection when the ligand is installed into the MOF, especially since this behaviour is not shared with the ethyl carbamate TPG (*vide infra*). The decrease in thermal deprotection temperature compared to the free ligand is not limited to this material, and has been observed in lon-e-NHBoc (Chapter 3), as well and in the IRMOF-10-NHBoc reported by the Telfer group.[102] PXRD of MOF-5-NHBoc post thermolysis indicated that the material had only a slight loss in crystallinity (Figure 2.12), however single crystal experiments could not be carried out as the conditions required for the thermolysis caused the crystals to crack.

TGA of 1,4-bdc-NHCOOEt (Figure 2.9) revealed a weight loss of 39% starting around 210 °C, which is greater than the 21.0% expected from the loss of CO_2 and ethene, and nearly three times the 13.4% expected weight loss of EtOH. Also, although the product of the thermolysis of 1,4-bdc-NHBoc remained a powder like the unheated material, the product of the thermolysis of 1,4-bdc-NHCOOEt became a solid cake in the sample pan (Figure

Figure 2.10 Images of 1,4-bdc-NHCOOEt before thermolysis (left), after thermolysis (middle), and cake removed from alumina pan (right).

2.10). This solid cake proved quite difficult to dissolve, and ^{1}H-NMR spectroscopic analysis of the material indicated no clear single species. It is believed that the 1,4-bdc-NHCOOEt polymerized upon thermolysis of the protecting group, as this would explain the change from a free-flowing powder to single solid cake as well as the drastic decrease in solubility of the material. The exact mechanism of this polymerisation is unknown, however it is theorized that it is related to the formation of an isocyanate functional group. Polymerisation would also explain the greater than expected weight loss, as CO_2 and H_2O can be lost during polymerisation. TGA of MOF-5-NHCOOEt revealed a weight loss of ~17% starting around 200 °C after an initial weight loss from occluded solvent. This is greater than the expected 12.1% for loss EtOH (and thus the formation of the isocyanate) and less than the 18.9% expected for loss of CO_2 and ethene. ^{1}H-NMR spectroscopic analysis of the material post thermolysis, however, revealed that all the 1,4-bdc-NHCOOEt had converted to 1,4-bdc-NH_2. It is possible that the conditions required to digest the material could have converted the 1,4-bdc-NCO to 1,4-bdc-NH_2 however, as mentioned above, this is unlikely. The most likely cause of the discrepancy between the weight loss seen in the TGA and the species in the ^{1}H NMR analysis is the poor separation of the thermal degradation steps in the TGA. As the TGA trace does not plateau after either the solvent loss nor the TPG thermolysis, it is not possible to exactly determine where the weight loss pertaining to the thermolysis begins or ends. This has meant that the region of weight loss had to be estimated, which can significantly affect the value of the weight loss. The differing behaviours of MOF-5-NHCOOEt and 1,4-bdc-NHCOOEt indicate that the immobilization of the ligand in the MOF framework prevents the polymerization reaction from occurring. PXRD of the MOF-5-NHCOOEt post thermolysis indicated that the material had a significant loss of crystallinity (Figure 2.12). However, since a lack of crystallinity does not preclude the presence of porosity further analyses on MOF-5-NHCOOEt were conducted.

After using TGA to determine the optimal temperature for the thermolysis of the protecting groups in the MOFs, efforts turned next to trialling the thermolysis of the MOFs on the activation port of the gas sorption instrument. It was important to do this since the thermolysis may behave differently on the activation port as the material is under vacuum on the port instead of under nitrogen on the TGA instrument, there is no solvent around to interact with the material during thermolysis, the heating method has changed from a furnace to a heating mantle with a glass sample tube acting as a physical barrier, and the quantity of material to be deprotected increased greatly from approximately 1-2 mg to around 50 mg. Throughout the rest of this chapter, materials with “ ^{t} ” postscript have undergone one exposure to thermolysis conditions and materials with “ ^{t2} ” postscript have undergone two exposures to thermolysis conditions. ^{1}H-NMR spectroscopic analysis of the material that

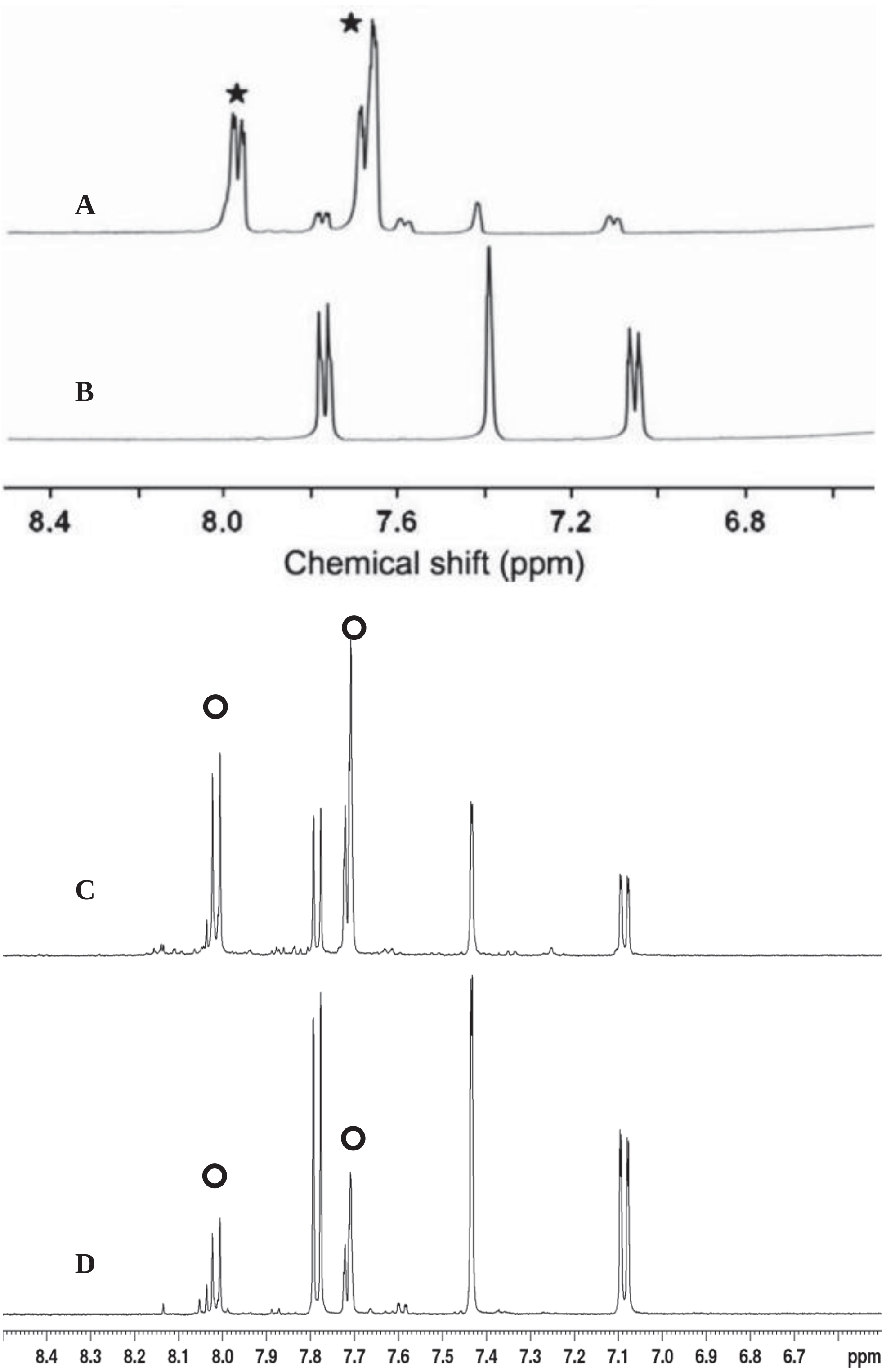

Figure 2.11 ^{1}H-NMR spectroscopic analysis of MIL-53(Al)-NCO (**A**) and MIL-53(Al)-NH_2 (**B**), MOF-5-NHCOOEt^{t2} (**C**), and MOF-5-NHBoc^{t2} (**D**). 1,4-bdc-NCO peaks marked with stars, and unknown peaks marked with circles. MIL-53 spectra reproduced from 2010 paper by Volkringer and Cohen.[152]

remained after heating at 160 °C for 12 hours on the activation port revealed a new thermolysis product for both MOF-5-NHCOOEt and MOF-5-NHBoc in addition to the 1,4-bdc-NH_2 seen on the TGA instrument. It is believed that this new species is either the isocyanate (1,4-bdc-NCO) that is believed to be responsible for the polymerization of 1,4-

bdc-NHCOOEt upon thermolysis, or the carbamic acid (1,4-bdc-NHCOOH) that would be the result of 1,4-bdc-NCO reacting with water. It is our opinion that the species is 1,4-bdc-NCO as an extensive literature search revealed a 2010 paper by Volkringer and Cohen[152] in which 1,4-bdc-NCO in incorporated into MIL-53(Al), a material first published by the Férey group.[153] Comparison of the ^{1}H-NMR spectra of MIL-53(Al)-NCO reported by Volkringer and Cohen (Figure 2.11) with the thermolysed products of MOF-5-NHCOOEt and MOF-5-NHBoc reveals a very close match to the unknown species. The results of mass spectroscopic analysis on partially thermolysed MOF-5-NHCOOEt further supports this result, with both 1,4-bdc-NHCOOEt$^-$ and 1,4-bdc-NCO$^-$ being observed in negative mode (Figure 2.24). In order to confirm that the species is indeed 1,4-bdc-NCO, the thermolysed materials were reacted separately with benzylamine and MeOH, compounds known to react with isocyanates to produce 1,4-bdc-benzylurea and 1,4-bdc-NHCOOMe respectively. Peculiarly, neither material reacted with either benzylamine or MeOH, despite the MeOH trials using the same conditions that Volkringer and Cohen used to react the MOF-bound isocyanates in their paper.[152] It is not known why the isocyanate species is proving abnormally inert in this work. Future work involving the screening of reaction conditions may provide insight into this apparent decrease in reactivity.

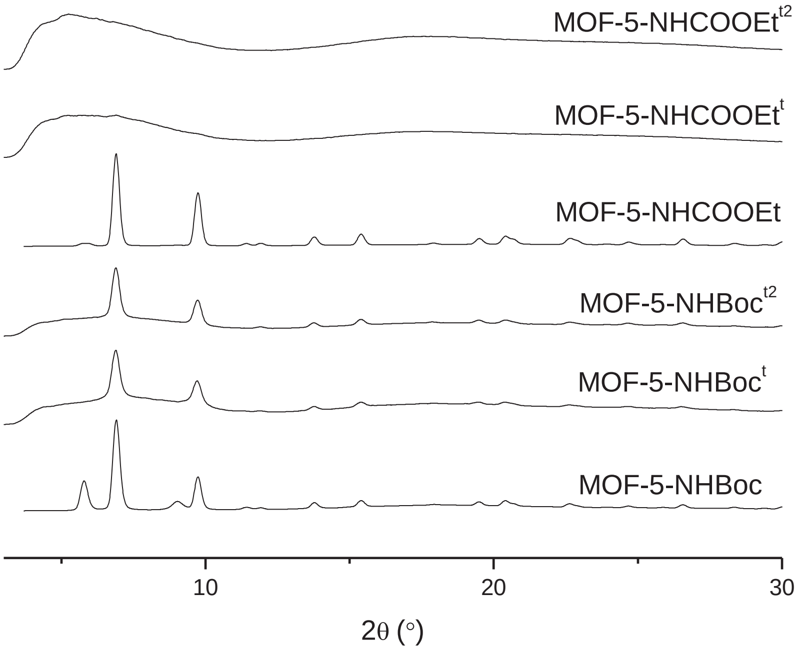

Figure 2.12 PXRD patterns for the MOF-5 analogues pre and post thermolysis.

In preparation for gas sorption, MOF-5-NHCOOEt and MOF-5-NHBoc were soaked in CH_2Cl_2 for 24 hours, changing the solvent four times over this period. This procedure replaces the solvent occluded within the MOFs with CH_2Cl_2 which has a lower boiling point that the solvents used in MOF synthesis. This allows for a gentler and more complete removal of solvent from the MOFs. The materials were then transferred to gas sorption sample tubes, ensuring that the materials remained under CH_2Cl_2 throughout the process. The samples were then placed on the activation ports and then the solvent removed by placing the materials under high vacuum for 12 hours at room temperature. ^{1}H-NMR

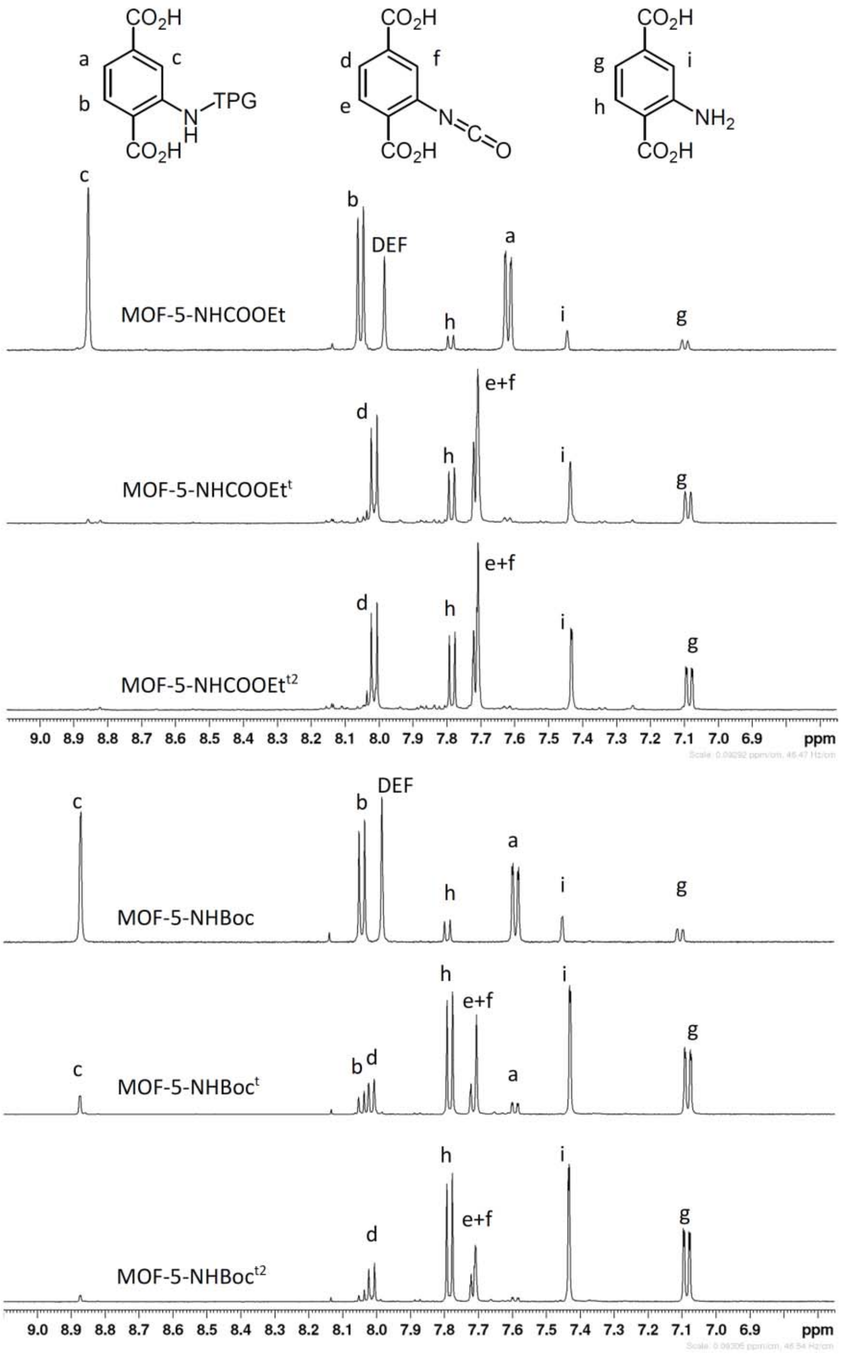

Figure 2.13 ^{1}H-NMR spectroscopic analysis of the pre- and post-thermolysis materials.

spectroscopic analysis of the activated materials revealed the complete removal of solvent from the MOF pores (Figure 2.6 and Figure 2.23), and PXRD of the activated materials revealed that crystallinity was maintained after undergoing the activation process (Figure 2.12). After gas sorption measurements were conducted, the materials were returned to the activation port and thermolysed at 160 °C for 12 hours to give MOF-5-NHCOOEt^{t} and MOF-5-NHBoc^{t}, after which gas sorption measurements were conducted on the thermolysed materials. The measurement of gas sorption isotherms is a process by which gravimetric uptakes of various gases are measured at various partial pressures (between 0.0001 and 1 atm for the isotherms in this work) and also at multiple temperatures (77 K, 273 K, and 298 K in this study). ^{1}H-NMR spectroscopic analysis after the gas sorption experiments reveal incomplete thermolysis (Figure 2.13) with 2.5 % of the TPG remaining in MOF-5-NHCOOEt^{t} and 10 % of the TPG remaining in MOF-5-NHBoc^{t}. The samples were then resubjected to the thermolysis conditions to give MOF-5-NHCOOEt^{t2} and MOF-5-NHBoc^{t2}, after which further gas sorption measurements were run. ^{1}H-NMR spectroscopic analysis of the materials revealed no TPG present in MOF-5-NHCOOEt^{t2}, but in MOF-5-NHBoc^{t2} there was 3.7 % of the TPG remaining (Figure 2.13). Figure 2.12 shows that MOF-5-NHBoc retained at least some crystallinity after being thermolysed twice, whereas MOF-5-NHCOOEt lost all crystallinity after just one round of thermolysis. The most likely cause of the differences in the stability of these MOFs is the differing products formed during thermolysis. The majority of MOF-5-NHBoc thermolysis products are CO_2 and isobutylene, whereas EtOH is the major thermolysis product in MOF-5-NHCOOEt. It is possible that at the elevated temperatures of thermolysis EtOH is destructive to the MOF-5 framework, and causes the loss of crystallinity in MOF-5-NHCOOEt after thermolysis.

For ease of comparison, Table 2.1 lists the maximum uptakes of gases measured for the MOF-5 analogues as well as the Brunauer-Emmett-Teller (BET) surface areas calculated for the materials. The results of N_2 uptake at 77 K (Figure 2.14) reveal moderate uptakes of the gas for all samples ranging from 440-678 cc/g at 1 atm, with the protected materials having approximately 2/3 of the uptake of their deprotected analogues. This is unsurprising as the pore volume available for guest molecules is significantly reduced in these materials due to the bulky TPGs. This also demonstrates that, whilst there was loss of crystallinity, little collapse has occurred in the thermolysed materials as this would significantly decrease the uptakes of gas molecules. This indicates that the majority of the decrease in crystallinity is due to the loss of long range order in the materials, rather than collapse of the framework. These isotherms were then used to calculate the BET surface areas of the materials (Figure 2.14 and Figure 2.25-Figure 2.30). The BET surface areas for the protected species are more

Table 2.1 BET surface areas (m^2/g) and maximum gas sorption uptakes at 1 atm (cc/g at STP) for MOF-5 analogues. *at 0.66 atm

		77 K		273 K			298 K		
	BET	N_2	H_2	N_2	CO_2	CH_4	N_2	CO_2	CH_4
MOF-5-NHCOOEt	1740	458	169	5.4	67.9	14.6	3.6	37.2	14.8
MOF-5-NHCOOEt^t	2350	621	163	3.8	49.1	14.5	3.8	25.1	9.0
MOF-5-NHCOOEt^{t2}	2390	626	163	5.6	49.6	11.9	0.0	24.3	6.8
MOF-5-NHBoc	1650	440	186	5.6	73.3	15.1	3.4	40.1	17.3
MOF-5-NHBoc^t	2490	650	172	2.4	48.3	14.2	3.6	23.5	8.8
MOF-5-NHBoc^{t2}	2620	678	170	5.6	46.2	10.0	0.0	20.6	4.4
MOF-5	2833		67*						

than 600 m^2/g lower than those of the thermolysed species. This is as expected since although the TPGs increase the total surface area within the MOF, the bulkiness of the side groups in conjunction with the narrow pores of the framework reduces the volume available

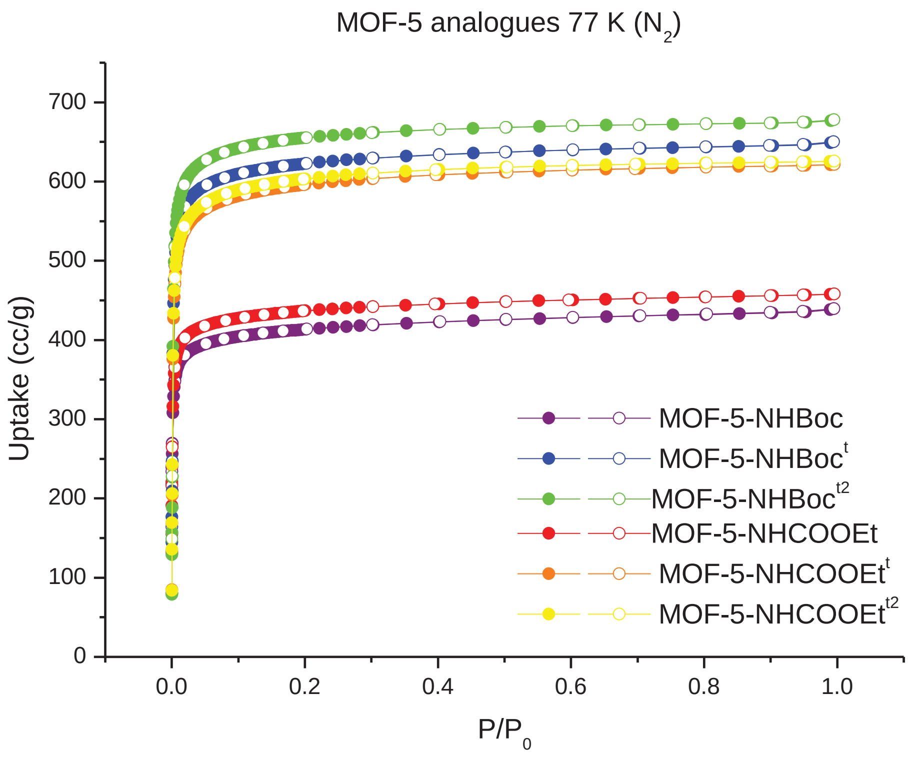

Figure 2.14 Gravimetric N_2 adsorption (filled) and desorption (open) isotherms measured at 77 K.

for N_2 molecules to occupy. The BET surface areas of the thermolysed species compare favourably to the literature values for MOF-5 and IRMOF-3 reported by the Yaghi group in 2005, with MOF-5-NHBoc^{t2} having the highest at 2620 m^2/g. Whilst not as high as the 2,833 m^2/g reported for MOF-5[154], it is significantly higher than the 2160 m^2/g reported for IRMOF-3.[154] This is unexpected as MOF-5-NHBoc^{t2} is essentially IRMOF-3 doped with ~20 % 1,4-bdc-NCO, which the results of MOF-5-NHCOOEt^{t} and MOF-5-NHCOOEt^{t2} indicate would decrease the surface area. It is not known why MOF-5-NHBoc has a higher surface area than IRMOF-3, though reasons that may be contributing to the differences include different activation procedures.

Hydrogen uptakes at 77 K fall between 160-186 cc/g at 1 atm, which are comparable to the values reported by the Yaghi group of ~160 cc/g for MOF-5 and ~170 cc/g for IRMOF-3 (values calculated from gravimetric uptakes).[155] Interestingly, MOF-5-NHBoc had the highest uptake of H_2 at 77 K, despite having the least available void space of the materials. It is possible that the conformations of the TPGs in the pores form smaller pockets of void space that, whilst inaccessible to N_2, are accessible to the much smaller H_2 molecule. In addition, the shape of the pore environment in MOF-5-NHBoc could be such that it promotes the adsorption of multiple layers of H_2 molecules.

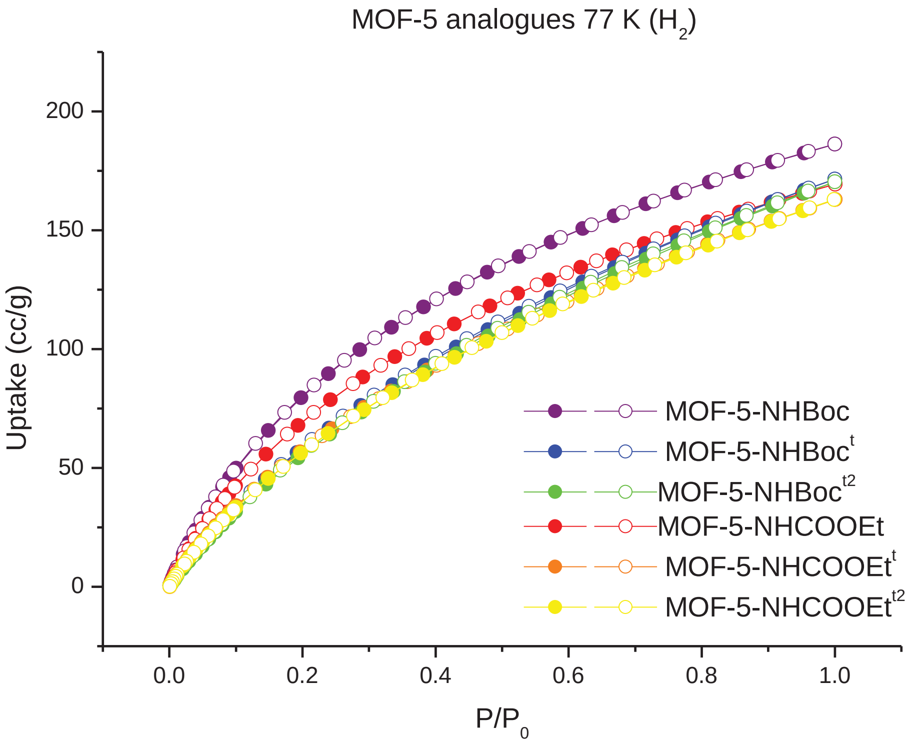

Figure 2.15 Gravimetric H_2 adsorption (filled) and desorption (open) isotherms measured at 77 K.

As can be seen in Figure 2.31, the uptakes of N_2 at 273 K by the materials range from 2.4 cc/g at 1 atm for MOF-5-NHBoc^{t} to 5.6 cc/g at 1 atm for MOF-5-NHCOOEt, MOF-5-NHBoc, and MOF-5-NHBoc^{t2}. Curiously, the materials that had been thermolysed twice showed better uptakes than the materials that had been thermolysed only once. This behaviour was not seen in any other of the gas sorption analyses (Table 2.1). This most likely occurred due to an error with maintaining the ice-water mixture used to collect 273 K isotherms, as overnight there is no one physically monitoring the instrument to ensure the ice is topped up. As this was only noticed after the collection of the twice thermolysed data, it was impossible to re-measure the isotherms, and it was deemed unnecessary to synthesise new material to repeat the isotherm.

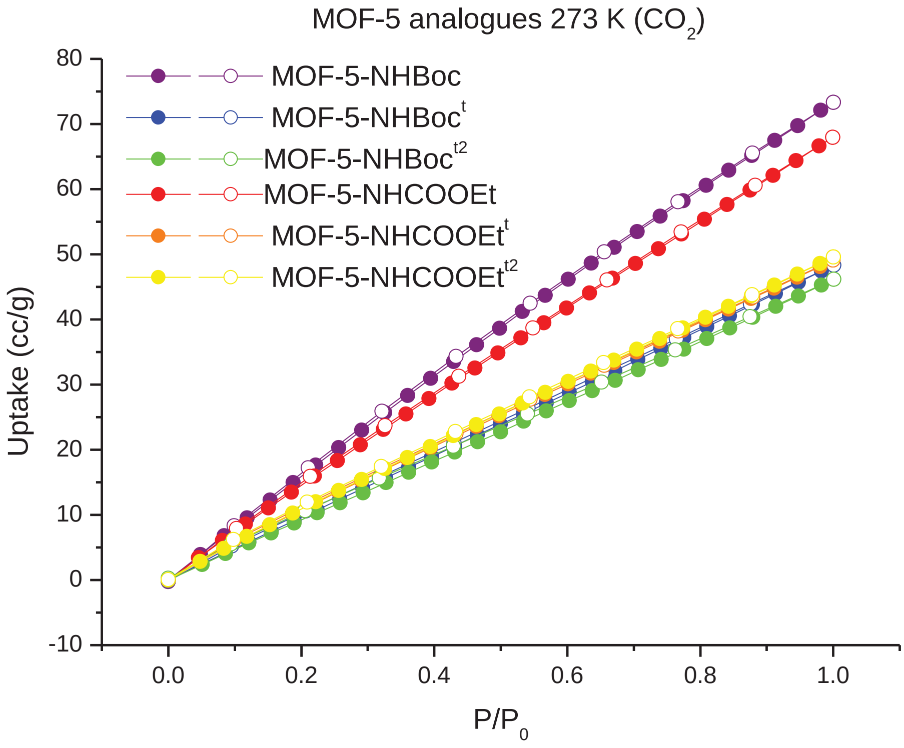

Figure 2.16 Gravimetric CO_2 adsorption (filled) and desorption (open) isotherms measured at 273 K.

The uptakes of CO_2 at 273 K (Figure 2.16) of the materials unexpectedly reveal that the protected species have higher uptakes than the thermolysed species, with MOF-5-NHBoc having the highest uptake at 73.3 cc/g at 1 atm. This indicates that the uptake of CO_2 is more greatly enhanced by the size and shape of the pore environment of the TPG containing MOFs than the increased polarity of the thermolysed MOFs. This trend is again seen in the uptakes of CH_4 at 273 K (Figure 2.32), where MOF-5-NHCOOEt (14.6 cc/g) and MOF-5-NHBoc (15.0 cc/g) have higher uptakes than their thermolysed counterparts. Curiously, the drop in uptake after the first round of thermolysis is less than the drop after the second round of thermolysis, despite the first round having the greater influence on the chemical species present.

Uptake of CO_2 at 298 K (Figure 2.17) by the materials mirrored the trend seen at 273 K, with the protected materials having higher uptakes than their thermolysed counterparts, with MOF-5-NHBoc having the highest uptake of 40.1 cc/g at 1 atm. These results compare favourably with the literature values of ~17.6 cc/g at 1 atm for MOF-5[156] and ~29.7 cc/g for IRMOF-3[157] (calculated from mmol/g values reported). Whilst the values of the thermolysed materials are ~4-9 cc/g lower than the literature value for IRMOF-3, this is likely caused by structural damage to the framework caused by the thermolysis conditions. These results again highlight that the size and shape of the pore environment appears to have a greater influence on CO_2 uptake than increasing the polarity of the pore surface.

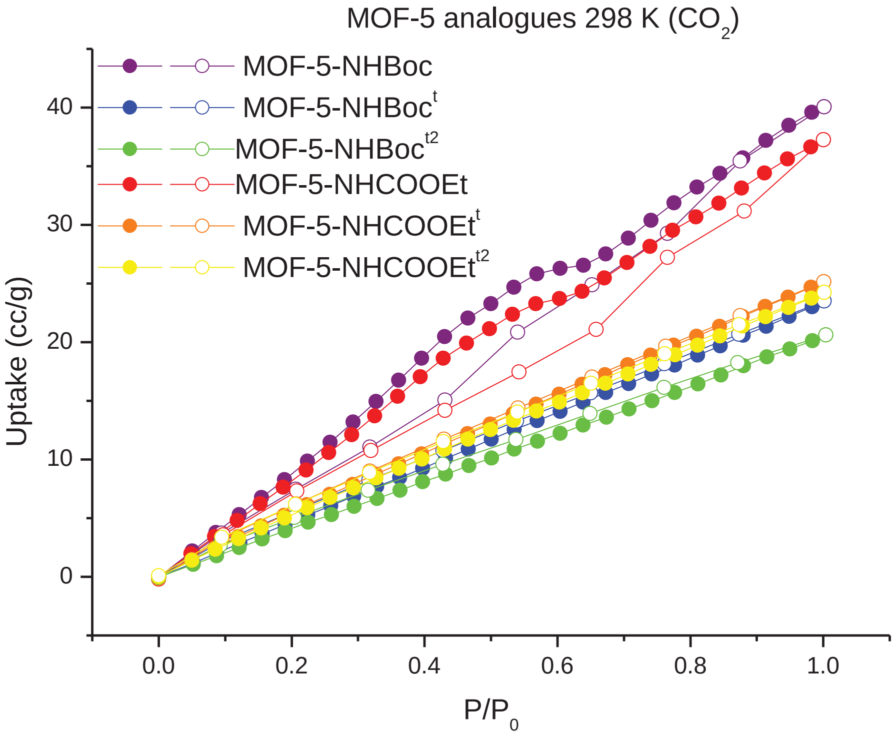

Figure 2.17 Gravimetric CO_2 adsorption (filled) and desorption (open) isotherms measured at 298 K.

The uptakes of CH_4 at 298 K (Figure 2.18) follow the same trend as at 273 K, with the protected materials having higher uptakes than their thermolysed counterparts, with MOF-5-NHBoc having the highest uptake of 17.3 cc/g at 1 atm. Interestingly, the uptakes of CH_4 by the protected materials are higher at 298 K than at 273 K, especially in MOF-5-NHBoc where there is a 2.2 cc/g increase in the uptake at 1 atm. This is substantially more than the literature values of ~3.1 cc/g at 1 atm for MOF-5[156] and ~9.2 cc/g at 1 atm for IRMOF-3[157] (calculated from mmol/g values reported).With such a high uptakes of CH_4 at 1 atm, it would be worth investigating the high pressure adsorption of MOF-5-NHBoc and MOF-5-NHCOOEt as potential materials for methane storage, though these measurements were not conducted as part of this work.

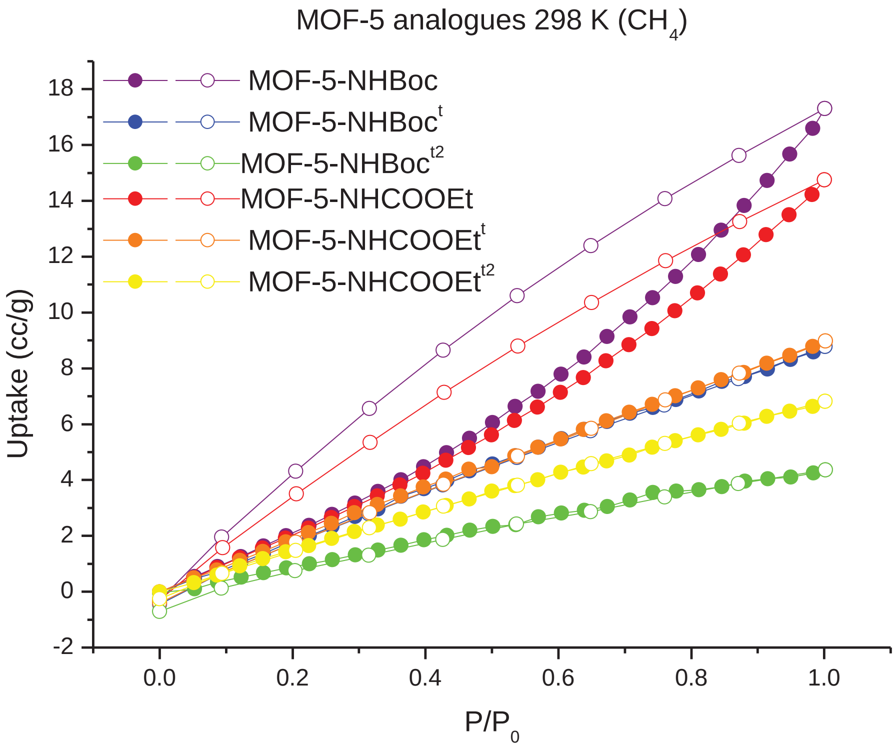

Figure 2.18 Gravimetric CH_4 adsorption (filled) and desorption (open) isotherms measured at 298 K.

2.3 Conclusion

In conclusion, two novel TPG containing ligands have been successfully installed into MOF-5. Thermolysis of the TPGs under vacuum was not clean, and afforded both 1,4-bdc-NCO and 1,4-bdc-NH_2 in differing ratios. Thermolysis of MOF-5-NHCOOEt generated mostly 1,4-bdc-NCO and thermolysis of MOF-5-NHBoc generated mostly 1,4-bdc-NH_2. Further work is required in order to determine the conditions necessary for clean thermolysis of the materials that does not results in loss of porosity. The anomalous low reactivity of the isocyanate in thermolysed MOF-5-NHCOOEt also should be examined in more depth. Except for N_2 at 77 K, the protected species had higher maximum uptakes at 1 atm for all gases at all temperatures than the thermolysed species as well as the literature values recorded. This indicates that at these relatively low loadings of gases the shape and size of the pore environment has a greater influence on gas uptake than the polarity of the surface. Furthermore, this work demonstrates that TPGs are compatible with MOF synthesis and can be successfully removed post synthetically by thermal deprotection with little impact on the porosity of the sample. Further work with these materials could investigate the high pressure isotherms of these MOFs to determine any potential applications for the materials, as well as to better understand the forces affecting the different gas sorption behaviours.

2.4 Experimental section

2.4.1 General procedures

All starting compounds and solvents were used as received from commercial sources without further purification unless otherwise noted. NMR spectra were recorded at room temperature on a Bruker-500 Avance instrument, with the use of the solvent proton as an internal standard. Elemental analyses were performed by the Campbell Microanalytical Laboratory at the University of Otago, New Zealand. Care was taken to limit the exposure of all MOFs to the atmosphere.

2.4.2 Ligand Synthesis

2.4.2.a 1,4-bdc-NHCOOEt

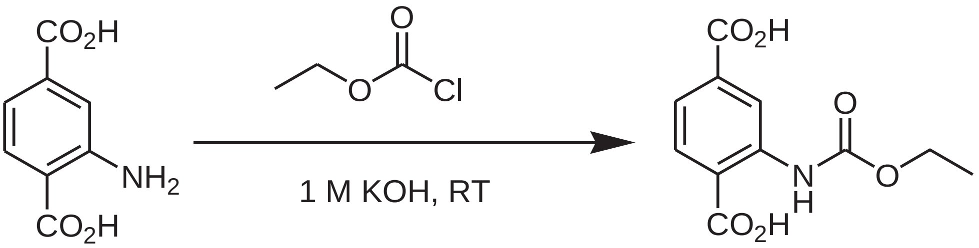

Ethyl chloroformate (1.60 g, 14.7 mmol) was added dropwise to a solution of 1,4-bdc-NH$_2$ (2.16 g, 11.9 mmol) in aqueous KOH (1 M, 40 mL) with stirring at room temperature. The reaction was allowed to stir for 4 hours before aqueous HCl (3 M) was added until no further precipitation was observed. The precipitated product was collected by filtration, washed with deionised water, recrystallized from hot methanol, and washed again with deionised water. The yellow solid product was then dried under vacuum. Yield: 2.84 g (89 % yield) 1,4-bdc-NHCOOEt containing a 5.9 % 1,4-bdc-NH$_2$ impurity. ^{1}H-NMR (500 MHz, DMSO-d_6): δ 1.27 (t, J = 7.1 Hz, 3H), 4.18 (dd, J = 14.2 Hz, 7.1 Hz, 2H), 7.63 (dd, J = 8.3 Hz, 1.6 Hz, 1H), 8.06 (d, J = 8.2 Hz, 1H), 8.87, (d, J = 1.6 Hz, 1H), 10.67 (s, 1H). Anal. calcd. for (1,4-bdc-NHCOOEt)$_{0.95}$(1,4-bdc-NH$_2$)$_{0.05}$: C, 52.22; H, 4.36; N, 5.64; Found: C, 51.76; H, 4.41; N, 5.39.

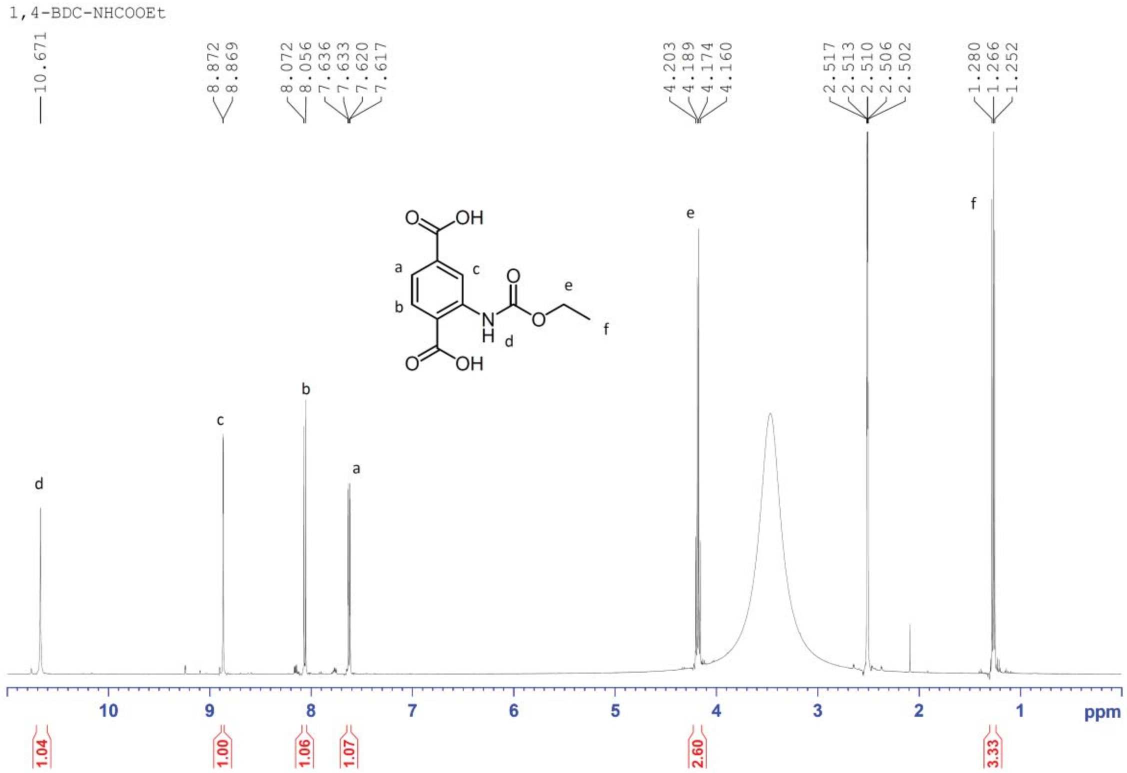

Figure 2.19 ^{1}H NMR spectroscopic analysis 1,4-bdc-NHCOOEt.

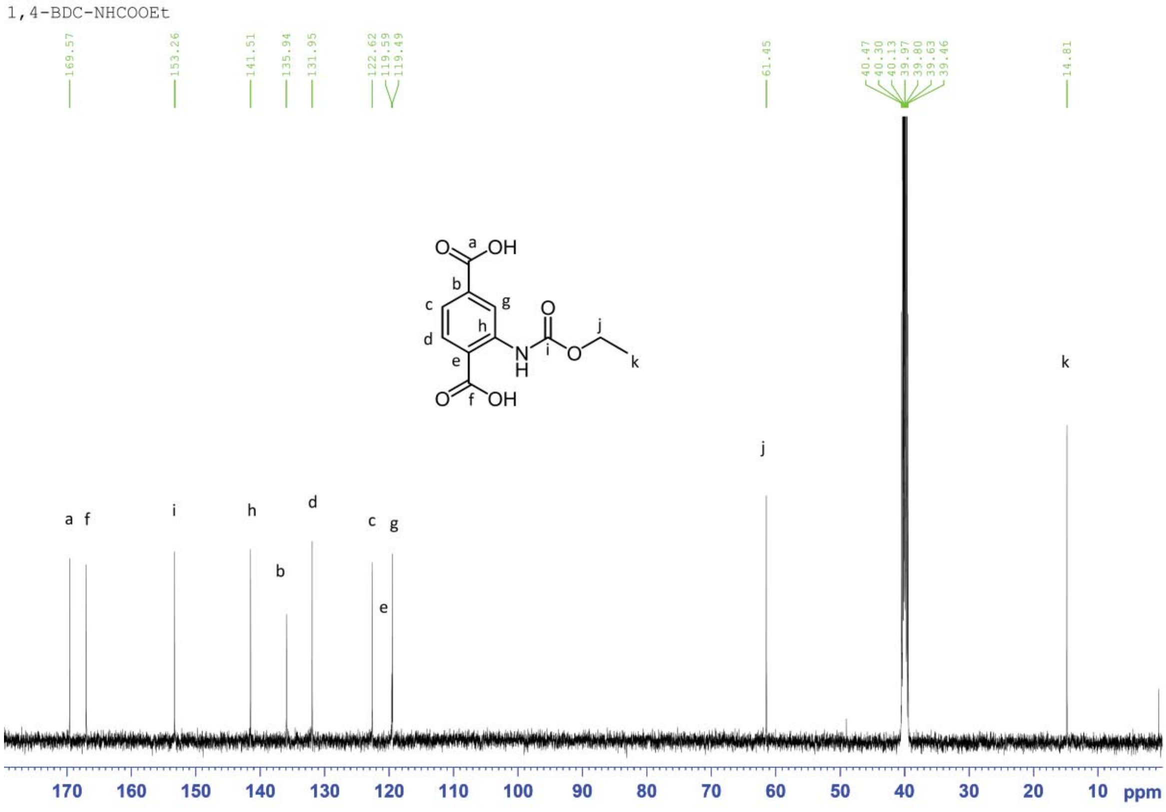

Figure 2.20 ^{13}C-NMR spectroscopic analysis of 1,4-bdc-NHCOOEt.

2.4.2b 2-*tert*-butoxycarbonylamino-1,4-benzenedicarboxylate

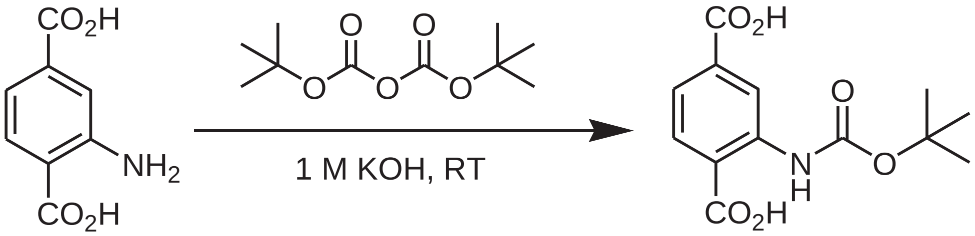

Di-*tert*-butyl dicarbonate (2.95 g, 13.5 mmol) in 1,4-dioxane (5 mL) was added slowly dropwise to 1,4-bdc-NH$_2$ (2.16 g, 11.9 mmol) in aqueous KOH (1 M, 40 mL) with stirring at room temperature. The reaction was allowed to stir at room temperature for 4 hours before the dropwise addition of further di-*tert*-butyldicarbonate (2.95 g, 13.5 mmol) in 1,4-dioxane (5 mL). The reaction was allowed to stir at room temperature for 4 hours before the dropwise addition of further di-*tert*-butyldicarbonate (2.95 g, 13.5 mmol) in 1,4-dioxane (5 mL). Precipitation was induced with the addition of aqueous HCl (3 M) until no further precipitation was observed. The precipitated product was collected by filtration, washed with deionised water, recrystallized from hot methanol, and washed again with deionised water. The yellow solid product was then dried under vacuum. Yield: 2.98 g (93 % yield) 1,4-bdc-NHBoc containing a 4.1 % 1,4-bdc-NH$_2$ impurity. ^{1}H-NMR (500 MHz, DMSO-*d*$_6$): δ 1.49 (s, 9H), 7.59 (dd, *J* = 8.2 Hz, 1.7 Hz, 1H), 8.04 (d, *J* = 8.3 Hz, 1H), 8.88 (d, *J* = 1.5 Hz, 1H), 10.46 (s, 1H). Anal. calcd. for (1,4-bdc-NHBoc)$_{0.95}$(1,4-bdc-NH$_2$)$_{0.05}$: C, 55.39; H, 5.31; N, 5.12; Found: C, 55.5; H, 5.32; N, 4.97.

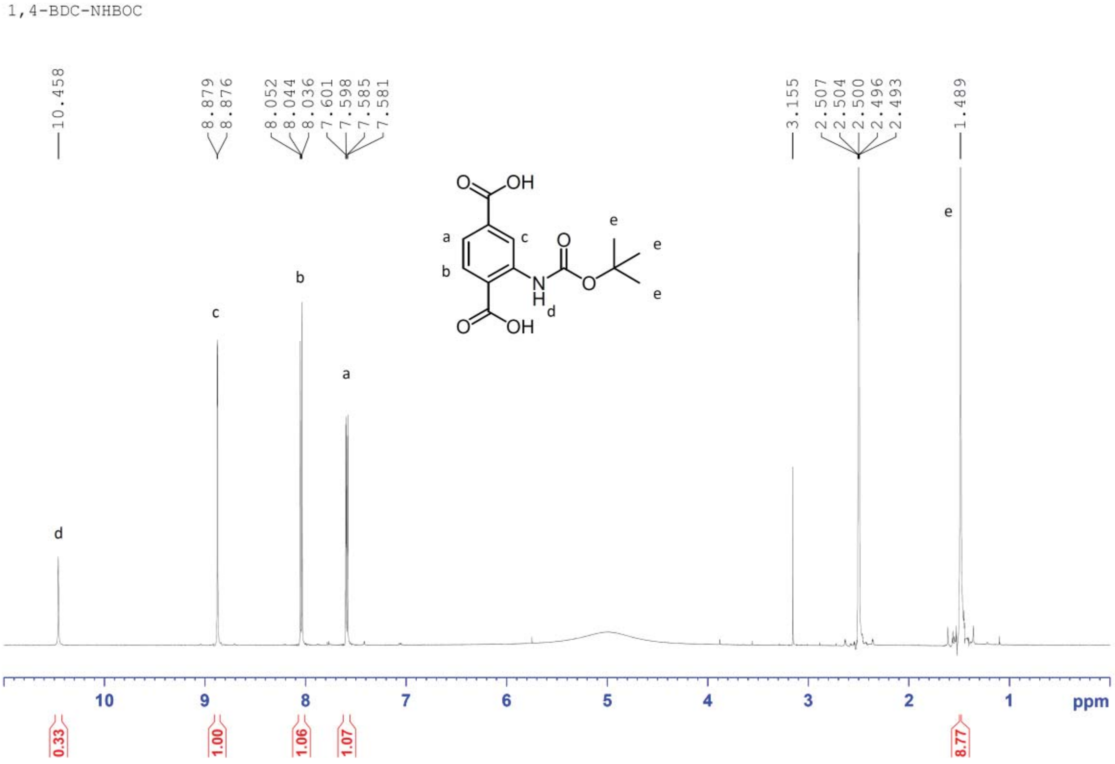

Figure 2.21 ^{1}H-NMR spectroscopic analysis of 1,4-bdc-NHBoc.

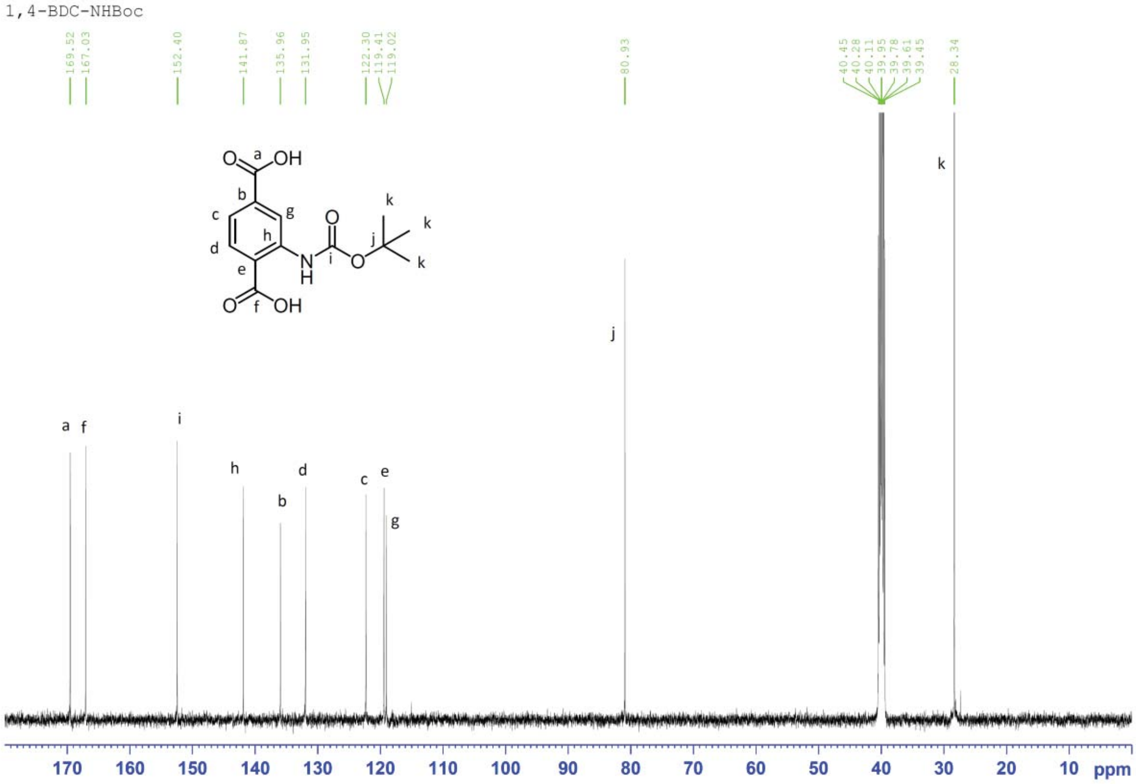

Figure 2.22 ^{13}C-NMR spectroscopic analysis of 1,4-bdc-NHBoc.

2.4.3 MOF synthesis and characterization

2.4.3a MOF-5-NHCOOEt

1,4-bdc-NHCOOEt (10.0 mg, 0.039 mmol) was combined with $Zn(NO_3)_2 \cdot 4H_2O$ (51.6 mg, 0.197 mmol) in dry DEF:MeOH (1:2, 2 mL) in a 20 mL vial pre-treated with Sigmacote and sonicated for 5 minutes before being heated in a 75 °C isothermal oven for 30 hours to obtain tan coloured crystals of MOF-5-NHCOOEt. Yield: 9.2 mg. Anal. calcd. for $[C_{33}H_{27}N_3O_{19}Zn_4].0.16(H_2O)$: C, 33.14; H, 3.82; N, 3.52; Found: C, 33.23; H, 3.27; N, 3.87. To scale up the synthesis, a parallel synthetic method was adopted (multiple vials using the scale described above).

2.4.3b MOF-5-NHBoc

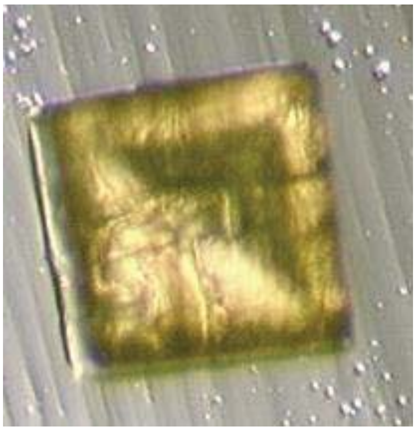

1,4-bdc-NHBoc (10.0 mg, 0.036 mmol) was combined with $Zn(NO_3)_2{\cdot}4H_2O$ (46.5 mg, 0.178 mmol) in dry DEF:MeOH (1:2, 2 mL) in a 20 mL vial pre-treated with Sigmacote and sonicated for 5 minutes before being heated in a 75 °C isothermal oven for 30 hours to obtain tan coloured crystals of MOF-5-NHBoc. Yield: 4.3 mg. Anal. calcd. for $[C_{39}H_{39}N_3O_{19}Zn_4]_{0.81}[C_{24}H_{15}N_3O_{13}Zn_4]_{0.19}.0.17(H_2O)$: C, 34.82; H, 4.36; N, 3.45; Found: C, 35.09; H, 3.76; N, 3.65. To scale up the synthesis, a parallel synthetic method was adopted (multiple vials using the scale described above).

2.4.4 ^{1}H NMR analysis of digested MOF samples

For ^{1}H NMR spectroscopy, the mother liquor of the as-synthesized MOF crystals was replaced with fresh dry DEF:MeOH (1:2) multiple times, followed by repeated washing and subsequent soaking in CH_2Cl_2 for several hours. The excess CH_2Cl_2 was then decanted and the samples placed under vacuum overnight to remove residual solvent from the pores. The crystals were then digested using the following protocol: 23 µL of a 35% DCl solution in D_2O was mixed with 1 mL of DMSO-d_6 to give a DCl/DMSO-d_6 stock solution. Around 5 mg of MOF was digested in 200 µL of this stock solution together with 400 µL of DMSO-d_6. Spectra were acquired immediately following dissolution, which took approximately 5 minutes.

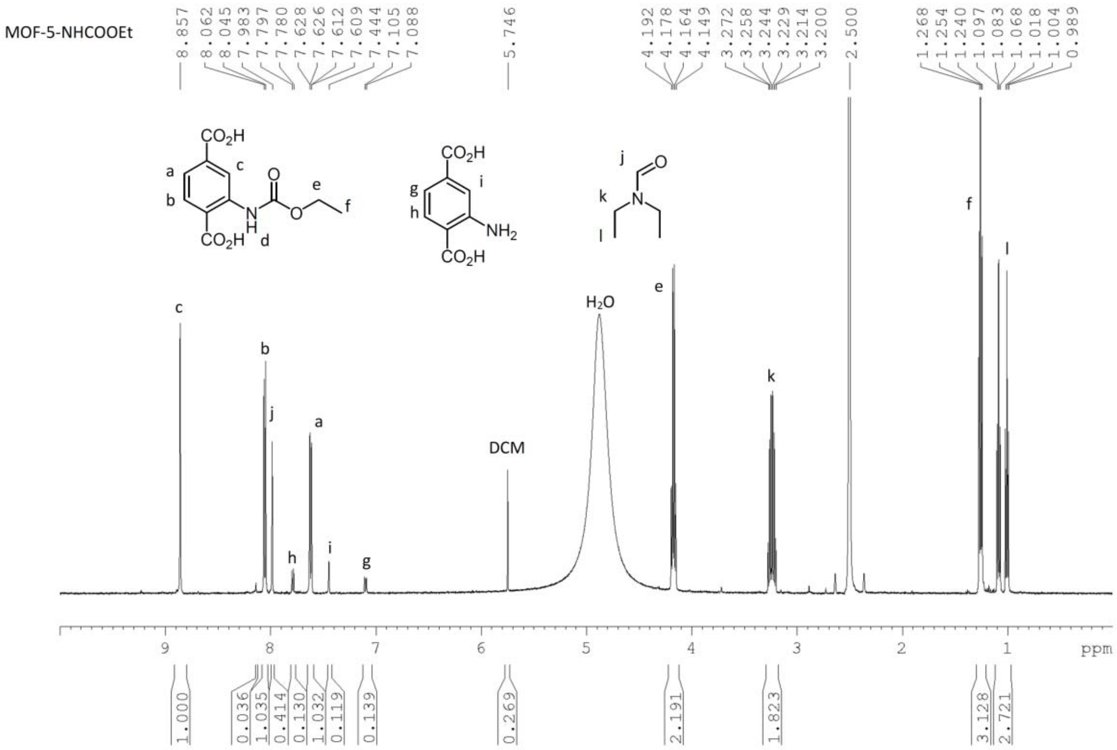

Figure 2.23 ^{1}H-NMR spectroscopic analysis of MOF-5-NHCOOEt digested in DMSO-d$_6$/DCl.

2.4.5 Thermogravimetric Analysis (TGA)

Thermogravimetric analyses were performed on a TA Instruments Q50 instrument. Freshly prepared MOF samples were prepared as for gas sorption (see section 2.4.9), except that the DCM was removed using a benchtop vacuum pump and were only under vacuum for 2 hours. Samples were then transferred to an aluminium sample pan and then measurements were commenced under an N_2 flow with a heating rate of 5 °C /min.

2.4.6 Single crystal X-ray diffraction

MOF crystals were mounted together with some dry DEF in a polymer sleeve on a Rigaku Spider diffractometer equipped with a MicroMax MM007 rotating anode generator (Cu_α radiation, 1.54180 Å), high-flux Osmic multilayer mirror optics, and a curved image-plate detector. Data were collected at 293 K and were integrated, scaled, and averaged with FS Process.[158] XPREP[159] was used to determine the space group and the structures were solved using SHELXS[159] and refined with SHELXL.[159]

All atoms were found in the electron density difference map, except for the side chains, which were subsequently modelled using Discovery Studio.[160] The atom positions were added to the model in representative positions and held fixed during refinement. All non-hydrogen, non-side chain atoms were refined anisotropically. Cif files for MOFs uploaded to http://tinyurl.com/sblackwoodMOFs.

Table 2.2 Crystallography data for MOF-5-NHCOOEt and MOF-5-NHBoc.

MOF	MOF-5-NHCOOEt	MOF-5-NHBoc
Formula	$C_{33}H_{27}N_3O_{19}Zn_4$	$C_{39}H_{39}N_3O_{19}Zn_4$
Formula weight	1031.05	1115.21
Crystal size (mm)	0.19 × 0.16 × 0.15	0.18 × 0.18 × 0.17
Temperature (K)	293	293
Wavelength (Å)	1.54187	1.54187
Crystal system	Cubic	Cubic
Space group	*F*m-3	*F*m-3
Unit cell length (Å)	25.618(6)	25.645(2)
Unit cell volume (Å^3)	16812(12)	16867(4)
Z	8	8
D_{calc} (g cm^{-3})	0.815	0.878
μ (mm^{-1})	1.64	1.66
F(000)	4144	4528
Reflns coll./unique, R_{int}	23353 / 1495, 0.0548	11885 / 804, 0.0631
Data range	8.0 Å > d > 0.81 Å	8.0 Å > d > 1.0 Å
Index ranges	$-31 \leq h \leq 31$, $-21 \leq k \leq 27$, $-28 \leq l \leq 31$	$-25 \leq h \leq 15$, $-25 \leq k \leq 25$, $-25 \leq l \leq 23$
Completeness	99.8%	99.7%
T_{min}, T_{max}	0.70, 1.00	0.46, 1.00
R indices for data with I>2σ(I)	$R_1 = 0.1726$; $wR_2 = 0.4809$	$R_1 = 0.1396$; $wR_2 = 0.3934$
R indices for all data	$R_1 = 0.2012$; $wR_2 = 0.4809$	$R_1 = 0.1545$; $wR_2 = 0.3934$
Largest difference peak and hole (e Å^{-3})	1.04 / −0.47	1.45 / −0.55

2.4.7 Powder X-ray diffraction patterns

All powder X-ray diffraction experiments were carried out on a Rigaku Spider X-ray diffractometer with Cu K_α radiation (Rigaku MM007 microfocus rotating-anode generator), monochromated and focused with high-flux Osmic multilayer mirror optics, and a curved image plate detector. The data were obtained from freshly prepared MOF samples that had been ground into slurry in a small amount of DEF and kept damp with DEF throughout the measurement. The two-dimensional images of the Debye rings were integrated with 2DP[161] (Version 1.0.3.4) to give 2θ vs I diffractograms. The predicted powder patterns of MOF-5-NHBoc and MOF-5-NHCOOEt was generated from their single-crystal structures using Mercury v3.8.

2.4.8 Mass Spectroscopy

Electrospray ionisation mass spectroscopy experiments were conducted by Dr. Marie Squire at the University of Otago. Thermolysed MOF samples were dissolved in MeOH:NEt$_3$ post partial thermolysis on the activation port (160 °C for 6 hours).

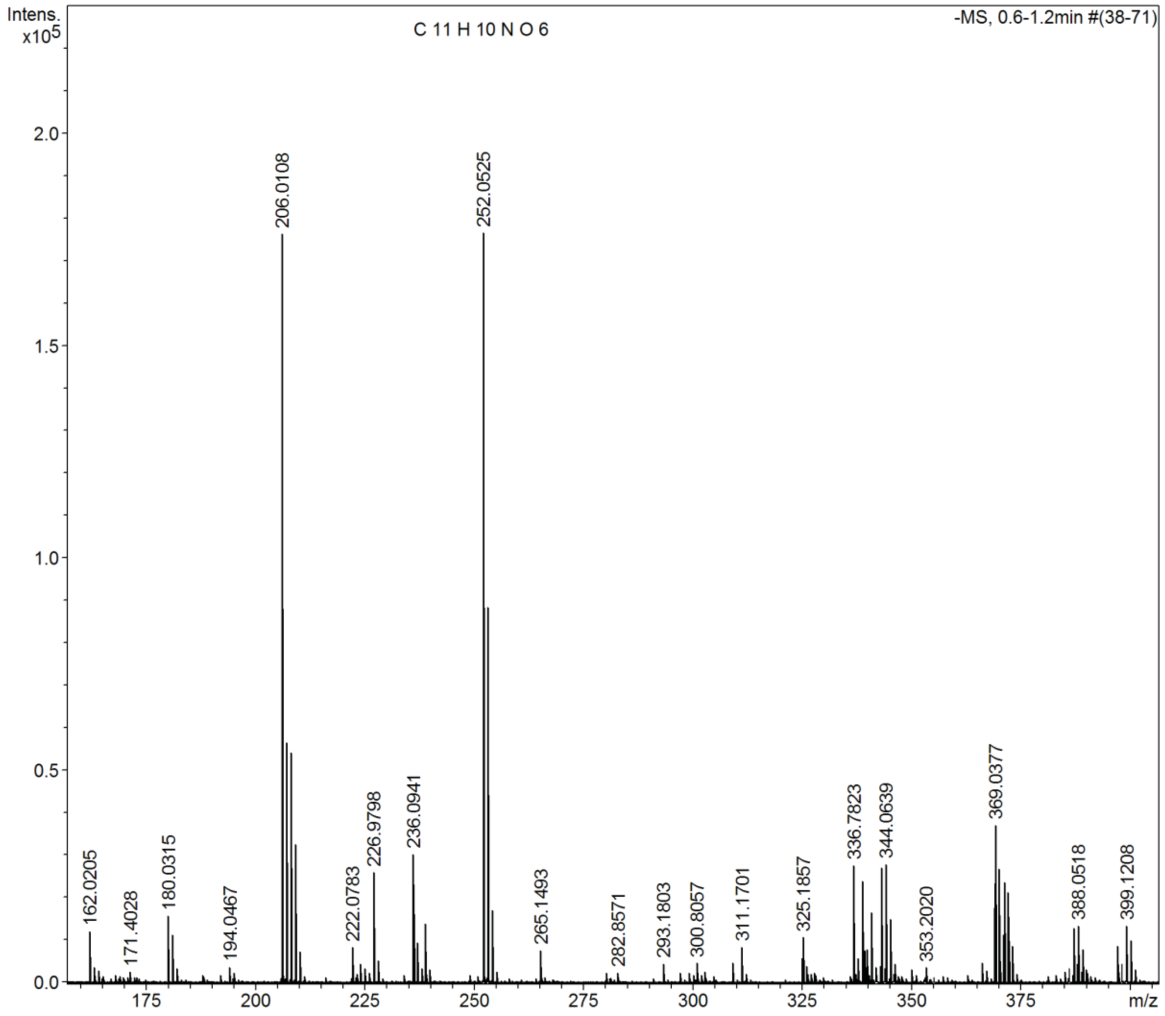

Figure 2.24 Mass spectroscopic analysis of partially thermolysed MOF-5-NHCOOEt in MeOH:NEt$_3$. Exact molecular weights: 1,4-bdc-NHCOOEt$^-$ = 252.05 m/z; 1,4-bdc-NCO$^-$ = 206.01 m/z.

2.4.9 Gas adsorption measurements

Low pressure adsorption isotherms were measured by a volumetric method using a Quantachrome Autosorb-iQ instrument. Freshly prepared MOF samples were washed with DEF:MeOH (1:2) and then activated by repeated washing and subsequent soaking in CH_2Cl_2

for several hours over the course of several days. The samples were then transferred to a pre-dried and weighed analysis tube, still covered with CH_2Cl_2. The sample tube was then heated at 1 ºC per minute to 30 ºC under vacuum then held under a dynamic vacuum at 10^{-6} Torr for 12 h. Accurate sample masses were calculated using degassed samples. All adsorption measurements used ultra-high purity gases.

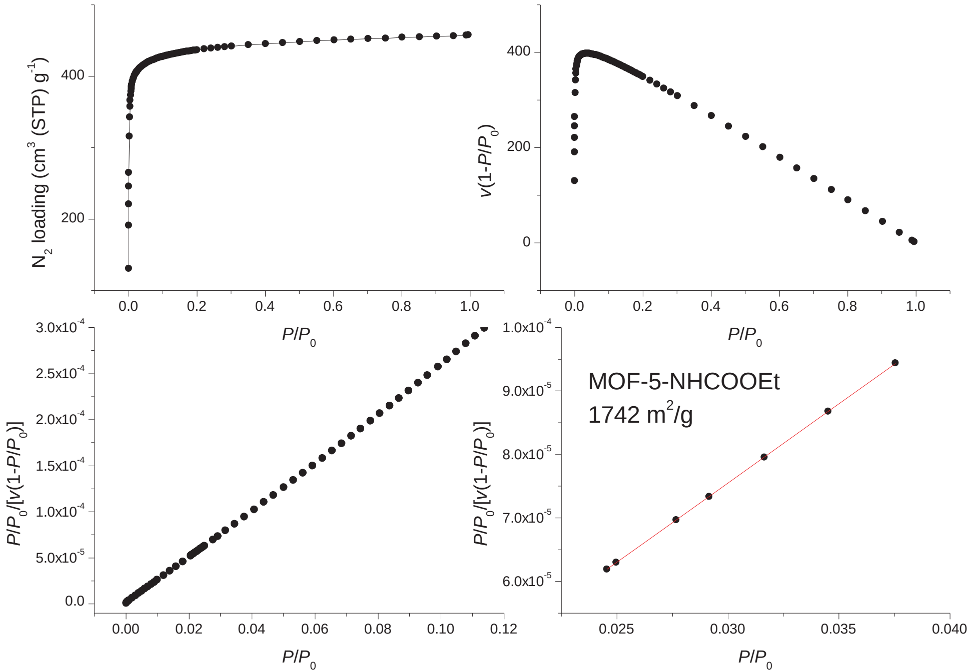

Equation	y = a + b*x	Pearson's r	1			Value	Std Error
Weight	No Weighting	Adj. R-Square	0.99999	P/P0/[v(1-P/P0)]	Intercept	5.80451E-7	7.1568E-8
Residual Sum of Squares	3.92991E-15				Slope	0.0025	2.35873E-6

Figure 2.25 N_2 adsorption isotherm at 77 K and BET surface area plots for MOF-5-NHCOOEt synthesized in DEF:MeOH (1:1).

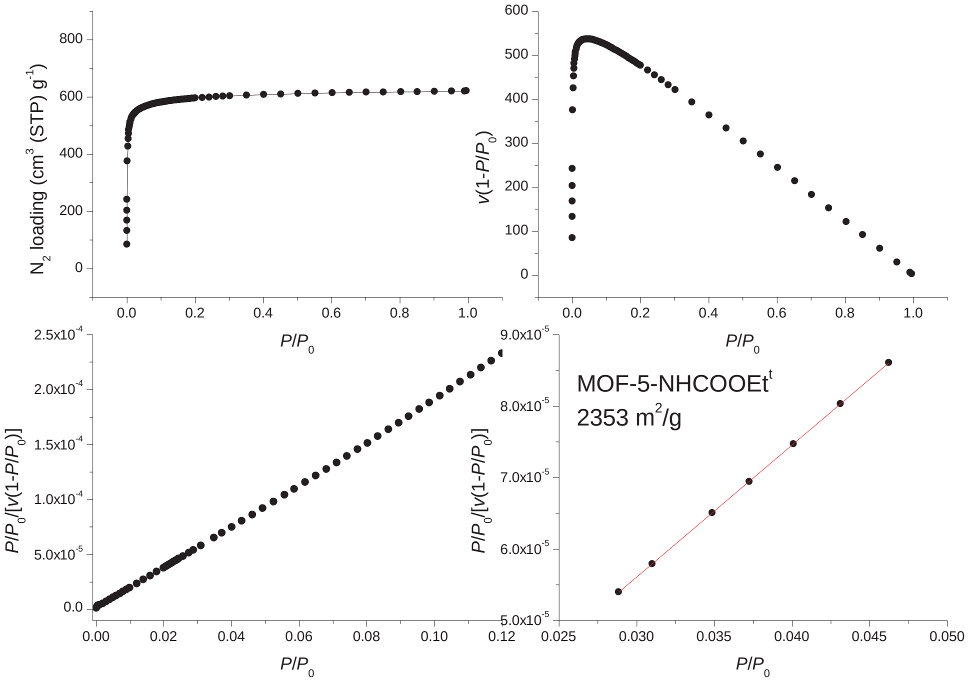

Equation	y = a + b*x	Pearson's r	1			Value	Std Error
Weight	No Weighting	Adj. R-Square	0.99999	P/P0/[v(1-P/P0)]	Intercept	7.20418E-7	9.13712E-8
Residual Sum of Squares	6.97244E-15				Slope	0.00185	2.41763E-6

Figure 2.26 N_2 adsorption isotherm at 77 K and BET surface area plots for MOF-5-NHCOOEt^t synthesized in DEF:MeOH (1:1).

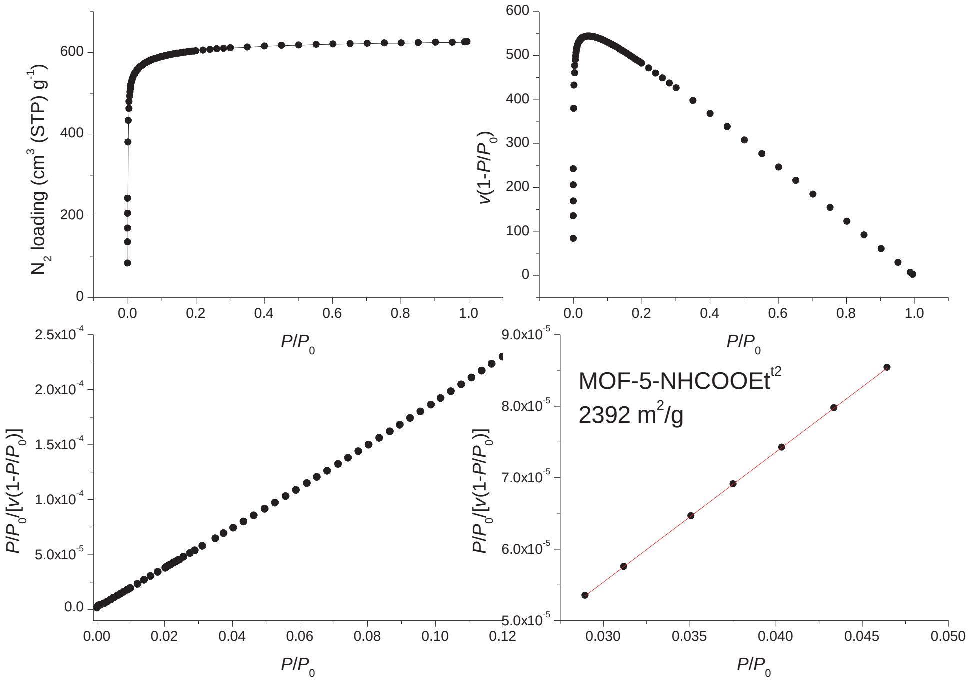

Equation	y = a + b*x	Pearson's r	1			Value	Std Error
Weight	No Weighting	Adj. R-Square	0.99999	P/P0/[v(1-P/P0)]	Intercept	7.11252E-7	9.19981E-8
Residual Sum of Squares	7.05897E-15				Slope	0.00182	2.41995E-6

Figure 2.27 N_2 adsorption isotherm at 77 K and BET surface area plots for MOF-5-NHCOOEt^{t2} synthesized in DEF:MeOH (1:1).

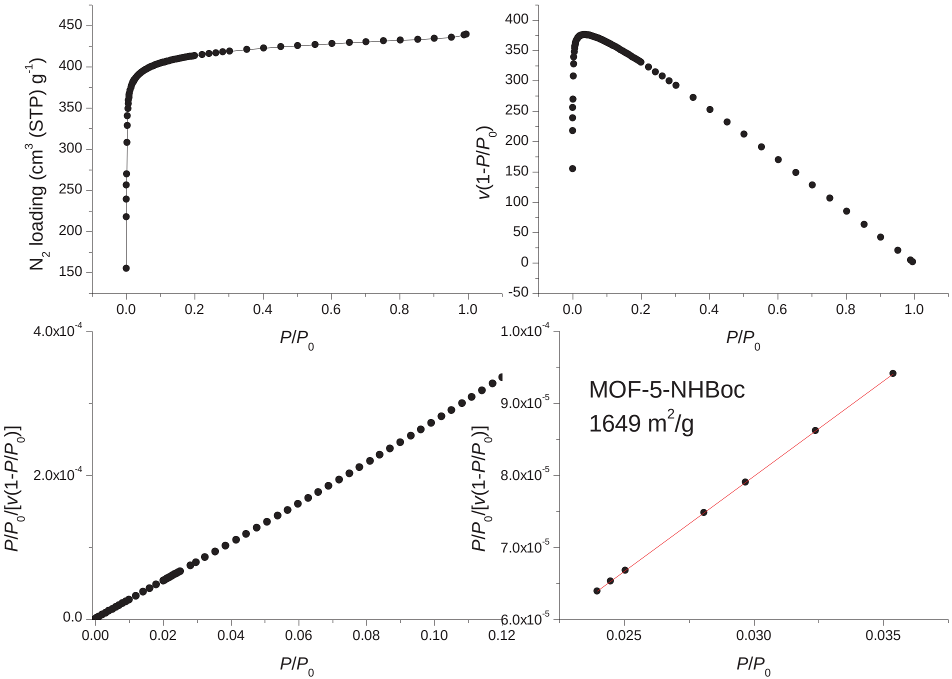

Equation	y = a + b*x	Pearson's r	1			Value	Std Error
Weight	No Weighting	Adj. R-Square	1	P/P0/[v(1-P/P0)]	Intercept	7.06232E-7	6.20638E-8
Residual Sum of Squares	2.63284E-15				Slope	0.00264	2.16201E-6

Figure 2.28 N_2 adsorption isotherm at 77 K and BET surface area plots for MOF-5-NHBoc synthesized in DEF:MeOH (1:1).

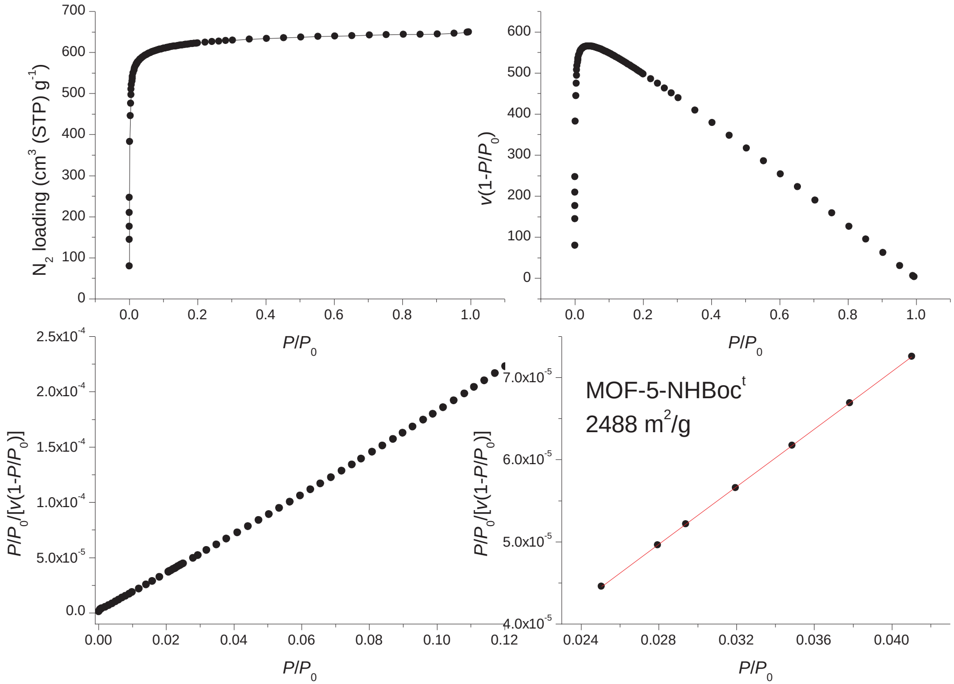

Equation	y = a + b*x	Pearson's r	1			Value	Std Error
Weight	No Weighting	Adj. R-Squar	0.99999	P/P0/[v(1-P/P0)]	Intercept	6.78671E-	6.73047E-8
Residual Sum of Squares	4.01085E-15				Slope	0.00175	2.03961E-6

Figure 2.29 N_2 adsorption isotherm at 77 K and BET surface area plots for MOF-5-NHBoc^t in DEF:MeOH (1:1).

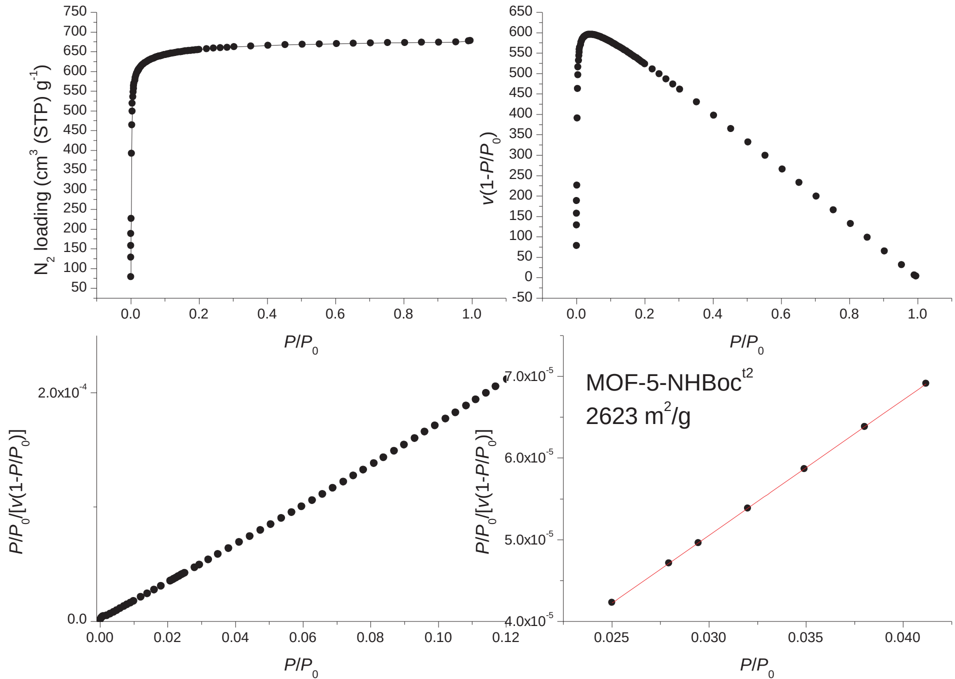

Equation	y = a + b*x	Pearson's r	1			Value	Std Error
Weight	No Weighting	Adj. R-Squar	0.99999	P/P0/[v(1-P/P0)]	Intercept	7.32173E-	7.28979E-8
Residual Sum of Squares	4.80358E-15				Slope	0.00166	2.2041E-6

Figure 2.30 N$_2$ adsorption isotherm at 77 K and BET surface area plots for MOF-5-NHBoc^{t2} synthesized in DEF:MeOH (1:1).

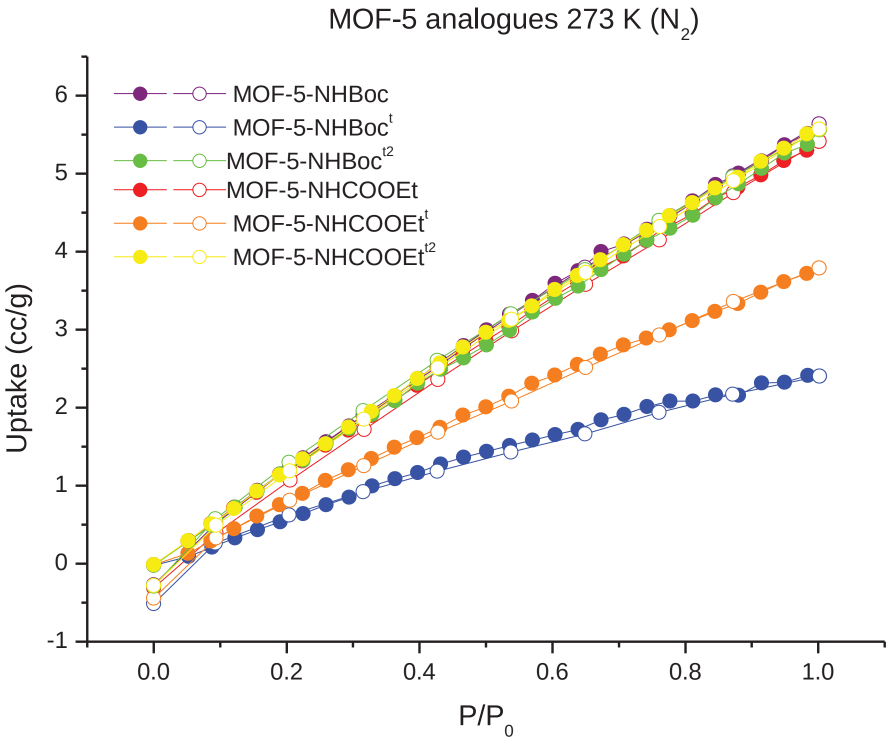

Figure 2.31 Gravimetric N$_2$ adsorption (filled) and desorption (open) isotherms measured at 273 K.

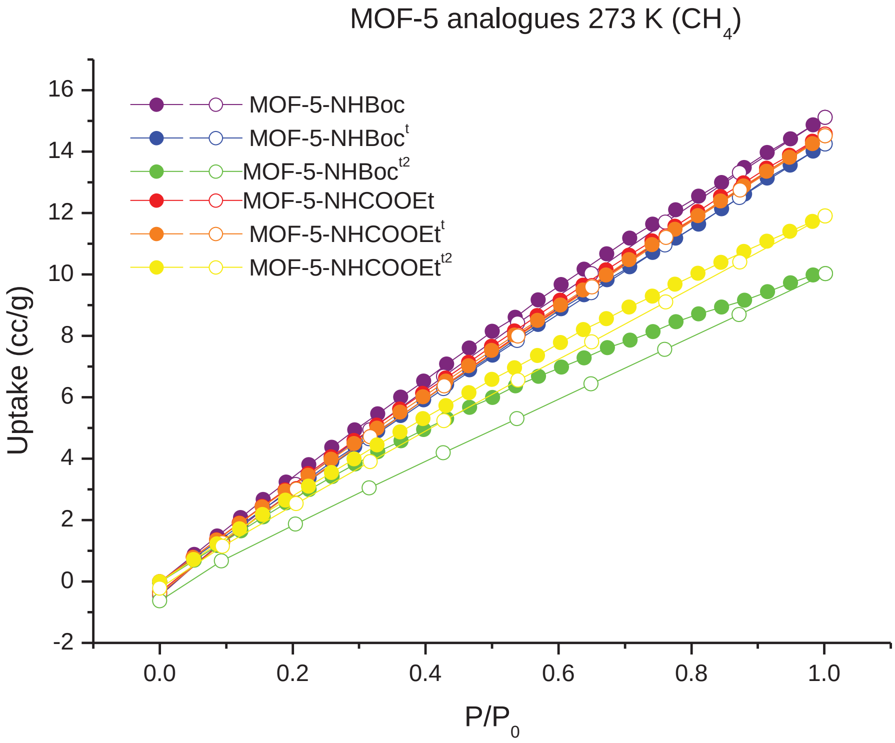

Figure 2.32 Gravimetric CH_4 adsorption (filled) and desorption (open) isotherms measured at 273 K.

Chapter 3 -Thermolabile Protecting Groups in tp-PMBB-1-lon-e

3.1 Introduction

After the successful incorporation of TPGs in MOF-5 type frameworks (Chapter 2), efforts were next turned to ternary MOFs (MOFs that are comprised of three distinct building blocks: two different ligands and a metal cluster. Ternary MOFs are of interest as they allow for the addition of multiple functionalities on the different ligands. In this chapter is reported the installation of TPGs in the known MOF tp-PMBB-1-lon-e-H ($[Zn_6(1,3\text{-}bdc)_6[Cr_3O(isonic)_6(H_2O)_2(OH)]]$). This MOF is henceforth referred to as lon-e. Figure 3.2 contains 1,3-benzenedicarboxylate (1,3-bdc) and isonicotinic acid (isonic).[162] This material is comprised of an undulating 2D sheet containing 1,3-bdc and zinc components that form a Kagomé lattice.[163] A kagomé lattice (also called trihexagonal tiling), named after Japanese basketry where this pattern has long been used, is a 2-D lattice comprised of regular

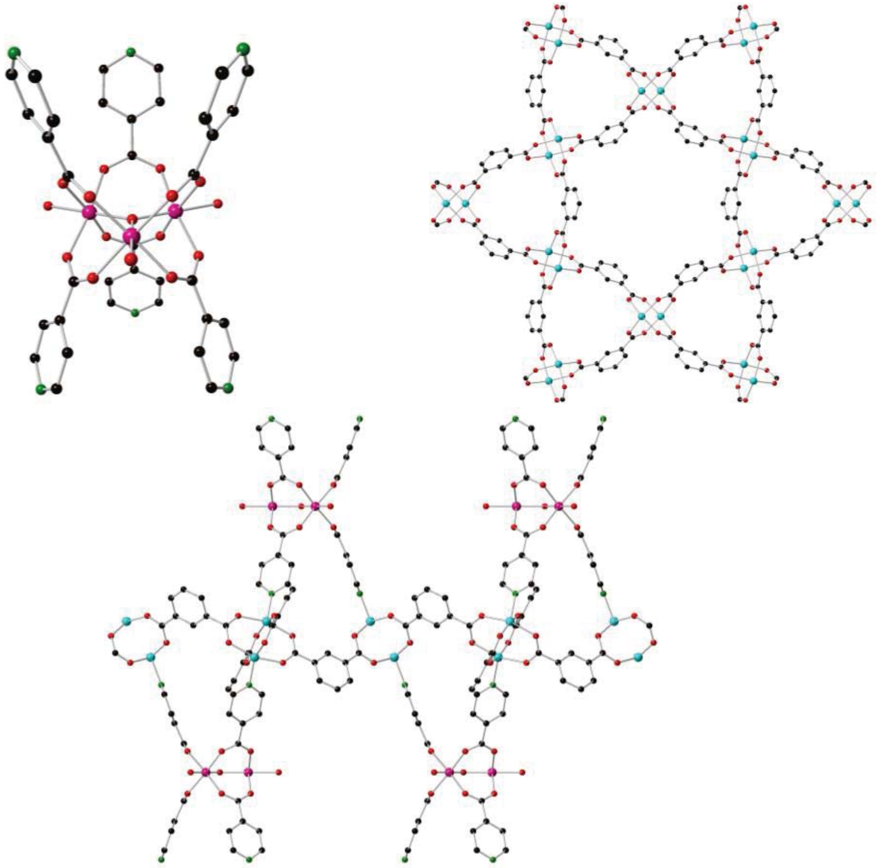

Figure 3.1 Structural components of lon-e-H as determined by SXRD. Clockwise from top left: tp-PMBB-1 complex (with depth perspective to aide visualisation); top view of kagomé lattice comprised of 1,3-bdc and Zn; side view of kagomé lattice with tp-PMBB-1 pillars. Atom colours: C = black, N = green, O = red, Zn = teal, Cr = magenta (hydrogen atoms omitted for clarity).

hexagons and triangles where each hexagon is surrounded by triangles and *vice versa*.[163] In this particular lattice, it is the paddlewheel connectivity of the Zn^{2+} metal ions and the 1,3-bdc-based linkers that forms both the hexagons and triangles that make up the kagomé lattice. The lattice is then pillared by tp-PMBB-1, a trigonal prismatic chromium-isonicotinic acid complex, to form the augmented lonsdaleite-e topology.[164,165] This lattice is then pillared by a trigonal prismatic chromium-isonicotinic acid complex. Lonsdaleite, named after Dame Kathleen Lonsdale who proved that benzene was flat through X-ray diffraction methods[166], is a rare allotrope of carbon, only occurring naturally when meteorites containing graphite impact on the Earth.[167] The heat and stress of this event causes the graphite to transform into diamond whilst retaining graphite's hexagonal lattice, giving rise to another common name for the material, hexagonal diamond. Other MOFs with this topology have been reported in the literature, from the relatively simple metal-formate MOFs of the Kim group[168] to the recent work of Patil *et al.* who used a tetrakis(4-cyanophenyl)adamant ligand to obtain both lonsdaleite and diamondoid MOFs.[169]

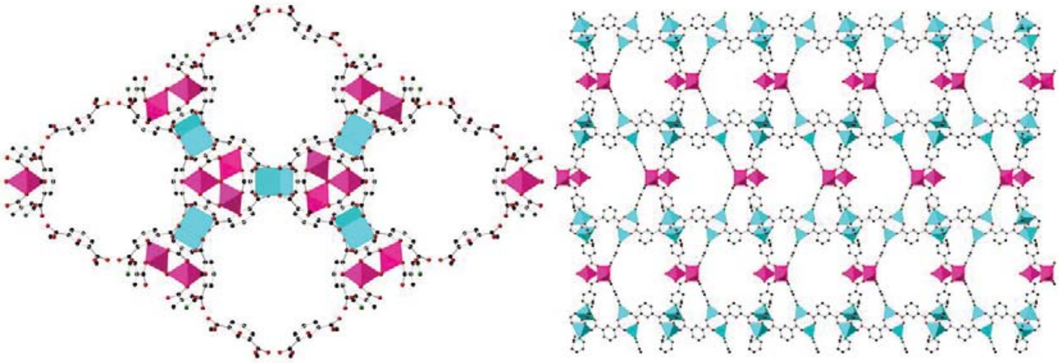

Figure 3.2 Structure of tp-PMBB-1-lon-e-H (lon-e) as determined by single crystal X-ray diffraction (SXRD) illustrating the Kagomé lattice (left) and pillaring of Kagomé lattice sheets (right). Atom colours: C = black, N = green, O = red, Zn = teal, Cr = magenta (hydrogen atoms omitted for clarity).

This MOF was reported by the Zaworotko group.[164,165] It is not uncommon to use pre-constructed SBUs in the synthesis of MOFs, with other examples in the literature such as: the Cohen group who have published multiple papers using metal dipyrrin complexes as metalloligands;[170,171] the Shimizu and Luo groups that have independently published papers using 2,2'-bipyridine based metalloligands;[172,173] and the Severin group that developed intricate polycarboxylate clathrochelate metalloligands to synthesise a variety of MOFs.[174]

In their 2013 paper, the Zaworotko group investigated the effect of altering the substituent at the 5 position of the 1,3-bdc (or in one case replacing the 1,3-bdc with 2,5-furandicarboxylate (fdc)) on gas sorption profiles. Of the five substituents that resulted in permanent porosity (-H, -*t*-Bu, $-NO_2$, -Br, and fdc), it was found that the MOF with the *t*-Bu substituent had the highest CO_2 uptake around room temperature. This may not necessarily have been expected, as it has been shown that polar groups can enhance CO_2 uptake.[89] The authors attributed this behaviour to the pore shape in each species rather than the surface areas or functionalities, and that the performance of lon-e-*t*-Bu is improved by "the confined pore space generated by the bulky *tert*-butyl groups."

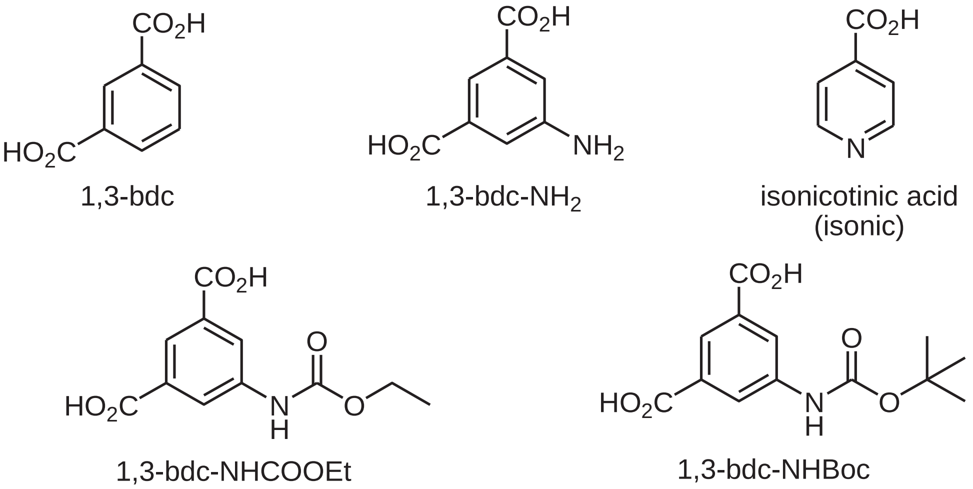

Figure 3.3 Ligands involved in the synthesis of lon-e and its analogues.

This material was of particular interest as the polar hydroxyl and amine functionalised materials (lon-e-OH/lon-e-NH_2) synthesised in the original paper exhibited no porosity. The TGA traces reported for the lon-e materials indicate that the MOFs are stable to above 300 °C, well above the typical temperatures of 100-200 °C used for thermal deprotection.[106] It was envisaged that it may be able to access a porous amine functionalised lon-e analogue, and possibly even an isocyanate functionalised analogue, through the use of a TPG on the amino group (Figure 3.3). A material produced in this way may exhibit porosity, unlike the

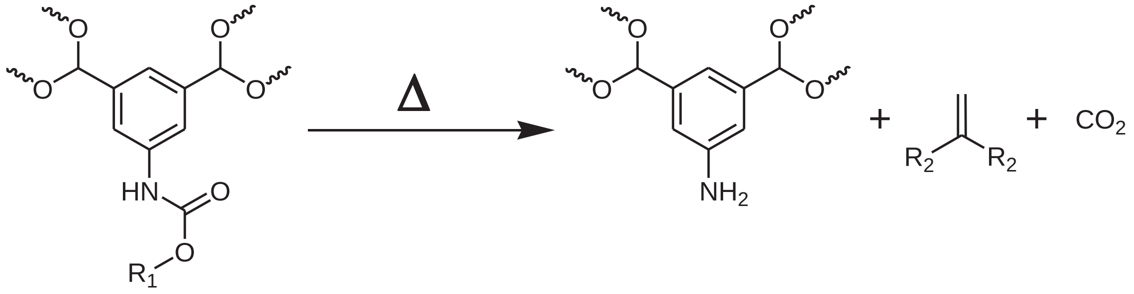

lon-e-NHCOOEt: R_1 = Et, R_2 = H. expected weight loss = 15.2 %
lon-e-NHBoc: R_1 = *t*-Bu, R_2 = Me. expected weight loss = 19.9 %

Figure 3.4 Scheme outlining thermolytic deprotection of TPGs in lon-e-NHTPG to generate lon-e-NH_2

directly synthesised MOF (i.e. the MOF synthesised using unprotected ligands). This is not the first example of a 1,3-bdc ligand containing a TPG. In 2013, the Mondal group published a lanthanide-based MOF with 5-azido-1,3-bdc (1,3-bdc-N_3) which was able to be thermolysed to 1,3-bdc-N:, a nitrene. They found that post thermolysis the mmol/g uptakes of CO_2 at 273 K at 1 atm increased by 30-50 %, a feature the authors attributed to the increased surface area of the deprotected materials.

3.2 Results and discussion

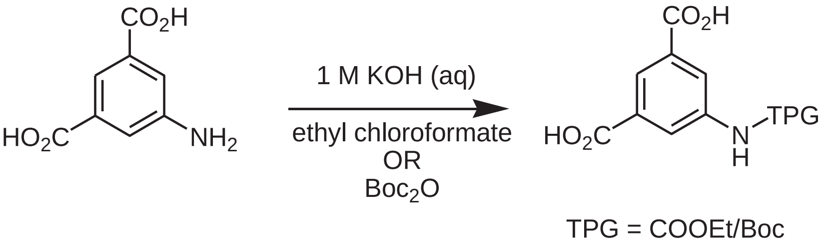

Figure 3.5 Generalised synthetic route to produce 1,3-bdc-NHTPG

The reaction of 5-amino-1,3-benzenedicarboxylate (1,3-bdc-NH_2) with ethyl chloroformate or Boc_2O in aqueous KOH (1 M) at room temperature afforded quantitative yields of 5-ethoxycarbonylamino-1,3-benzendicarboxylate (1,3-bdc-NHCOOEt) and 5-*tert*-butoxycarbonylamino-1,3-benzenedicarboxylate (1,3-bdc-NHBoc), respectively. Stock solutions of $[Cr_3O(isonic)_6(H_2O)_2(OH)](NO_3)_6 \cdot 2H_2O$ (prepared using a literature procedure[162]) and $Zn(NO_3)_2.4H_2O$ in DMF were combined with 1,3-bdc-NHCOOEt/NHBoc, MeOH, and additional DMF before reacting in a 65 °C oven for 18 hours. This afforded green hexagonal shaped crystals (Figure 3.5). These crystals were washed three times with dry DMF to remove any impurities, including microcrystalline powder phases, then washed twice with and stored in dry acetonitrile. The synthesis of lon-e-NHCOOEt and lon-e-NHBoc deviated slightly from the synthesis of lon-e-NH_2, both by

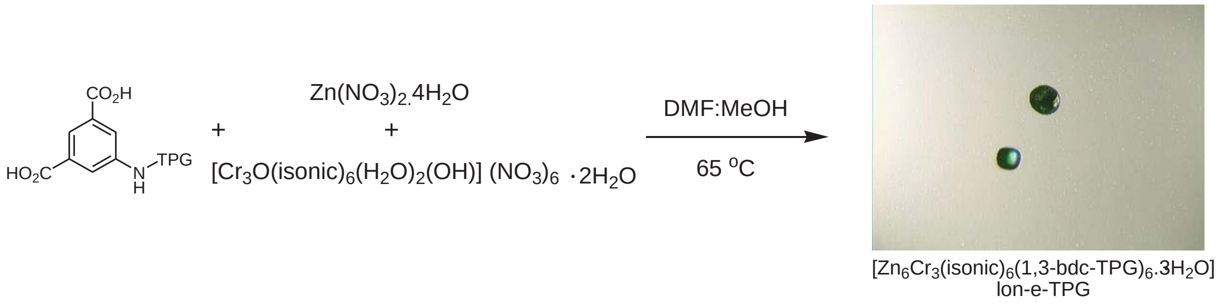

Figure 3.6 Generalised synthetic route to lon-e-NHCOOEt and lon-e-NHBoc.

slightly altering the solvent ratios used and also by not pre-dissolving the 1,3-bdc based ligands in stock solutions. These deviations were implemented in order to improve the yields, as using the conditions used in the literature resulted in very low yields when using the TPG containing ligands. It should be noted that copious amounts of amorphous powder was produced during this synthesis in addition to large green single crystals, though this appears to be in keeping with the literature results, where the crystals were washed to remove similar powder phases.[162] Experimental powder X-ray diffraction (PXRD) patterns of the green crystals match fairly well to the PXRD pattern calculated for lon-e-NH_2 (Figure 3.7), indicating that the produced materials were isostructural with the reported lon-e MOFs. Single crystal X-ray diffraction (SXRD) of the materials allowed for direct comparison of the crystal structures and confirmed them as the target MOFs.

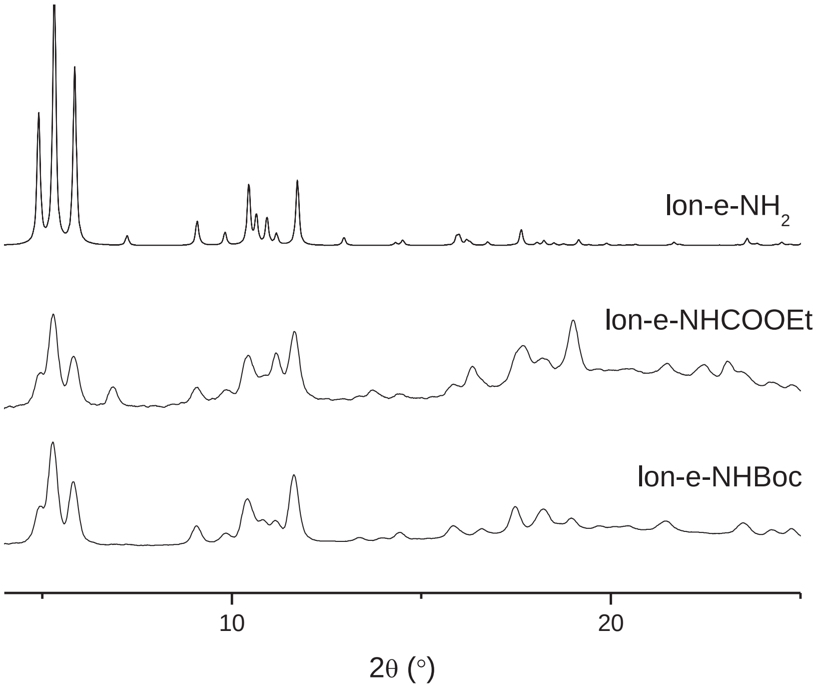

Figure 3.7 Powder X-ray diffraction (PXRD) patterns of three related MOFs. Lon-e-NH_2 pattern calculated from literature cif file.

Prior to ^{1}H-NMR spectroscopic analysis, the excess acetonitrile was decanted and the remaining solvent present removed under dynamic vacuum at room temperature. ^{1}H-NMR spectroscopic analysis (Figure 3.7) was carried out by digesting the MOF materials in DMSO-d_6/DCl. This revealed that both protecting groups had mostly survived the synthesis intact, with less than < 5 % deprotection in both cases. The isonicotinic acid was present in amounts much lower than the 1:1 ratio expected from the MOF stoichiometry. The ratio of isonicotinic acid to 1,3-bdc-TPG varied amongst NMR samples, and ranged from 0.15:1 to

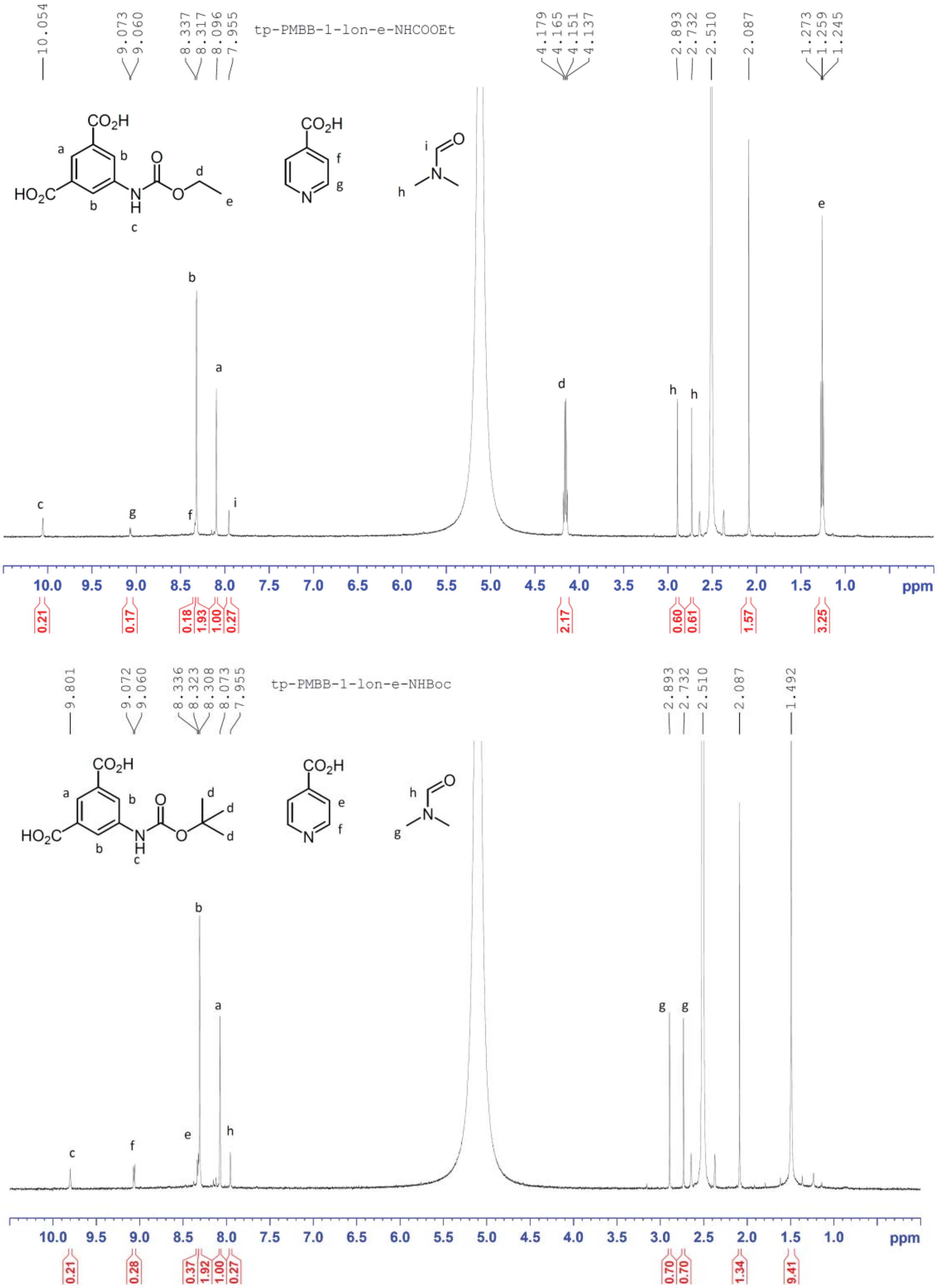

Figure 3.8 ^{1}H-NMR spectra of digested activated lon-e-NHCOOEt (top) and lon-e-NHBoc (bottom) showing degree of deprotection occurring during synthesis.

0.3:1 between samples. Since PXRD and SXRD (*vide infra*) showed that the desired MOF had formed, this is ascribed to the isonicotinic acid not fully dissociating from the paramagnetic chromium ions, resulting in the peaks belonging to the bound isonicotinic acids broadening to the extent where they become obscured in the noise of the spectral baselines. Also at odds with the PXRD and SXRD data were the elemental analysis results. For both lon-e-NHCOOEt and lon-e-NHBoc the percentage of carbon recorded by >6% and >4% respectively. This is unexpected as both samples had been activated as for gas sorption, meaning that there should be very little solvent present. Furthermore, even assuming a large portion of solvent remained, it was not possible to possible to calculate values that agreed with the experimental percentages.

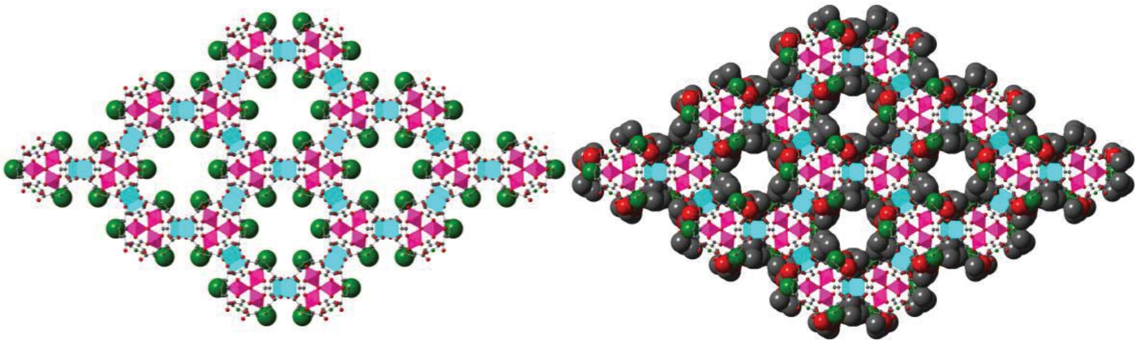

Figure 3.9 Structures of lon-e-NH_2 (left) and lon-e-NHBoc (right) as determined by SXRD. The pendant groups have been rendered in space filling mode. The side chains in lon-e-NHBoc have been modelled as they were not detected in the SXRD data. Atom colours: C = grey, N = green, O = red, Zn = teal, Cr = magenta (hydrogen atoms omitted for clarity).

SXRD experiments confirmed that the materials obtained retained the same lonsdaleite-e framework topology as the parent frameworks reported by Zaworotko et al, achieved through pillaring of the Kagomé lattice sheets. The frameworks in this work contain infinite hexagonal pores down the c-axis, into which the side groups are projected (Figure 3.9). Due to the large quantity of occluded solvent and the rotational disorder inherent in the side chains it was not possible to ascertain the coordinates of the TPGs from the single crystal data. The presence of the side groups was confirmed by ^{1}H-NMR spectra of the digested MOFs (Figure 3.7). In addition, use of the SQUEEZE command in PLATON[175] on the single crystal data without modelled side chains revealed 1050 electrons per unit cell in void space in lon-e-NHCOOEt, and 1104 electrons per unit cell in void space in lon-e-NHBoc. In both cases this more than accounts for the presence of six side chains per unit cell (which would be 240 and 336 electrons for lon-e-NHCOOEt and lon-e-NHBoc respectively). The remainder can be assigned to occluded DMF and MeOH solvent molecules. It should be noted that in all data sets collected for lon-e-NHCOOEt and lon-e-NHBoc a highly disordered DMF molecule was observed at the apex of the trigonal-pyramidal pore formed by the tp-PMBB-1 SBU. It was not able to accurately assign the coordinates of the component atoms of the DMF due to the high degree of disorder present, so the DMF has not been included in the crystal structures, and is the source of the high residual electron density reported in Table 3.1.

Table 3.1 Crystallography data of lon-e-NHCOOEt and lon-e-NHBoc

MOF	**lon-e-NHCOOEt**	**lon-e-NHBoc**
Formula	$C_{102}H_{83}Cr_3N_{12}O_{52}Zn_6$	$C_{114}H_{108}Cr_3N_{12}O_{52}Zn_6$
Formula weight	2858.03	3026.34
Crystal size (mm)	0.12 x 0.11 x 0.05	0.15 x 0.14 x 0.06
Temperature (K)	293	293
Wavelength (Å)	1.54187	1.54187
Crystal system	Hexagonal	Trigonal
Space group	*P*63/mmc	*P*-31c
Unit cell lengths (Å)	a = 19.0486(3)	a = 19.0678(4)
	b = 19.0486(3)	b = 19.0678(4)
	c =35.992(3)	c =36.010(3)
Unit cell angles (°)	α = 90.0	α = 90.0
	β = 90.0	β = 90.0
	γ = 120.0	γ = 120.0
Unit cell volume (Å^3)	11310.1(9)	11338.4(9)
Z	2	2
D_{calc} (g cm^{-3})	0.839	0.886
μ (mm^{-1})	2.28	2.29
F(000)	2896	3088
Reflns coll./unique, R_{int}	99549 / 4127, 0.0491	94695 / 7416, 0.0610
Data range	8.0 Å > d > 0.81 Å	8.0 Å > d > 0.81 Å
Index ranges	$-19 \leq h \leq 23$, $-23 \leq k \leq 15$, $-44 \leq l \leq 44$	$-21 \leq h \leq 14$, $-23 \leq k \leq 23$, $-35 \leq l \leq 44$
Completeness	99.2%	99.3%
T_{min}, T_{max}	0.662, 1.00	0.638, 1.00
R indices for data with $I>2\sigma(I)$	$R_1 = 0.1411$; $wR_2 = 0.4340$	$R_1 = 0.1783$; $wR_2 = 0.5071$
R indices for all data	$R_1 = 0.1470$; $wR_2 = 0.4340$	$R_1 = 0.2028$; $wR_2 = 0.5071$
Largest difference peak and hole (e Å^{-3})	5.00/-0.58	4.23 / −0.87

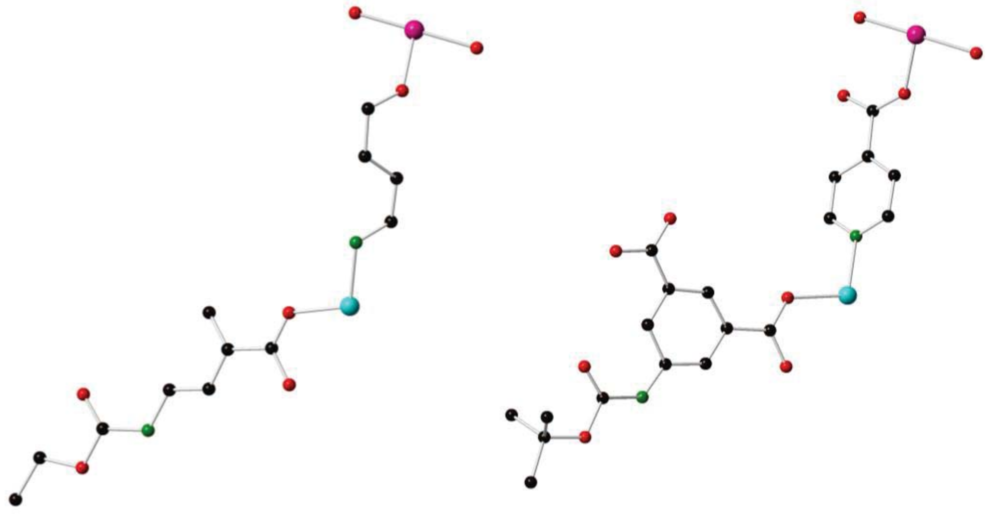

Figure 3.10 Asymmetric unit cells for lon-e-NHCOOEt (left) and lon-e-NHBoc (right) determined from experimental SXRD data.

Perhaps the biggest difference in the two crystal structures is that lon-e-NHBoc was found to belong to the trigonal P-31c space group, whereas lon-e-NHCOOEt retained the hexagonal P63/mmc space group shared with the other lon-e MOFs. As can be seen in the asymmetric unit (ASU) of these materials (Figure 3.10), lon-e-NHBoc lacks some of the symmetry elements present in loon-e-NHCOOEt, most noticeably the mirror planes that duplicate the half ligands present in the ASU to give the full ligands present in the unit cell.

In order to determine the conditions required for the thermal deprotection of the TPGs, preliminary TGA experiments were conducted on both the free ligands and the MOFs (Figure 3.11). The expected products of the thermal deprotection of the ligands were 1,3-bdc-NH_2 and 1,3-bdc-NCO. The formation of 1,3-bdc-NH_2 would release CO_2 and either ethene for 1,3-bdc-NHCOOEt or isobutylene for 1,3-bdc-NHBoc. The formation of 1,3-bdc-NCO would release EtOH for 1,3-bdc-NHCOOEt and *t*-BuOH for 1,3-bdc-NHBoc. More detail on the thermolysis process for these TPGs can be found in Chapter 2 where the thermal deprotections of the analogous materials 1,4-bdc-NHCOOEt and 1,4-bdc-NHBoc are described in greater detail.

The TGA trace of 1,3-bdc-NHCOOEt reveals a 50% weight loss starting at around 230 °C, nearly double the expected 28.5% weight loss associated with CO_2 and ethene (Figure 3.12). This indicates that a similar polymerisation effect is occurring in 1,3-bdc-NHCOOEt as happened with 1,4-bdc-NHCOOEt in Chapter 2. However, unlike with 1,4-

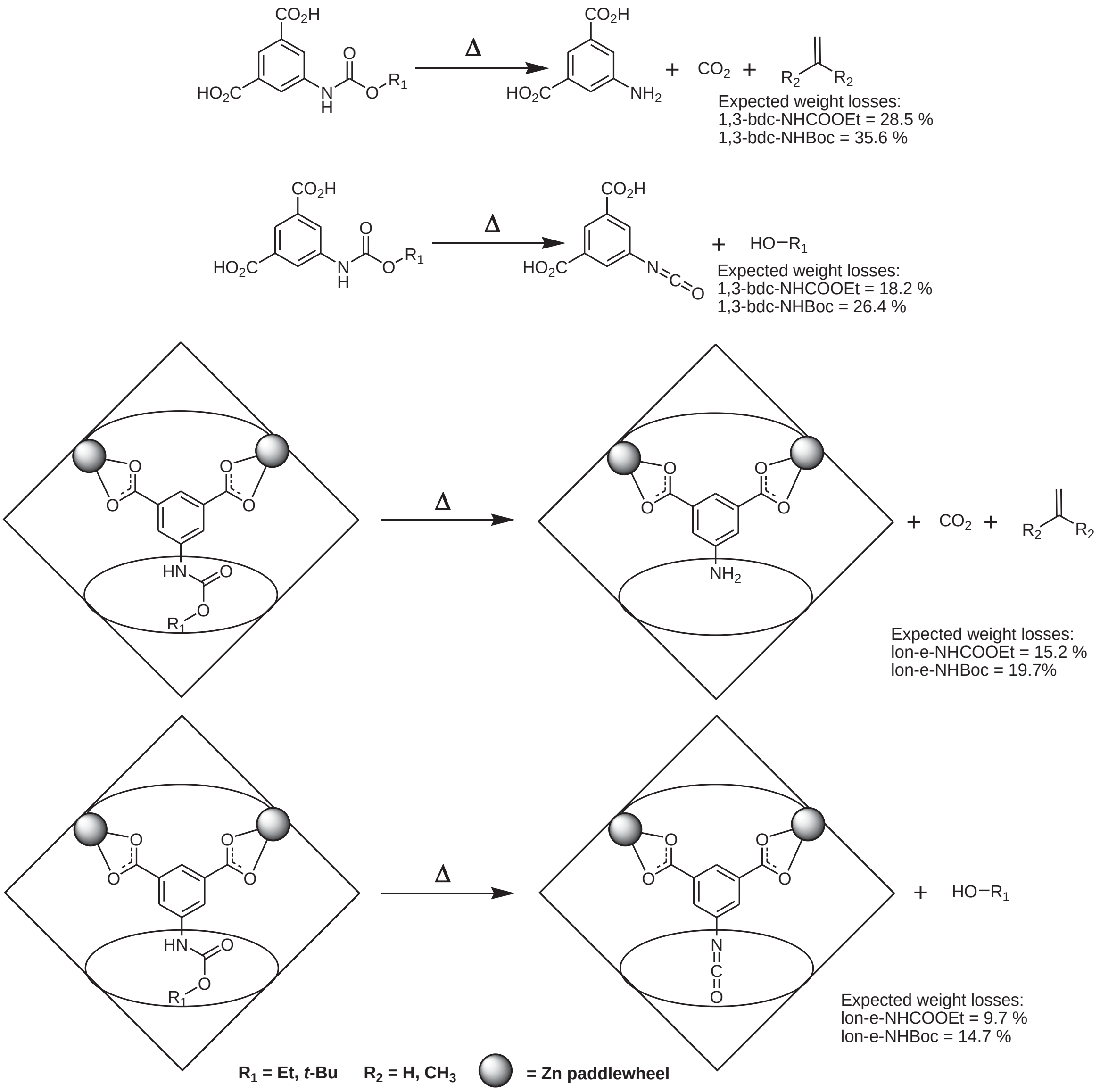

Figure 3.12 General schemes for the thermolysis of carbamate esters in the free ligand (top) and lon-e MOF (bottom), including expected weight losses.

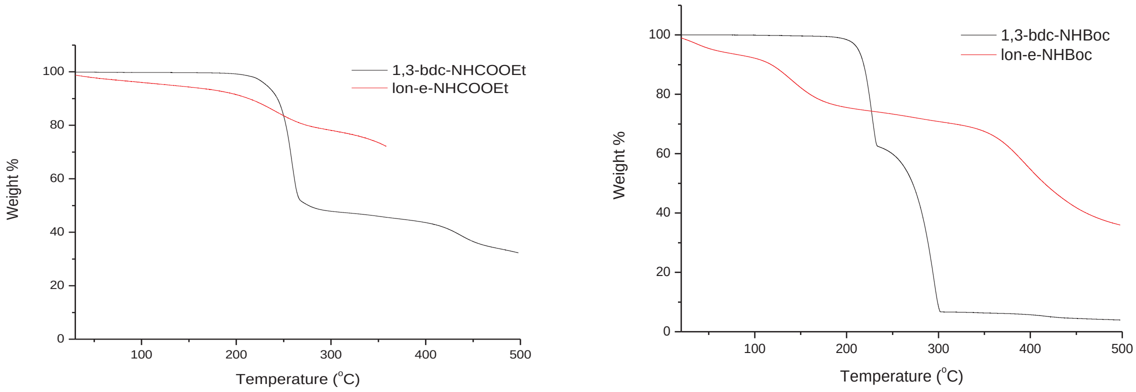

Figure 3.11 Thermogravimetric analysis (TGA) traces of 1,3-bdc-NHCOOEt & lon-e-NHCOOEt (left) and 1,3-bdc-NHBoc & lon-e-NHBoc (right).

bdc-NHCOOEt, there was no obvious "cake" that formed with 1,3-bdc-NHCOOEt and the material was more readily dissolved. ^{1}H-NMR spectroscopic analysis of the thermolysed 1,3-bdc-NHCOOEt revealed a similar pattern of new peaks as occurred with 1,4-bdc-NHCOOEt, further supporting the polymerisation hypothesis. The TGA trace of lon-e-NHCOOEt reveals an approximate 16% weight loss starting at around 200 °C. This matches closely to the expected 15.2% weight loss for CO_2 and ethene, indicating that the isocyanate is not forming in the MOF. This is most likely due to the presence of the residual DMF in the pores, as how the presence of solvents can affect thermolysis results in other materials has been observed by this group in other materials.

PXRD of lon-e-NHCOOEt post thermolysis revealed complete loss in crystallinity (Figure 3.13). It had been noted during activation of the materials for gas sorption that the materials were fragile and prone to collapse (*vide infra*), and it is believed that the same collapse may have been happening during the deprotection in the TGA apparatus where the samples are exposed to the atmosphere after analysis.

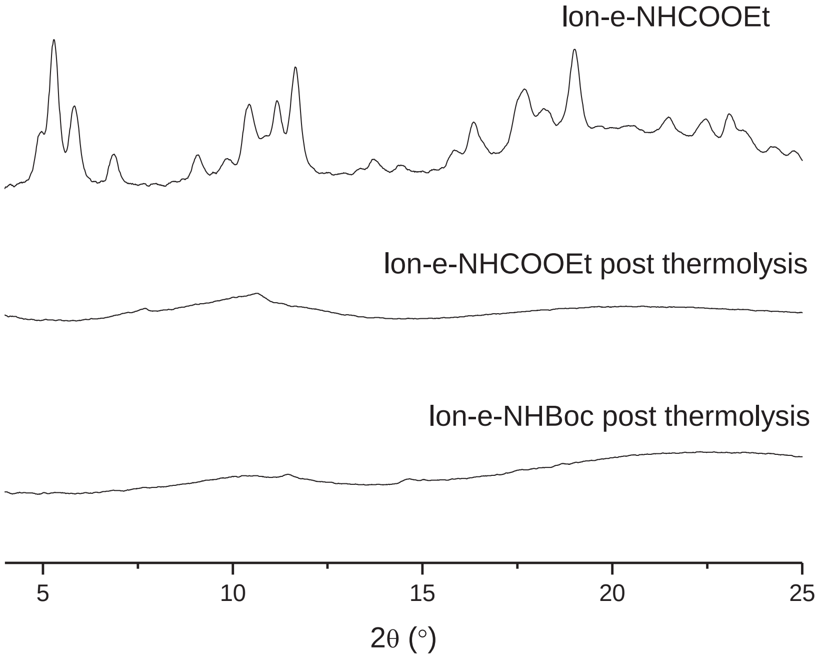

Figure 3.13 PXRD patterns of lon-e-NHCOOEt post activation (top), lon-e-NHCOOEt post thermolysis (middle), and lon-e-NHBoc post thermolysis (bottom).

The TGA trace of 1,3-bdc-NHBoc results revealed an approximately 37% weight loss starting around 200 °C. This closely matches the 35.6% expected weight loss for CO_2 and isobutylene. This indicates that the ligand is forming 1,3-bdc-NH_2 upon thermolysis. The TGA trace of lon-e-NHBoc revealed that the Boc TPG starts to be thermolysed at around

110 °C. This is deprotection temperature is approximately 90 °C lower than in the free ligand. It is not known exactly why there is this discrepancy in deprotection temperatures, though it is consistent with 1,4-bdc-NHBoc results in Chapter 2. PXRD data collected on samples following thermolysis revealed complete loss in crystallinity (Figure 3.13). As with lon-e-NHCOOEt above, it is believed that the collapse may have been occurring due to exposure to the atmosphere, and thus continued with the experiments.

Trial thermolyses were then conducted using the activation ports on the gas sorption instrument, where the samples are placed under vacuum and then heated using heating mantles. Conditions were scanned until the lowest temperatures that still attained near-complete deprotection (determined by ^{1}H-NMR) were found, 12 h at 130 °C for lon-e-NHBoc and 12 h at 200 °C for lon-e-NHCOOEt. PXRD revealed that these materials had lost all crystallinity. However, it was hoped that the materials would retain porosity despite the loss of crystallinity.

The protected MOFs were activated by supercritical CO_2 exchange, a process by which a solvent (in this case acetonitrile) is exchanged with liquid CO_2 through repeated washing and soaking, after which the CO_2 is transformed into its supercritical phase. This allows for a gentle removal of solvent from the pores of the MOF, and is often used to prevent pore collapse when more traditional methods fail. ^{1}H-NMR spectroscopic analysis of the activated materials revealed near complete removal of solvent, with only 0.6-0.7 DMF molecules present per unit cell (Figure 3.7). It should be noted that it was not possible to fully remove this residual DMF by any means, even when using harsher conditions that resulted in pore collapse the DMF was still present. As the Zaworotko group did not report any NMR data in the original paper, it is not possible to determine if this behaviour is shared with the literature MOFs. Due to the resistance of this DMF to removal, and the fact that there is less than one per unit cell, this DMF can be reasonably assigned as the highly disordered DMF seen in the SXRD data (*vide supra*).

By using the N_2 isotherms collected at 77 K, it is possible to calculate the Brunauer-Emmett-Teller (BET) surface areas of the internal pore systems of the materials. BET values of 213 ± 1 m^2/g and 323 ± 1 m^2/g were calculated for lon-e-NHCOOEt and lon-e-NHBoc respectively from the experimental data (Figure 3.14). These values are much lower than the literature value of 1649 m^2/g for lon-e, however this is consistent with the large steric bulky groups blocking internal void spaces and reducing pore size. *Tert*-butyl functionalized lon-e (lon-e-*t*-Bu) has a BET surface area of 546 m^2/g, approximately 1/3 the surface area of lon-e, and the substituents present in lon-e-NHCOOEt and lon-e-NHBoc are significantly larger than *t*-Bu. It is possible that the discrepancy between the literature results and those obtained in this study is due to the continued presence of DMF after activation, which could be preventing full access to the internal void space. It should be noted that it was not possible to replicate the gas sorption isotherms reported for lon-e-H by the Zaworotko group.[162] Attempts using the literature activation method (exchange of solvent with MeCN, degassing at room temperature) resulted in incredibly low uptakes (approximately 24 cc/g for N_2 at 77 K), whilst supercritical CO_2 activation of lon-e-H resulted in the sample failing to collect any data points, despite leaving the experiment running for an extended period. It is not known as to why supercritical CO_2 activation failed to properly activate the lon-e-H material as it typically a more effective method for evacuating solvent from pores than removal of low boiling point solvents under vacuum.[176] However, it is envisaged that the bulky TPGs present in our sample would both prevent the collapse of the pores, and also open up the pores upon their removal, so the investigation was continued.

It is unusual that lon-e-NHCOOEt has a lower BET surface area than lon-e-NHBoc which has a bulkier side group, and the decrease in surface area has been attributed to the bulkiness of the side groups. It is possible that in lon-e-NHCOOEt the side chains are able to pack together to more effectively block void space (it was not possible to directly observe these chains crystallographically), or possibly are better able to block pore windows than the side chains in lon-e-NHBoc. It was also noticed that the desolvated frameworks are much more prone to collapse than other MOFs such as MOF-5, and necessitated the use of supercritical CO_2 activation, a much gentler technique than the typical method of using a dynamic vacuum and low boiling point solvent. It is possible that, despite the utmost care being taken, the frameworks may have partially collapsed during transfer from the activation apparatus to the sample tubes. This could explain the lower than expected BET surface areas and/or the unexpected lower BET surface area of lon-e-NHCOOEt with respect to lon-e-NHBoc as either the lon-e-NHCOOEt experienced partial collapse whereas lon-e-NHBoc did not, or both experienced partial collapse but -NHBoc is better at resisting pore collapse than -NHCOOEt.

Whilst the BET surfaces areas of lon-e-NHCOOEt and lon-e-NHBoc are dramatically lower than that of lon-e-*t*-Bu, the total uptakes of N_2 at 77 K for these materials are quite similar, with approximately 90 cm^3/g and 140 cm^3/g for lon-e-NHCOOEt/-NHBoc respectively (Figure 3.14) and approximately 140 cm^3/g for lon-e-*t*-Bu.[162] This disparity between total uptake and BET surface area has arisen from the difference in the shapes of the isotherms, with lon-e-*t*-Bu having the typical very steep initial uptake until the maximum loading has been established followed by a plateau region, and whereas lon-e-NHCOOEt/NHBoc have a shorter initial steep uptake region followed by a long shallower

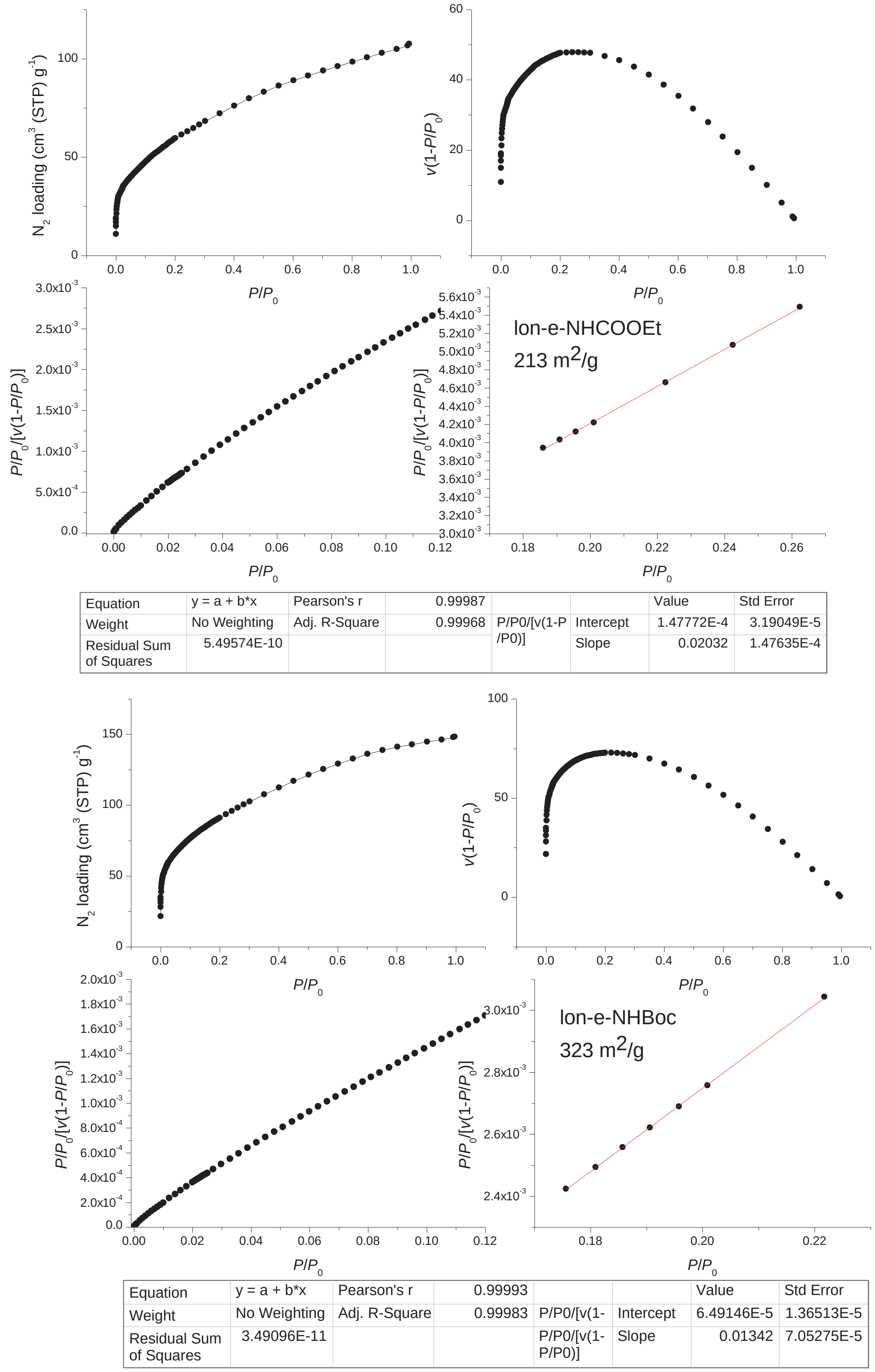

Equation	y = a + b*x	Pearson's r	0.99987			Value	Std Error
Weight	No Weighting	Adj. R-Square	0.99968	P/P0/[v(1-P/P0)]	Intercept	1.47772E-4	3.19049E-5
Residual Sum of Squares	5.49574E-10				Slope	0.02032	1.47635E-4

Equation	y = a + b*x	Pearson's r	0.99993			Value	Std Error
Weight	No Weighting	Adj. R-Square	0.99983	P/P0/[v(1-	Intercept	6.49146E-5	1.36513E-5
Residual Sum of Squares	3.49096E-11			P/P0/[v(1-P/P0)]	Slope	0.01342	7.05275E-5

Figure 3.14 BET surface area calculations for lon-e-NHCOOEt (top) and lon-e-NHBoc (bottom).

uptake region that never plateaus. This is important as BET calculations involve points in the initial uptake region, which are markedly different in lon-e-NHCOOEt/NHBoc than in the other lon-e analogues. This is potentially a result of the limitations of using N_2 at 77 K, where there are instances of the N_2 molecules having insufficient energy to diffuse into the

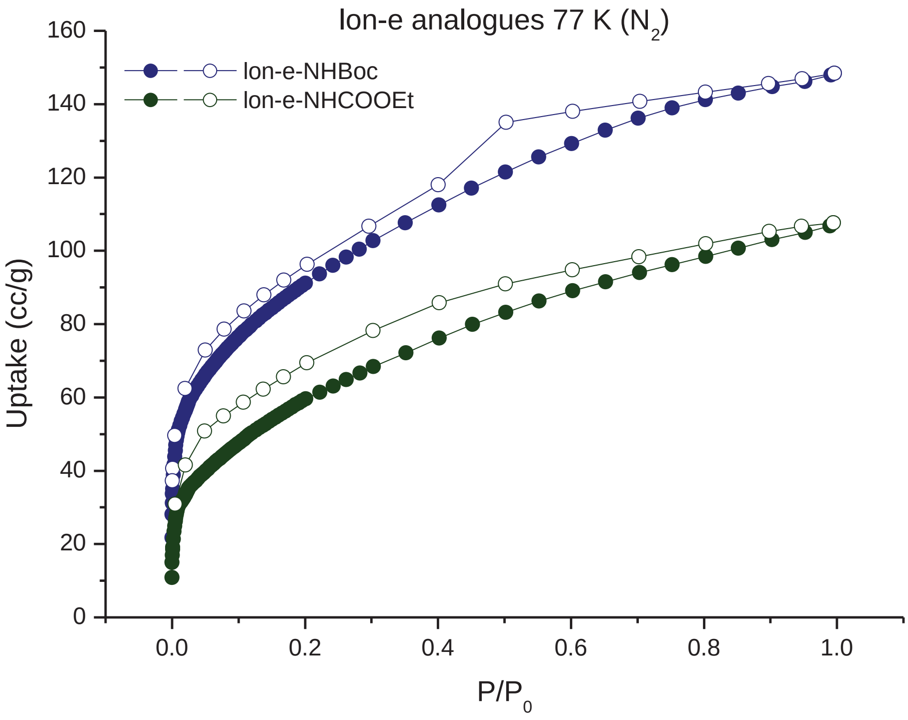

Figure 3.15 Gravimetric N_2 adsorption (filled) and desorption (open) isotherms measured at 77 K.

pores. This can result in decreased uptakes of N_2 despite the material being highly porous to other gases at 77 K, such as H_2.[177] Though there has not been an obvious decreases in the uptakes of lon-e-NHCOOEt and lon-e-NHBoc compared to their literature counterparts, it is not inconceivable that this phenomenon could impact on the rate of gas uptake into the more occluded pores of the lon-e-TPG species. This in turn, would affect the shape of the isotherm which, as mentioned previously, significantly impacts the BET calculations. The new materials lon-e-NHCOOEt and lon-e-NHBoc demonstrated moderate H_2 uptakes at 77 K of approximately 50 cm^3/g and 55 cm^3/g respectively (Figure 3.20), however H_2 uptake at 77 K was not reported for any of the literature materials so it is not possible to comment on their relative performances. The new materials also demonstrated low uptake of CO_2 and CH_4 at 273 K (Figure 3.21 and Figure 3.22), however neither exhibited any uptake of N_2 at 273 K. Unfortunately, the uptakes for lon-e-NHCOOEt and lon-e-NHBoc were between 30 – 50 % the uptake of CH_4 at 273 K of other lon-e analogues, and between 25 – 30 % the uptake of CO_2 at 273 K of other lon-e analogues.[162] The comparisons worsen at 298 K, where neither lon-e-NHCOOEt or lon-e-NHBoc demonstrate appreciable CH_4 uptakes whereas the literature analogues boast 8-11 cm^3/g uptakes at 1.05 atm, and CO_2 uptakes of lon-e-

NHCOOEt and lon-e-NHBoc (Figure 3.23) are between 12 – 25 % and 20 – 30 % the uptakes of other lon-e analogues respectively.[162]

Non-deterred by the lacklustre results of lon-e-NHCOOEt and lon-e-NHBoc, the thermolysis of the materials was carried out on the activation ports of the gas sorption instrument using the conditions determined through the trial experiments above (12 hours at 200/130 °C 12 hours for lon-e-NHCOOEt and lon-e-NHBoc respectively, confirmed by ^{1}H-NMR spectroscopy). Unfortunately, it was discovered that post thermolysis neither material exhibited appreciable uptake of any gas, indicating that the porosity of the materials is destroyed during the thermolysis process. In addition, PXRD of the thermolysed samples post gas sorption revealed that all crystallinity in the materials had been lost as well (Figure 3.13).

It is believed that the poor stabilities of lon-e-NHCOOEt and lon-e-NHBoc, as observed during trial activations prior to gas sorption analyses, combined with the extended times at high temperatures required to completely thermolyse the materials result in collapse of the frameworks, and subsequent loss of both crystallinity and porosity. It is apparent that this framework lacked the sufficient durability and resistance to heat to be appropriate for use with the TPGs used in this research and, unless TPGs with suitably low deprotecting temperatures are developed, it is the author's recommendation to avoid any future work incorporating TPGs into this framework.

3.3 Conclusion

In conclusion, it has been demonstrated that TPGs are compatible with mixed ligand synthesis and are not limited to IRMOF-type materials, as it was possible to obtain the target TPG containing structures. It has also been demonstrated that MOF stability is crucial to the use of TPGs as the lon-e framework, despite having promising TGA traces, was too unstable to thermolyse the TPGs and retain either porosity or crystallinity. It is the recommendation of the author that in future works any promising frameworks are tested for their compatibility by treating the parent frameworks with the conditions typically required for thermolysis and then their BET measured and compared with the literature value. If there has been only a small drop in porosity, then it can be considered that the material is sufficiently stable to be compatible with use of TPGs to introduce new functionality.

3.4 Experimental section

3.4.1 General procedures

All starting compounds and solvents were used as received from commercial sources without further purification unless otherwise noted. NMR spectra were recorded at room temperature on a Bruker-500 Avance instrument, with the use of the solvent proton as an internal standard. Elemental analyses were performed by the Campbell Microanalytical Laboratory at the University of Otago, New Zealand. Care was taken to limit the exposure of all MOFs to the atmosphere.

3.4.2 Ligand Synthesis

3.4.2a1,3-bdc-NHCOOEt.

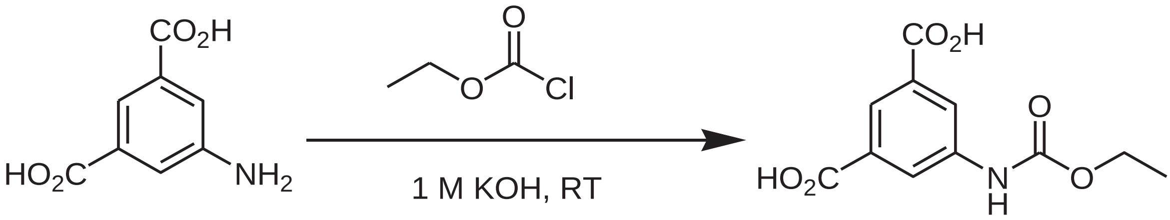

1,3-bdc-NH$_2$ (402.3 mg, 2.22 mmol) was dissolved in 1 M aqueous KOH solution (7.6 mL) at room temperature. Ethyl chloroformate (260 µL, 2.73 mmol) was added slowly over approximately 30 minutes. The reaction was then allowed to stir at room temperature for a further 3 hours. 0.2 M HCl was added slowly to the reaction mixture until copious white precipitate formed, which was collected by filtration. 0.2 M HCl solution was added to the filtrate to induce further precipitation, which was then collected as before. The precipitate was then washed with cold water and dried on the filter, followed by drying under high vacuum. This afforded 545 mg of product (2.15 mmol, 97%).

Figure 3.16 ^{1}H-NMR spectroscopic analysis of 1,3-bdc-NHCOOEt.

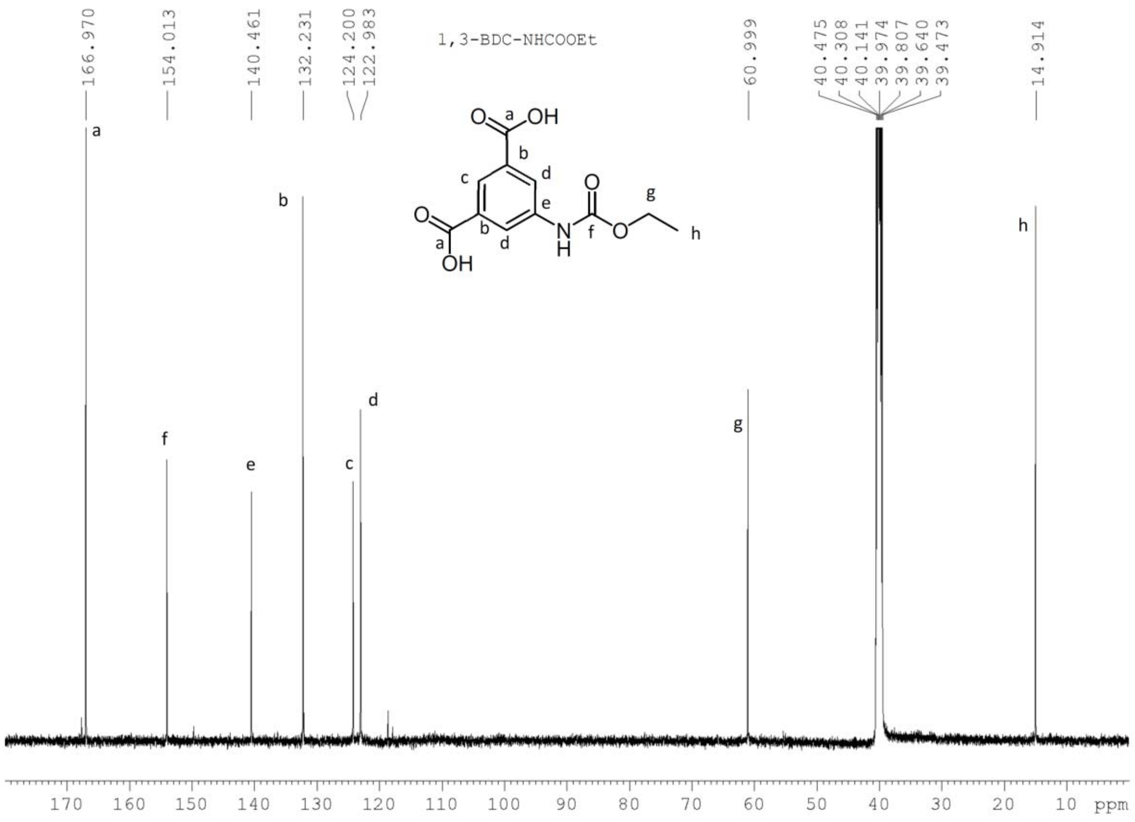

Figure 3.17 ^{13}C-NMR spectroscopic analysis of 1,3-bdc-NHCOOEt.

3.4.2b 1,3-bdc-NHBoc

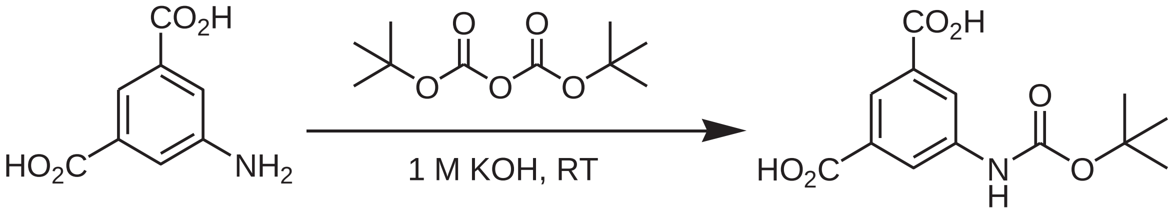

1,3-bdc-NH$_2$ (429.3 mg, 2.37 mmol) was dissolved in 1 M aqueous KOH solution (10 mL) with stirring. The reaction was then cooled in an ice bath and Boc$_2$O (526.2 mg, 2.41 mmol) in 1,4-dioxane (4.5 mL) was added slowly over the course of approximately 2 hours. The reaction was then stirred on ice for a further 3 hours, and then stirred at room temperature overnight. The solution was then acidified with 0.2 M HCl solution until copious amounts of white precipitate formed, which was collected by filtration. 0.2 M HCl solution was added to the filtrate to induce further precipitation, which was then collected as before. The solid material was then washed with cold water, dried on the filter and then dried under high vacuum, affording 653.3 mg (1.92 mmol, 98 %).

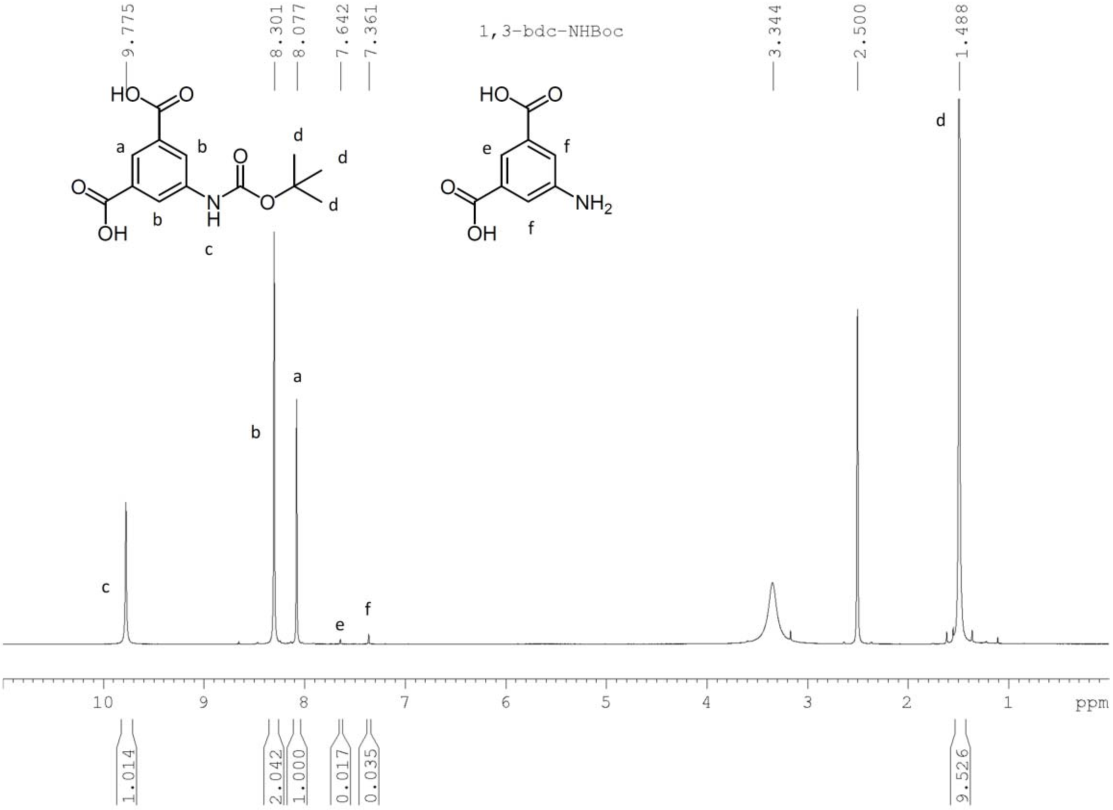

Figure 3.18 ^{1}H-NMR spectroscopic analysis of 1,3-bdc-NHBoc.

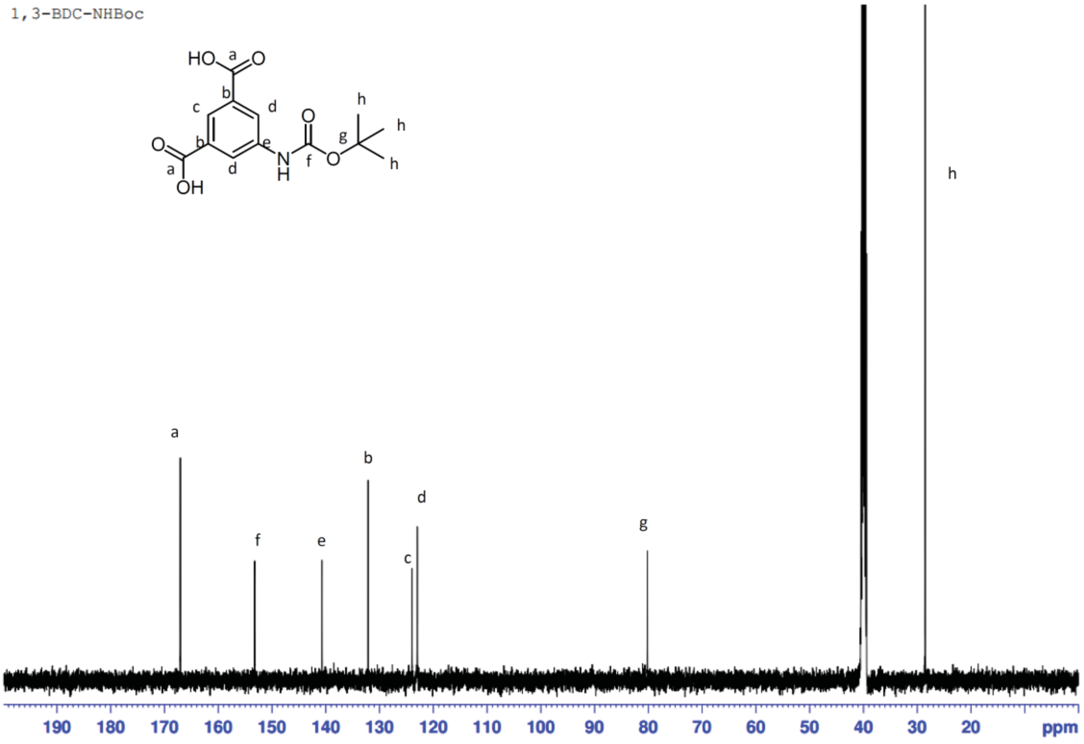

Figure 3.19 ^{13}C-NMR spectroscopic analysis of 1,3-bdc-NHBoc.

3.4.2c tp-PMBB-1

tp-PMBB-1 ([$Cr_3O(isonic)_6(H_2O)_2(NO_3)](NO_3)_6$) was prepared as per the literature.[162]

3.4.3 MOF synthesis and characterization

3.4.3a lon-e-NHCOOEt

Solutions of reagents were prepared as follows: tp-PMBB-1 (159.4 mg, 0.114 mmol)) in dry DMF (10 mL); $Zn(NO_3)_2.4H_2O$ (742.6 mg, 2.840 mmol) in dry DMF (10 mL). tp-PMBB-1 solution (1 mL), $Zn(NO_3)_2$ solution (0.5 mL), DMF (3.25 mL), and MeOH (1.5 mL) was added to 1,3-bdc-NHCOOEt (54.0 mg, 0.213 mmol) in a 20 mL scintillation vial and sonicated for 5 mins before being heated in a 65 °C isothermal oven for 18 hours. The green hexagonal crystals were collected and washed with DMF (3 x 10 mL) and acetonitrile (2 x 5mL) to remove any powdered product. The samples were left in acetonitrile prior to activation.

Yield: 20.2 mg. Anal. calcd. for [$C_{115}H_{102}Cr_3N_{12}O_{55}Zn_6$].2(DMF): C, 45.04; H, 3.62; N, 6.08; Found: C, 51.73; H, 3.58; N 5.94. To scale up the synthesis, a parallel synthetic method was adopted (multiple vials using the scale described above) as scaling up of the reactions resulted in markedly lower yields.

3.4.3b lon-e-NHBoc

Solutions of reagents were prepared as follows: tp-PMBB-1 (159.4 mg, 0.114 mmol)) in dry DMF (10 mL); $Zn(NO_3)_2.4H_2O$ (742.6 mg, 2.840 mmol) in dry DMF (10 mL). tp-PMBB-1 solution (1 mL), $Zn(NO_3)_2$ solution (0.5 mL), DMF (3.25 mL), and MeOH (1.5 mL) was added to 1,3-bdc-NHBoc (59.9 mg, 0.213 mmol) in a 20 mL scintillation vial and sonicated for 5 mins before being heated in a 65 °C isothermal oven for 18 hours. The green hexagonal crystals were collected and washed with DMF (3x 10 mL) and acetonitrile (2x 5mL) to remove any powdered product. The samples were left in acetonitrile prior to activation.

Yield: 27.4 mg. Anal. calcd. for $[C_{103}H_{78}Cr_3N_{12}O_{55}Zn_6]$.2(DMF): C, 42.81; H, 3.03; N, 6.41; Found: C, 47.26; H, 3.14; N 5.83. To scale up the synthesis, a parallel synthetic method was adopted (multiple vials using the scale described above) as scaling up of the reactions resulted in markedly lower yields

3.4.4 ^{1}H-NMR spectroscopic analysis of digested MOF samples

For ^{1}H-NMR spectroscopy, the mother liquor of the as-synthesized MOF crystals was replaced with fresh dry acetonitrile multiple times, followed by repeated washing and subsequent soaking in CH_2Cl_2 for several hours. The excess CH_2Cl_2 was then decanted and the samples placed under vacuum overnight to remove residual solvent from the pores. The crystals were then digested using the following protocol: 23 µL of a 35% DCl solution in D_2O was mixed with 1 mL of DMSO-d_6 to give a DCl/DMSO-d_6 stock solution. Around 5 mg of MOF was digested in 200 µL of this stock solution together with 400 µL of DMSO-d_6. Spectra were acquired immediately following dissolution.

3.4.5 Thermogravimetric Analysis (TGA)

Thermogravimetric analyses were performed on a TA Instruments Q50 instrument. Freshly prepared MOF samples were prepared as for gas sorption (see section 3.4.8). Samples were then transferred to an aluminium sample pan and then measurements were commenced under an N_2 flow with a heating rate of 5 °C /min.

3.4.6 Single crystal X-ray diffraction

MOF crystals were mounted together with some dry DEF in a polymer sleeve on a Rigaku Spider diffractometer equipped with a MicroMax MM007 rotating anode generator

(Cu_{α} radiation, 1.54180 Å), high-flux Osmic multilayer mirror optics, and a curved image-plate detector. Data were collected at 293 K and were integrated, scaled, and averaged with FS Process.[158] XPREP[159] was used to determine the space group and the structures were solved using SHELXS[159] and refined with SHELXL.[159]

All atoms were found in the electron density difference map, except for the side chains, which were subsequently modelled using Discovery Studio.[160] The atom positions were added to the model in representative positions and held fixed during refinement. All non-hydrogen, non-side chain atoms were refined anisotropically. Cif files for MOFs uploaded to http://tinyurl.com/sblackwoodMOFs.

3.4.7 Powder X-ray diffraction patterns

All powder X-ray diffraction experiments were carried out on a Rigaku Spider X-ray diffractometer with Cu K_{α} radiation (Rigaku MM007 microfocus rotating-anode generator), monochromated and focused with high-flux Osmic multilayer mirror optics, and a curved image plate detector. The data were obtained from freshly prepared MOF samples that had been ground into slurry in a small amount of DEF and kept damp with DEF throughout the measurement. The two-dimensional images of the Debye rings were integrated with 2DP[161] (Version 1.0.3.4) to give 2θ vs I diffractograms. The predicted powder patterns of MOF-5-NHBoc and MOF-5-NHCOOEt was generated from their single-crystal structures using Mercury v3.0.

3.4.8 Gas adsorption measurements

Low pressure adsorption isotherms were measured by a volumetric method using a Quantachrome Autosorb-iQ instrument. Freshly prepared MOF samples were washed with acetone multiple times prior to soaking in fresh acetone for several hours. The samples were then transferred to cellulose thimbles for supercritical CO_2 activation, ensuring a covering of acetone over the samples was maintained. The samples were then placed into a Tousimis Samdri-PVT-3D critical point dryer, the solvent exchanged with supercritical CO_2 and allowed to soak in supercritical CO_2 for 1 hour. This process was repeated 6 times before letting the samples soak for 16 hours. The supercritical CO_2 was then slowly bled off until the samples were solvent free. The dried samples were then transferred to a pre-dried and weighed analysis tube under a constant positive flow of argon atmosphere. After weighing, the sample tubes were then placed directly onto the analysis ports without further activation. Accurate sample masses were calculated using degassed samples. All adsorption measurements used ultra-high purity gases.

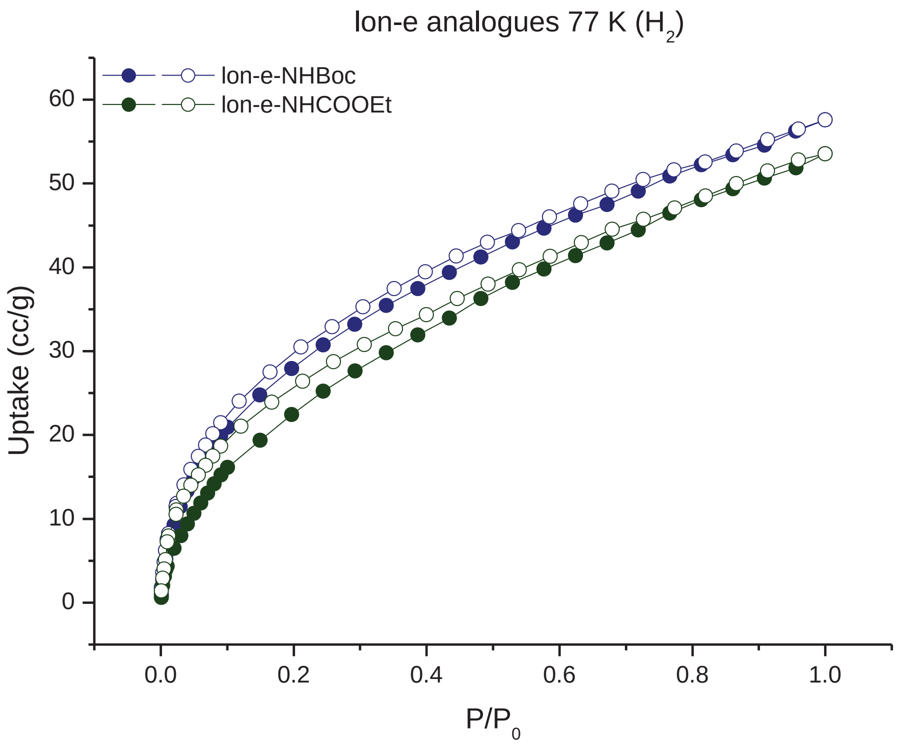

Figure 3.20 Gravimetric H_2 adsorption (filled) and desorption (open) isotherms measured at 77 K.

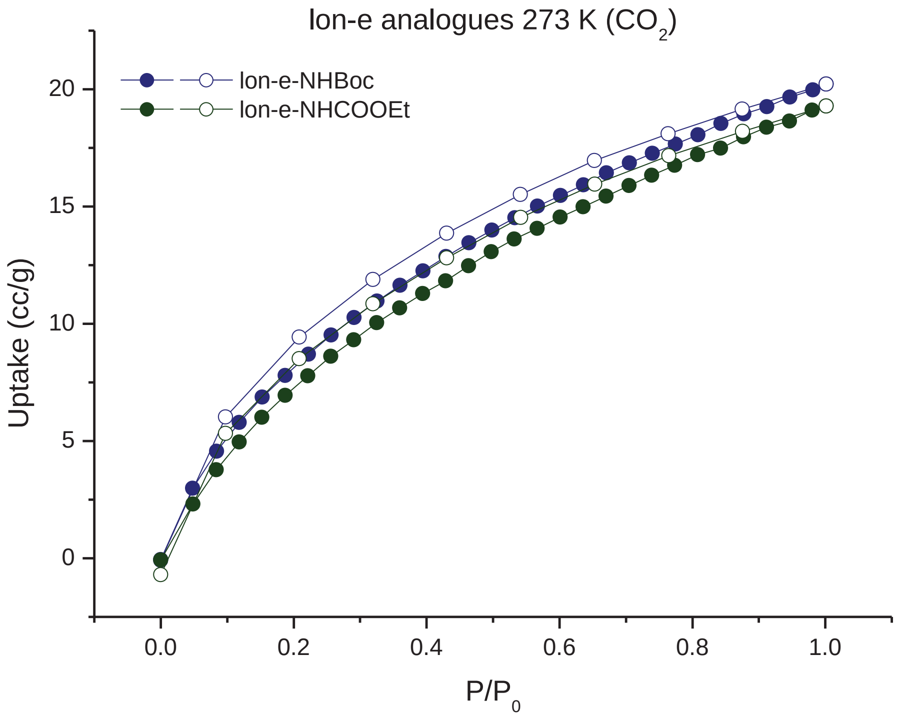

Figure 3.21 Gravimetric CO_2 adsorption (filled) and desorption (open) isotherms measured at 273 K.

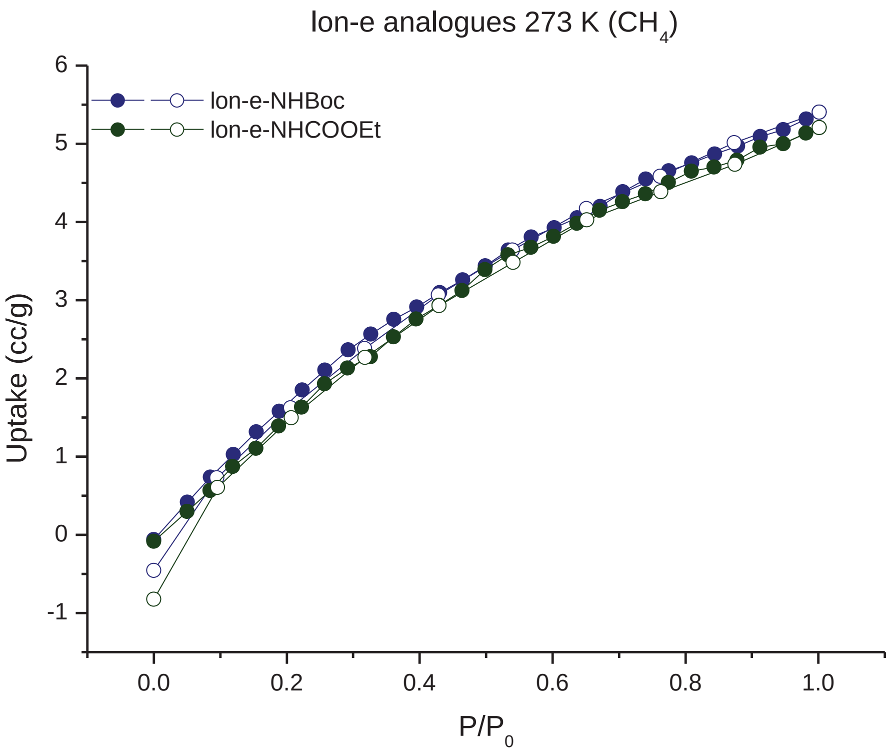

Figure 3.22 Gravimetric CH_4 adsorption (filled) and desorption (open) isotherms measured at 273 K.

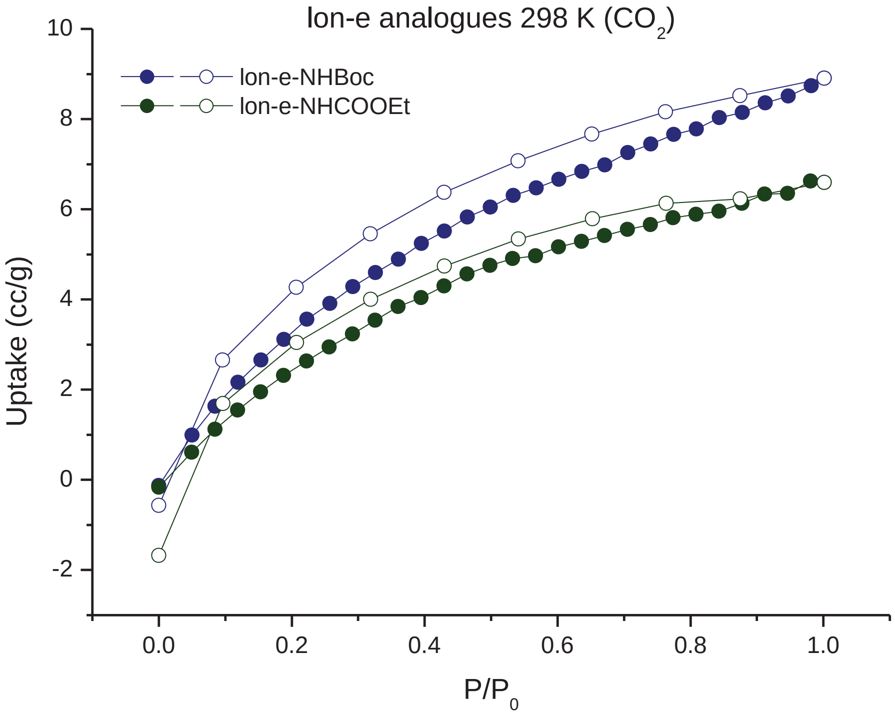

Figure 3.23 Gravimetric CO_2 adsorption (filled) and desorption (open) isotherms measured at 298.

Chapter 4 - Thermolabile Protecting Groups in Mixed bpy/bpdc Frameworks

4.1 Introduction

Having demonstrated the compatibility of carboxylate ligands with TPGs, it was decided to turn to ligands with other types of ester thermolysis binding groups to expand this group's ligand library, and, by extension, the number of MOFs that can be targeted for TPG incorporation. The N-donor type ligand 4,4'-bipyridine (bpy, Figure 4.1) was chosen due to its ability to be incorporated into a large number of MOFs. It was decided to synthesise amino- and carboxyl- functionalised bpy materials. The amino functionalised bpy is a continuation of the previous amine based TPG chemistry conducted by our group. The carboxyl functionality was chosen to improve gas uptakes/selectivities, act as a catalyst, and as a tag to attach further functionalities to. Carboxylates are strong metal binding groups, and as such present a challenge to direct incorporation into MOFs. This makes them desirable targets for the TPG methodology. It was decided to protect the carboxyl group as the *tert*-butyl ester, as it is known that this ester readily undergoes thermolytic cleavage to give the free carboxyl group and isobutylene.[178]

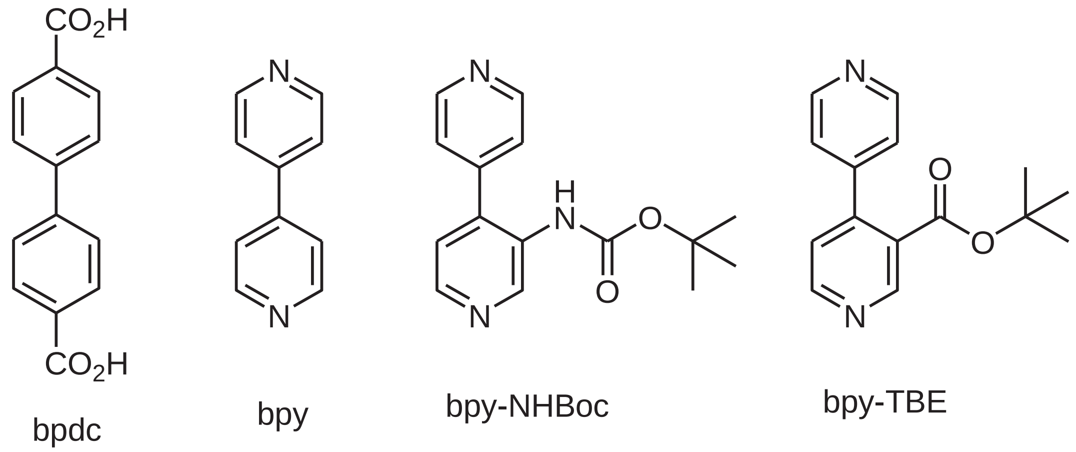

Figure 4.1 Ligands involved in the synthesis of BMOF-1, MUF20-Aβ, and MUF20-Aγ.

This chapter will report the installation of two bpy-based TPG containing ligands into the known MOF BMOF-1-bpdc[179] ($[Zn_2(bpdc)_2(bpy)]$). The BMOF-1-bpdc framework is comprised of two Zn^{2+} ions binding with a carboxylate from each of four bpdc ligands to form a paddlewheel SBU (Figure 4.2). These paddlewheels are all joined by additional paddlewheels at the other carboxylates on the bpdc ligands to form 2-D sheets. The vacant metal sites on the zinc(II) ions allow for pillaring of these sheets by bpy-based ligands. This type of framework is known as a pillar-layer framework, and many examples are known in

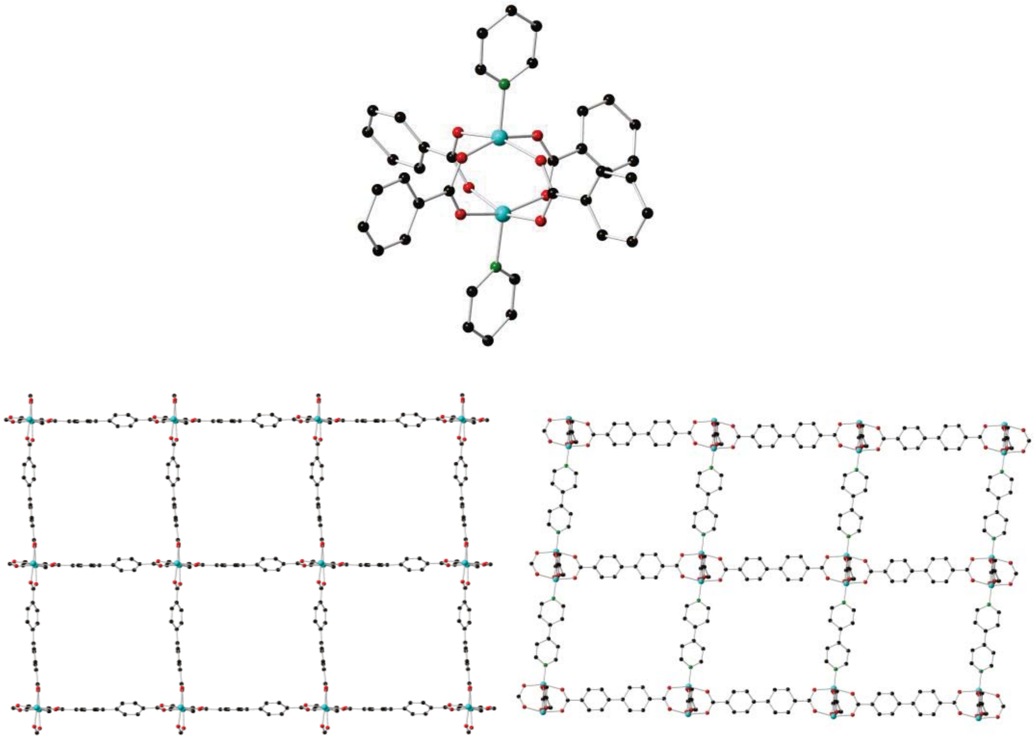

Figure 4.2 Structures of BMOF-1-bpdc determined by SXRD. Top: Zn paddlewheel SBU. Bottom left: top down view of Zn-bpdc sheets. Bottom right; side view of Zn-bpdc sheets pillared by bpy. Second framework omitted for clarity. Atom colours: C = black, N = green, O = red, Zn = teal (hydrogens omitted for clarity).

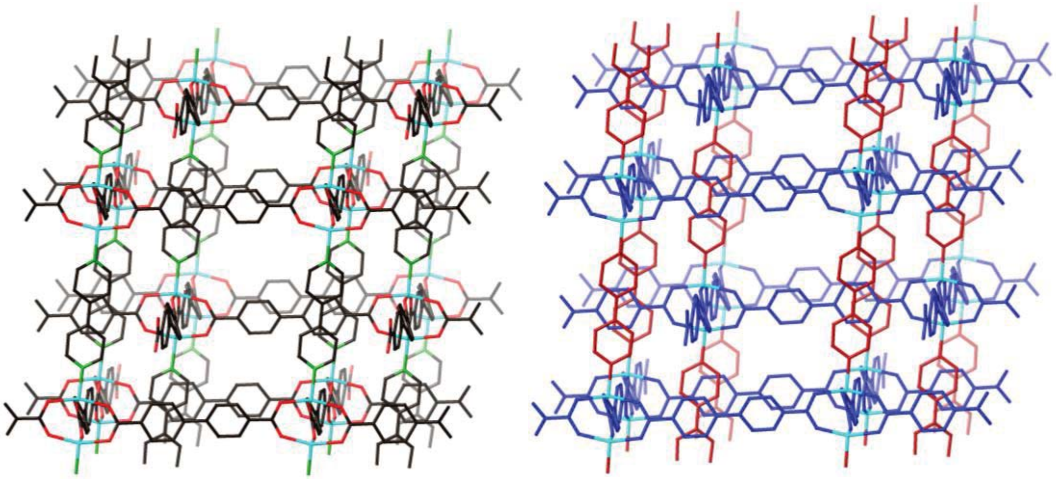

Figure 4.3 Single crystal x-ray structure of BMOF-1-bpdc illustrating the pillar-layer structure (left). In the rendering on the right the ligands have been coloured and the secondary framework rendered lighter to better visualise the structure. Atom colours: C = black, N = green, O = red, Zn = teal (hydrogens omitted for clarity). Ligand colours: bpdc – blue, bpy -red.

the literature.[180-185] As seen in Figure 4.3, BMOF-1-bpdc is an interpenetrated structure, i.e. a second framework grows in the pores of the first framework. This presented another question for this research; would the incorporation of TPG containing ligands supress the interpenetration seen in the parent framework? It is highly plausible that this could occur

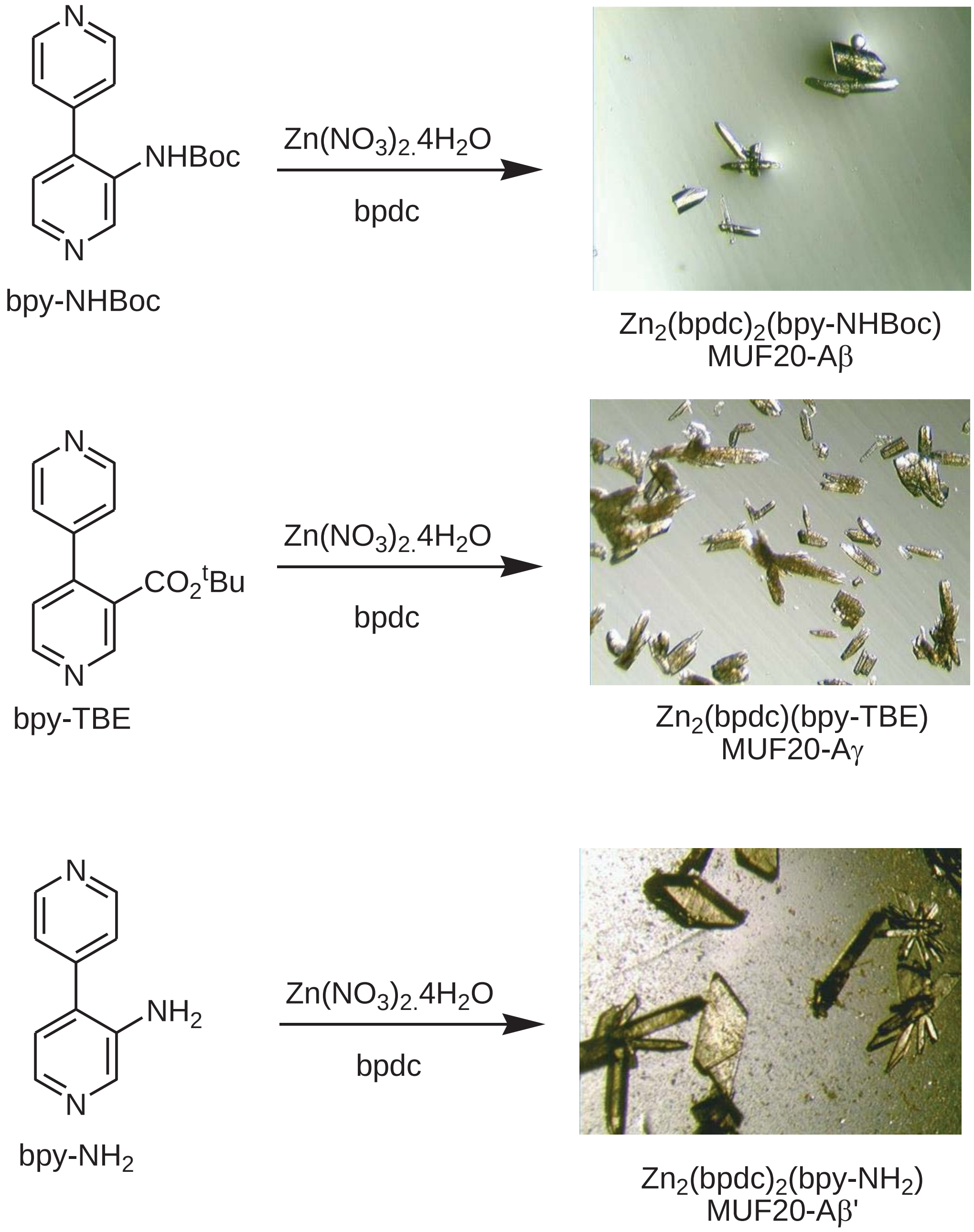

Figure 4.4 Generalised synthetic route to MUF20-Aβ, MUF20-Aγ, and MUF20-Aβ’.

since the two frameworks in BMOF-1-bpdc are closely packed and the TPG-containing side chains are bulky. This combination could potentially make the non-interpenetrated framework either the thermodynamically preferred phase, or the kinetic product as the formation of the interpenetrated phase may be retarded. There are pros (such as improved stability) and cons (such as a decrease in gravimetric pore volume) to interpenetration so the ability to control it is highly desirable.[186-190]

The two ligands used in this research are 2-*tert*-butoxycarbonylamino-4,4’-bipyridine (bpy-NHBoc), and 2-*tert*-butoxycarbonyl-4,4’-bipyridine (bpy-TBE) (Figure 4.1). These two ligands were combined with 4,4’-biphenyldicarboxylate (bpdc) and zinc nitrate to form materials analogous to BMOF-1-bpdc, referred to henceforth as MUF20-Aβ and MUF20-Aγ for bpy-NHBoc and bpy-TBE respectively (Figure 4.4). MUF in this instance stands for Massey University Framework, and has been used by this group previously for naming new materials.[189,191,192] Whilst not a new framework topology, when it was first discovered by our group the group was unaware of the existence of BMOF-1-bpdc and thus named it MUF20-Aα, and this nomenclature has continued since our discovery of BMOF-1-bpdc as a convenient shorthand, and will continue in this thesis. The direct synthesis of the unprotected analogues of MUF20-Aβ and MUF20-Aγ were also attempted using bpy-NH_2 and bpy-CO_2H respectively. However, only bpy-NH_2 was successfully incorporated into a BMOF-1-bpdc analogue (MUF20-Aβ’, Figure 4.4).

4.2 Results and discussion

Unlike in chapters 2 and 3, synthesis of the ligands for this research was non-facile. Figure 4.5 outlines the various reaction pathways trialled to synthesize bpy-NHBoc. The initial approach (Route A) was to protect 3-aminopyridine and then to use this in a Suzuki-coupling to generate the product. This route was chosen due to the well-known chemistry involved, our group’s previous success in using this method to generate functionalized ligands, and known literature syntheses of 4,4’-bipyridines using Suzuki coupling reactions.[193,194] The reaction pathway progressed as expected until after the Suzuki coupling, where a 10 % bpy impurity was found after the synthesis, which can be attributed to the homocoupling of 4-pyridinylboronic acid. Altering the reaction conditions was also attempted to see if it was possible to form bpy-NHBoc without the bpy side-product forming.

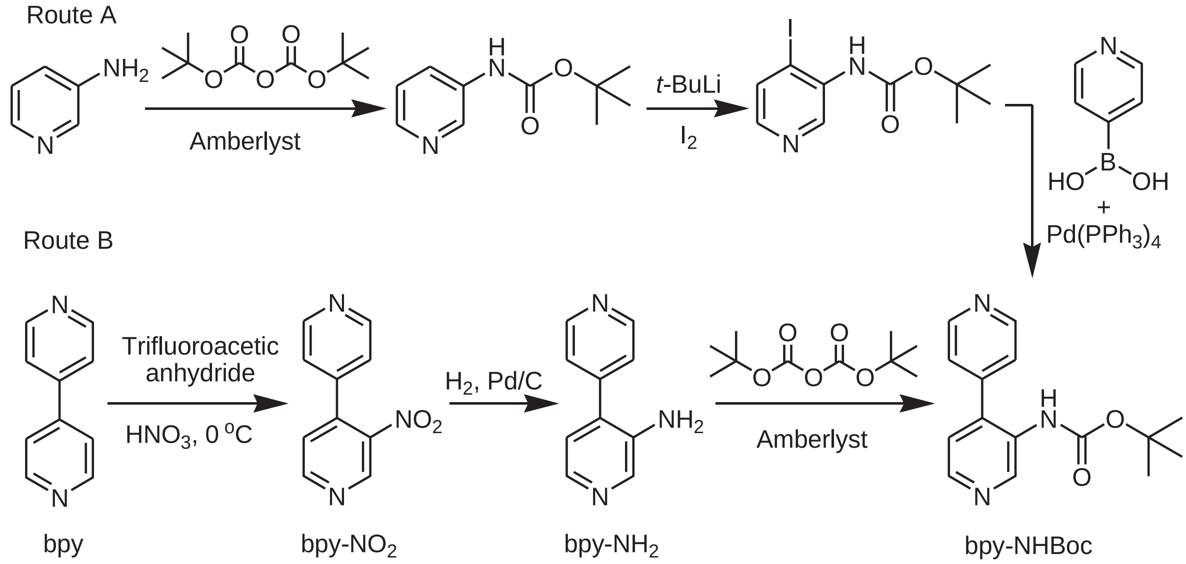

Figure 4.5 Synthetic approaches to the synthesis of bpy-NHBoc.

However, even using very low ratios of 4-pyridinylboronic acid it was not possible to form bpy-NHBoc without bpy also forming, even with copious amounts of starting material remaining. When this failed, much effort was then expended trying to determine the conditions needed to separate the bpy. It could not be removed by numerous flash chromatographic efforts nor recrystallization. It was finally discovered the HPLC could separate the bpy and bpy-NHBoc, however only 35 mg at a time and using high volumes of high quality solvent. It was decided that this was an impractical purification method.

Route B (Figure 4.5) was then attempted. The nitration of bpy was first attempted using the standard conditions for nitrating aromatic compounds (refluxing in conc. HNO_3/H_2O_4). Unfortunately, even after a reaction time of two weeks the bpy had failed to react. A subsequent literature search revealed the conditions used by Zhang *et al.* (first step of route B, Figure 4.5).[195] With this method, trifluoroacetic anhydride (TFAA) is cooled to 0 °C under inert atmosphere. Bpy is then added and the reaction left to stir at 0 °C for 1 hr under an inert atmosphere. Fuming HNO_3 is then added slowly, and the reaction left to stir on ice for 2 days before working up. This method is very low yielding (< 20 %) due to the incomplete nitration of the starting material, significant production of the doubly-nitrated 3,3'-dinitro-bpy, poor separation of the products by silica gel chromatography, and the poor extraction of the products from the reaction mixture. However, due to the relative cheapness of the reagents, it was possible to conduct sufficient parallel syntheses to obtain the amounts of 3-nitro-4,4'-bipyridine (bpy-NO_2) necessary to complete these studies. Parallel syntheses were performed as increasing the scale of the reaction dramatically reduced the yield. To converted the bpy-NO_2 to 3-amino-4,4'-bipyridine (bpy-NH_2) the material was dissolved in DCM:MeOH and placed in a hydrogenator with 10% Pd on charcoal (Pd/C) catalyst. The reaction was then pressurized to 50 psi with H_2 and agitated for 18 hours. The reaction mixture was then passed through a Celite plug and the solvent removed *in vacuo*, affording quantitative a yield of bpy-NH_2. The method used to hydrogenate the bpy-NO_2 to bpy-NH_2 differed from that used by Zhang *et al*., who refluxed the material in ethanol with hydrazine hydrate and Pd/C for 2 hours.

To protect the amino group, bpy-NH_2 was dissolved in EtOH, Amberlyst resin 15 added to the reaction mixture, the vessel placed under Ar atmosphere, and stirred at room temperature. Boc_2O in THF was then added dropwise over three additions, each four hours apart, and the reaction then left to stir at room temperature overnight. The reaction mixture was then filtered to remove the resin, and the material purified by silica gel flash chromatography, affording bpy-NHBoc in >30 % yields. Amberlyst resin 15 was used as it gave better yields than other methods trialled, and has also been used in similar reactions.[196]

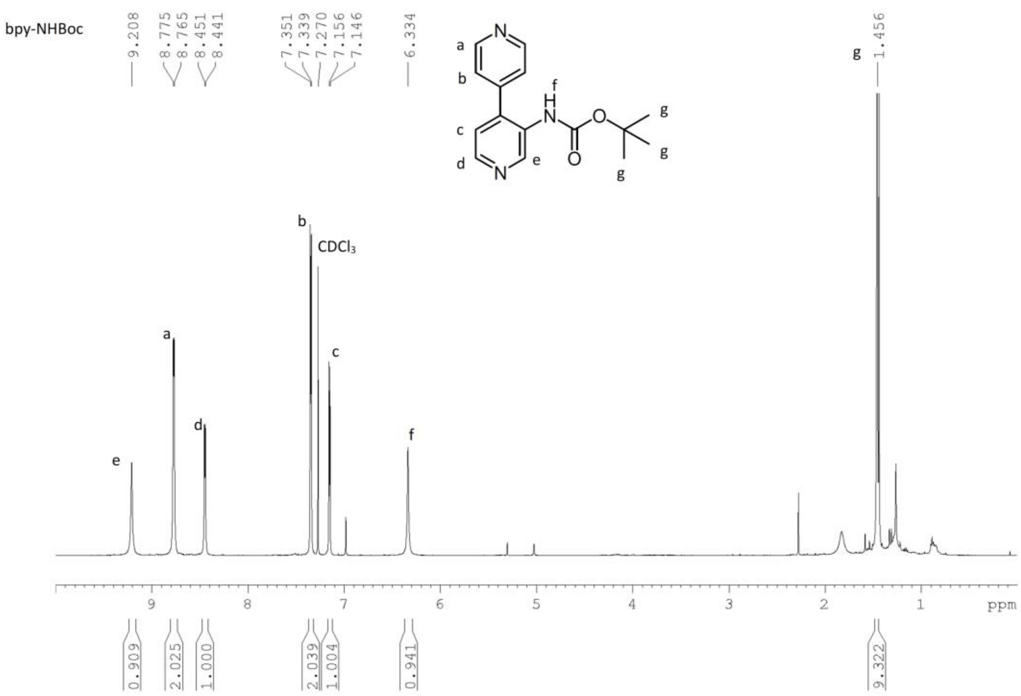

Figure 4.6 ^{1}H-NMR spectroscopic analysis of bpy-NHBoc in $CDCl_3$

Pyridyl rings are electron deficient relative to phenyl rings. This presents an obstacle to the acylation of bpy through electrophilic aromatic substitution. In light of this, it was decided to purchase a more advanced precursor to bpy-TBE in order to expedite the process of incorporating the ligands into MOFs. 3-Ethoxycarbonyl-4,4'-bipyridine (bpy-COOEt, Figure 4.7) was purchased from an overseas supplier. Reacting the bpy-COOEt in MeOH at 45 °C with KOH for 1 hour gave 3-carboxy-bpy (bpy-CO_2H) in quantitative yields. The bpy-CO_2H was then dissolved in THF with a catalytic amount of dimethylaminopyridine (DMAP) and brought to reflux under inert atmosphere. Boc_2O in THF was then added dropwise in two additions four hours apart, and after a further four hours the reaction was worked up to give bpy-TBE in >85% yield.

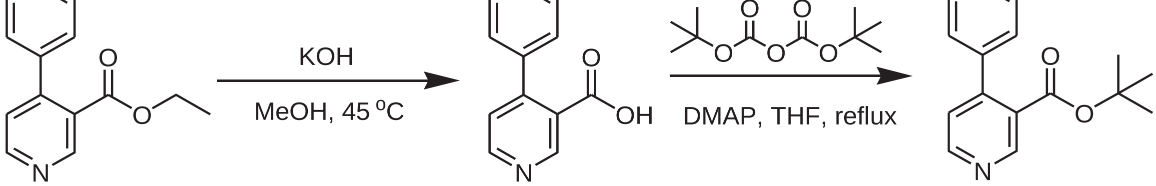

Figure 4.7 Synthetic scheme for conversion of bpy-COOEt to bpy-TBE.

Figure 4.8 ^{1}H-NMR spectroscopic analysis of bpy-TBE in $CDCl_3$.

Bpy-NHBoc and bpy-TBE were individually combined with bpdc and zinc(II) nitrate to generate crystalline materials. ^{1}H-NMR spectroscopic analysis of these materials digested with DMSO-d_6/DCl revealed that both ligands had been successfully incorporated with no observable deprotection (Figure 4.9). These ^{1}H NMR spectra also show that the ligands are present in a 2:1 bpy:bpdc ratio, corresponding to the expected formula of [Zn_2(bpdc)(bpy)]. It was found that the framework synthesis was very susceptible to changes in the functionalisation of the bpy ligand. This resulted in significant deviations from the literature synthesis of BMOF1-bpdc as either an undesired phase would form, or the ratio of bpy to bpdc would be lower than the 2:1 reported. Altered ratios are not uncommon with N-donor type ligands, whose lack of charge means that they can be removed/omitted without disrupting the metal cluster (compare MOF-14[197] with FJI-1[198]/DUT-23[1]), and is actually a trait that has been exploited.[192] Experimental PXRD patterns of the produced materials (Figure 4.10) match closely to the PXRD pattern calculated from the literature cif file for BMOF-1-bpdc, strongly indicating that the materials synthesised were MUF20/BMOF-1-bpdc analogues. However, as explained below, due to the flexible nature of these frameworks allowing for the peak positions to shift in PXRD patterns for these materials, the matching nature of the PXRD patterns is of less significance than in rigid frameworks, such as MOF-5, where the peak positions do not shift.

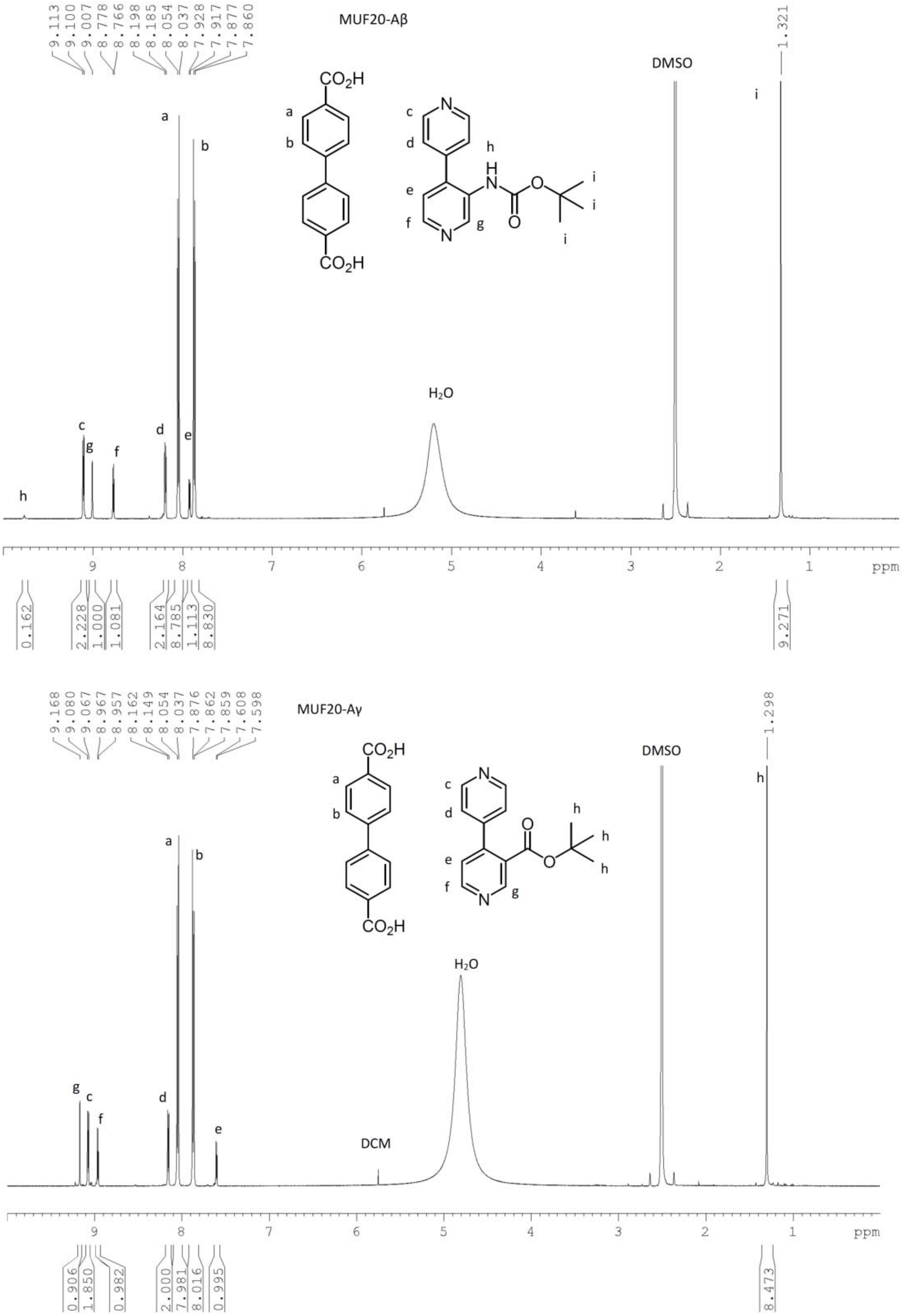

Figure 4.9 ^{1}H NMR spectra of digested MUF20-Aβ (top) and MUF20-Aγ (bottom) in DMSO-d_6/DCl.

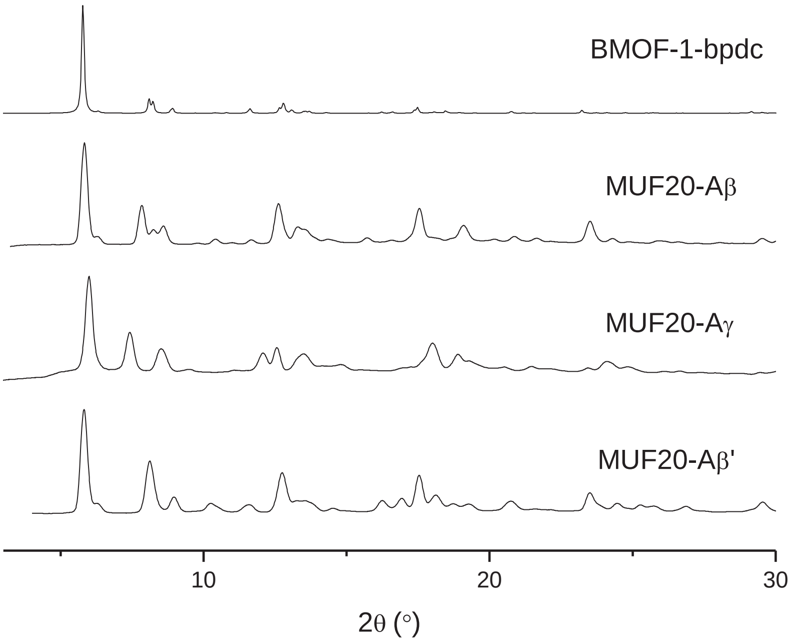

Figure 4.10 PXRD patterns for the parent material BMOF-1-bpdc (calculated from literature .cif file) and the novel materials MUF20-Aβ, MUF20-Aγ, and MUF20-Aβ' (obtained experimentally).

In this work, it was found that whilst both syntheses used 1.25 mL of MeOH:DMF (4:1) and 15 hours in an 85 °C oven, MUF20-Aβ required a 1:1.7:0.92 ratio of bpdc:bpy-NHBoc:Zn, whereas MUF20-Aγ required a 1:1.67:0.93 ratio of bpdc:bpy-TBE:Zn. The synthesis of MUF20-Aγ afforded reasonable quantities of phase pure material (~8 mg bpy-TBE gave ~ 13 mg MUF20-Aγ). However, the crystals were of poor quality for SXRD, and a second synthesis with a 5-fold dilution of the reaction mixture was required to obtain SXRD quality crystals. It should be noted that during this synthesis approximately 80 % of the solvent volume was lost (attributed to the MeOH gradually evaporating from the reaction mixture), however it was found that this solvent loss improved the crystal quality compared to the samples where no solvent loss occurred. PXRD data for MUF20-Aβ and MUF20-Aγ revealed that the peaks in the PXRD patterns of these materials would shift depending on how long the sample had been removed from solvent. Due to the wide angles available to the Zn-N bond, the angle between the bpy pillars and Zn-bpdc sheets can change substantially. This motion can reduce the distance between the planes of the Zn-bpdc sheets. Such framework flexibility is a feature of BMOF-1-bpdc, as noted by Cohen's group.[179] It is believed that as the solvent evaporates, the forces holding the sheets apart decrease, and so the inter-sheet distances decrease, resulting in the change in the peak positions observed in the PXRD patterns. It is also possible that the shift in the PXRD peaks is due to the movement of the two frameworks with respect to one another, rather than an intra-framework shift. In this instance this is unlikely as upon desolvation it is expected that the

Table 4.1 Crystallography data of MUF20-Aβ, MUF20-Aγ, and MUF20-Aβ'

MOF	**MUF20-Aβ**	**MUF20-Ay**	**MUF20-Aβ'**
Formula	$C_{98}H_{93}N_{10}O_{24}Zn_4$	$C_{43}H_{32}N_2O_{10}Zn_2$	$C_{38}H_{24}N_3O_8Zn_2$
Formula weight	2057.31	867.44	781.34
Crystal size (mm)	0.61 x 0.25 x 0.15	0.47 × 0.30 × 0.15	0.41 × 0.17 × 0.19
Temperature (K)	153	153	163
Wavelength (Å)	1.54187	1.54187	1.54187
Crystal system	Triclinic	Monoclinic	Triclinic
Space group	*P*-1	$P2_1/c$	*P*-1
Unit cell lengths (Å)	a = 15.197(3) b = 15.230(3) c = 28.095(5)	a = 14.1030(3) b = 15.2176(4) c = 29.468(2)	a = 13.993(5) b = 15.164(5) c = 15.182(5)
Unit cell angles (°)	α = 93.602(7) β = 94.013(7) γ = 95.751(7)	α = 90 β = 92.409(7) γ = 90	α = 78.235(5) β = 85.479(5) γ = 82.408(5)
Unit cell volume ($Å^3$)	6438.0(19)	3185.0(7)	3121.7(18)
Z	2	4	2
D_{calc} (g cm^{-3})	1.061	0.912	0.831
μ (mm^{-1})	1.34	1.26	1.21
F(000)	2126	1776	794.0
Reflns coll./unique, R_{int}	69099 / 1749, 0.0687	52955 / 12177, 0.0608	32293 / 4256, 0.0930
Data range	8.0 Å > d > 0.95 Å	8.0 Å > d > 0.81 Å	8.0 Å > d > 1.15 Å
Index ranges	$-15 \leq h \leq 15$, $-15 \leq k \leq 16$, $-29 \leq l \leq 26$	$-17 \leq h \leq 12$, $-17 \leq k \leq 18$, $-32 \leq l \leq 36$	$-10 \leq h \leq 12$, $-13 \leq k \leq 13$, $-13 \leq l \leq 13$
Completeness	98.7 %	98.0 %	99.5 %
T_{min}, T_{max}	0.466, 1.00	0.443, 1.00	0.248, 1.00
R indices for data with $I>2\sigma(I)$	$R_1 = 0.2613$; $wR_2 = 0.6293$	$R_1 = 0.1441$; $wR_2 = 0.4833$	$R_1 = 0.2702$; $wR_2 = 0.6203$
R indices for all data	$R_1 = 0.3208$; $wR_2 = 0.6293$	$R_1 = 0.1688$; $wR_2 = 0.4833$	$R_1 = 0.2949$; $wR_2 = 0.6203$
Largest difference peak and hole (e $Å^{-3}$)	2.97 / −1.45	1.55 / −1.11	1.55 / −1.51

frameworks would pack closely to maximise inter-framework interactions. However, with the MUF20 materials the frameworks are already closely packed when solvated (*vide infra*) and thus it is unlikely that there would be any significant shifting of the inter-framework distances.

With the functionalised MUF20-Aβ and MUF20-Aγ, SXRD data revealed similar 2-D Zn-bpdc sheets pillared by bpy-type ligands topology as that found in the parent BMOF-1-bpdc. This includes the second interpenetrating framework that was envisaged could have

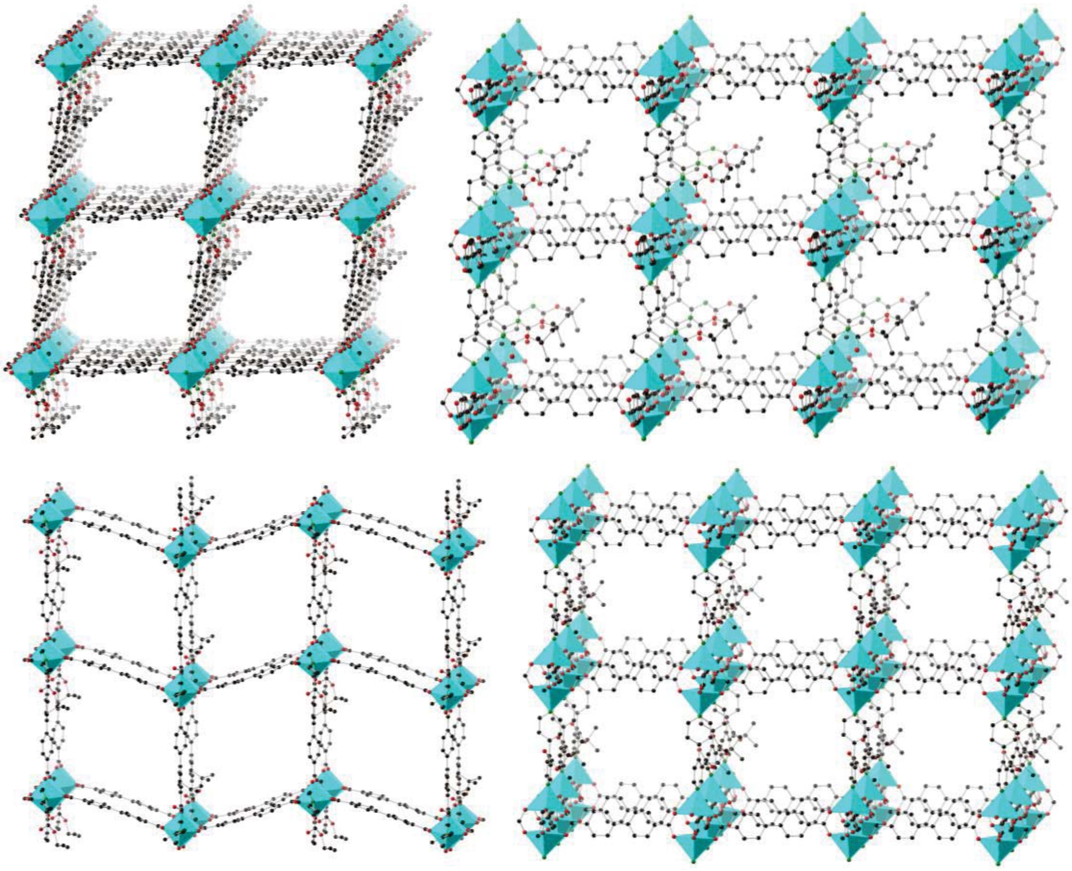

Figure 4.11 Structures determined by SXRD of MUF20-Aβ (top) and MUF20-Aγ (bottom) depicting top-down views of the Zn-bpdc frameworks (left) and side views of the pillared layers (right). Second framework omitted for clarity. Atom colours: C = black, N = green, O = red, Zn = teal (hydrogen atoms omitted for clarity).

been inhibited by the presence of the bulky protecting groups. It was pleasing to be able to observe all of the non-hydrogen atoms in both MUF20-Aβ and MUF-20Aγ, though in MUF20-Aβ SADI (same distance) constraints were required to fix the side chains in chemically sensible positions. Surprisingly, though the data for MUF20-Aβ appears to be of good quality (with diffraction observed out to 0.95 Å, the visibility of all side chain atoms, and a R_{int} value of 6.87 %) the refinement statistics indicate that the model still has some

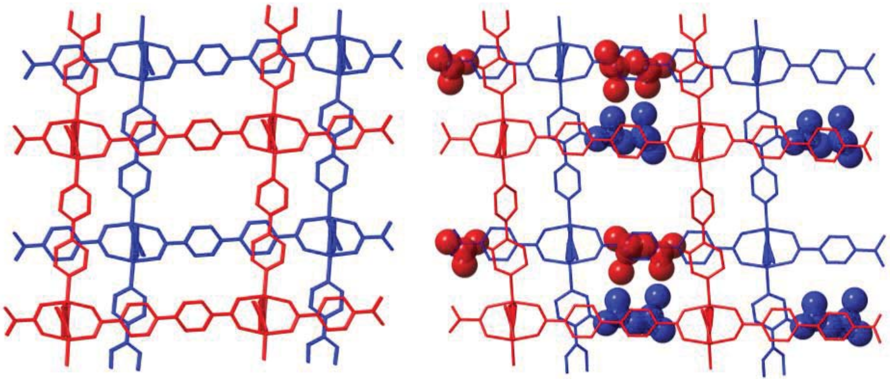

Figure 4.12 Structures determined by SXRD of BMOF-1-bpdc (left) and MUF20-Aβ (right) demonstrating the overlap of the interpenetrating framework Zn-bpdc sheets with respect to the bpy pillars of the first framework, and *vice versa*. For clarity; individual frameworks are coloured red and blue, TPGs rendered as spheres, and hydrogen atoms omitted.

deficiencies. With such data, one could expect R_1 to drop below 20%, however it was not possible to drop R_1 to <26%. Even through using the SQUEEZE command, where the electron density of void space is removed from the calculations, R_1 only decreased to ~19%, which is a higher value than expected. Furthermore, it was necessary to fix the positions of several atoms in order to allow the refinement to converge. These issues with the model are quite at odds with the data, and further efforts are being expended to develop a better fitting model that resolves these issues. Despite these shortcomings, the overall structural model is reliable. The structure is in accord with expectations based on our other observations and literature results.

In both MUF20-Aβ and MUF20-Aγ the Zn-bpdc sheets of the first framework overlap with the functionalised pyridyl ring of the bpy in the interpenetrating framework (Figure 4.12). This closely matches the parent BMOF-1-bpdc framework where this intersection occurs at a single pyridyl group of the bpy ligand and not in the middle of the ligand. It is believed that the intersection occurs at the functionalised ring and not the unfunctionalised ring as this allows for greater van der Waals interactions between the frameworks, as the TPGs are oriented to maximise their interaction with the interpenetrating framework.

Upon closer examination of each framework, more differences become apparent. An unforeseen deviation from the parent framework was observed in MUF20-Aγ where the bpdc ligands along one axis of the sheet bend causing a zig-zag pattern, whereas the bpdc ligands along the perpendicular axis remain linear as in BMOF-1-bpdc and MUF20-Aβ (Figure 4.13). In addition, though it might be expected that the bpdc ligands along the zig-zag axis in the interpenetrating framework would have the same "phase" as the first

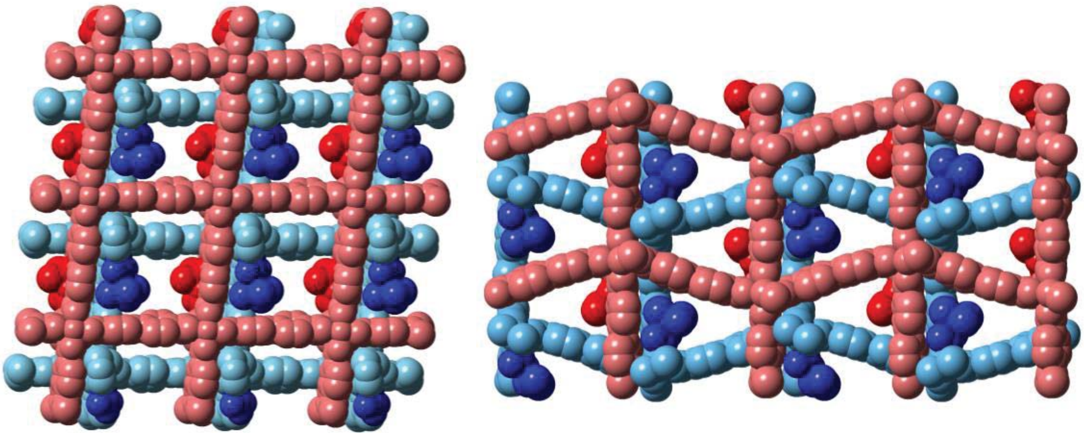

Figure 4.13 Structures determined by SXRD for MUF20-Aβ (left) and MUF20-Aγ (right) showing top-down view of Zn-bpdc sheets with space-filling rendering. Frameworks individually coloured in pink and light blue, with TPGs in red and dark blue to aide in visualisation. Hydrogens omitted for clarity.

framework, it is in fact "out of phase" so that the "peaks" of the interpenetrating network align with the "troughs" of the first network and *vice versa*. It is strongly believed that this unexpected behaviour occurs to improve the Van der Waals interactions between the *t*-butyl group of the TBE TPG and the phenyl ring of two bpdc ligands, as shown in Figure 4.13 where the TBE is a near perfect fit for the void space created at the intersection. The bending of the bpdc ligand is not observed in MUF20-Aβ as the NHBoc group is sufficiently bulky to interact with the phenyl ring of the opposite BPDC ligand without having to distort the structure away from that of the parent framework.

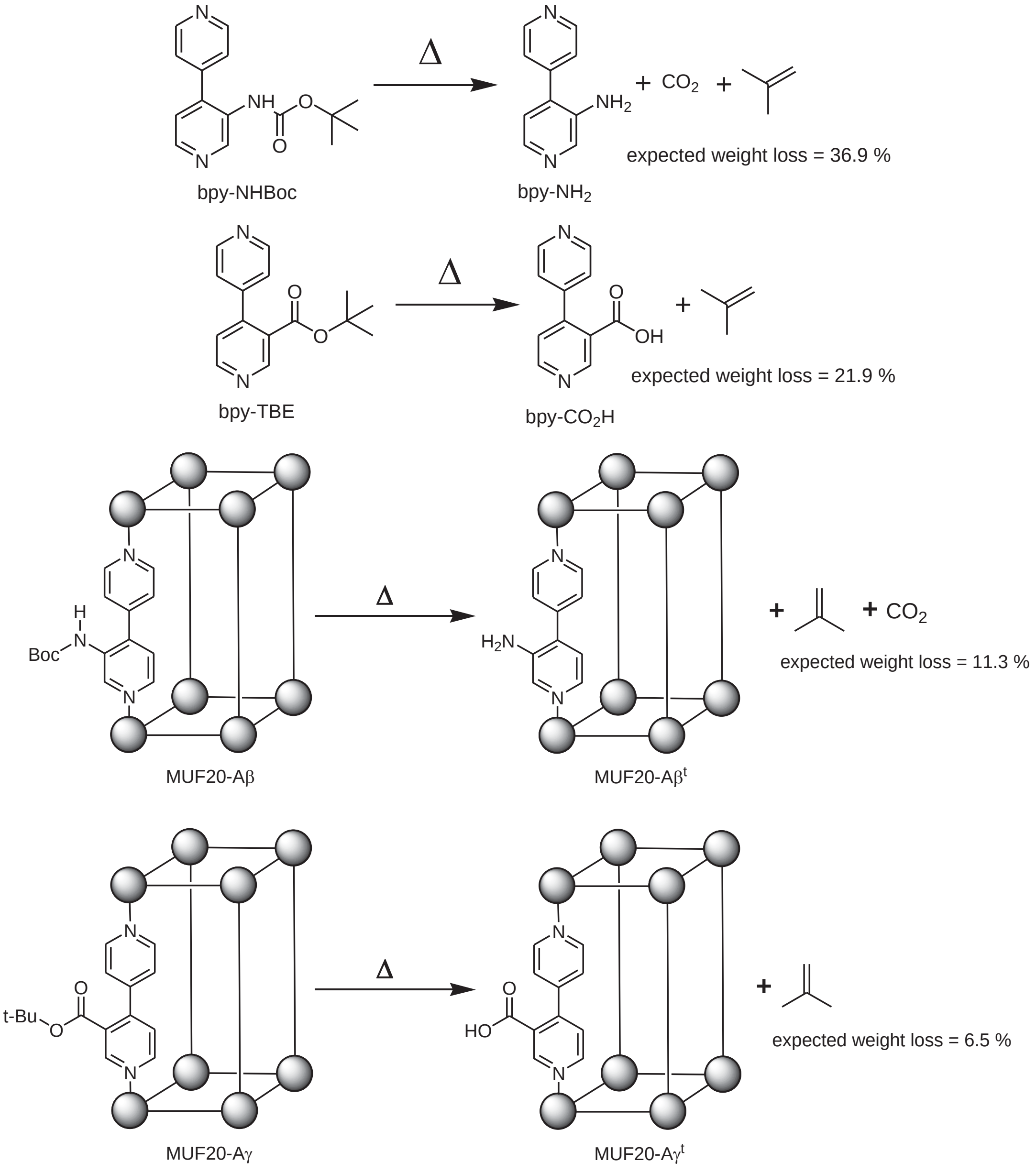

Figure 4.14 Thermolysis schemes for bpy-NHBoc and bpy-TBE as free ligands (top) and in MOFs (bottom), including expected weight losses.

The thermolytic reactions expected for the bpy-NHBoc and bpy-TBE ligands are outlined in Figure 4.14. The bpy-NHBoc thermolysis is analogous to the 1,4-bdc-NHBoc and 1,3-bdc-NHBoc thermolyses observed in the previous two chapters, with the only expected product being bpy-NH_2 through the loss of isobutylene and CO_2. The bpy-TBE thermolysis is the first thermolysis of an ester presented in this thesis, however thermolysis of certain esters to give carboxylates is a well-known process.[199] As shown in Figure 4.14, upon heating the tert-butyl ester decomposes to bpy-CO_2H and isobutylene is given off as a gas. In order to determine the optimal conditions for thermolysis of the protecting groups, TGAs were conducted on the free ligands to determine the temperatures at which weight losses occurred (Figure 4.15). The TGAs also revealed much greater (>50%) than the expected weight losses for both bpy-NHBoc and bpy-TBE. However, ^{1}H-NMR spectroscopic analysis revealed only protected and deprotected ligand, with no unknown species present. To determine whether the weight losses were due to particles of the sample being expelled from the pan, possibly due to superheating of solvent trapped in the oily material, some runs were conducted where a second aluminium pan was placed on top of the sample pan. This proved to be partially successful, since this decreased the magnitude of the weight loss, but not down to the weight losses expected. This indicated that the sample was not being forcibly ejected from the pan, rather that the material was evaporating as the temperature increased. Experiments using slower heating rates as well as holding the temperature constant for extended periods were conducted to determine if the processes could be separated, however none was successful. From these experiments, however, it is clear that the onset of thermal deprotection of bpy-TBE occurs around 150 °C and around 140 °C for bpy-NHBoc.

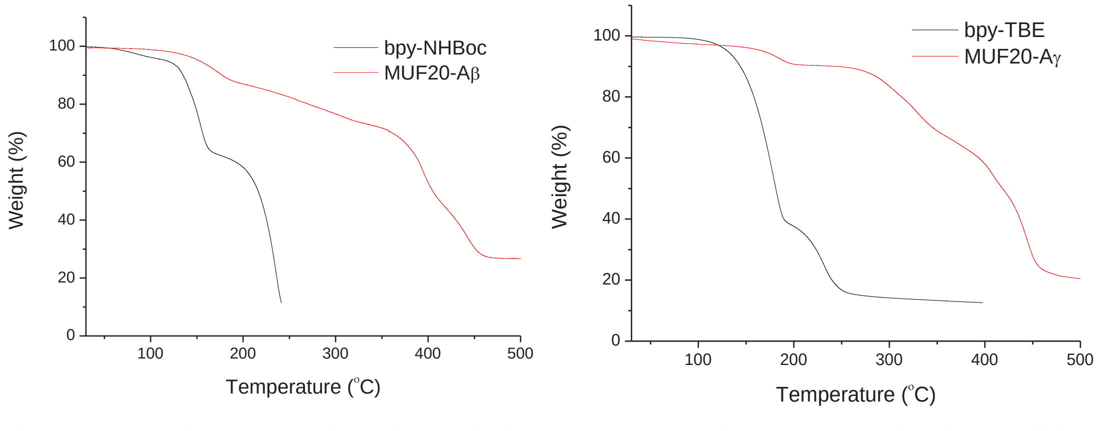

Figure 4.15 Thermogravimetric analysis (TGA) traces for MUF20 related materials.

TGA of MUF20-Aβ revealed an approximate weight loss of 12% starting around 130 °C. This agrees well with the expected weight loss of 11.3% for CO_2 and isobutylene. This result indicates that bpy-NHBoc is thermolysing to bpy-NH_2. Also, the close match with the expected weight loss reveals that the bpy species are not being lost in the same manner as in the free ligand. This indicates that the incorporation of the bpy species into the framework has supressed the volatility seen in the free ligand. This is expected, as the bpy species are bound to two zinc(II) ions, increasing the energy barrier to volatilisation. TGA of MUF20-Aγ reveals an approximately 6.6 % weight loss starting around 130 °C. This matches very closely to the expected weight loss of 6.5 % for isobutylene. This result indicates that isobutylene is being released and bpy-CO_2H formed as expected.

Once initial conditions were determined, MOF samples were then placed on the activation ports of the gas sorption instrument and conditions trialled until complete deprotection was achieved while maximum porosity and crystallinity was retained. These conditions were found to be 10 hours at 165 °C for both MUF20-Aβ and MUF20-Aγ. Unfortunately, PXRD experiments indicate that a significant loss of crystallinity is unavoidable in both MUF20-Aβ^t and MUF20-Aγ^t (Figure 4.16)

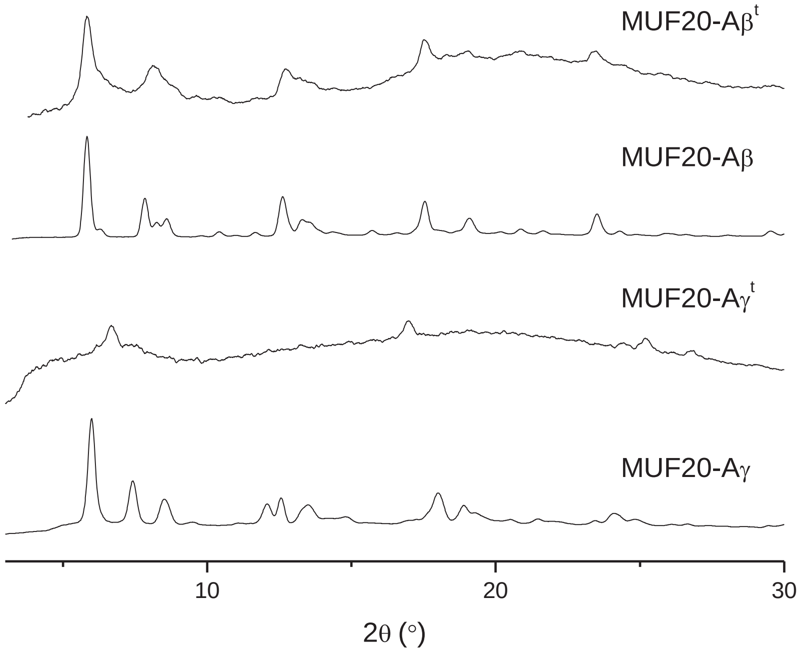

Figure 4.16 PXRD patterns of thermally deprotected materials MUF20-Aβ^t and MUF20-Aγ^t. PXRD patterns of MUF20-Aβ and MUF20-Aγ included for comparison.

Since a loss of crystallinity does not necessarily mean a loss of porosity, gas sorption experiments were still conducted on the thermolysed materials. Measurements were conducted both before and after thermolysis. Prior to gas sorption, freshly prepared MOF samples were washed with MeOH and then activated by repeated washing and subsequent soaking in CH_2Cl_2 for several hours. The samples were then transferred to a pre-dried and weighed analysis tube, still covered with CH_2Cl_2. Excess CH_2Cl_2 was removed with a

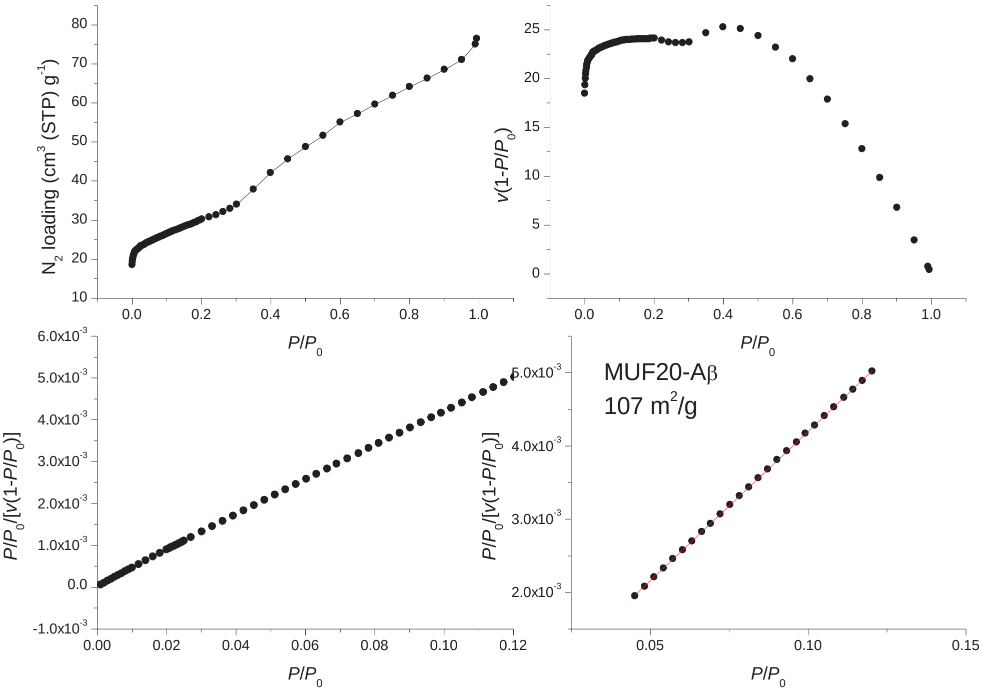

Equation	y = a + b*x	Pearson's r	0.99998			Value	Std Error
Weight	No Weighting	Adj. R-Squar	0.99995	P/P0/[v(1-P/P0)]	Intercept	1.24059E-	4.79988E-6
Residual Sum of Squares	9.90357E-10				Slope	0.04073	5.59683E-5

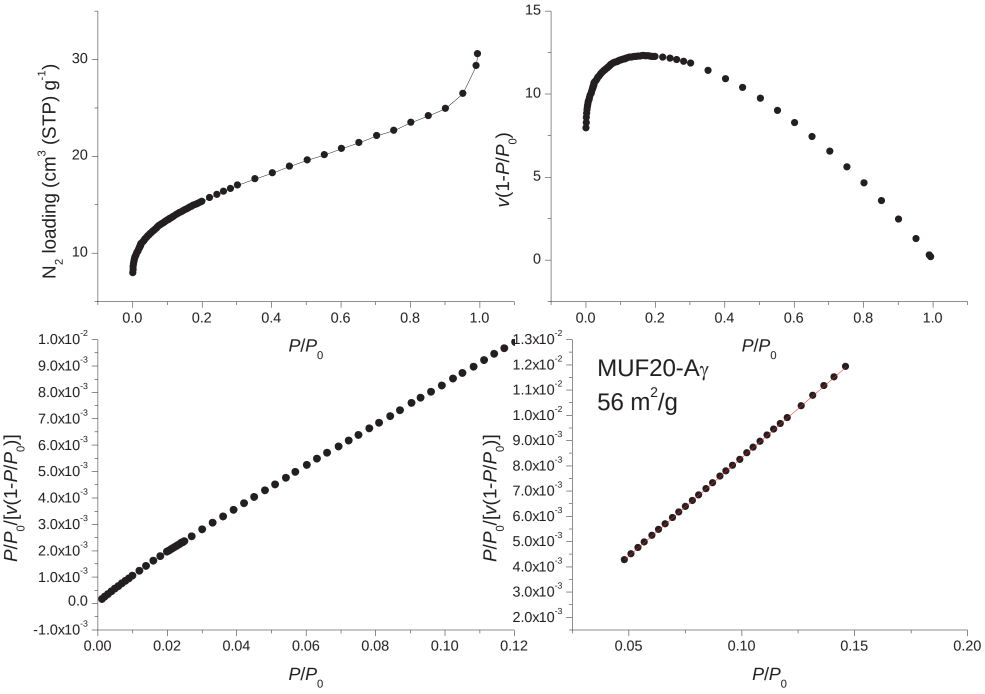

Equation	y = a + b*x	Pearson's r	0.99999			Value	Std Error
Weight	No Weighting	Adj. R-Square	0.99999	P/P0/[v(1-P/P0)]	Intercept	5.29255E-4	5.24752E-6
Residual Sum of Squares	1.907E-9				Slope	0.07788	5.4088E-5

Figure 4.17 BET surface area calculations for MUF20-Aβ (top) and MUF20-Aγ (bottom).

Pasteur pipette and then the sample tube was heated at 1 ºC per minute to 30 ºC under vacuum then held under a dynamic vacuum at 10^{-6} Torr for 10 h. Measurements using N_2 at 77 K (Figure 4.18) were used to calculate the Brunauer-Emmett-Teller (BET) surface areas for

MUF20-Aβ and MUF20-Aγ, which were found to be 107 m^2/g and 56 m^2/g respectively (Figure 4.17). Although these values are low, they are similar to the surface area of 60 m^2/g reported for BMOF-1-bpdc.[179] It was not possible to calculate the BET surface areas for MUF20-Aβ^t or MUF20-Aγ^t as the uptakes of these materials were too low and the shapes of uptakes unsuitable for this calculation. The total uptakes of these materials at 1 atm follow a similar trend, with ~76 cm^3/g for MUF20-Aβ and ~30 cm^3/g MUF20-Aγ, both of which are significantly more than the ~20 cm^3/g for BMOF-1-bpdc reported by the Cohen group.

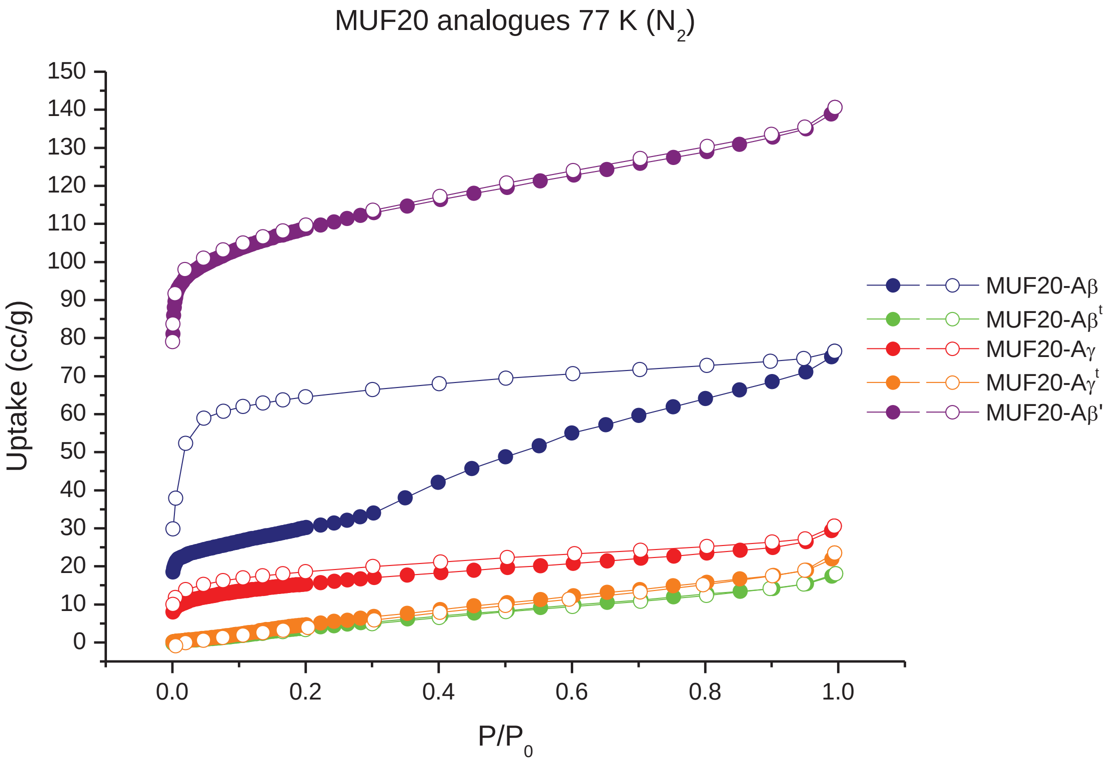

Figure 4.18 Gravimetric N$_2$ adsorption (filled) and desorption (open) isotherms measured at 77 K.

The uptakes of H$_2$ by MUF20-Aβ and MUF20-Aγ at 77 K were low, with total uptakes at 1 atm of ~23 cm^3/g for MUF20-Aβ and ~20 cm^3/g for MUF20-Aγ (Figure 4.19). Unfortunately, the literature does not report any gas sorption isotherms save the N$_2$ isotherm at 77 K, thus comparisons with the parent MOF are not possible. After thermolysis, both MOFs experienced significant decreases in uptake, with MUF20-Aβ^t dropping to ~25 % of the uptake of MUF20-Aβ and MUF20-Aγ^t dropping to ~40 % of the uptake of MUF20-Aγ. Not only does the uptake of MUF20-Aγ decrease by a lower percentage than MUF20-Aβ when thermolysed, MUF20-Aγ^t has a higher gravimetric uptake than MUF20-Aβ^t. The higher uptake of MUF20-Aγ^t with respect to MUF20-Aβ^t is not unexpected as MUF20-Aγ^t has a free carboxylate group, and it has been shown that increasing the polarity of the pore surface can increase gas uptakes.[200]

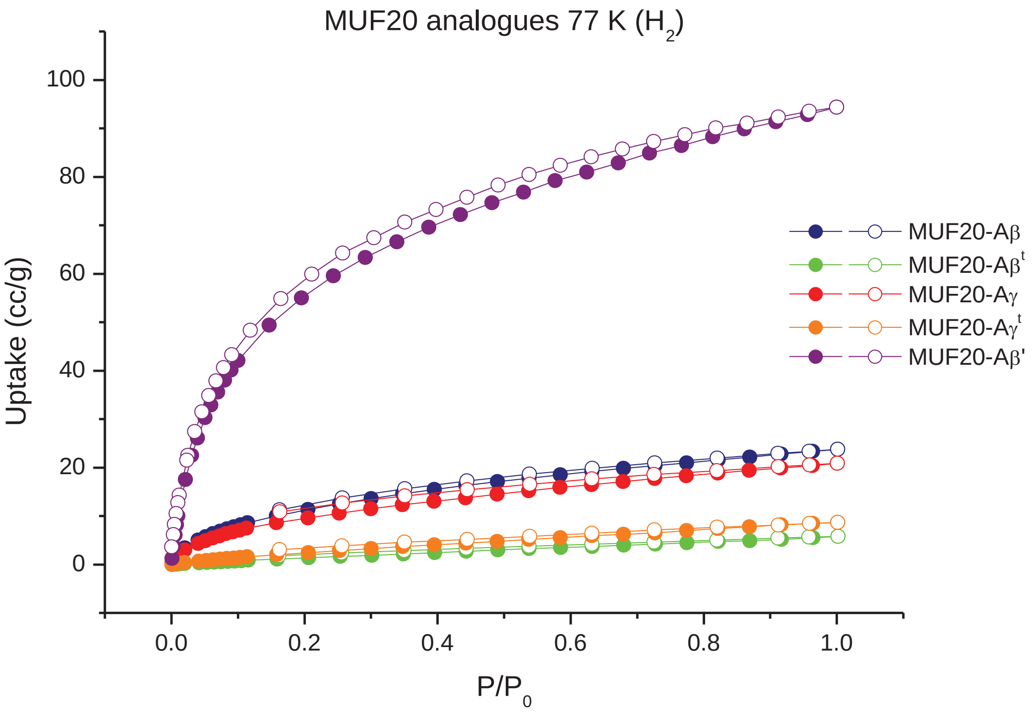

Figure 4.19 Gravimetric H_2 adsorption (filled) and desorption (open) isotherms measured at 77 K.

At 273 K, the N_2 uptakes show MUF20-Aγ having a total uptake of ~1.5 cm^3/g and MUF20-Aβ having no significant uptake (Figure 4.33). Interestingly, post thermolysis only MUF20-Aβ^t revealed any appreciable uptake, and actually surpasses the total uptake of MUF20-Aγ at ~2.0 cm^3/g. It is not known why this change has occurred, though since the uptakes are so low the matter was not explored in depth. The uptakes of CO_2 at 273 K for the MUF20 materials, whilst not high, are significantly higher than the uptakes of N_2 at this temperature, which is expected as CO_2 has an increased affinity for binding to surfaces due to its polar nature. The uptakes for MUF20-Aβ and MUF20-Aγ were ~14 cm^3/g and ~17 cm^3/g at 1 atm respectively (Figure 4.20). It is not known as to why MUF20-Aγ has a higher uptake of CO_2 than MUF20-Aβ when MUF20-Aβ has a higher surface area than MUF20-Aγ, especially due to CO_2 having a smaller kinetic diameter than N_2. After thermolysis, MUF20-Aβ^t demonstrated a dramatic increase in CO_2 uptake, reaching ~23 cm^3/g at 1 atm, whilst MUF20-Aγ^t revealed a decrease in uptake, only reaching ~12 cm^3/g. A similar trend is also observed with CH_4 uptake at 273 K, with MUF20-Aβ having a total uptake of ~ 2.0 cc/g at 1 atm and then MUF20-Aβ^t ~8.4 cc/g total uptake at 1 atm, and MUF20-Aγ having a total uptake of ~5.4 cc/g at 1 atm and MUF20-Aγ^t having a total uptake of 2.7 cc/g at 1 atm (Figure 4.21). It is not known why MUF20-Aβ^t has demonstrated an increase in uptake whereas MUF20-Aγ^t has decreased in uptake, though it is possible that the MUF20-Aβ framework is more resistant to collapse during thermolysis or that MUF20-Aγ^t is more prone to collapse post thermolysis.

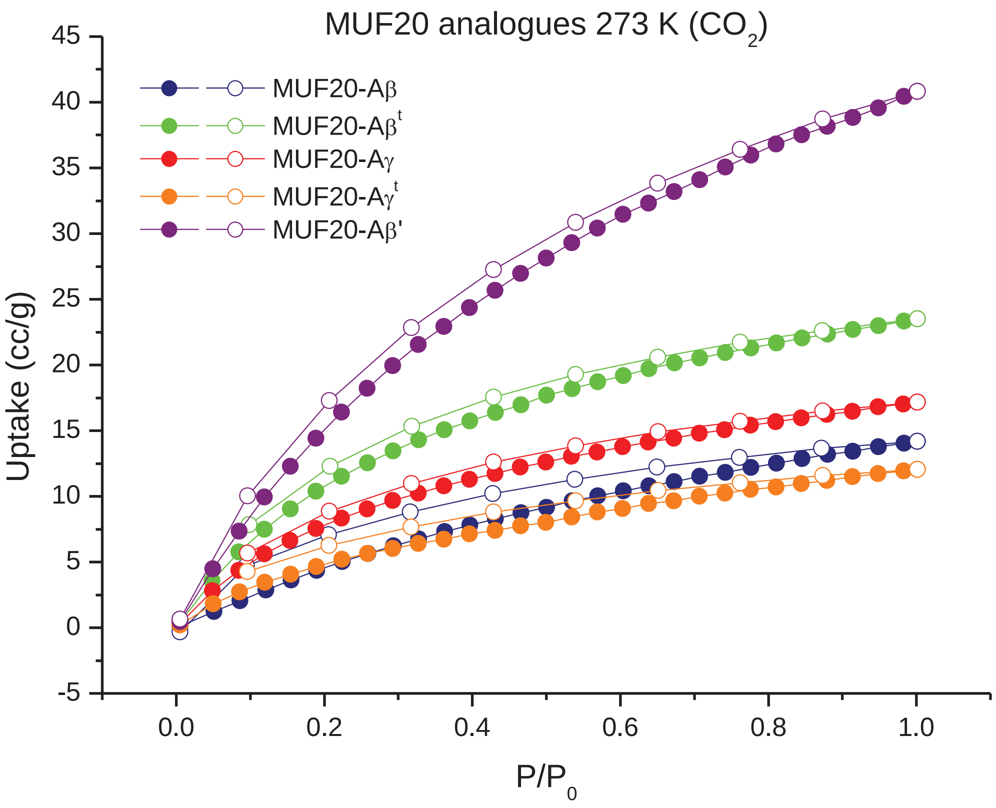

Figure 4.20 Gravimetric CO_2 adsorption (filled) and desorption (open) isotherms measured at 273 K.

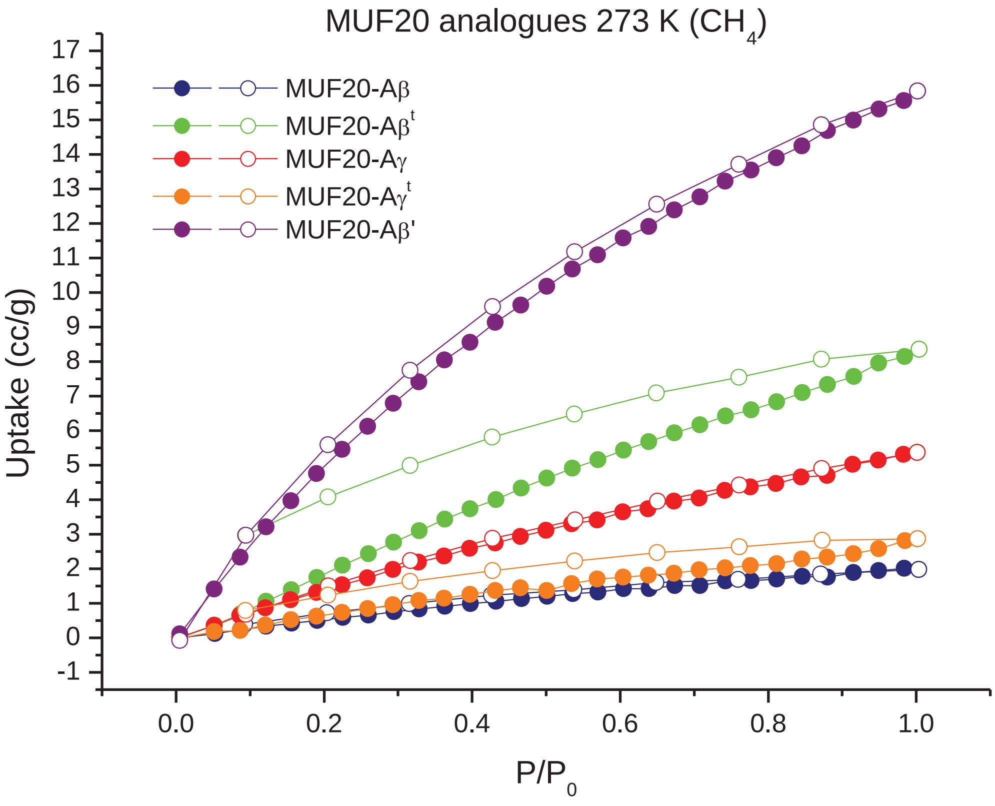

Figure 4.21 Gravimetric CH_4 adsorption (filled) and desorption (open) isotherms measured at 273 K.

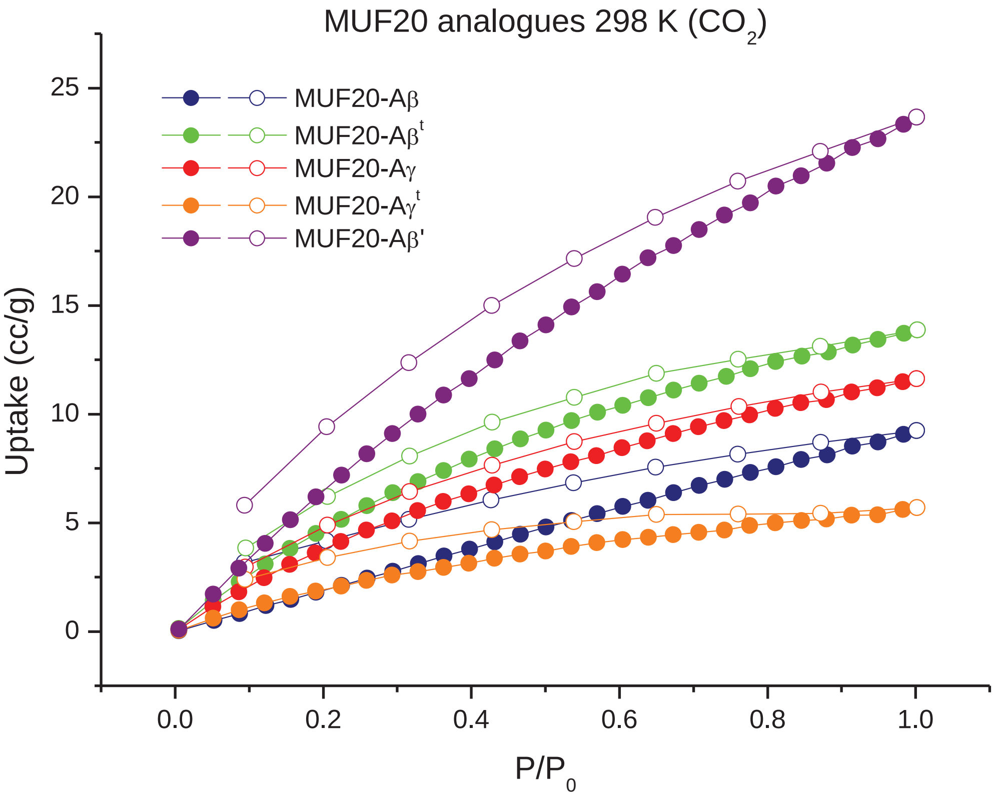

Figure 4.22 Gravimetric CO_2 adsorption (filled) and desorption (open) isotherms measured at 298 K.

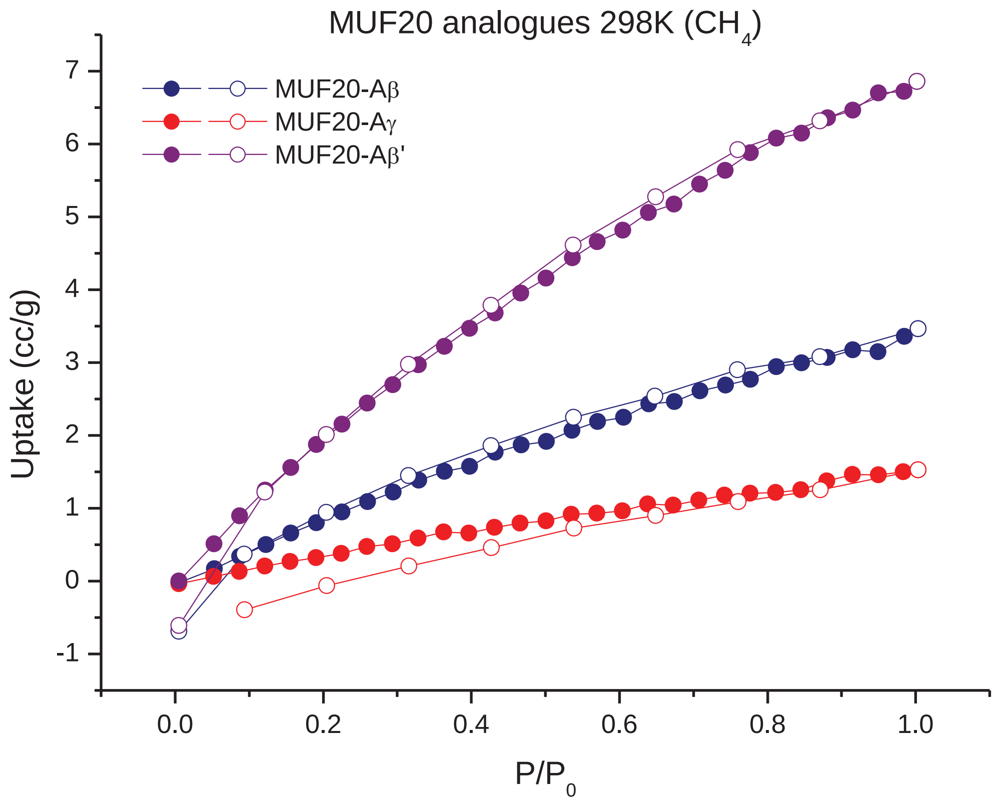

Figure 4.23 Gravimetric CH_4 adsorption (filled) and desorption (open) isotherms measured at 273 K.

After measuring the isotherms for the protected and thermally deprotected MOFs, the direct synthesis using ligands without protecting groups was investigated, to give MUF20-Aβ' and MUF20-Aγ'. It was found that the conditions required to generate MUF20-Aβ' were similar to those required for MUF20-Aγ with ratios of 1:1.62:0.85 for bpdc:bpy-NH_2:$Zn(NO_3)_2.4H_2O$ (vs 1:1.67:0.93 for MUF20-Aγ) and the same 4:1 MeOH:DMF ratio. It was also found that it was possible to scale up the reaction into a 25 mL Schott bottle, something that was not possible with the protected MOFs. It was not possible to synthesise MUF20-Aγ' directly despite trying many different synthesis conditions. It is believed that since the free carboxylate group in the bpy-CO_2H is a stronger metal binding moiety than N-donor pyridyl nitrogens, the bpy-CO_2H will preferentially bind through the carboxylate group and thus deviate the structure away from the desired framework topology.

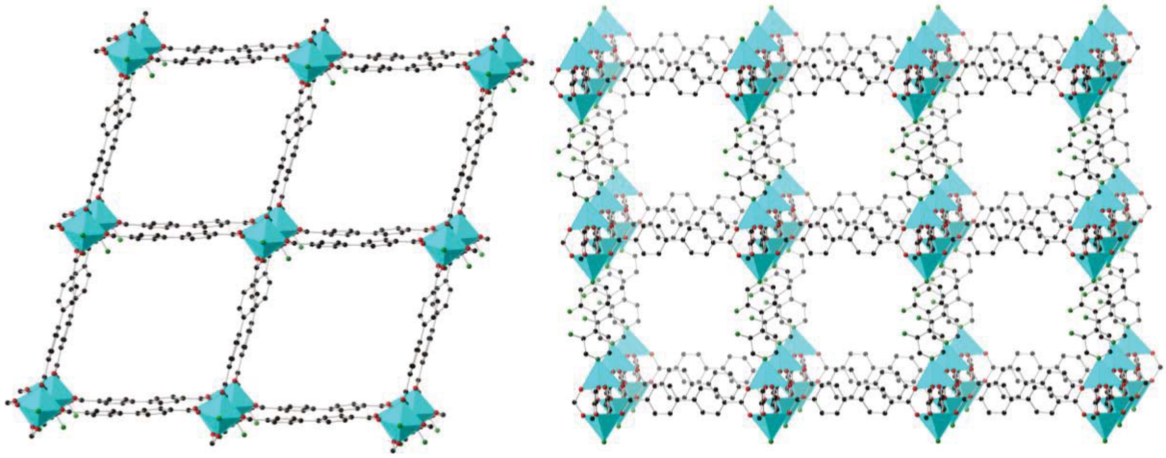

Figure 4.24 Structure determined by SXRD of MUF20-Aβ' depicting top-down views of the Zn-bpdc frameworks (left) and side views of the pillared layers (right). Second framework omitted for clarity. Atom colours: C = black, N = green, O = red, Zn = teal (hydrogen atoms omitted for clarity).

SXRD data for MUF20-Aβ'revealed a very similar structure to MUF20-Aβ, with near straight bpdc ligands along both axes and similar inter-lattice relative position and distances (Figure 4.24). However, whereas the ASU of MUF20-Aβ has two bpy-NHBoc ligands, the ASU of MUF20-Aβ' has only one bpy-NH_2 ligand, much like the ASU of MUF20-Aγ which contains only one bpy-TBE ligand. Another difference between the protected and directly synthesised MOFs is that the amine functional group is disordered over two positions in MUF20-Aβ' whereas in MUF20-Aβ the side chains are not disordered. This is a rare example where through using the protected ligands it has been possible to direct the functional groups into an ordered arrangement when using the unprotected ligands results in a randomisation of the functional groups' positions. The NHBoc and TBE TPGs have attractive interactions with the second lattice which impose a directing force on the ligand, resulting in the ordered TPG positioning seen in the MOFs. This observation could prove useful in future work where precise positioning of the functional groups may be desirable. It should be noted that MUF20-Aβ' suffers from poor refinement statistics in a similar way to MUF20-Aβ, despite having good quality data (R_{int} = 6.08%). As with MU20-Aβ, further efforts are ongoing to develop a model for MUF20-Aβ' which resolves these issues.

Prior to gas sorption, MUF20-Aβ' was activated in the same manner as MUF20-Aβ and MUF20-Aγ (*vide supra*). Gas sorption measurements revealed MUF20-Aβ' outperformed all other MUF20 species for all gases at all temperatures. MUF20-Aβ' also demonstrated the highest BET value of the MUF20 materials, at 413 m^2/g (Figure 4.25). Whilst the increased uptake with respect to MUF20-Aβ^t is not unexpected as a small degree of framework collapse is expected after thermolysis, the degree by which MUF20-Aβ' uptakes more gas than MUF20-Aβ^t is unexpected.

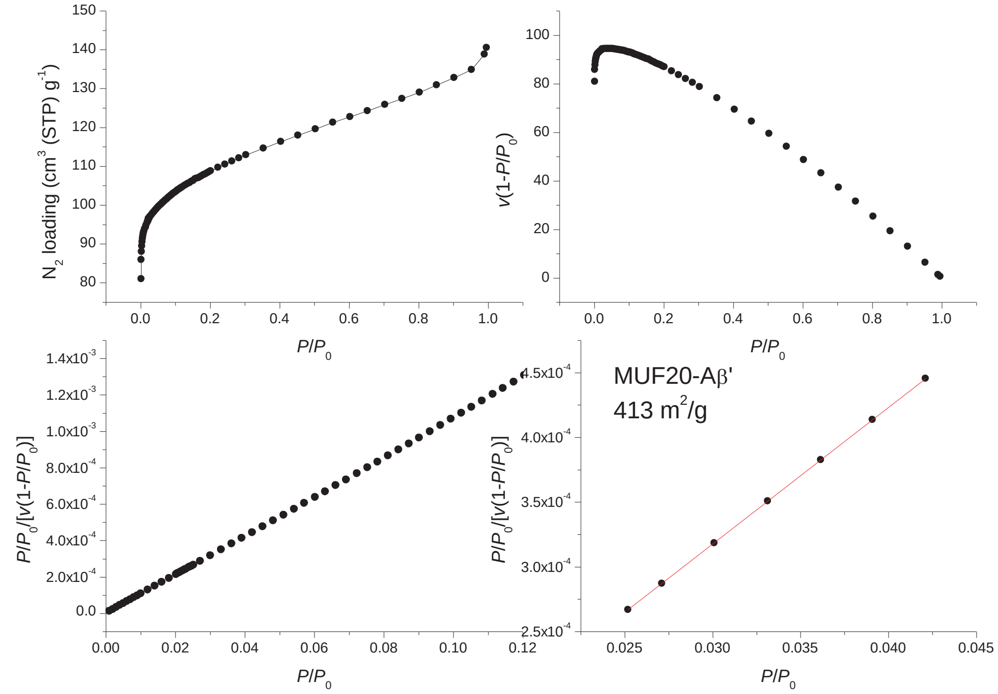

Equation	y = a + b*x	Pearson's r	1			Value	Std Error
Weight	No Weighting	Adj. R-Square	1	P/P0/[v(1-P/P0)]	Intercept	1.30895E-6	1.3674E-7
Residual Sum of Squares	1.91848E-14				Slope	0.01055	4.05018E-6

Figure 4.25 BET surface area calculations for MUF20-Aβ'.

MUF20-Aβ' has a significantly higher capacity for adsorbing guest molecules than MUF20-Aβ^t. This would indicate that: the pores in MUF20-Aβ^t have largely collapsed, or the structure of MUF20-Aβ' inherently leads to a higher capacity. Due to the inability to remove the observed hysteresis in some of the gas sorption measurements of MUF20-Aβ' (*vide infra*) in addition to the knowledge that these frameworks lose significant crystallinity during thermolysis, it was concluded that the dramatically lower uptake is due to the incomplete collapse of the thermally deprotected framework and not the result of any inherent benefits of the MUF20-Aβ' framework. Whilst the differences in uptakes between MUF20-Aβ^t and MUF20-Aβ' indicate that most of the MUF20-Aβ^t framework collapsed during thermolysis, it is possible that a much smaller amount of the framework collapsed in such a way as to block off larger portions of the MOF, preventing gas molecules from accessing the open void spaces beyond.

As can be seen in many of the gas sorption isotherms, some of the materials demonstrated a small degree of hysteresis between the adsorption and desorption isotherms. In order to determine the optimal equilibration time for the gas sorption measurements, some tests were conducted on MUF20-Aβ' at 298 K using CO_2 as the adsorbate. It was decided to examine CO_2 as it would give an upper bound for the take it would take to collect the isotherms. This is due to CO_2 having the greatest affinity for the framework, and thus requires a longer equilibration time than N_2 and CH_4. It was decided to conduct this investigation at 298 K as the measurements are faster at 298 K than at 273 K due to the increased thermal energy of the system allowing for faster transport of the gas molecules within the MOF. This would allow us to extend the equilibration time and still complete the measurements in a reasonable amount of time. Figure 4.26 shows that as the equilibration time was increased from 2 minutes to 8 minutes (our standard equilibration time for 298 K isotherms) and then to 24 minutes, the total uptake of CO_2 increased as well as the degree of hysteresis observed. At first this result confused us until a conference paper by Illam Park[201] was found in which computational studies revealed that as equilibration time increases adsorption increases before it starts decreasing and is eventually eliminated (Figure 4.27). When compared with Park's results, it can be assumed that the 8 min equilibration time is to the left of the peak of maximum hysteresis as the 24 min equilibration time has greater hysteresis. What is not known is whether the 24 min equilibration is before or after the peak of maximum hysteresis, though in either instance the equilibration time would need to be many times longer (in the order of hours) in order to completely remove the hysteresis. Based on these observations, it was determined that it would not be possible to collect a data set without hysteresis in a practical timeframe, and thus it was decided to keep with the eight-minute standard equilibration time for such measurements.

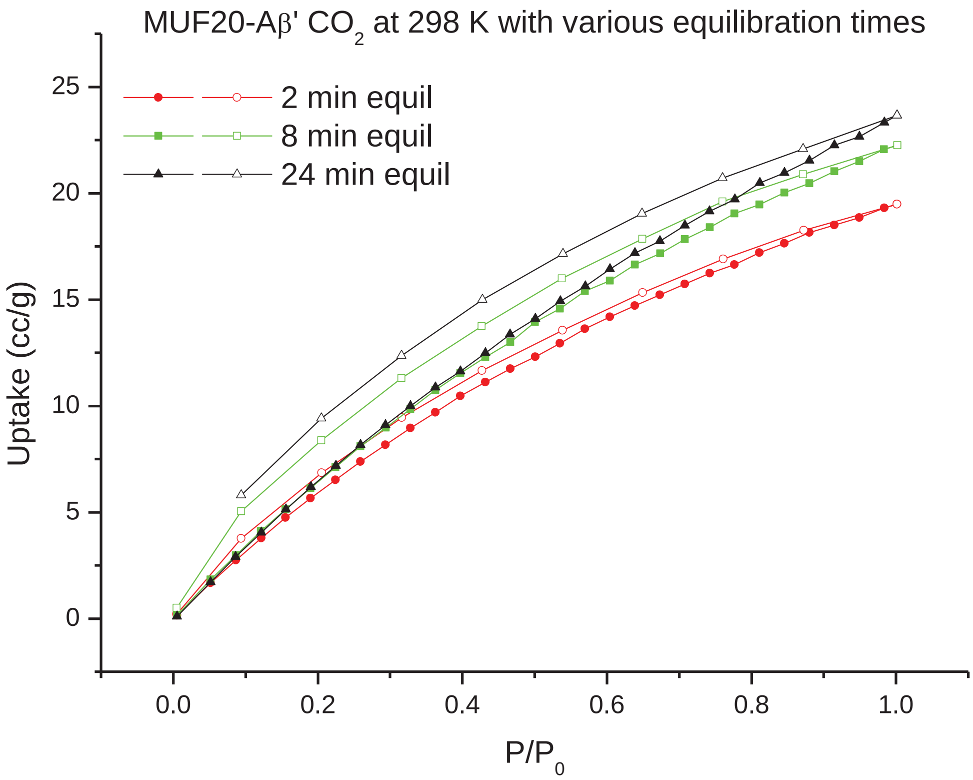

Figure 4.26 Gas sorption isotherms for MUF20-Aβ’ with equilibration times of 2, 8, and 24 mins.

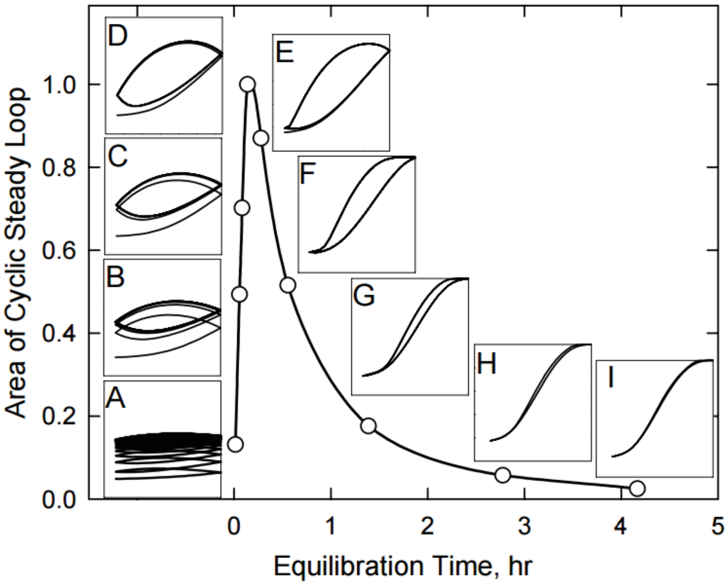

Figure 4.27 Plot of area of cyclic steady loop vs equilibration time demonstrating how the degree of hysteresis can change with time. Reproduced from Illam Park’s 2001 conference paper.[201]

4.3 Conclusion

In conclusion, the synthesis of two bpy-based TPG containing ligands was achieved, as well as the synthesis of five new MOFs. It has been possible to use bpy-TBE to obtain MUF20-Aγ and subsequently MUF20-Aγ^t via thermal deprotection, a MOF that was not obtainable by direct synthesis with bpy-CO_2H. It was also possible to introduce ordering of functional groups in MUF20-Aβ, MUF20-Aβ^t, MUF20-Aγ, and MUF20-Aγ^t, a feature not present in MUF20-Aβ'. It appears that both MUF20-Aβ^t and MUF20-Aγ^t had significant amounts of framework decomposition/collapse as a result of the thermal deprotection process. Whilst not as severe as the complete collapse observed in the lon-e materials in chapter 3, the dramatic differences between MUF20-Aβ^t and MUF20-Aβ' are an indication that it is desirable to utilise TPGs with more thermally stable frameworks. However, despite this, all MUF20 materials demonstrated greater N_2 uptake at 77 K than the unfunctionalised parent BMOF-1-bpdc material.

4.4 Experimental section

4.4.1 General procedures

All starting compounds and solvents were used as received from commercial sources without further purification unless otherwise noted. NMR spectra were recorded at room temperature on a Bruker-500 Avance instrument, with the use of the solvent proton as an internal standard. Elemental analyses were performed by the Campbell Microanalytical Laboratory at the University of Otago, New Zealand. Care was taken to limit the exposure of all MOFs to the atmosphere.

4.4.2 Ligand Synthesis

4.4.2a bpy-CO_2H

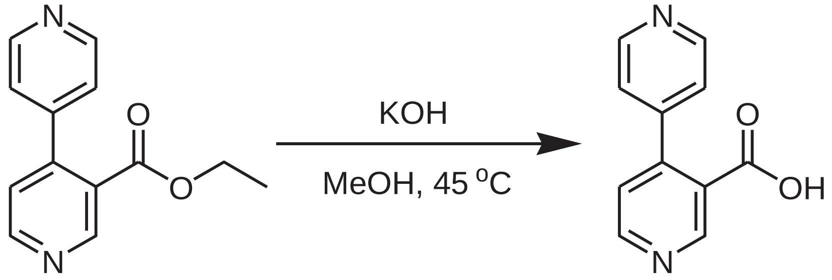

Bpy-COOEt (2.18 mmol) and KOH (4.71 mmol) were combined in MeOH (1.5 mL) and heated to 45 °C for 1 hour with stirring. The reaction was quenched with H_2O (5 mL) and aqueous HCl (1 M) added until the pH was approximately 3. The solution was passed through Sephadex and the solvent removed *in vacuo*. This material was used crude for the next synthetic step with no further purification. Yield: 432 mg (99 %).

4.4.2b bpy-TBE

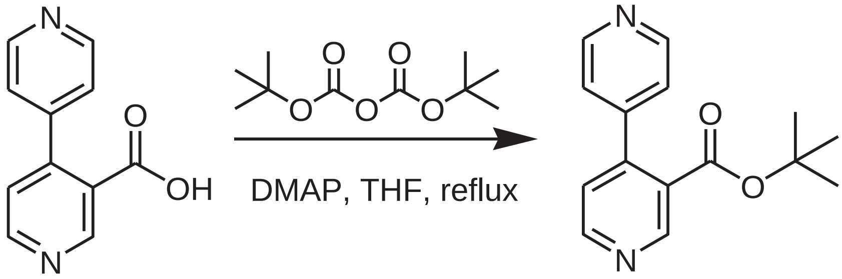

bpy-CO_2H (2.16 mmol) and dimethylaminopyridine (0.19 mmol) were combined in THF (10 mL) and brought to reflux under Ar atmosphere. Di-*tert*-butyl dicarbonate (6.75 mmol) in THF (5 mL) was added slowly dropwise, and the reaction refluxed for 4 hours under Ar atmosphere. Di-*tert*-butyl dicarbonate (6.75 mmol) in THF (5 mL) was then added slowly dropwise, and the reaction refluxed for 4 hours under Ar atmosphere. The solvent was then removed *in vacuo*. The solid material was then taken up in DCM and passed through a silica plug, washing with DCM and eluting with DCM:Et_2O:MeOH (13:13:1). The solvent was then removed *in vacuo*, affording a solid brown product. Yield: 478 mg (85.8 %). ^{1}H-NMR (500 MHz, $CDCl_3$): δ 1.26 (s, 9H), 7.18 (dd, *J* = 5.0 Hz, 0.4 Hz, 1H), 7.20 (dd, *J* = 4.4 Hz, 1.6 Hz, 2H), 8.65 (dd, *J* = 4.5 Hz, 1.6 Hz, 2H), 8.71 (d, *J* = 5.0 Hz, 1H), 9.04 (s, 1H).

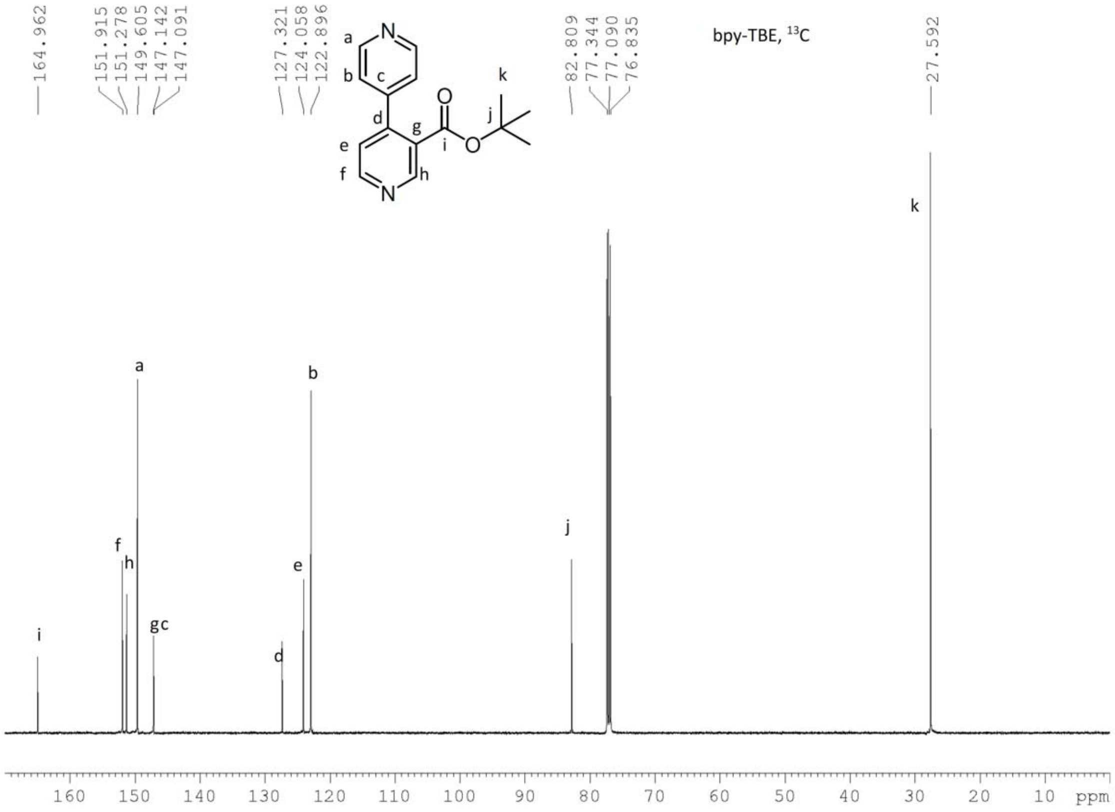

Figure 4.28 ^{13}C-NMR spectroscopic analysis of bpy-TBE in $CDCl_3$.

4.4.2c 3-nitro-4,4’-bipyridine

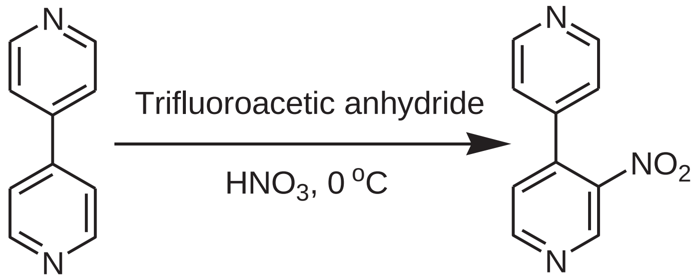

The following reaction was carried out in a room refrigerated to 2 °C. Trifluoroacetic anhydride (4 mL, 28.3 mmol) was cooled to 0 °C in a refrigerated room and bpy (3.23 mmol) slowly added with stirring. The reaction was stirred for a further 2 hours at 0 °C under an Ar. Concentrated nitric acid (400 µL) was added slowly at 0 °C with stirring. The reaction was then left to stir open to the atmosphere for 5 min to prevent pressure build up (failure to do so had resulted in the rubber septum being forcibly ejected from the reaction vessel), then replaced under Ar atmosphere. The reaction was then allowed to stir for 40 hours at 0 °C. The reaction mixture was slowly added to a solution of $Na_2S_2O_5$ (3.68 mmol) in H_2O (5 mL) at 0 °C with stirring. The reaction was stirred for a further 6 hours at

0 °C. The reaction was then neutralized with KOH solution (6 M, aqueous), extracted into DCM, the combined organic extracts dried over $MgSO_4$, and the solvent removed *in vacuo*. The thick oil obtained contained a mixture of bpy, bpy-NO_2, and 3,3'-dinitro-bpy. The material was purified by silica gel flash chromatography (DCM:Et_2O:MeOH, 13:13:1), which afforded the pure material. Yield: 113 mg (0.56 mmol, 17 %). ^{1}H-NMR spectroscopic analysis matched that reported by Zhang *et al*.[195]

4.4.2d 3-amino-4,4'-bipyridine

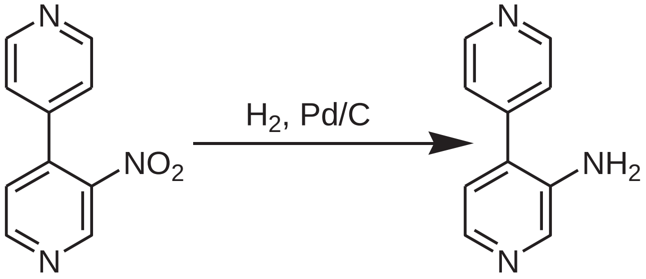

Bpy-NO_2 (113 mg, 0.56 mmol) and palladium on charcoal (10% Pd by weight, 13 mg) were combined in DCM:MeOH (10 mL, 1:1) and placed under H_2 atmosphere (50 psi) with agitation for 18 hours. The reaction was returned to atmospheric pressure, filtered through Celite and the solvent removed *in vacuo*, affording an amber oil. Yield: 96 mg (>95 %). ^{1}H-NMR spectroscopic analysis matched that reported by Zhang *et al*.[195]

4.4.2e 3-*tert*-butoxycarbonylamino-4,4'-bipyridine

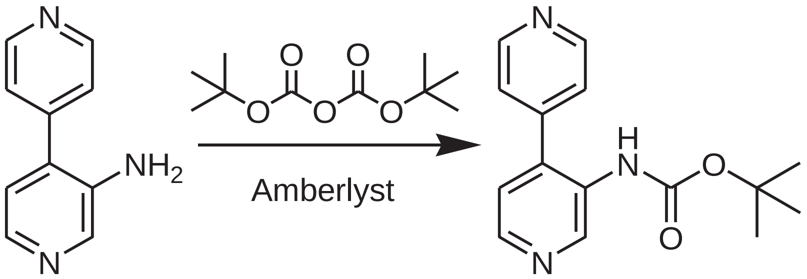

Amberlyst resin 15 (approx. 50 spheres) was added to bpy-NH_2 (2.77 mmol) in absolute EtOH (10 mL) under Ar atmosphere. Di-*tert*-butyl dicarbonate (3.89 mmol) in THF (5 mL) was added slowly dropwise, and the reaction allowed to stir at room temperature over 4 hours. Di-*tert*-butyl dicarbonate (3.89 mmol) in THF (5 mL) was then added slowly dropwise, and the reaction allowed to stir at room temperature over 4 hours. Di-*tert*-butyl dicarbonate (3.89 mmol) in THF (5 mL) was then added slowly dropwise, and the reaction allowed to stir at room temperature overnight. The reaction was then filtered to remove the solid resin and the solvent removed *in vacuo*. The material was then purified by silica gel flash chromatography (DCM:Et_2O:MeOH, 13:13:1). Yield: 275 mg (36.5 %). ^{1}H-NMR (500 MHz, $CDCl_3$): δ 1.46 (s, 9H), δ 6.33 (s, 1H), 7.15 (d, *J* = 4.8 Hz, 1H), 7.35 (d, *J* = 5.8 Hz, 2H), 8.45, (d, *J* = 4.8 Hz, 1H), 8.77, (d, *J* = 4.9 Hz, 2H), 9.21 (s, 1H).

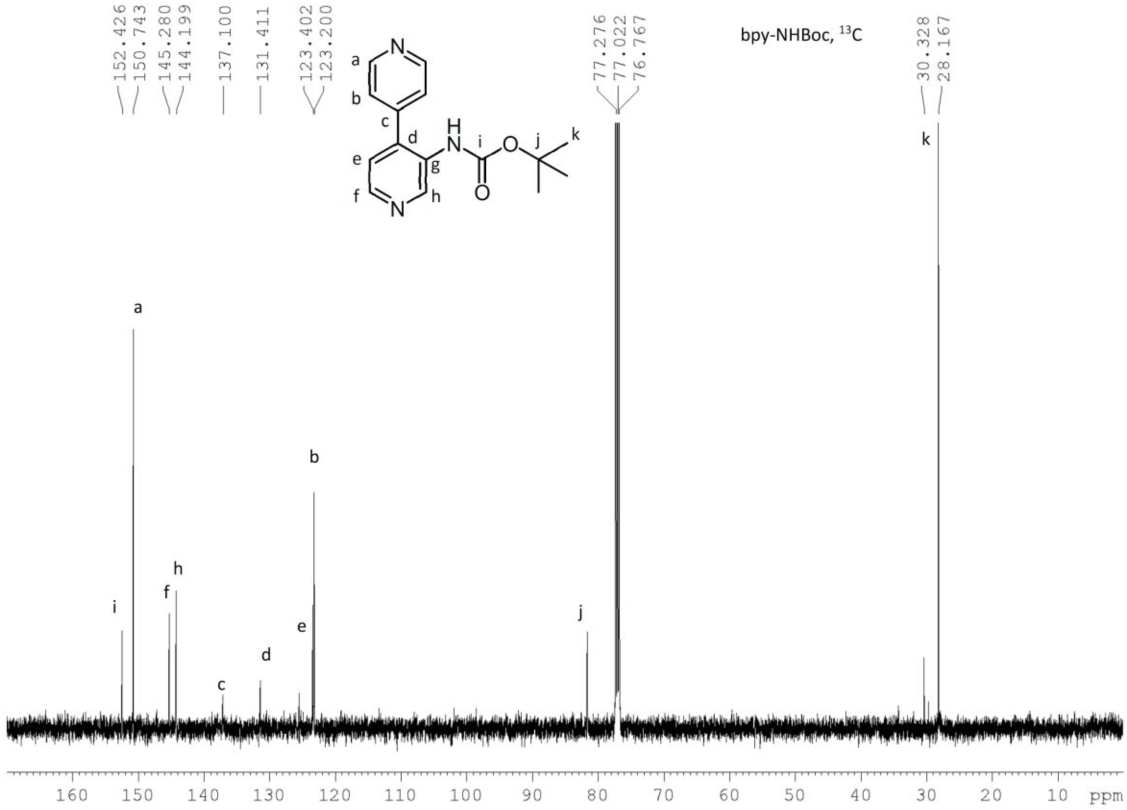

Figure 4.29 ^{13}C-NMR spectroscopic analysis of bpy-NHBoc in $CDCl_3$.

4.4.3 MOF synthesis and characterization

4.4.3a MUF-20Aβ

Bpdc (2.4 mg, 0.010 mmol), bpy-NHBoc (4.7 mg, 0.017 mmol) and $Zn(NO_3)_2.4H_2O$ (2.4 mg, 0.0092 mmol) were combined in a 4 mL scintillation vial. MeOH (1.0 mL) was then added and the mixture briefly sonicated before addition of DMF (0.25 mL). After sonicating a second time the vial was placed in an oven at 85 °C for 15 hours. Colourless needle clusters formed. Yield: 16.1 mg. Anal. calcd. for [$C_{86}H_{66}N_6O_{20}Zn_4$]: C, 58.52; H, 3.77; N, 4.76; Found: C, 58.31; H, 3.41; N, 4.59. To scale up the synthesis, a parallel synthetic method was adopted (multiple vials using the scale described above).

4.4.3b MUF-20Aβ^t

MUF-20Aβ was thermolysed on the activation port of the gas sorption instrument. The sample was placed under vacuum and then heated to 165 °C for 10 hours. The sample was then backfilled with N_2 before being transferred to the gas sorption measurement port.

4.4.3b MUF-20Aβ’

Bpdc (12.5 mg, 0.052 mmol), bpy-NH_2 (14.4 mg, 0.084 mmol), and $Zn(NO_3)_2.4H_20$ (11.6 mg, 0.044 mmol) were combined in a 25 mL Schott bottle lined with Sigmacote. Anhydrous MeOH (5.0 mL) was then added, and the suspension briefly sonicated before the addition anhydrous DMF (1.25 mL) followed by re-subjection to brief sonication before placing in an oven at 85 °C for 18 hours. After 10 mins in the oven, the lid of the Schott bottle was re-tightened and Teflon tape placed around the join of the lid and bottle. Yield: 13.4 mg. Anal. calcd. for [$C_{38}H_{24}N_2O_8Zn_2$]: C, 59.48; H, 3.15; N, 3.65; Found: C, 59.26; H, 3.53; N, 3.58.

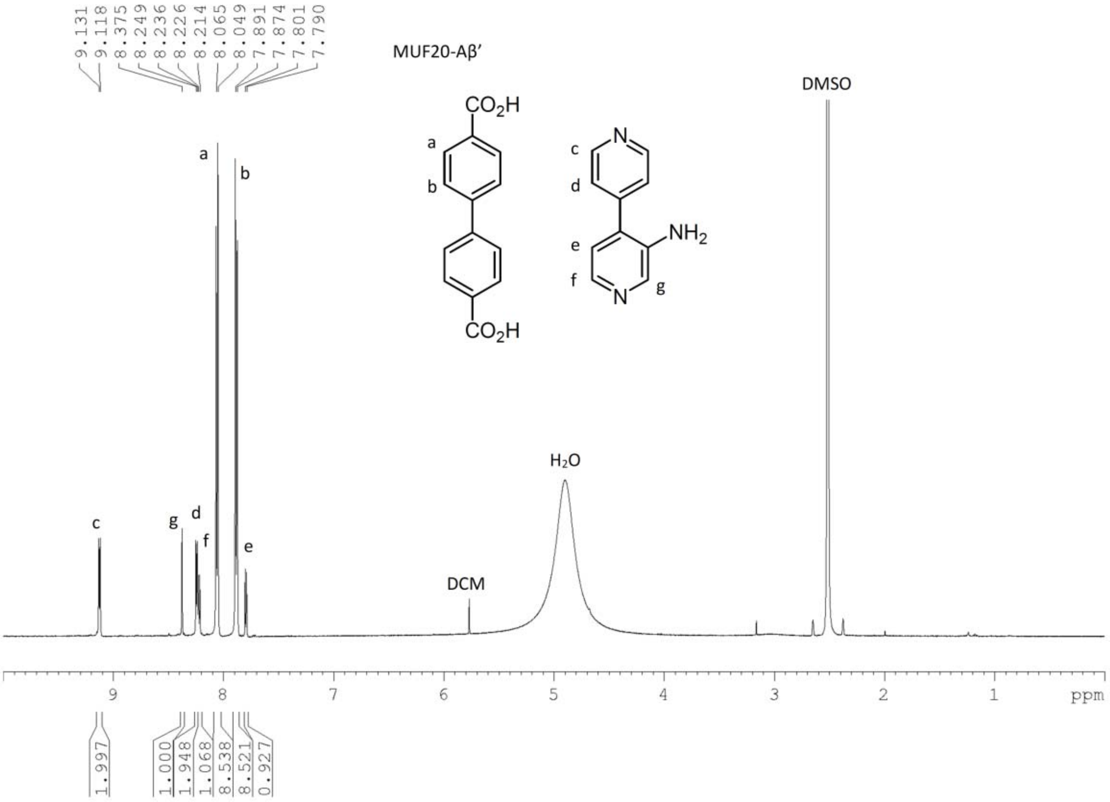

Figure 4.30 ^{1}H-NMR spectroscopic analysis of digested MUF20-Aβ’ in DMSO-d_6/DCl.

4.4.3b MUF-20Aγ

Bpdc (5.0 mg, 0.021 mmol), bpy-TBE (8.8 mg, 0.034 mmol) and $Zn(NO_3)_2.4H_2O$ (5.1 mg, 0.020 mmol) were combined in a 4 mL scintillation vial. MeOH (1.0 mL) was then added and the mixture briefly sonicated before addition of DMF (0.25 mL). After sonicating a second time the vial was placed in an oven at 85 °C overnight. Colourless needle clusters formed. Yield: 13.2 mg. Anal. calcd. for [$C_{43}H_{32}N_2O_{10}Zn_2$]: C, 59.53; H, 3.72; N, 3.23; Found: C, 58.97; H, 3.93; N, 3.23. To scale up the synthesis, a parallel synthetic method was adopted (multiple vials using the scale described above).

Single crystal synthesis: Bpdc (5.0 mg, 0.021 mmol), bpy-TBE (8.8 mg, 0.034 mmol) and $Zn(NO_3)_2.4H_2O$ (5.1 mg, 0.020 mmol) were combined in a 20 mL scintillation vial. MeOH (4.0 mL) was then added and the mixture briefly sonicated before addition of DMF (1.0 mL). After sonicating a second time the vial was placed in an oven at 85 °C overnight. Approximately 80 % of the solvent volume was lost during the synthesis. Whilst appearing cracked on the surface, the flat needles diffracted intensely to the edge and a good SXRD data set was obtained.

4.4.3b MUF-20Aγ^t

MUF-20Aγ was thermolysed on the activation port of the gas sorption instrument. The sample was placed under vacuum and then heated to 165 °C for 10 hours. The sample was then backfilled with N_2 before being transferred to the gas sorption measurement port.

4.4.4 ^{1}H NMR analysis of digested MOF samples

For ^{1}H NMR spectroscopy, the mother liquor of the as-synthesized MOF crystals was replaced with fresh dry MeOH multiple times, followed by repeated washing and subsequent soaking in CH_2Cl_2 for several hours. The excess CH_2Cl_2 was then decanted and the samples placed under vacuum overnight to remove residual solvent from the pores. The crystals were then digested using the following protocol: 23 μL of a 35% DCl solution in D_2O was mixed with 1 mL of DMSO-d_6 to give a DCl/DMSO-d_6 stock solution. Around 5 mg of MOF was digested in 200 μL of this stock solution together with 400 μL of DMSO-d_6. Spectra were acquired immediately following dissolution.

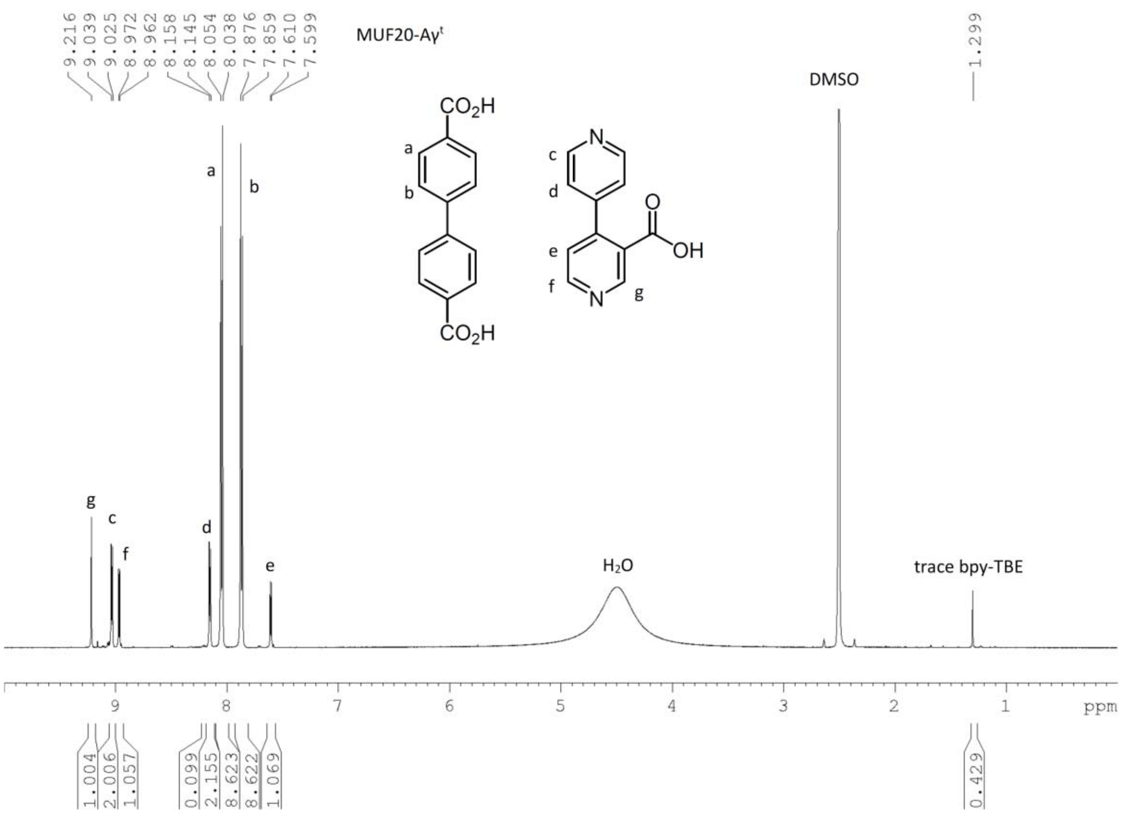

Figure 4.31 ^{1}H-NMR spectroscopic analysis of digested MUF20-Aγ^t in DMSO-d_6/DCl.

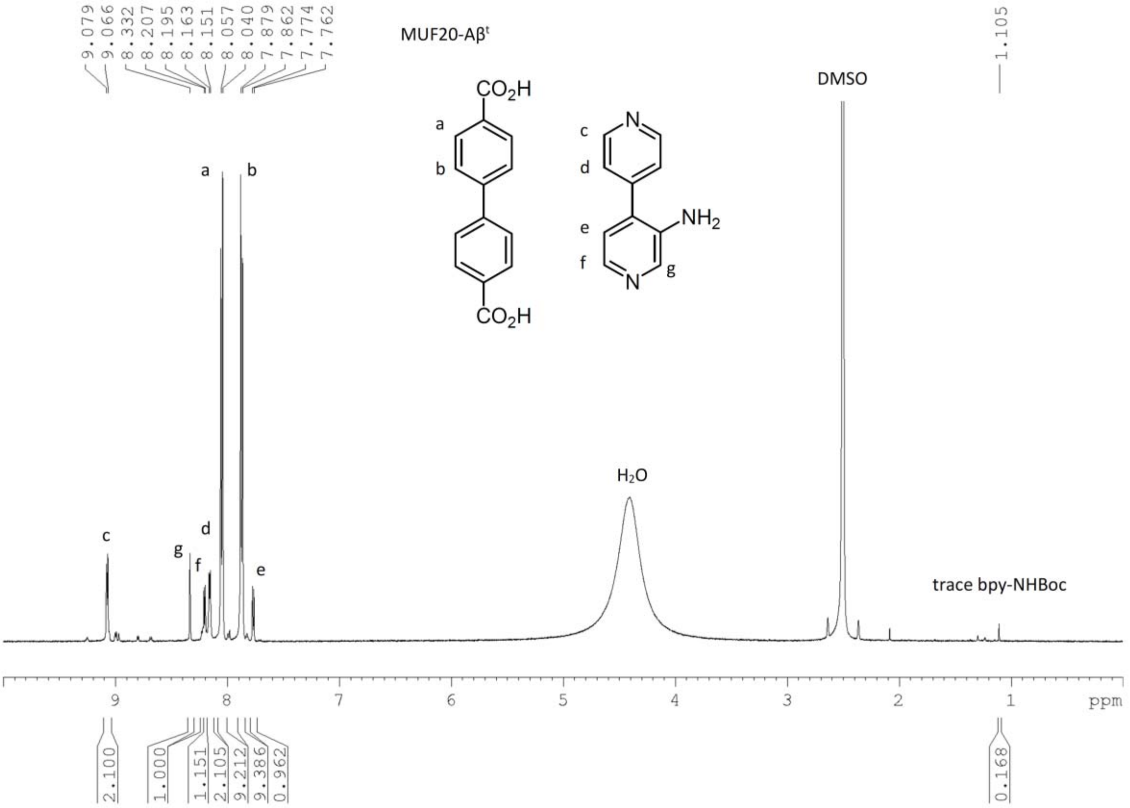

Figure 4.32 ^{1}H-NMR spectroscopic analysis of digested MUF20-Aβ^t in DMSO-d_6/DCl.

4.4.5 Thermogravimetric Analysis (TGA)

Thermogravimetric analyses were performed on a TA Instruments Q50 instrument. Freshly prepared MOF samples were prepared as for gas sorption (see section 4.4.8). Samples were then transferred to an aluminium sample pan and then measurements were commenced under an N_2 flow with a heating rate of 5 °C /min.

4.4.6 Single crystal X-ray diffraction

MOF crystals were mounted together with some dry DEF in a polymer sleeve on a Rigaku Spider diffractometer equipped with a MicroMax MM007 rotating anode generator (Cu_α radiation, 1.54180 Å), high-flux Osmic multilayer mirror optics, and a curved image-plate detector. Data were collected at the temperatures listed in Table *4.1*and were integrated, scaled, and averaged with FS Process.[158] XPREP was used to determine the space group and the structures were solved using SHELXS and refined with SHELXL.[159] All non-hydrogen atoms were found in the electron density difference map. All hydrogen atoms were calculated using the appropriate restraints. All non-hydrogen atoms were refined anisotropically. Cif files for MOFs uploaded to http://tinyurl.com/sblackwoodMOFs.

4.4.7 Powder X-ray diffraction patterns

All powder X-ray diffraction experiments were carried out on a Rigaku Spider X-ray diffractometer with Cu K_α radiation (Rigaku MM007 microfocus rotating-anode generator), monochromated and focused with high-flux Osmic multilayer mirror optics, and a curved image plate detector. The data were obtained from freshly prepared MOF samples that had been ground into slurry in a small amount of DEF and kept damp with DEF throughout the measurement. The two-dimensional images of the Debye rings were integrated with 2DP[161] to give 2θ vs I diffractograms. The predicted powder patterns of BMOF-1-bpdc, MUF20-Aβ, MUF20-Aγ, and MUF20-Aβ’ were generated from their single-crystal structures using Mercury v3.0.

4.4.8 Gas adsorption measurements

Low pressure adsorption isotherms were measured by a volumetric method using a Quantachrome Autosorb-iQ instrument. Freshly prepared MOF samples were washed with MeOH and then activated by repeated washing and subsequent soaking in CH_2Cl_2 for several hours. The samples were then transferred to a pre-dried and weighed analysis tube, still covered with CH_2Cl_2. Excess CH_2Cl_2 was removed with a Pasteur pipette and then the sample tube was heated at 1 ºC per minute to 30 ºC under vacuum then held under a dynamic vacuum at 10^{-6} Torr for 10 h. Accurate sample masses were calculated using degassed samples. All adsorption measurements used ultra-high purity gases.

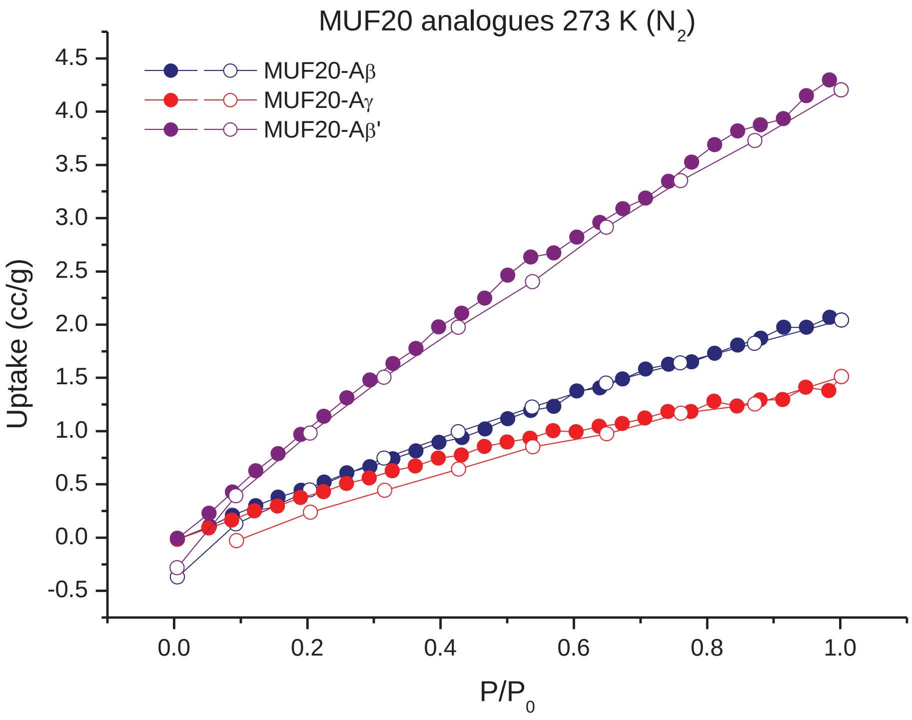

Figure 4.33 Gravimetric N_2 adsorption (filled) and desorption (open) isotherms measured at 273 K.

Chapter 5 - Thermolabile Protecting Groups in DUT-23

5.1 Introduction

As seen in Chapters 3 and 4, thermal stability is a key component to consider when determining MOFs to target for TPG incorporation. In addition, MOFs that are not prone to collapse when desolvated are desirable as the materials will need to survive extended periods without solvent in order to obtain the thermolysed product. Armed with this knowledge, the next material targeted was chosen for its physical and thermal stability, and our sights settled upon DUT-23[1] ($[M_2(btb)_{4/3}(bpy)]$, Figure 5.1). DUT-23, published in September of 2011 by the Kaskel group, was actually first published by the Hong group in July of 2011. It was dubbed FJI-1 by this group. Despite this, the material is most commonly referred to as DUT-23, most likely due to the field's knowledge of other members of the DUT family, such as DUTs 4-12.[202-207] It also may be due to the Kaskel group reporting the material made using Zn, Co, Cu, and Ni, whereas the Hong group only reported the synthesis of Zn-DUT-23. DUT-23 is comprises a net formed by btb (1,3,5-tris-(4-carboxyphenyl)benzene, Figure 5.2) and a metal (Zn/Co/Cu/Ni). The open metal sites of the M-btb paddlewheel SBUs are then bridged by bpy to generate an extended pto net. The pto network topology, whose name is derived from the material Pt_3O_4 (platinum (II,IV) oxide), is an example of a 3,4-connected network with a cubic space group.[208] The DUT-23 framework is interesting in that the bpy ligands are not required in a structural sense, the M-btb network can form without the bpy.

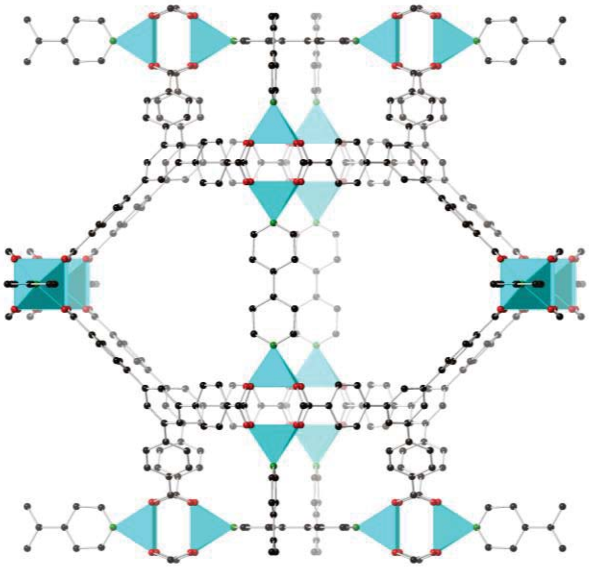

Figure 5.1 Structure of Zn-DUT-23 determined by SXRD data. Atom colours: C = black, N = green, O = red, and Zn = teal (hydrogen atoms and disorder of bpy omitted for clarity).[1]

However, the incorporation of bpy prevents the interpenetration of the M-btb structure. If it is not present then the interpenetrated MOF-14 is observed to form[197] (when M=Cu(II)). As the bpy does not play a vital structural role in the formation of DUT-23, and the fact that there is a large pore volume around the bpy ligand in the crystal structure, the material appeared to be a good candidate for the inclusion of TPG containing bpy ligands. These reasons, coupled with the stability of the material mentioned earlier, are why DUT-23 was chosen as the target MOF for the installation of TPGs. In this chapter is reported the installation of bpy-TBE into Zn-DUT-23 and Cu-DUT-23. As Chapter 4 reports the synthesis of bpy-TBE, the details of its synthesis will not be detailed in this chapter.

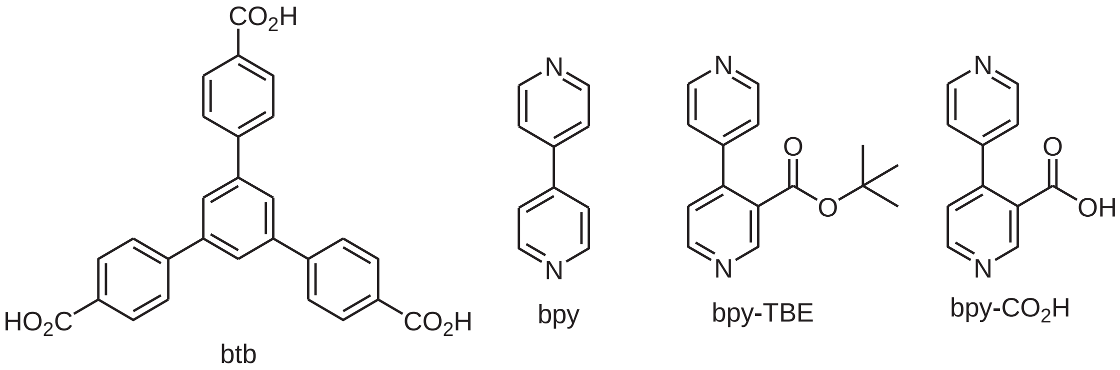

Figure 5.2 Ligands involved in the synthesis of DUT-23 and its analogues.

5.2 Results and discussion

The syntheses of Zn-DUT-23-TBE and Cu-DUT-23-TBE was achieved by combining btb, bpy and either $Zn(NO_3)_2.4H_2O$ or $Cu(NO_3)_2 \cdot 3H_2O$ in 0.74 mL of a DMF:EtOH:TFA solvent stock solution (5 mL: 5 mL: 2 drops), and then heating in a 75 °C oven for 18 hours (Figure 5.3). The above syntheses were based on the synthesis of Cu-DUT-23 reported by the Kaskel group, but with some alterations to improve reaction yields. Firstly, the ligands were dissolved separately from the metal salts as it was found that a large amount of precipitation of a competing phase occurred as soon as the solvent was added when using $Cu(NO_3)_2.3H_2O$. By dissolving the metal separately, it was possible to ensure all materials were fully in solution before combining prior to being placed in the oven. The ligand and metal feed ratios were altered from 0.27:0.25:1 bpy:btb:M reported by the Kaskel group, to 1:0.9:1 bpy-TBE:btb:M, as it was found that either a competing phase was also being obtained, or that DUT-23-TBE was being obatined with a reduced ratio of bpy-TBE to btb. The reduced ratio of a N-donor type ligand is not an uncommon issue, and was discussed in Chapter 4. In addition, the temperature of the oven was altered slightly from the 80 °C used by the Kaskel group to the 75 °C reported in this work. It was found that the TPGs better survived the synthesis at this temperature, and there was no apparent adverse effect on the materials obtained.

Zn-DUT-23-TBE was obtained as medium to large tan-coloured block-shaped crystals.

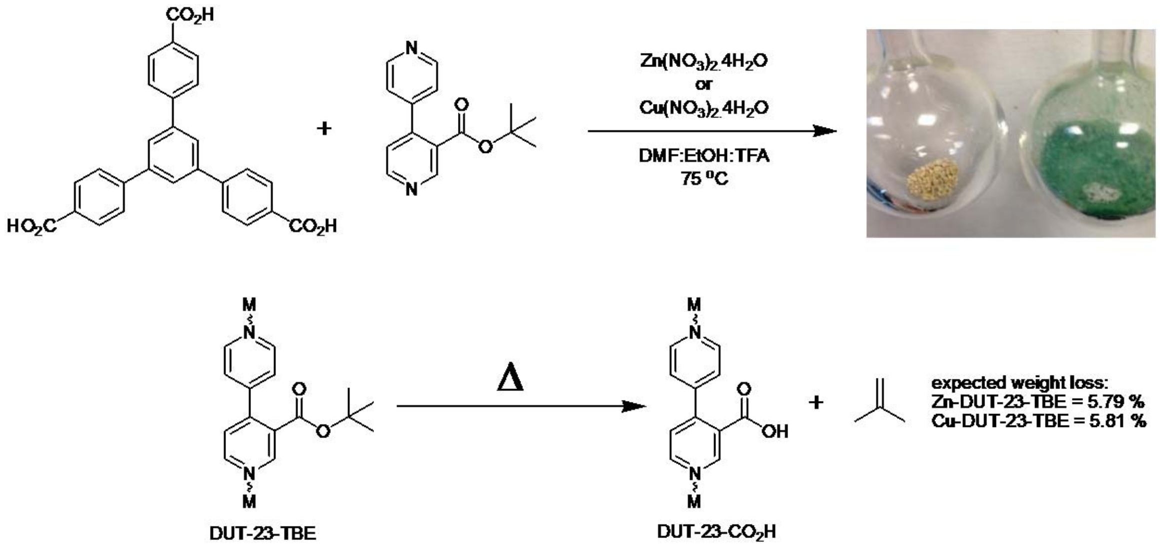

Figure 5.3 Top: general synthetic approach to DUT-23-TBE materials, showing desolvated Zn-DUT-23-TBE (left) and Cu-DUT-23-TBE (right). Bottom: General thermolysis of bpy-TBE in DUT-23-TBE, with expected weight losses of isobutylene.

These were ideal for SXRD data collection (*vide infra*). Cu-DUT-23-TBE, however, was only ever obtained as a teal powder, despite trialling numerous conditions (changing solvent, concentration, and/or temperature, using a modulator, etc.) to obtain large single crystals. ^{1}H-NMR spectroscopic analysis of the MOFs presented some challenges in confirming the identity of the materials. ^{1}H-NMR spectroscopic analysis of the digested Zn-DUT-23-TBE revealed a 1:1.6 ratio of bpy-TBE to btb (expected ratio was 1:1.33), indicating that there is a deficit of bpy-TBE in the structure, with nearly 17 % of the bpy-TBE sites vacant. This is not unexpected given that the bpy does not play a direct structural role in the lattice. Similar observations have been made by other members of our group.[192] Despite trying numerous conditions it was not possible to incorporate a higher level of bpy-TBE into the framework through direct synthesis. Soaking the material in a 1 M solution of bpy-TBE in MeOH or DCM was undertaken to determine if the uptake could be increased by post synthetic exchange (PSE) of the bpy-TBE with what is presumably bound solvent molecules. PSE is a common method for incorporating metals and ligands into MOFs when their incorporation is not possible or reduced when using direct synthesis methods.[28,29,209,210] Unfortunately, PSE was not able to noticeably improve the uptake of bpy-TBE into Zn-DUT-23-TBE. It is not possible to compare my findings with those of the Kaskel or Hong groups as neither reported any NMR spectra for their synthesised MOFs, nor did the Zou group who published a paper in 2012 on the same material, though they dubbed it SUMOF-1.[211] However, the literature elemental analysis values matched the calculated values reported by the Kaskel, Hong, and Zou groups.

Cu-DUT-23-TBE presented its own NMR spectroscopy challenge in that Cu^{2+} is paramagnetic and must be removed from the sample before a meaningful spectrum can be recorded. Numerous attempts were made to remove the Cu^{2+} from the samples including the use of a Sephadex cation exchange resin, precipitation by $NaHSO_3$, and precipitation by salicylaldoxime. The most effective route, however, was discovered by a fellow student Seok June Lee who was also working with copper MOFs. He found that dissolving his MOFs in KOH/D_2O and letting them stand overnight resulted in the formation of a black precipitate. By filtering off the precipitate he was left with a solution of his ligands that he was then able to analyse by NMR spectroscopy. Using this method, it was possible to obtain the spectra that clearly show the species present (Figure 5.5). These spectra also revealed an apparent excess of bpy-TBE, with a 1:0.45 ratio of bpy-TBE:bpdc, instead of the expected ratio of 1:1.33 bpy-TBE:btb. This is most likely an artefact of the sample preparation rather than the

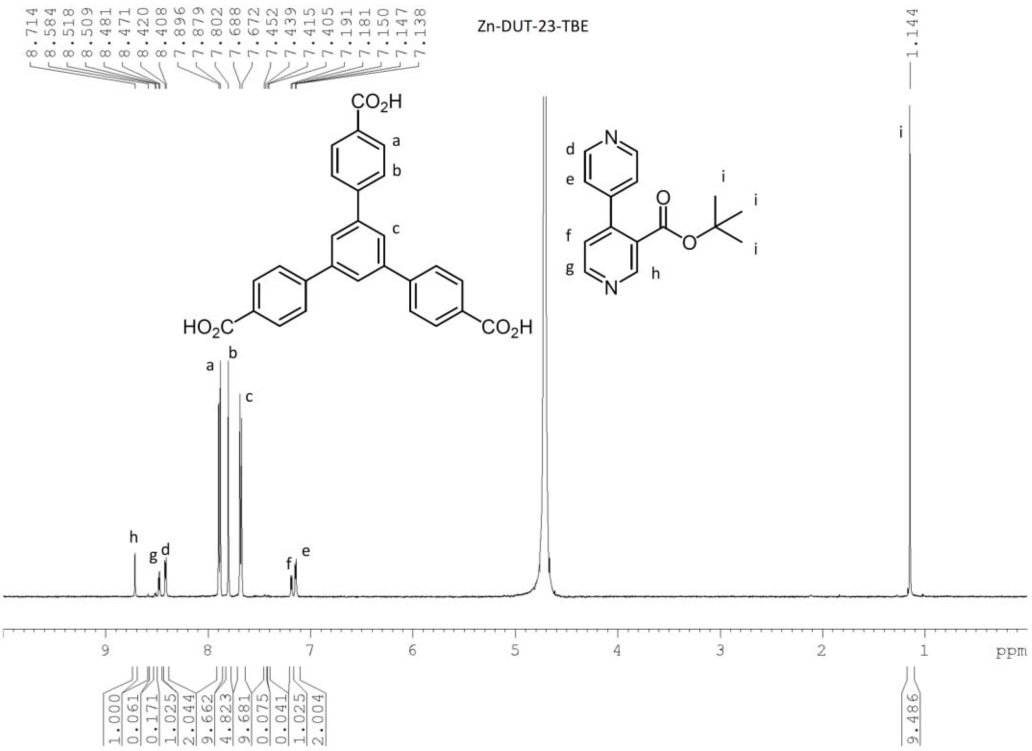

Figure 5.4 ^{1}H-NMR spectrum of Zn-DUT-23-TBE digested in D_2O/KOH.

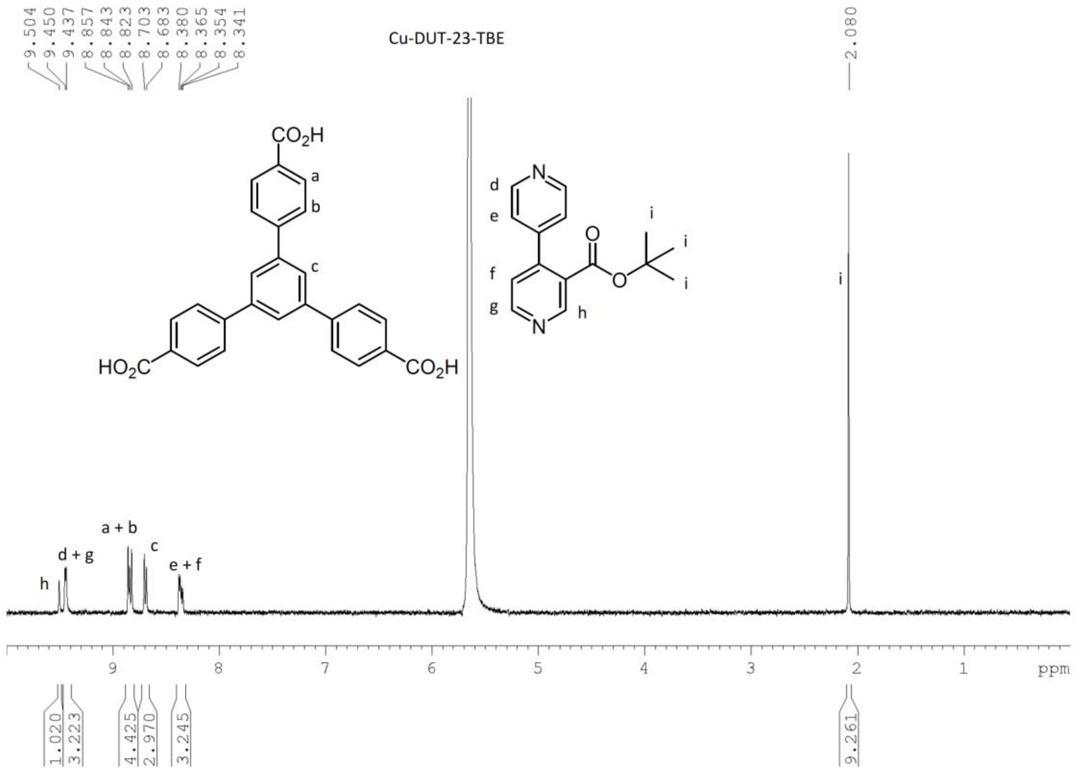

Figure 5.5 ^{1}H-NMR spectrum of digested Cu-DUT-23-TBE digested in D_2O/KOH.

presence of excess bpy-TBE in the framework as it is highly unlikely that Cu-DUT-23-TBE would have nearly three times the theoretical maximum incorporation of bpy-TBE when it was not possible to reduce the bpy-TBE deficit in Zn-DUT-23-TBE to less than 17 %. As such, these NMR were used in a qualitative manner, and other analytical techniques have been relied upon to confirm the nature of the Cu material (*vide infra*).

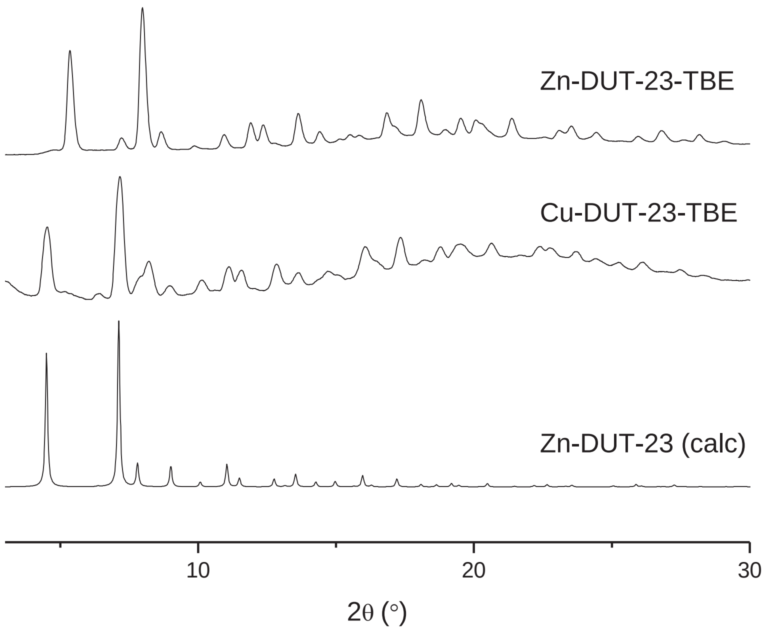

Figure 5.6 PXRD patterns of Zn-DUT-23-TBE (top), Cu-DUT-23-TBE (middle), and Zn-DUT-23 (bottom, calculated from literature cif file).

Unlike the ^{1}H-NMR spectroscopic analysis of these materials, the PXRD data for Zn-DUT-23-TBE and Cu-DUT-23-TBE offer little ambiguity that the materials are indeed DUT-23 analogues. As can be seen in Figure 5.6, the experimental PXRD patterns of the DUT-23-TBE species closely match the predicted PXRD patterns for the parent materials. The PXRD data also reveal no obvious additional crystalline species, indicating that the compounds have been synthesised phase pure. Furthermore, the elemental analysis of Cu-DUT-23-TBE revealed a close match to the predicted values, strongly indicating that the material synthesised was the target material.

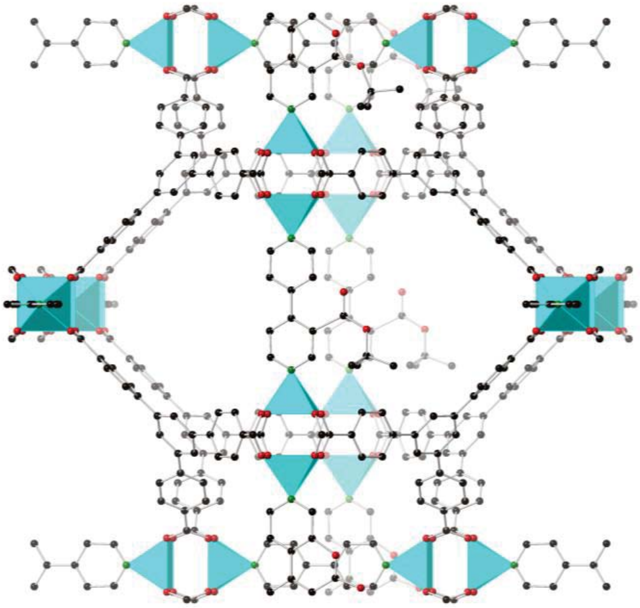

Figure 5.7 Structure determined by SXRD for Zn-DUT-23-TBE, shown without disorder. Atom colours: C = black, N = green, O = red, and Zn = teal (hydrogen atoms omitted for clarity).

As mentioned above, whilst it was not possible to synthesise a SXRD quality crystal for Cu-DUT-23-TBE, Zn-DUT-23-TBE offered excellent quality crystals. Zn-DUT-23-TBE is a cubic structure, and shares the same space group as the parent material Zn-DUT-23, *P*m-3n. As expected, Zn-DUT-23-TBE has a very similar asymmetric unit (ASU) to Zn-DUT-23 (Figure 5.8). Both parent and substituted frameworks ASUs only contain 1/3 of a btb ligand and ¼ of the bpy ligand, with the bpy ligand in both cases having 2-fold rotational disorder. The extended pto topology of these frameworks appears to be quite rare, though other extended pto frameworks such as DUT-6[203] do exist. Despite the high quality data (diffraction observed to a resolution of 0.81 Å), it was not possible to ascertain the coordinates of the TBE from the SXRD data which necessitated the modelling of the TBE groups. The high degree of symmetry in the ASU results in only ¼ of the bpy-TBE being present, resulting in positional disorder of the TBE across 4 atoms (much like the disorder

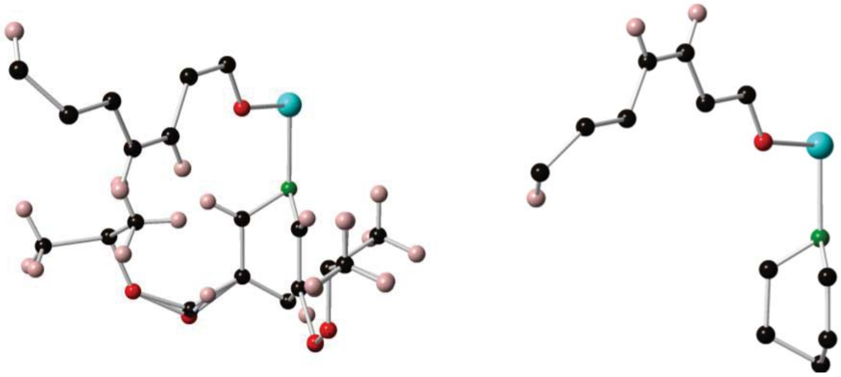

Figure 5.8 ASUs determined by SXRD for Zn-DUT-23-TBE (left) and Zn-DUT-23 (right). The pyridyl hydrogen atoms in Zn-DUT-23 were absent from the literature cif file. Atom colours: C = black, N = green, H = pink, O = red, and Zn = teal.

present in MOF-5-NHBoc and MOF-5-NHCOOEt in Chapter 2). In addition, there is significant additional disorder in the bpy-TBE in that it occupies two positions that differ by rotation around the Zn-N bonds. This disorder effectively positions the TBE group over eight different sites (Figure 5.7). This results in the six electrons of carbon atom attached to the pyridyl ring being averaged out to 0.75 electrons at each position, which decreases the corresponding peaks in the Fourier map. Compounding the issue is that the data were collected at room temperature, which means that the TBE group is unlikely to be frozen out and experiences dynamic disorder.

The direct syntheses of Zn-DUT-23-CO$_2$H and Cu-DUT-23-CO$_2$H using bpy-CO$_2$H as the ligand were also investigated. Numerous conditions were trialled, including altering reaction temperature, concentration, ligand ratio, and varying the solvent systems used. Despite this, it was not possible to obtain either Zn-DUT-23-CO$_2$H or Cu-DUT-23-CO$_2$H by direct synthesis.

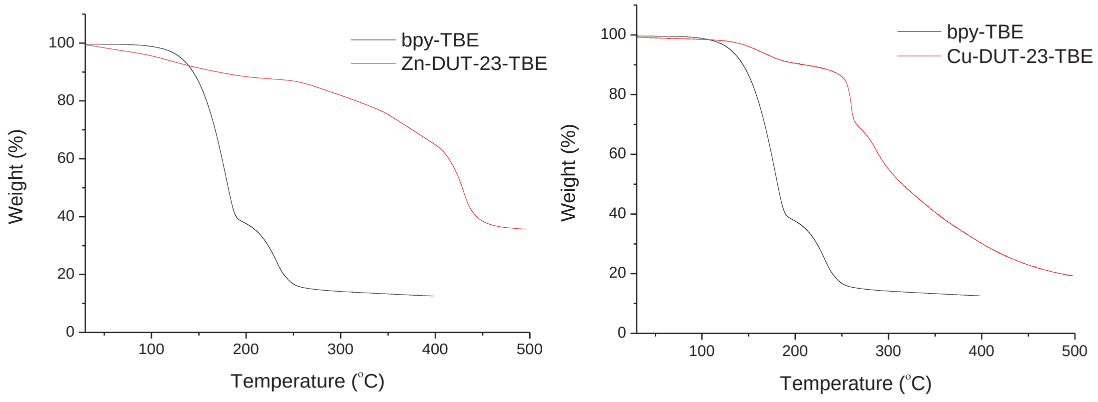

Figure 5.9 TGA trace of Zn-DUT-23-TBE (left) and Cu-DUT-23-TBE (right). Bpy-TBE trace included for comparison.

After determining that the target materials had been synthesised, albeit with bpy-TBE defects, the thermolysis of the materials was investigated to determine the optimal conditions for thermal deprotection. TGA of Zn-DUT-23-TBE revealed an initial continuous weight loss until approximately 250 °C (Figure 5.9). ^{1}H-NMR spectroscopic analysis after this point revealed the complete conversion of bpy-TBE to bpy-CO_2H in the material. This means that the weight loss is most likely to be the result of the combination of solvent loss and evolution of isobutylene from the sample. However, the sample was prepared as for gas sorption, except for the use of a benchtop vacuum pump for 2 hours as opposed to activated on the activation port. ^{1}H-NMR of the material prior to TGA revealed no protonated solvent present other than H_2O which was present in all D_2O NMR samples conducted (Figure 5.4). This indicates that the solvent most likely to be present is H_2O as its presence can be masked by the large H_2O peak intrinsic to the NMR solvents used. This H_2O is most likely coordinated to the open metal sites of the zinc(II) ions present at the defect sites within the MOF. This is supported by the absence of this solvent behaviour in Cu-DUT-23-TBE (Figure 5.9). The TGA trace of Cu-DUT-23-TBE shows an initial weight loss of approximately 6% starting at around 130 °C. This compares favourably with the expected 5.8% weight loss for a defect-free Cu-DUT-23-TBE. ^{1}H-NMR spectroscopic analysis of the material after this weight loss revealed no bpy-TBE remaining, with only bpy-CO_2H and btb observed in the spectrum.

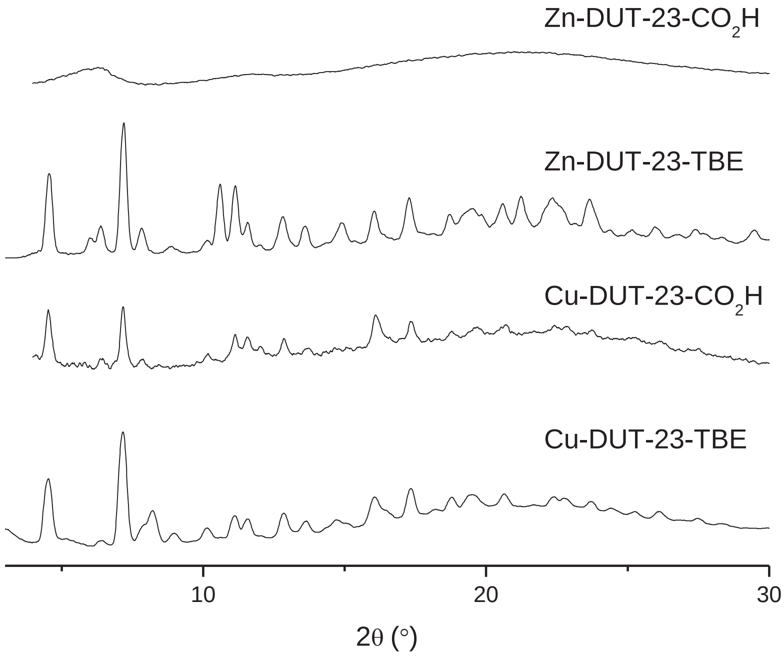

Figure 5.10 PXRD patterns for Zn-DUT-23-TBE and Cu-DUT-23-TBE pre- and post-thermolysis.

Thermolysis conditions trialled on the activation port of the gas sorption instrument until the conditions were found that resulted in complete thermal deprotection whilst retaining maximum crystallinity. The optimal thermolysis conditions were found to be 160 °C for 12 hours under vacuum. This resulted in complete deprotection in Zn-DUT-23-TBE and near-complete deprotection in Cu-DUT-23-TBE with <2 % TBE remaining intact. Unfortunately, as seen in Figure 5.10, there was complete loss of crystallinity in Zn-DUT-23-TBE following thermolysis. However, Cu-DUT-23-TBE retained much of its crystallinity. The disparity between the Zn and Cu materials was not unexpected, as it is known that Cu MOFs are often more stable than their Zn analogues.[212]

Zn-DUT-23-TBE and Cu-DUT-23-TBE were activated prior to gas sorption analysis. This was achieved by using supercritical CO_2, akin to the lon-e species in Chapter 3. In this instance EtOH was used rather than acetonitrile as this was the method used by the Kaskel group.[1] The activated materials were transferred to the gas sorption instrument, taking care to limit the exposure to air, and gas adsorption isotherms were measured (Figure 5.11 to Figure 5.18 and Figure 5.21 to Figure 5.24). The samples were then thermolysed on the activation port of the instrument before being returned to the analysis port for measurements on the deprotected frameworks. N_2 adsorption at 77 K for these materials showed Cu-DUT-23-TBE has the highest uptake with a plateau around 500 cc/g, compared with the approximately 160 cc/g uptake of Zn-DUT-23-TBE. Both of the thermolysed samples performed worse than their protected counterparts, with the uptake of Cu-DUT-23-CO_2H plateauing around 200 cc/g and Zn-DUT-23-CO_2H having a maximum uptake of around 20 cc/g. The sharp uptakes by the Cu species after a partial pressure of 0.8 are characteristic of inter-particulate adsorption common in samples that comprise sub-micron sized particles. It should be noted that it was not possible to conduct our normal 115 data point isotherm on the protected materials as the samples took an impractically long time to collect even a single data point. This meant that it was necessary to alter the method to a 20 data point isotherm in order to collect a data set in a practical amount of time. These isotherms were used to calculate the BET surface areas of the materials (Figure 5.11 and Figure 5.12), with Cu-DUT-23-TBE having the highest surface area at 1917 m^2/g. This is significantly lower than the surface area for Cu-DUT-23 reported by Kaskel's group to be 4730 m^2/g.[1] Whilst the drop in surface area can be attributed to the occlusion of void space by the TBE group, this is unlikely as the positioning of the TBE within the MOF pore would make it near impossible for the TBE group to block access to any significant portion of the pores. In addition, the TBE group has no apparent effect on the migration of solvent molecules through the framework as Figure 5.4 and Figure 5.5 clearly show the complete lack of solvent present,

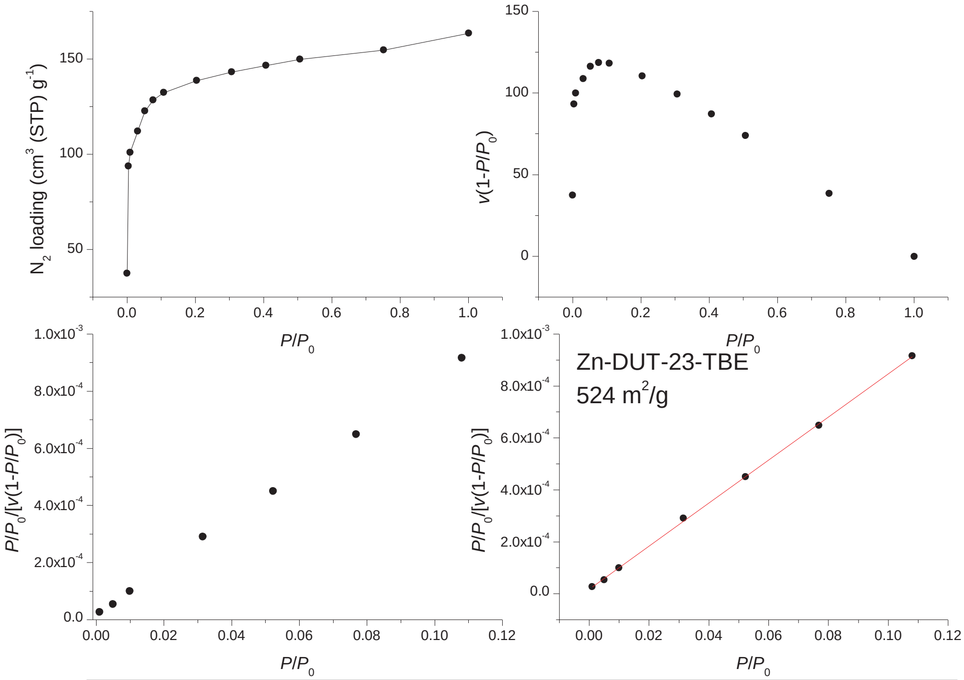

Equation	y = a + b*x	Pearson's r	0.99985			Value	Std Error
Weight	No Weighting	Adj. R-Squar	0.99964	P/P0/[v(1-	Intercept	1.78187E-5	3.55244E-6
Residual Sum of Squares	2.03211E-10			P/P0/[v(1- P/P0)]	Slope	0.00829	6.41987E-5

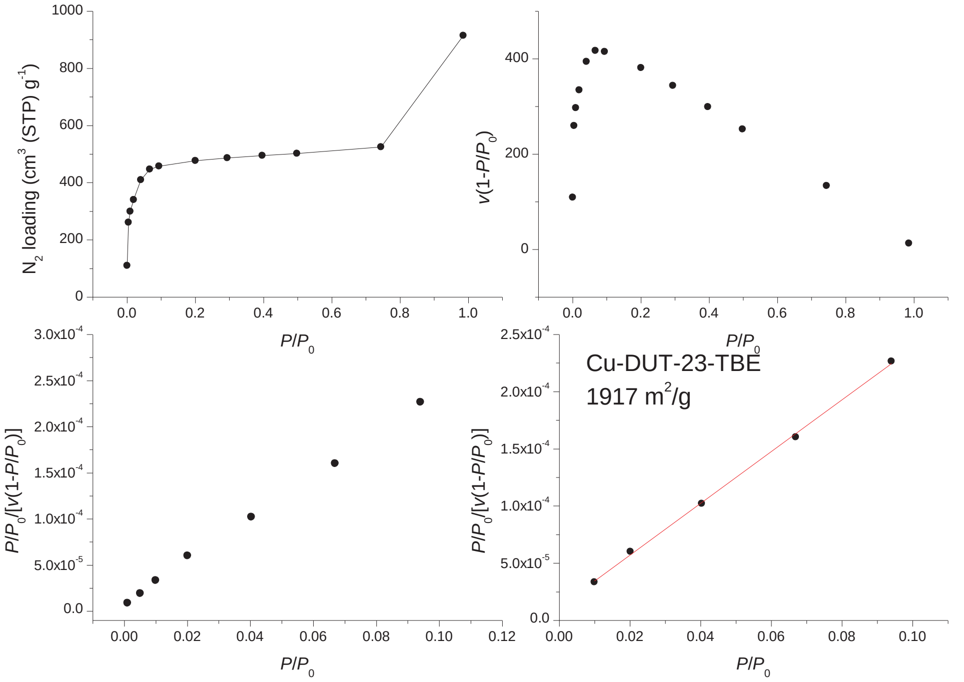

Equation	y = a + b*x	Pearson's r	0.99956			Value	Std Error
Weight	No Weighting	Adj. R-Squar	0.99882	P/P0/[v(1-	Intercept	1.18966E-	2.16373E-6
Residual Sum of Squares	2.15942E-11			P/P0/[v(1- P/P0)]	Slope	0.00226	3.89395E-5

Figure 5.11 N_2 adsorption isotherm at 77 K and BET surface area plots for Zn-DUT-23-TBE (top) and Cu-DUT-23-TBE (bottom) synthesized in DMF:EtOH:TFA (5mL:5mL:2drops).

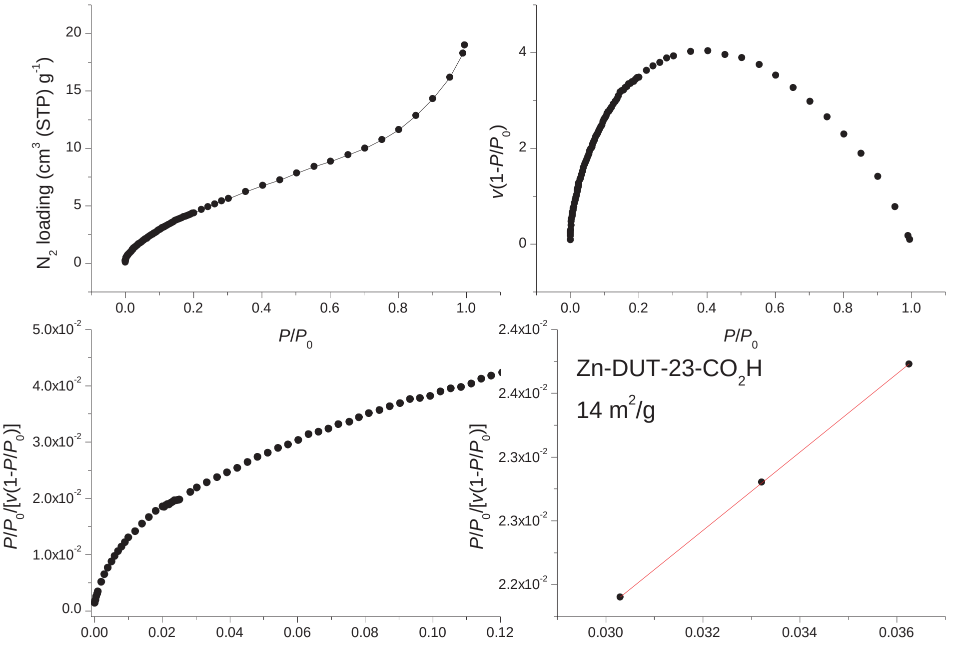

Equation	y = a + b*x	Pearson's r	0.99998			Value	Std Error
Weight	No Weighting	Adj. R-Square	0.99993	P/P0/[v(1-P	Intercept	0.0126	6.00613E-5
Residual Sum of Squares	5.74688E-11			P/P0/[v(1-P /P0)]	Slope	0.30704	0.0018

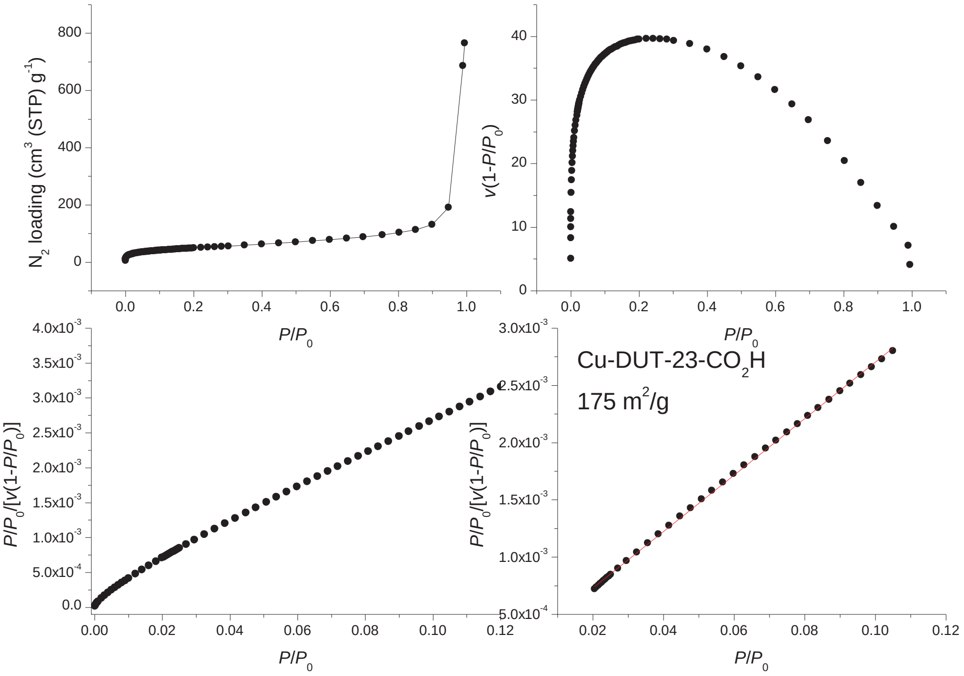

Equation	y = a + b*x	Pearson's r	0.99981			Value	Std Error
Weight	No Weighting	Adj. R-Square	0.99962	P/P0/[v(1-	Intercept	2.36905E-4	4.90049E-6
Residual Sum of Squares	6.45285E-9			P/P0/[v(1-P/P0)]	Slope	0.02467	8.05405E-5

Figure 5.12 N_2 adsorption isotherm at 77 K and BET surface area plots for Zn-DUT-23-CO_2H (top) and Cu-DUT-23-CO_2H (bottom) synthesized in DMF:EtOH:TFA (5mL:5mL:2drops).

and since N_2 is significantly smaller than DMF and EtOH it is reasonable to assume that N_2 would be similarly unaffected. The two most likely potential causes of these decreases in uptake are collapse of the framework and the presence of a non-porous secondary phase. It is hypothesized that pore collapse is the most likely cause since the decrease in BET surface areas is so large (Cu-DUT-23-TBE has 41 % of Cu-DUT-23's surface area, and Zn-DUT-23-TBE has 12 % of Zn-DUT-23's surface area) that it would require the majority of the material to be non-porous. It is highly unlikely that the presence of a predominant second phase would go unnoticed through ^{1}H-NMR spectroscopy, optical microscopy, and PXRD analyses. Thus the lack of porosity is derived from framework collapse rather than a secondary phase. This is further supported by the knowledge that Cu-DUT-23-TBE is significantly more resistant to structural damage occurring during thermolysis than Zn-DUT-23-TBE, and Cu-DUT-23-TBE has significantly greater N_2 uptake than Zn-DUT-23-TBE, indicating greater collapse has occurred in the Zn species. This is supported by the 2014 review by the Bosch, Zhang, and Zhou, where it is noted that Zn paddlewheel metal clusters with open axial metal sites are prone to collapse upon desolvation, whereas their Cu counterparts proved more resistant.[212]

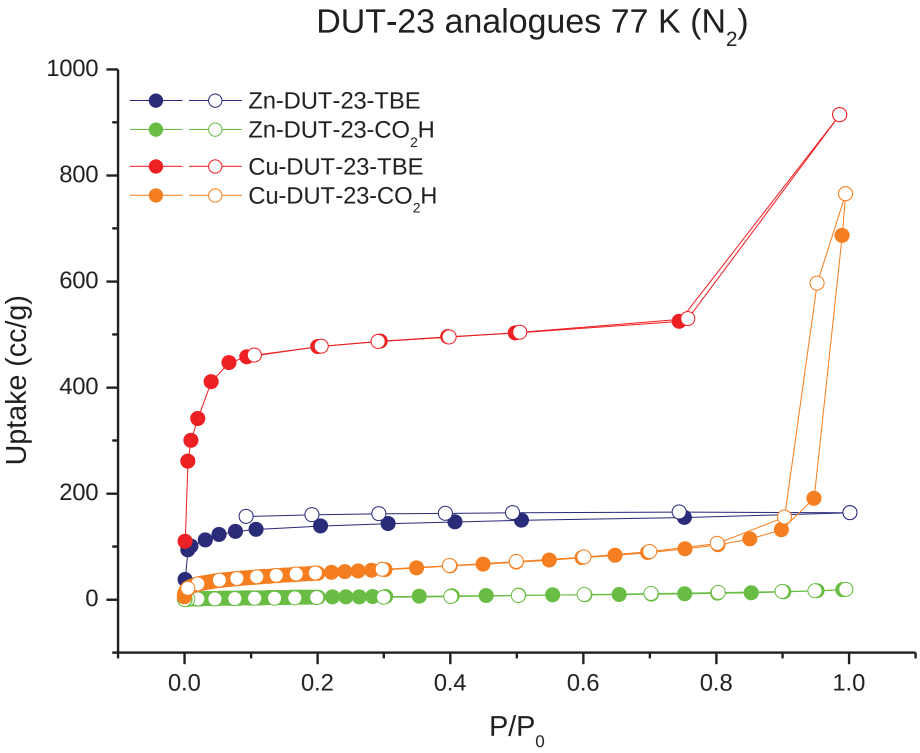

Figure 5.13 Gravimetric N_2 adsorption (filled) and desorption (open) isotherms measured at 77 K.

H_2 uptakes of the materials at 77 K are reasonable, with maximum uptakes at 1 atm of ~ 50 cc/g for Zn-DUT-23-TBE, ~ 100 cc/g for Cu-DUT-23-TBE, ~20 cc/g for Zn-DUT-23-CO_2H, and ~ 40 cc/g for Cu-DUT-23-CO_2H. These uptakes are significantly lower than the uptakes reported by the Kaskel group of ~150 cc/g for Zn-DUT-23 and ~180 cc/g for Cu-DUT-23 (calculated from gravimetric uptakes reported), which was expected after the decreased N_2 uptakes seen above.

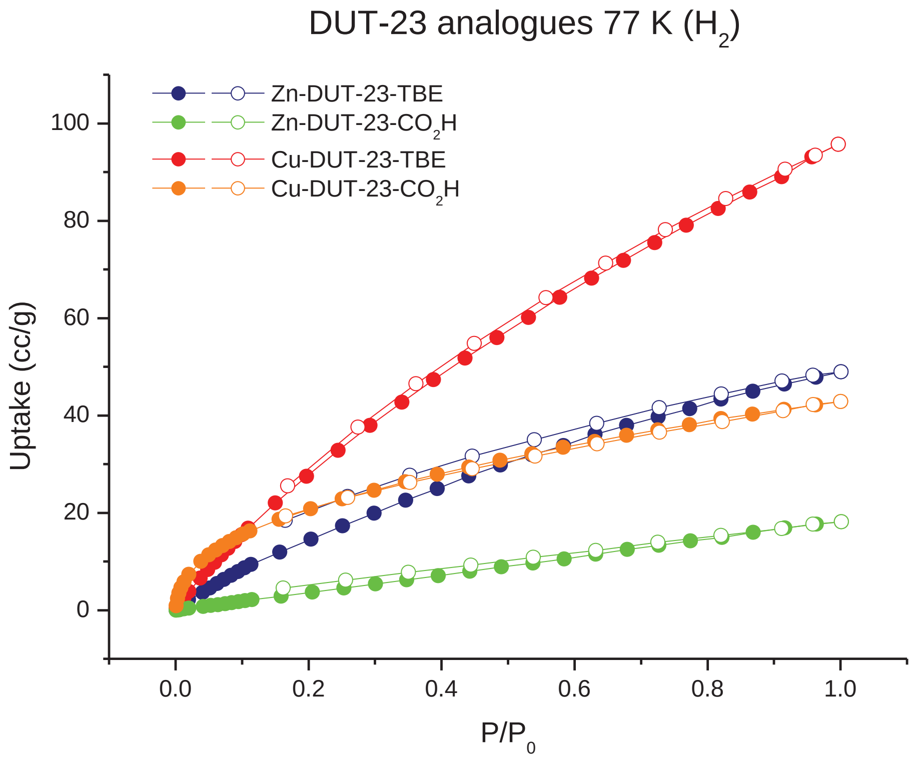

Figure 5.14 Gravimetric H_2 adsorption (filled) and desorption (open) isotherms

N_2 uptakes at 195 K reveal that Cu-DUT-23-TBE has the highest uptake of ~17 cc/g (Figure 5.21). Unfortunately, the literature sources do not report any N_2 uptakes above 77 K for other DUT-23-type MOFs, so no comparisons to the literature materials can be made. The uptake of CO_2 at 195 K by Cu-DUT-23-TBE was ~ 410 cc/g, and Cu-DUT-23-CO_2H had an uptake of ~ 60 cc/g (Figure 5.15). Though the uptake of CO_2 by Cu-DUT-23-TBE is reasonably high, it is only about 1/3 that of MOF-177, one of the best CO_2 adsorbing MOFs.[213] Interestingly, neither of the Zn frameworks (protected and deprotected) collected a single data point for CO_2 at 195 K, despite allowing the runs to continue after the Cu species had finished their collections. This points to extremely slow adsorption kinetics under these conditions. It is possible that the equilibration time was insufficient to allow the CO_2 to properly infiltrate the materials at this temperature, though due to time pressures on the apparatus this issue was not addressed in this work. As no CO_2 uptakes for Zn-DUT-23 or Cu-DUT-23 were reported in the literature no comparisons can be made to the literature materials. However, literature data for CO_2 adsorption at 195 K for IRMOF-3 and MOF-

177, though having markedly higher uptakes than Cu-DUT-23-TBE, share similar isotherm patterns with low initial uptake and then dramatic uptake after around 0.2 atm.[213]

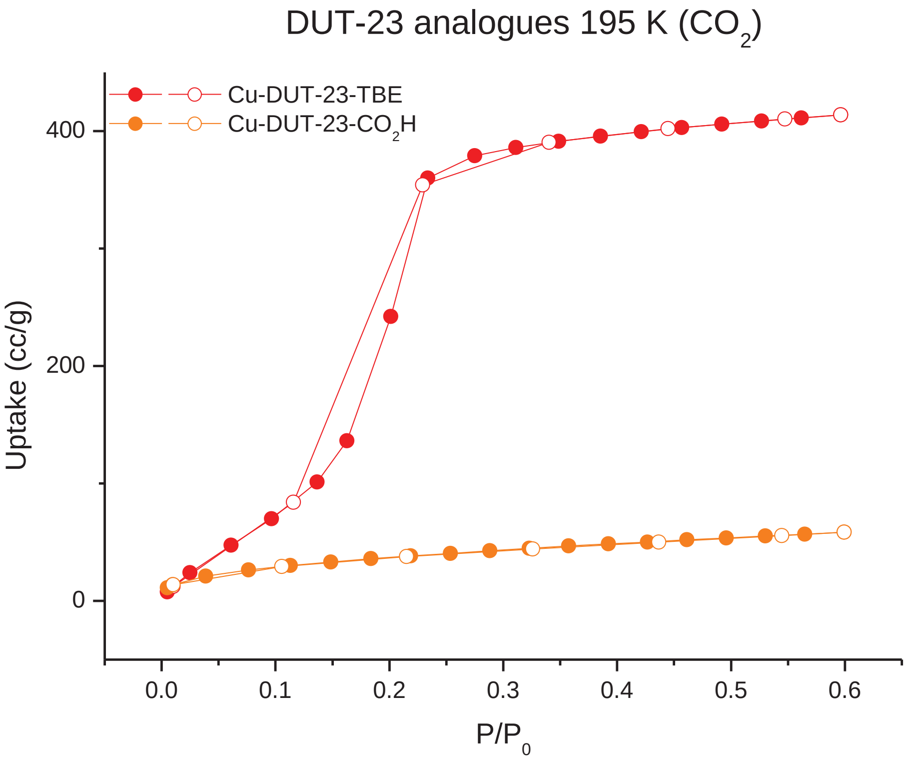

Figure 5.15 Gravimetric CO_2 adsorption (filled) and desorption (open) isotherms measured at 195 K.

At 273 K, the N_2 uptakes of the materials reveal that again Cu-DUT-23-TBE has the highest uptake with only ~3 cc/g uptake, and neither thermolysed species having any appreciable uptake of N_2 at this temperature (Figure 5.22). The CH_4 uptakes at 273 K are slightly higher than the N_2 uptakes, as expected due to the large size of CH_4. Maximum uptakes at 1 atm of ~6 cc/g for Zn-DUT-23-TBE, ~ 8 cc/g for Cu-DUT-23-TBE, ~ 2.5 cc/g for Zn-DUT-23-CO_2H, and ~ 3 cc/g for Cu-DUT-23-CO_2H (Figure 5.17) are observed. Since no low pressure CH_4 uptakes have been reported in the literature for DUT-23 MOFs, no comparisons with the literature materials can be made. Interestingly, the uptakes of CO_2 at 273 K show that Zn-DUT-23-TBE has the highest uptake with ~33 cc/g, whereas Cu-DUT-23-TBE has only ~ 28 cc/g at 1 atm. Whilst both thermolysed materials have maximum uptakes of ~14 cc/g, it should be noted that it is believed that Zn-DUT-23-CO_2H has suffered significantly greater pore collapse than Cu-DUT-23-CO_2H and this result indicates that, were the degree of collapse the same in both samples, Zn-DUT-23-CO_2H would have greater uptake. A greater degree of open metal sites caused by bpy-TBE deficits is the most likely cause for the improved CO_2 uptake in the Zn species, as open metal sites are known to improve uptake of CO_2 into MOFs.[214,215] However, due to the paramagnetic nature of Cu

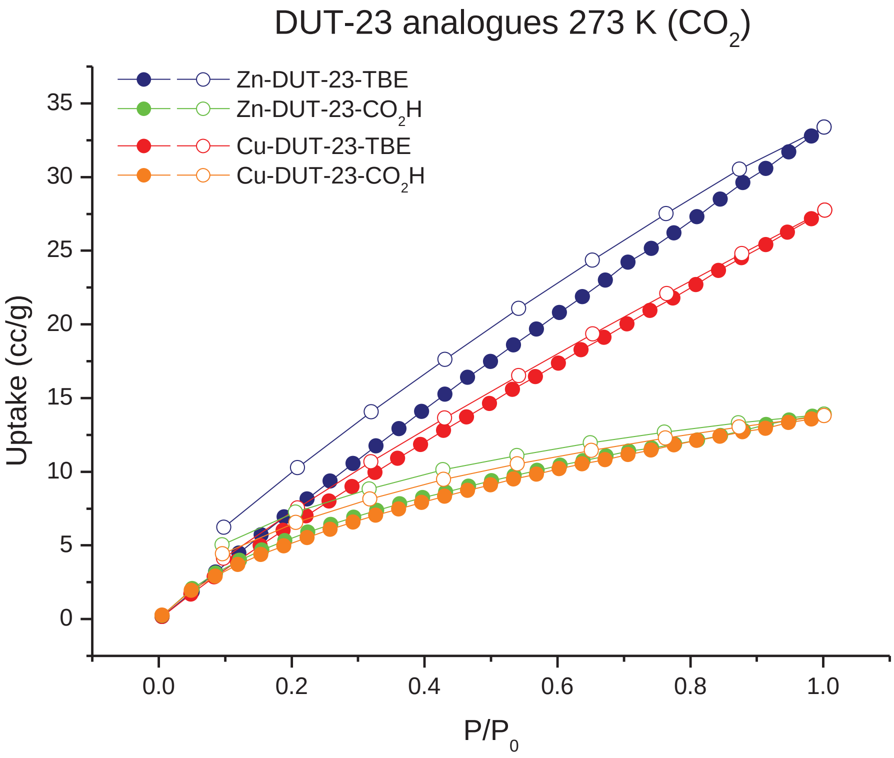

Figure 5.16 Gravimetric CO_2 adsorption (filled) and desorption (open) isotherms measured at 273 K.

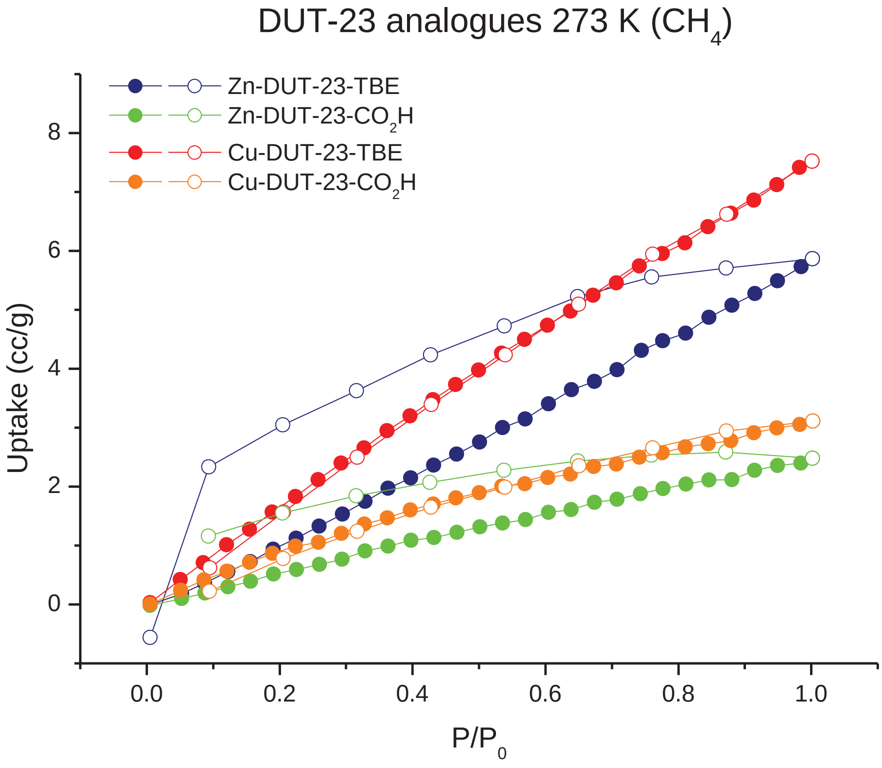

Figure 5.17 Gravimetric CH_4 adsorption (filled) and desorption (open) isotherms measured at 273 K.

as well as the propensity of the species to form powders, it has not been possible to determine if this is the case. Future work to determine the coordination environment of the metals in these materials may include techniques such as X-ray absorption near edge structure (XANES) spectroscopy, a technique that measures the absorption of soft X-rays.[216] Whilst requiring a synchrotron X-ray source, this method is beneficial in that it can be performed on powder samples such as Cu-DUT-23-TBE.

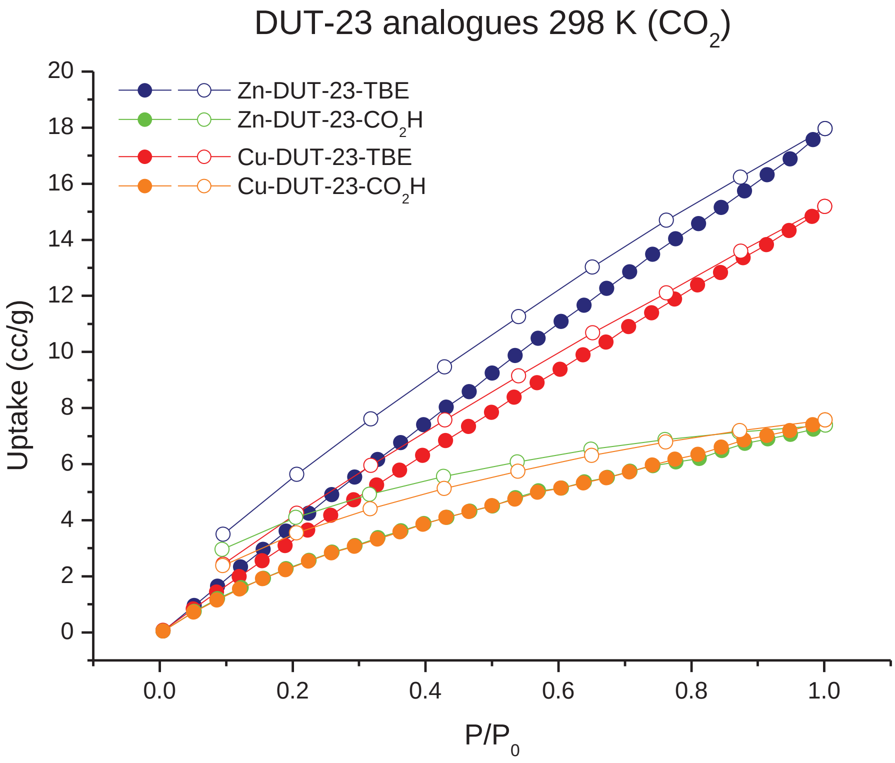

Figure 5.18 Gravimetric CO_2 adsorption (filled) and desorption (open) isotherms measured at 298 K.

At 298 K, only Cu-DUT-23-TBE had any appreciable N_2 uptake, with a maximum uptake of ~1.7 cc/g at 1 atm (Figure 5.23). CH_4 uptakes at 298 K were also very low, though higher than the N_2 uptakes, as expected due to the higher polarity of CO_2. Zn-DUT-23-TBE and Cu-DUT-23-TBE exhibit maximum uptakes at 1 atm of ~3.6 and ~4.4 cc/g, respectively (Figure 5.24). Neither of the thermolysed species had any appreciable uptake of CH_4 at 298 K. Uptakes for CO_2 retained the trends seen at 273 K, with Zn-DUT-23-TBE having the highest uptake of ~ 18 cc/g at 1 atm, followed by Cu-DUT-23-TBE with a maximum uptake at 1 atm of ~ 15 cc/g, and then the thermolysed species with maximum uptakes at 1 atm of ~ 7.5 cc/g each (Figure 5.18).

The gas sorption results show that in all cases, thermolysis of the materials resulted in decreased uptakes for all gas and temperatures, which was expected given the loss of crystallinity observed in the PXRD data above (Figure 5.10). What was unexpected after the relatively poor uptake of N_2 at 77 k for Zn-DUT-23-TBE and the lack of data collection for CO_2 at 195 K for the Zn species, was that the Zn samples had higher uptakes CO_2 uptakes than the Cu species at 273 K and 298 K. Unfortunately, these uptakes are still relatively low, but it would be very interesting to see how these may improve once the issues around the low N_2 uptakes at 77 K with respect to the literature materials are resolved.

5.3 Conclusion

In conclusion, it is possible to install bpy-TBE into Zn-DUT-23 and Cu-DUT-23 to give Zn-DUT-23-TBE and Cu-DUT-23-TBE. It was subsequently possible to thermally deprotect the materials to give Zn-DUT-23-CO_2H and Cu-DUT-23-CO_2H, materials that were not able to be directly synthesised using bpy-CO_2H. Unfortunately, the gas uptakes of these materials were lower than expected compared to the literature values. This has been attributed to pore collapse, with the Cu species being more resistant to the collapse than the Zn species, whilst the Zn species demonstrated higher uptakes of CO_2 than their Cu analogues. Further work is needed to clarify if pore collapse is indeed the cause of the reduced gas uptakes and how to prevent this from occurring.

5.4 Experimental section

5.4.1 General procedures

All starting compounds and solvents were used as received from commercial sources without further purification unless otherwise noted. NMR spectra were recorded at room temperature on a Bruker-500 Avance instrument, with the use of the solvent proton as an internal standard. Elemental analyses were performed by the Campbell Microanalytical Laboratory at the University of Otago, New Zealand. Care was taken to limit the exposure of all MOFs to the atmosphere.

5.4.2 Ligand Synthesis

5.4.2a bpy-TBE

bpy-TBE was synthesized according to the following route with detail procedures and characterization data of its intermediates available in Chapter 4.

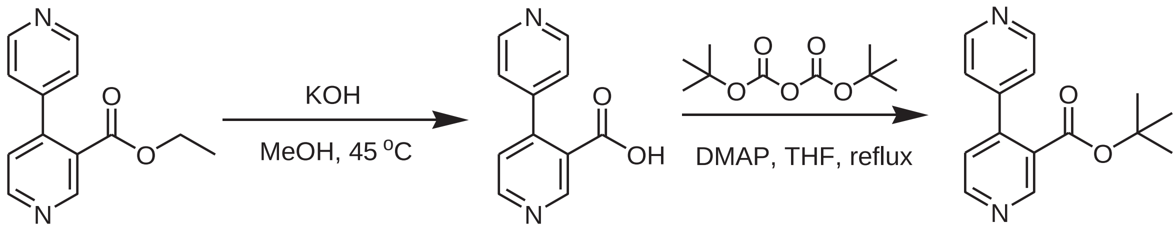

5.4.3 MOF synthesis and characterization

5.4.3a Zn-DUT-23-TBE

In a 4 mL scintillation vial, bpy-TBE (10 mg, 0.039 mmol) and btb (15.4 mg, 0.035 mmol) were dissolved in 0.37 mL of the solvent system with sonication (DMF:EtOH:TFA, 5 mL: 5 mL: 2 drops, anhydrous). $Zn(NO_3)_2{\cdot}4H_2O$ (10.2 mg, 0.039 mmol) was dissolved in 0.37 mL of the solvent system with sonication (DMF:EtOH:TFA, 5 mL: 5 mL: 2 drops). The metal containing solution was then added to the ligand solution, the vial sealed, Teflon tape applied to the join of the lid, and the reaction placed in the oven at 75 °C. After 18 hours, the tan-coloured block shaped crystals were removed from the oven, washed with fresh reaction solvent, washed with dry MeOH three times, and then stored in dry MeOH. Yield: 4.2 mg. Anal. calcd. for [$C_{51}H_{36}N_2O_{10}Zn_2$] with 17 % bpy-TBE deficiency: C, 62.87; H, 3.59; N, 2.41 Found: C, 64.21; H, 3.69; N, 2.73. To scale up the synthesis, a parallel synthetic method was adopted (multiple vials using the scale described above) as scale up markedly decreased the yield.

5.4.3b Cu-DUT-23-TBE

In a 4 mL scintillation vial, bpy-TBE (10 mg, 0.039 mmol) and btb (15.4 mg, 0.035 mmol) were dissolved in 0.37 mL of the solvent system with sonication (DMF:EtOH:TFA, 5 mL: 5 mL: 2 drops, anhydrous). $Cu(NO_3)_2{\cdot}3H_2O$ (9.4 mg, 0.039 mmol) was dissolved in 0.37 mL of the solvent system with sonication (DMF:EtOH:TFA, 5 mL: 5 mL: 2 drops). The metal containing solution was then added to the ligand solution, the vial sealed, Teflon tape applied to the join of the lid, and the reaction placed in the oven at 75 °C. After 18 hours, the teal powder crystals were removed from the oven, washed with fresh reaction solvent, washed with dry MeOH three times, and then stored in dry MeOH. Centrifugation was used to separate the powder from the solvent during the various wash steps. Yield: 7.3 mg. Anal. calcd. for [$C_{51}H_{36}N_2O_{10}Cu_2$]: C, 63.30; H, 3.75; N, 2.90 Found: C, 63.54; H, 3.89; N, 2.87. To scale up the synthesis, a parallel synthetic method was adopted (multiple vials using the scale described above) as scale up markedly decreased the yield.

5.4.4 ^{1}H NMR analysis of digested MOF samples

For ^{1}H NMR spectroscopy, the samples were prepared as for gas sorption. The crystals were then digested using 600 µL of 1 M KOH/D_2O solution. Spectra for the Zn samples were obtained immediately after dissolution. Cu samples were left to stand overnight and the black precipitate that formed filtered off the following morning, after which spectra were immediately obtained.

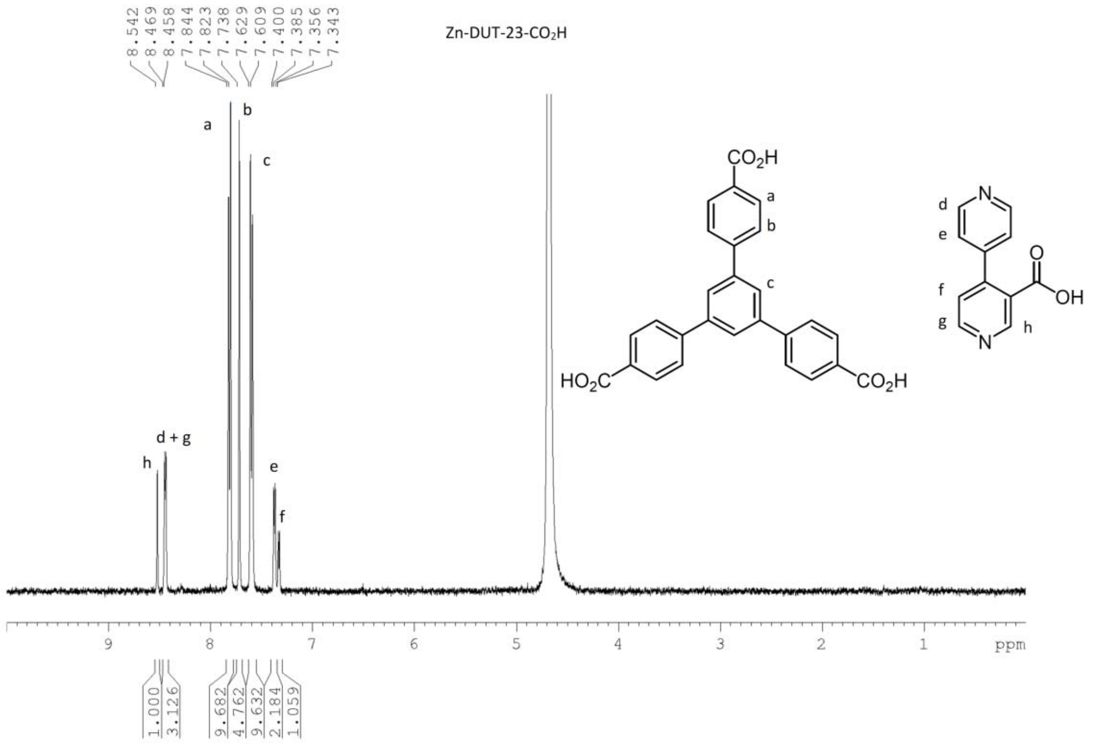

Figure 5.19 ^{1}H-NMR spectroscopic analysis of digested Zn-DUT-23-CO_2H in DMSO-d_6/DCl.

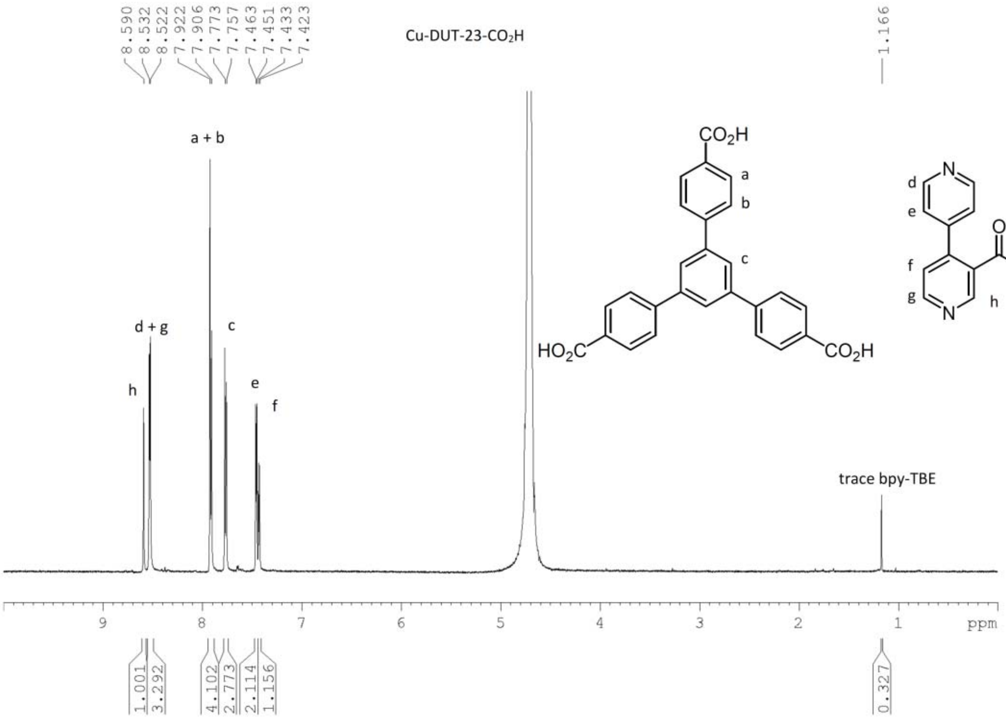

Figure 5.20 ^{1}H-NMR spectroscopic analysis of digested Cu-DUT-23-CO_2H in DMSO-d_6/DCl.

5.4.5 Thermogravimetric Analysis (TGA)

Thermogravimetric analyses were performed on a TA Instruments Q50 instrument. Freshly prepared MOF samples were prepared as for gas sorption (see section 5.4.8). Samples were then transferred to an aluminium sample pan and then measurements were commenced under an N_2 flow with a heating rate of 5 °C /min.

5.4.6 Single crystal X-ray diffraction

MOF crystals were mounted together with some dry DEF in a polymer sleeve on a Rigaku Spider diffractometer equipped with a MicroMax MM007 rotating anode generator (Cu_α radiation, 1.54180 Å), high-flux Osmic multilayer mirror optics, and a curved image-plate detector. Data were collected at 293 K and were integrated, scaled, and averaged with FS Process.[158] XPREP[159] was used to determine the space group and the structures were solved using SHELXS[159] and refined with SHELXL.[159]

All atoms were found in the electron density difference map, except for the side chains, which were subsequently modelled using Discovery Studio.[160] The atom positions were added to the model in representative positions and held fixed during refinement. Bpy-TBE was modelled as having 83% occupancy due to defects. All non-hydrogen, non-side chain atoms were refined anisotropically. Cif files for MOFs uploaded to http://tinyurl.com/sblackwoodMOFs.

Table 5.1 Crystallography data of Zn-DUT-23-TBE

MOF	**Zn-DUT-23-TBE**
Formula	$C_{48.4}H_{33.8}N1.7O_{9.7}Zn_{2}$
Formula weight	924.50
Crystal size (mm)	0.30 x 0.28 x 0.25
Temperature (K)	293
Wavelength (Å)	1.54187
Crystal system	Cubic
Space group	*P*m-3n
Unit cell length (Å)	27.7189(3)
Unit cell angles (°)	90.0
Unit cell volume (Å^3)	21297.5(7)
Z	6
D_{calc} (g cm^{-3})	0.432
μ (mm^{-1})	0.57
F(000)	2840
Reflns coll./unique, R_{int}	78338 / 3723, 0.0567
Data range	8.0 Å > d > 0.81 Å
Index ranges	$-30 \leq h \leq 29$, $-33 \leq k \leq 18$, $-23 \leq l \leq 33$
Completeness	99.8 %
T_{min}, T_{max}	0.682, 1.00
R indices for data with $I > 2\sigma(I)$	$R_1 = 0.0966$; $wR_2 = 0.3452$
R indices for all data	$R_1 = 0.1054$; $wR_2 = 0.3452$
Largest difference peak and hole (e Å^{-3})	0.63/-0.73

5.4.7 Powder X-ray diffraction patterns

All powder X-ray diffraction experiments were carried out on a Rigaku Spider X-ray diffractometer with Cu K_α radiation (Rigaku MM007 microfocus rotating-anode generator), monochromated and focused with high-flux Osmic multilayer mirror optics, and a curved image plate detector. The data were obtained from freshly prepared MOF samples that had been ground into slurry in a small amount of DEF and kept damp with DEF throughout the measurement. The two-dimensional images of the Debye rings were integrated with 2DP[161] (Version 1.0.3.4) to give 2θ vs I diffractograms.

5.4.8 Gas adsorption measurements

Low pressure adsorption isotherms were measured by a volumetric method using a Quantachrome Autosorb-iQ instrument. Freshly prepared MOF samples were washed with acetone multiple times prior to soaking in fresh acetone for several hours. The samples were then transferred to cellulose thimbles for supercritical CO_2 activation, ensuring a covering of acetone over the samples was maintained. The samples were then placed into a Tousimis Samdri-PVT-3D critical point dryer, the solvent exchanged with supercritical CO_2 and allowed to soak in supercritical CO_2 for 1 hour. This process was repeated 6 times before letting the samples soak for 16 hours. The supercritical CO_2 was then slowly bled off until the samples were solvent free. The dried samples were then transferred to a pre-dried and weighed analysis tube under a constant positive flow of argon atmosphere. After weighing, the sample tubes were then placed directly onto the analysis ports without further activation. Accurate sample masses were calculated using degassed samples. All adsorption measurements used ultra-high purity gases.

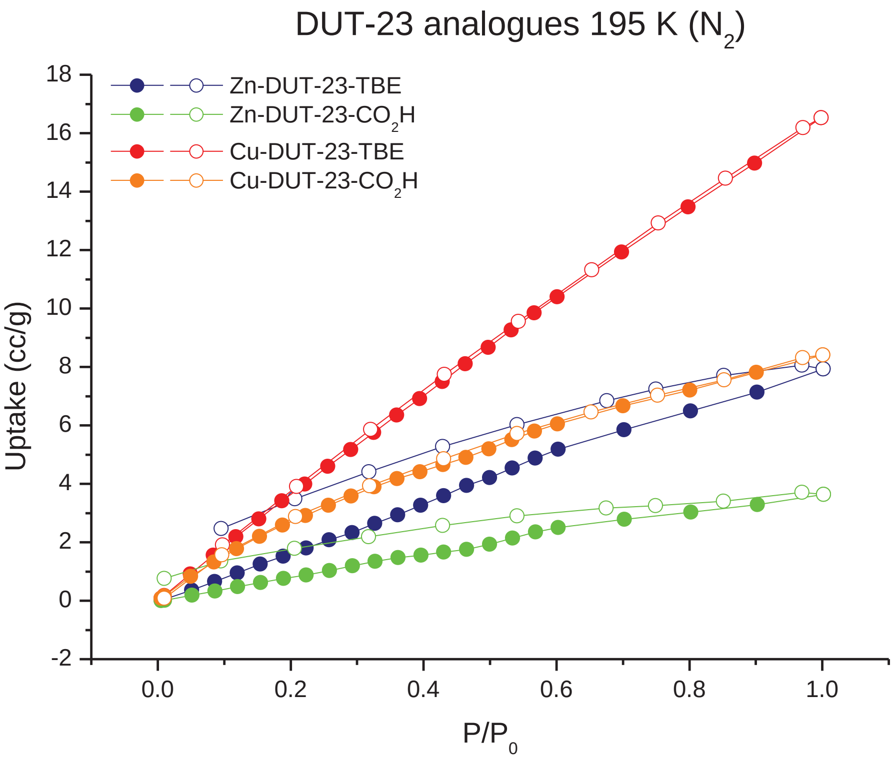

Figure 5.21 Gravimetric N_2 adsorption (filled) and desorption (open) isotherms measured at 195 K.

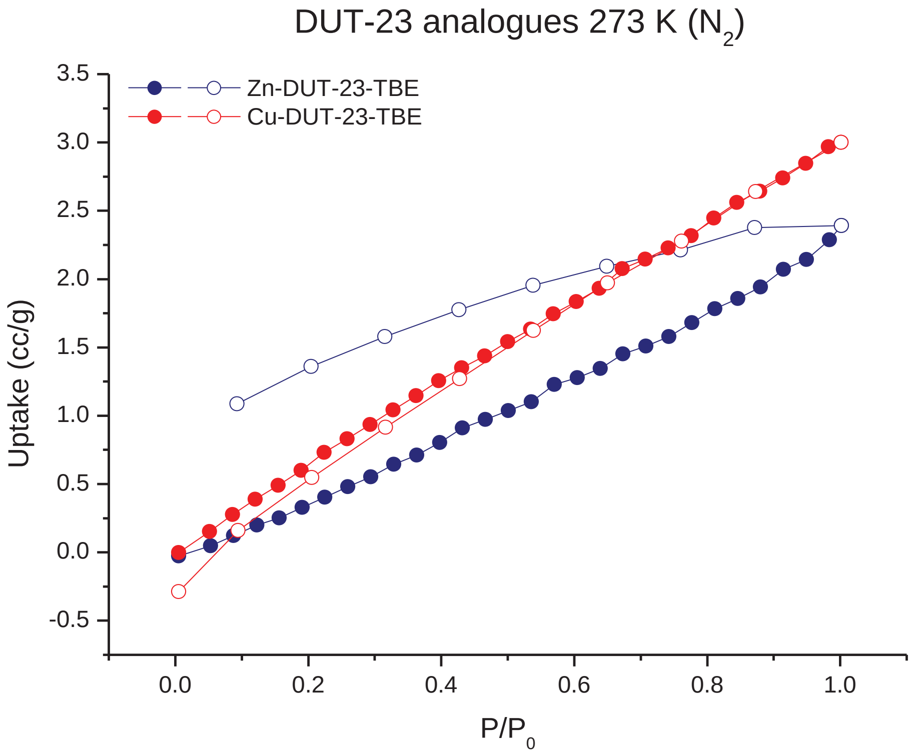

Figure 5.22 Gravimetric N_2 adsorption (filled) and desorption (open) isotherms measured at 273 K.

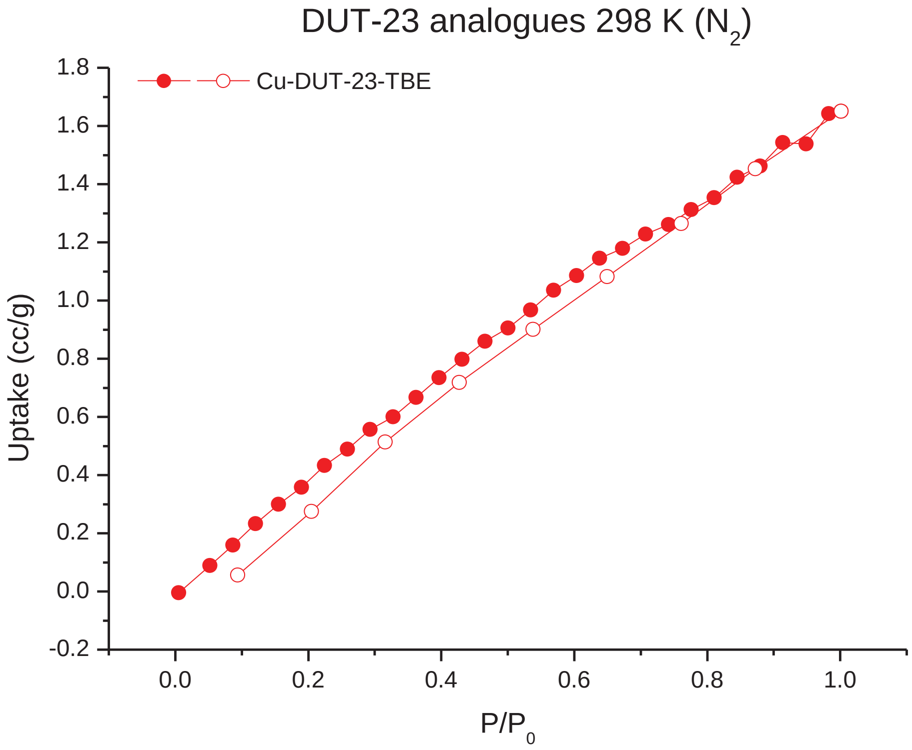

Figure 5.23 Gravimetric N_2 adsorption (filled) and desorption (open) isotherms measured at 298 K.

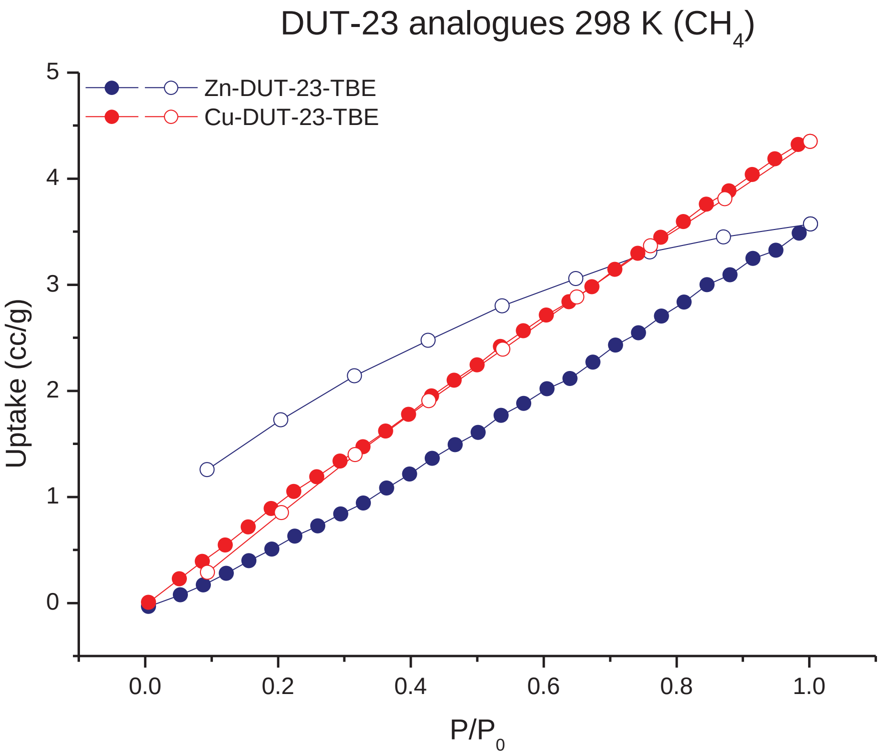

Figure 5.24 Gravimetric CH_4 adsorption (filled) and desorption (open) isotherms measured at 298 K.

Chapter 6 - Summary and Perspectives

6.1 Thesis Summary

Prior to the work carried out for this thesis, there were no publications in which bpy was used as a ligand backbone, or in which a carboxylate was incorporated into a MOF using a TPG. Also, to the best of our knowledge there are no examples in the literature of an ethyl carbamate TPG in MOFs.

In this thesis the range of TPG protected ligands has been expanded to include 1,4-bdc (Chapter 2) and bpy (Chapters 4 and 5). The bpy-NHBoc and bpy-TBE materials are the first examples of N-donor type ligands protected by TPGs. Furthermore, the bpy-TBE ligand is the first example of a TPG protected carboxylate in a MOF.

In Chapter 2, 1,4-bdc-NH_2 was protected as both the ethyl carbamate and the *tert*-butylcarbamate, giving 1,4-bdc-NHCOOEt and 1,4-bdc-NHBoc, which were then incorporated into a MOF-5-type framework. It was envisaged that thermolysis of the carbamate esters could generate an isocyanate group, though this was not expected for 1,4-bdc-NHBoc due to the tendency of *tert*-butylcarbamates to decompose to the amine. Despite thermolysis on the TGA apparatus only generating the amine, it was found that thermolysis under vacuum enabled not only enabled ~ 60 % conversion of the ethylcarbamate to 1,4-bdc-NCO, but also a ~20 % conversion of the *tert*-butylcarbamate to 1,4-bdc-NCO. The MOF-5 analogues in this work also proved sufficiently stable to survive the thermolysis conditions with little discernible effect on the porosity of the material.

In Chapter 3, 1,3-bdc-NH_2 was protected as both the ethyl carbamate and the *tert*-butylcarbamate, giving 1,3-bdc-NHCOOEt and 1,3-bdc-NHBoc, which there then incorporated into a lon-e-type framework. It became apparent the lon-e was a poor choice of MOF for use with TPGs as the framework was prone to collapse from desolvation, and it was not possible to thermolyse the materials without complete collapse of the MOFs.

In Chapter 4, bpy-NH_2 and bpy-CO_2H were protected with TPGs to give bpy-NHBoc and bpy-TBE, respectively. The ligands were combined with bpdc and zinc to obtain the BMOF-1-bpdc analogues MUF20-Aβ and MUF20-Aγ. Whilst the thermolysed materials MUF20-Aβ^t and MUF20-Aγ^t demonstrated significant gas uptakes compared to their protected counterparts, comparison of MUF20-Aβ^t with the directly synthesised material MUF20-Aβ’ revealed significantly higher uptakes than the thermolysed materials. This discrepancy indicates that the BMOF-1-bpdc/MUF20 framework is partially degraded under thermolysis conditions. These results strongly imply that this framework is not compatible with TPGs. However, TPGs did allow for the installation of a carboxylate group into the BMOF-1-bpdc/MUF20 framework which was not obtainable through direct synthesis methods.

In Chapter 5, bpy-TBE was combined with btb and Zn/Cu to obtain Zn-DUT-23-TBE and Cu-DUT-23-TBE. These materials were then thermolysed to produce Zn/Cu-DUT-23-CO_2H, materials that were not able to be directly synthesised using bpy-CO_2H. Unfortunately, the thermolysed materials demonstrated significant decreases in uptakes compared to their protected counterparts. However, the TPG containing materials also had markedly lower uptakes than the parent Zn-DUT-23 and Cu-DUT-23 materials, which has been attributed to pore collapse. This partial pore collapse may have sufficiently weakened the MOF framework to increase its sensitivity to the thermolysis conditions, resulting in a much larger decrease in uptake than would have been the case with a defect free material.

The results of this thesis revealed that MOF stability is a key factor in the compatibility of a material. Specifically, the MOF must be resistant to solvent removal and subsequent heating at elevated temperatures for extended periods. This is most clearly observed in Chapter 3, where the lon-e materials were very susceptible to solvent removal, and later were completely collapsed by thermolysis. These findings have led to the recommendations outlined in section 6.2 for the screening of MOFs for their compatibility with TPGs.

6.2 Recommendations for screening of MOFs compatible with TPGs

Due to the difficulties encountered in this work as a result of poor MOF stability, it is the recommended that the following screening method be employed prior to any attempts to incorporate TPGs into a new MOF:

1. Trial desolvations of the MOF should be conducted in order to determine its resistance to desolvation. PXRD is a good preliminary measure of stability at this point, however gas sorption measurements are the best way to determine if the material has retained its porosity. Typically, only N_2 at 77 K isotherms would need to be measured, but in some cases H_2 at 77 K and/or CO_2 at 195 K measurements may be desirable.
2. The desolvated MOF should be treated with conditions similar to those expected for thermolysis. For example, if the target TPG is a Boc-protected amine, then 160 °C for 10 hours is a good approximation for the thermolysis in the final material. The porosity of this material should then be measured using gas

adsorption measurements. On multi-port systems, it may useful to run both the pre- and post-heat treated samples in parallel as a time saving measure.

3. Compare the pre- and post-heat treatment uptakes for the MOF. If there is a significant decrease in uptake post thermolysis, then the MOF is most likely incompatible with TPGs. The pre-thermolysis uptakes should also be compared to literature values reported for the material. If there is a significant discrepancy between the uptakes, then it may mean that the material was incompletely activated. Incomplete activation can cause degradation of the MOF during thermolysis, as the elevated temperatures can cause the remaining solvent to induce MOF collapse. If this is observed, then proper activation and subsequent heat treatment should be conducted before excluding the material from TPG studies.
4. An additional criterion for the screening of potential MOFs is the MOF's stability to exposure to the atmosphere. This is not a vital property of the material as there a protocols for handling sensitive materials, however the ease of handling such materials, and the removal of the uncertainty of the cause of collapse can hasten the screening process as less duplicate experiments would need to be run.

By following the procedure above, it should be possible to effectively screen MOFs for their compatibility with TPGs. This should reduce the amount time and materials expended on investigating sub-optimal materials.

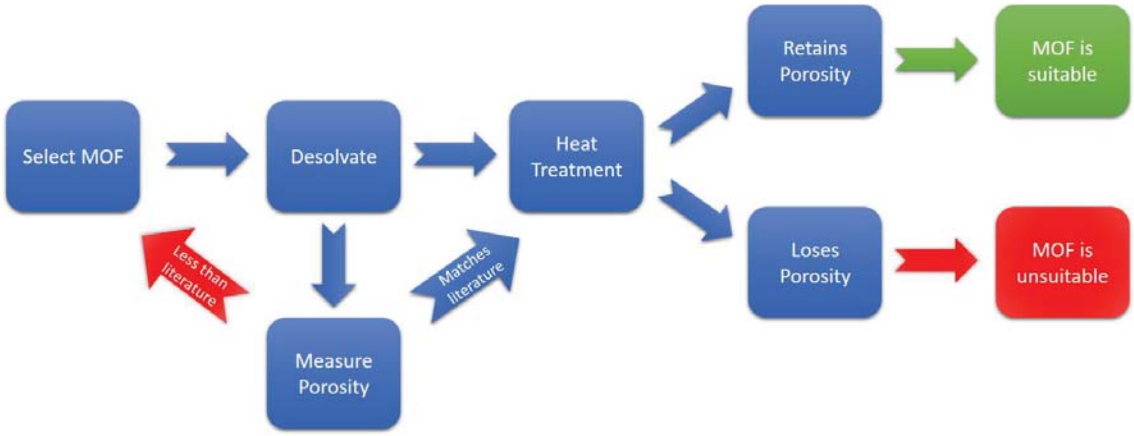

Figure 6.1 Flow chart outlining the screening process for determining if a MOF is compatible with TPGs.

6.3 Exploring more TPGs, functional groups, and ligand backbones

Having demonstrated the viability of TPGs, future work should expand the materials and functional groups accessible to researchers. This can be achieved in three main ways, expanding the number of usable TPGs, increasing the number of functional groups that can be protected, and also by expanding the library of ligand backbones that can be functionalised.

By expanding the number of TPGs that can be used, it is possible to access new functional groups. It is also possible that TPGs with lower thermal deprotection temperatures could be obtained, a potentially desirable trait in that it results in gentler thermolysis conditions and thus can be used in less stable MOFs. Furthermore, it may be possible to design TPGs that can direct the formation of a desired material by inhibiting the formation of competing phases. For example, with a sufficiently bulky TPG it may be possible to prevent the interpenetration observed in the MUF20 series. An alternative approach may be to link two ligands with a TPG containing linker so that the ligands remain a set distance apart during synthesis, after which the linker can be cleaved, leaving behind two functionalised independent ligands.

Expanding the number of functional groups able to be protected by TPGs is a key driver of research into TPGs as it contributes towards to an overarching goal of MOF chemistry, the tuning of the chemistry of MOF pores. It is not always necessary to develop new TPGs to protect new functionalities. This has been demonstrated in the published works of the Telfer group in which both amine and proline functionalities were protected with Boc groups. It would be reasonable to expect that this can be extrapolated out to other functionalities. For example, it can be envisaged that guanidine groups could be protected as carbamate esters, and that an amine acid functional group could be protected as an ester and carbamate esters (Figure 6.2). Further functionalities can also be protected, as demonstrated in current DNA technology where phosphate groups are protected as phosphonate ester TPGs.[217] It would be reasonable infer that the protection of sulfonate groups as sulfonate ester TPGs is also possible. Also of interest would be the addition of alkyl spacers between the ligand backbone and the functional group of interest. Whilst not increasing the number of functional groups protected by TPGs, the addition of a linker would introduce some flexibility into the side

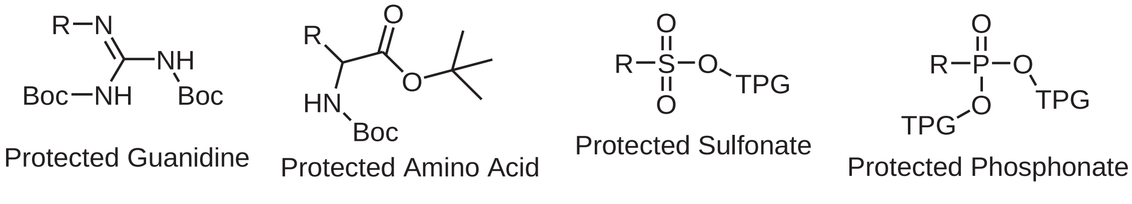

Protected Guanidine

Protected Amino Acid

Protected Sulfonate

Protected Phosphonate

Figure 6.2 examples of new functional groups the can be protected with TPGs.

chain and allow the functional group to adopt new conformations, potentially allowing for more favourable interactions to occur between the functional group and guest molecules.

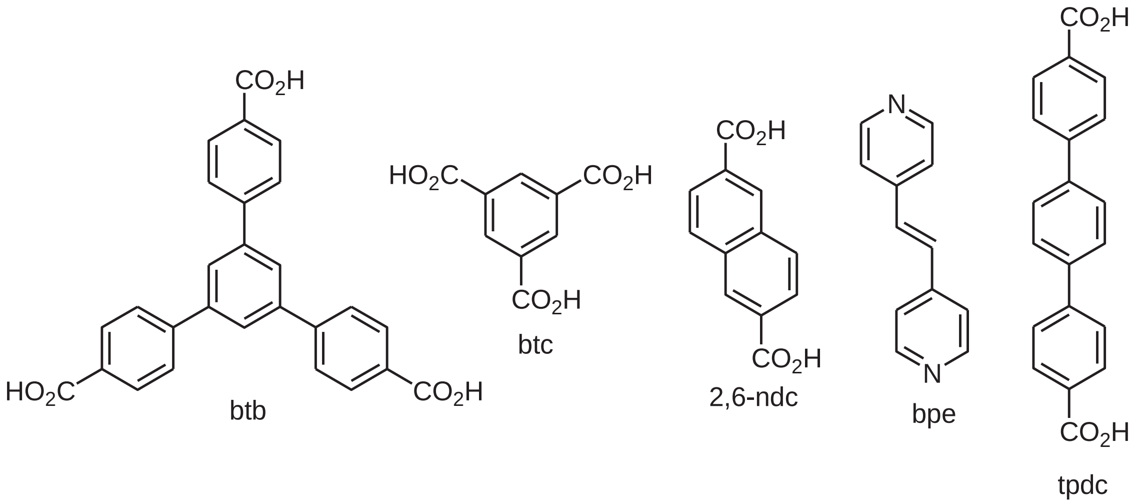

Figure 6.3 Ligands used in the synthesis of multiple MOFs.

Increasing the number of functionalised ligand backbones will allow for the introduction of functional groups into more MOFs, in addition to allowing the incorporation of multiple functionalised ligands in the same MOF. Heather Jameson, a fellow PhD student in the Telfer group, is currently investigating the introduction of multiple functional groups in the MUF20 series using the functionalised bpy ligands covered in the work in combination with functionalised bpdc ligands. There are a great many ligands that have been incorporated into MOFs and the functionalisation of any of them would allow for the incorporation of functional groups into more MOFs. In order to maximise returns on the time and materials required to develop new compounds, it is recommended that ligands that are targeted are compatible with a wide range of MOFs or are utilised in the synthesis of a specific target MOF. Examples of ligands used in the synthesis of multiple MOFs and thus prime targets for functionalisation include bpe, btb, btc, 2,6-ndc, and tpdc (Figure 6.3). Truxenetricarboxylate (Figure 6.4) is an example of a ligand that is not widely used but is present in a very interesting material, MUF-77.[191] Developed by Lujia Liu during his PhD studies in the Telfer group, MUF-77 is a rare example of a quaternary MOF, containing one metal and three ligands. Not only is MUF-77 a stable material, the highly ordered nature of the ligands within the pore allow for a great deal of control over how any functional groups are directed in the MOF. So far, the only functionalisation of truxenetricarboxylate to be incorporated into MUF-77 is the addition of alkyl chains to the five-membered rings adjacent to central benzene ring. These alkyl chains improve the stability of material to water vapour, but do not introduce any chemical functionality to the material. As the peripheral benzene rings are unfunctionalised (save for the binding carboxylates), it is possible to install functional groups at these positions without necessitating the replacement of the alky chains. Through functionalising the truxenetricarboxylate ligand, it would be possible to access MUF-77 analogues with three functionalised ligands using TPGs. This would allow for the tuning of the chemistry of the pore to an unprecedented degree, giving MUF-77 analogues the potential to function as artificial enzymes.

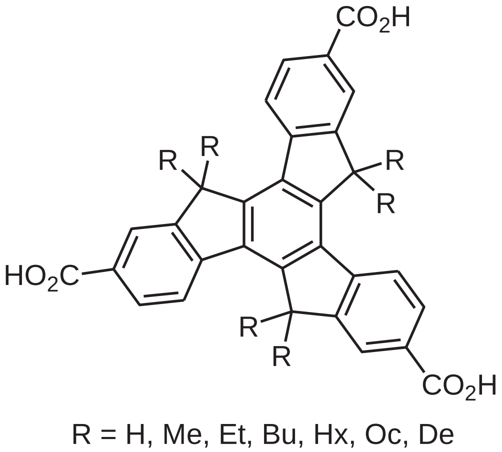

Figure 6.4 Truxenetricarboxylate and the alkyl analogues incorporated into the MUF-77 materials.

Chapter 7 - References

1 Klein, N., Senkovska, I., Baburin, I. A., Grünker, R., Stoeck, U., Schlichtenmayer, M., Streppel, B., Mueller, U., Leoni, S., Hirscher, M. & Kaskel, S. Route to a Family of Robust, Non-interpenetrated Metal–Organic Frameworks with pto-like Topology. *Chem. – Eur. J.* **17**, 13007-13016 (2011).

2 Hoskins, B. F. & Robson, R. Infinite polymeric frameworks consisting of three dimensionally linked rod-like segments. *J. Am. Chem. Soc.* **111**, 5962-5964 (1989).

3 Hoskins, B. F. & Robson, R. Design and construction of a new class of scaffolding-like materials comprising infinite polymeric frameworks of 3D-linked molecular rods. A reappraisal of the zinc cyanide and cadmium cyanide structures and the synthesis and structure of the diamond-related frameworks $[N(CH_3)_4][CuIZnII(CN)_4]$ and CuI[4,4',4'',4'''-tetracyanotetraphenylmethane]$BF_4.xC_6H_5NO_2$. *J. Am. Chem. Soc.* **112**, 1546-1554 (1990).

4 Yaghi, O. M., Li, G. & Li, H. Selective binding and removal of guests in a microporous metal-organic framework. *Nature* **378**, 703-706 (1995).

5 Öhrström, L. in *ChemViews* (www.chemistryviews.org, 2013).

6 Batten Stuart, R., Champness Neil, R., Chen, X.-M., Garcia-Martinez, J., Kitagawa, S., Öhrström, L., O'Keeffe, M., Paik Suh, M. & Reedijk, J. Terminology of metal–organic frameworks and coordination polymers (IUPAC Recommendations 2013). *Pure Appl. Chem.* **85**, 1715 (2013).

7 Dybtsev, D. N., Nuzhdin, A. L., Chun, H., Bryliakov, K. P., Talsi, E. P., Fedin, V. P. & Kim, K. A Homochiral Metal–Organic Material with Permanent Porosity, Enantioselective Sorption Properties, and Catalytic Activity. *Angew. Chem., Int. Ed.* **45**, 916-920 (2006).

8 Kitagawa, S., Kitaura, R. & Noro, S.-i. Functional Porous Coordination Polymers. *Angew. Chem., Int. Ed.* **43**, 2334-2375 (2004).

9 Haneda, T., Kawano, M., Kojima, T. & Fujita, M. Thermo-to-Photo-Switching of the Chromic Behavior of Salicylideneanilines by Inclusion in a Porous Coordination Network. *Angew. Chem., Int. Ed.* **46**, 6643-6645 (2007).

10 Eddaoudi, M., Kim, J., Rosi, N., Vodak, D., Wachter, J., O'Keeffe, M. & Yaghi, O. M. Systematic Design of Pore Size and Functionality in Isoreticular MOFs and Their Application in Methane Storage. *Science* **295**, 469-472 (2002).

11 Huang, X.-C., Lin, Y.-Y., Zhang, J.-P. & Chen, X.-M. Ligand-Directed Strategy for Zeolite-Type Metal–Organic Frameworks: Zinc(II) Imidazolates with Unusual Zeolitic Topologies. *Angew. Chem., Int. Ed.* **45**, 1557-1559 (2006).

12 Park, K. S., Ni, Z., Côté, A. P., Choi, J. Y., Huang, R., Uribe-Romo, F. J., Chae, H. K., O'Keeffe, M. & Yaghi, O. M. Exceptional chemical and thermal stability of zeolitic imidazolate frameworks. *Proc. Natl. Acad. Sci. U. S. A.* **103**, 10186-10191 (2006).

13 Cavka, J. H., Jakobsen, S., Olsbye, U., Guillou, N., Lamberti, C., Bordiga, S. & Lillerud, K. P. A New Zirconium Inorganic Building Brick Forming Metal Organic Frameworks with Exceptional Stability. *J. Am. Chem. Soc.* **130**, 13850-13851 (2008).

14 Chui, S. S. Y., Lo, S. M. F., Charmant, J. P. H., Orpen, A. G. & Williams, I. D. A Chemically Functionalizable Nanoporous Material $[Cu_3(TMA)_2(H_2O)_3]n$. *Science* **283**, 1148-1150 (1999).

15 Barthelet, K., Marrot, J., Riou, D. & Férey, G. A Breathing Hybrid Organic–Inorganic Solid with Very Large Pores and High Magnetic Characteristics. *Angew. Chem.* **114**, 291-294 (2002).

16 Li, H., Eddaoudi, Mohamed, O'Keeffe, M., Yaghi, O. M. Desgin and Synthesis of an Exceptionally Stable and Highly Porous Metal-Organic Framework. *Nature* **402**, 4 (1999).

17 Prussian Blue. In *Wikipedia*. Retrieved June 23, from https://en.wikipedia.org/wiki/Prussian_blue.

18 Cychosz, K. A. & Matzger, A. J. Water Stability of Microporous Coordination Polymers and the Adsorption of Pharmaceuticals from Water. *Langmuir* **26**, 17198-17202 (2010).

19 Küsgens, P., Rose, M., Senkovska, I., Fröde, H., Henschel, A., Siegle, S. & Kaskel, S. Characterization of metal-organic frameworks by water adsorption. *Microporous Mesoporous Mater.* **120**, 325-330 (2009).

20 Seo, Y.-K., Yoon, J. W., Lee, J. S., Hwang, Y. K., Jun, C.-H., Chang, J.-S., Wuttke, S., Bazin, P., Vimont, A., Daturi, M., Bourrelly, S., Llewellyn, P. L., Horcajada, P., Serre, C. & Férey, G. Porous Materials: Energy-Efficient Dehumidification over Hierachically Porous Metal–Organic Frameworks as Advanced Water Adsorbents (Adv. Mater. 6/2012). *Adv. Mater. (Weinheim, Ger.)* **24**, 710-710 (2012).

21 Férey, G., Mellot-Draznieks, C., Serre, C., Millange, F., Dutour, J., Surblé, S. & Margiolaki, I. A Chromium Terephthalate-Based Solid with Unusually Large Pore Volumes and Surface Area. *Science* **309**, 2040-2042 (2005).

22 Bromberg, L., Diao, Y., Wu, H., Speakman, S. A. & Hatton, T. A. Chromium(III) Terephthalate Metal Organic Framework (MIL-101): HF-Free Synthesis, Structure, Polyoxometalate Composites, and Catalytic Properties. *Chem. Mater.* **24**, 1664-1675 (2012).

23 Akiyama, G., Matsuda, R., Sato, H., Takata, M. & Kitagawa, S. Cellulose Hydrolysis by a New Porous Coordination Polymer Decorated with Sulfonic Acid Functional Groups. *Adv. Mater. (Weinheim, Ger.)* **23**, 3294-3297 (2011).

24 Li, B., Leng, K., Zhang, Y., Dynes, J. J., Wang, J., Hu, Y., Ma, D., Shi, Z., Zhu, L., Zhang, D., Sun, Y., Chrzanowski, M. & Ma, S. Metal–Organic Framework Based upon the Synergy of a Brønsted Acid Framework and Lewis Acid Centers as a Highly Efficient Heterogeneous Catalyst for Fixed-Bed Reactions. *J. Am. Chem. Soc.* **137**, 4243-4248 (2015).

25 Lin, Y., Yan, Q., Kong, C. & Chen, L. Polyethyleneimine Incorporated Metal-Organic Frameworks Adsorbent for Highly Selective CO_2 Capture. *Sci. Rep.* **3**, 1859 (2013).

26 Lin, Y., Lin, H., Wang, H., Suo, Y., Li, B., Kong, C. & Chen, L. Enhanced selective CO_2 adsorption on polyamine/MIL-101(Cr) composites. *Journal of Materials Chemistry A* **2**, 14658-14665 (2014).

27 Mondloch, J. E., Katz, M. J., Planas, N., Semrouni, D., Gagliardi, L., Hupp, J. T. & Farha, O. K. Are Zr_6-based MOFs water stable? Linker hydrolysis vs. capillary-force-driven channel collapse. *Chem. Commun.* **50**, 8944-8946 (2014).

28 Kim, M., Cahill, J. F., Fei, H., Prather, K. A. & Cohen, S. M. Postsynthetic Ligand and Cation Exchange in Robust Metal–Organic Frameworks. *J. Am. Chem. Soc.* **134**, 18082-18088 (2012).

29 Kim, M., Cahill, J. F., Su, Y., Prather, K. A. & Cohen, S. M. Postsynthetic ligand exchange as a route to functionalization of 'inert' metal-organic frameworks. *Chem. Sci.* **3**, 126-130 (2012).

30 Wang, T. C., Bury, W., Gómez-Gualdrón, D. A., Vermeulen, N. A., Mondloch, J. E., Deria, P., Zhang, K., Moghadam, P. Z., Sarjeant, A. A., Snurr, R. Q., Stoddart, J. F., Hupp, J. T. & Farha, O. K. Ultrahigh Surface Area Zirconium MOFs and Insights into the Applicability of the BET Theory. *J. Am. Chem. Soc.* **137**, 3585-3591 (2015).

31 Park, J., Feng, D. & Zhou, H.-C. Structure-Assisted Functional Anchor Implantation in Robust Metal–Organic Frameworks with Ultralarge Pores. *J. Am. Chem. Soc.* **137**, 1663-1672 (2015).

32 Sun, J., Zhou, Y., Chen, Z., Tu, B., Weng, L. & Zhao, D. Synthesis and Structure of a New Open Metal-organic-inorganic Hybrid Framework $[Sn(SO_4)(BDC)(H_2O)]$(BDC=Terephthalic acid). *Chem. J. Chin. Univ.* **24**, 1555-1557 (2003).

33 Chen, W., Wang, J.-Y., Chen, C., Yue, Q., Yuan, H.-M., Chen, J.-S. & Wang, S.-N. Photoluminescent Metal−Organic Polymer Constructed from Trimetallic Clusters and Mixed Carboxylates. *Inorg. Chem.* **42**, 944-946 (2003).

34 Hausdorf, S., Baitalow, F., Seidel, J. & Mertens, F. O. R. L. Gaseous Species as Reaction Tracers in the Solvothermal Synthesis of the Zinc Oxide Terephthalate MOF-5. *J. Phys. Chem. A* **111**, 4259-4266 (2007).

35 Yaghi, O. M., Davis, C. E., Li, G. & Li, H. Selective Guest Binding by Tailored Channels in a 3-D Porous Zinc(II)−Benzenetricarboxylate Network. *J. Am. Chem. Soc.* **119**, 2861-2868 (1997).

36 Li, H., Davis, C. E., Groy, T. L., Kelley, D. G. & Yaghi, O. M. Coordinatively Unsaturated Metal Centers in the Extended Porous Framework of $Zn_3(BDC)_3 \cdot 6CH_3OH$ (BDC = 1,4-Benzenedicarboxylate). *J. Am. Chem. Soc.* **120**, 2186-2187 (1998).

37 Ni, Z. & Masel, R. I. Rapid Production of Metal−Organic Frameworks via Microwave-Assisted Solvothermal Synthesis. *J. Am. Chem. Soc.* **128**, 12394-12395 (2006).

38 Liang, W. & D'Alessandro, D. M. Microwave-assisted solvothermal synthesis of zirconium oxide based metal-organic frameworks. *Chem. Commun.* **49**, 3706-3708 (2013).

39 Son, W.-J., Kim, J., Kim, J. & Ahn, W.-S. Sonochemical synthesis of MOF-5. *Chem. Commun.*, 6336-6338 (2008).

40 Jung, D.-W., Yang, D.-A., Kim, J., Kim, J. & Ahn, W.-S. Facile synthesis of MOF-177 by a sonochemical method using 1-methyl-2-pyrrolidinone as a solvent. *Dalton Trans.* **39**, 2883-2887 (2010).

41 Ameloot, R., Stappers, L., Fransaer, J., Alaerts, L., Sels, B. F. & De Vos, D. E. Patterned Growth of Metal-Organic Framework Coatings by Electrochemical Synthesis. *Chem. Mater.* **21**, 2580-2582 (2009).

42 Friscic, T. & Fabian, L. Mechanochemical conversion of a metal oxide into coordination polymers and porous frameworks using liquid-assisted grinding (LAG). *CrystEngComm* **11**, 743-745 (2009).

43 Friščić, T., Reid, D. G., Halasz, I., Stein, R. S., Dinnebier, R. E. & Duer, M. J. Ion- and Liquid-Assisted Grinding: Improved Mechanochemical Synthesis of Metal–Organic Frameworks Reveals Salt Inclusion and Anion Templating. *Angew. Chem.* **122**, 724-727 (2010).

44 Baeg, J. Y. & Lee, S. W. A porous, two-dimensional copper coordination-polymer containing guest molecules: hydrothermal synthesis, structure, and thermal property of [Cu(BDC)(bipy)](BDCH$_2$) (BDC=1,4-benzenedicarboxylate; bipy=4,4′-bipyridine). *Inorg. Chem. Commun.* **6**, 313-316 (2003).

45 Choi, E.-Y., Park, K., Yang, C.-M., Kim, H., Son, J.-H., Lee, S. W., Lee, Y. H., Min, D. & Kwon, Y.-U. Benzene-Templated Hydrothermal Synthesis of Metal–Organic Frameworks with Selective Sorption Properties. *Chem. – Eur. J.* **10**, 5535-5540 (2004).

46 Yang, E.-C., Zhao, H.-K., Ding, B., Wang, X.-G. & Zhao, X.-J. Four Novel Three-Dimensional Triazole-Based Zinc(II) Metal−Organic Frameworks Controlled by the Spacers of Dicarboxylate Ligands: Hydrothermal Synthesis, Crystal Structure, and Luminescence Properties. *Cryst. Growth Des.* **7**, 2009-2015 (2007).

47 Bosch, M., Yuan, S. & Zhou, H.-C. in *The Chemistry of Metal–Organic Frameworks* 137-170 (Wiley-VCH Verlag GmbH & Co. KGaA, 2016).

48 Farha, O. K., Özgür Yazaydın, A., Eryazici, I., Malliakas, C. D., Hauser, B. G., Kanatzidis, M. G., Nguyen, S. T., Snurr, R. Q. & Hupp, J. T. De novo synthesis of a metal–organic framework material featuring ultrahigh surface area and gas storage capacities. *Nat Chem* **2**, 944-948 (2010).

49 Alezi, D., Belmabkhout, Y., Suyetin, M., Bhatt, P. M., Weseliński, Ł. J., Solovyeva, V., Adil, K., Spanopoulos, I., Trikalitis, P. N., Emwas, A.-H. & Eddaoudi, M. MOF Crystal Chemistry Paving the Way to Gas Storage Needs: Aluminum-Based soc-MOF for CH_4, O_2, and CO_2 Storage. *J. Am. Chem. Soc.* **137**, 13308-13318 (2015).

50 Luo, F., Yan, C., Dang, L., Krishna, R., Zhou, W., Wu, H., Dong, X., Han, Y., Hu, T.-L., O'Keeffe, M., Wang, L., Luo, M., Lin, R.-B. & Chen, B. UTSA-74: A MOF-74 Isomer with Two Accessible Binding Sites per Metal Center for Highly Selective Gas Separation. *J. Am. Chem. Soc.* **138**, 5678-5684 (2016).

51 Xue, D.-X., Belmabkhout, Y., Shekhah, O., Jiang, H., Adil, K., Cairns, A. J. & Eddaoudi, M. Tunable Rare Earth fcu-MOF Platform: Access to Adsorption Kinetics Driven Gas/Vapor Separations via Pore Size Contraction. *J. Am. Chem. Soc.* **137**, 5034-5040 (2015).

52 Jiang, J., Furukawa, H., Zhang, Y.-B. & Yaghi, O. M. High Methane Storage Working Capacity in Metal–Organic Frameworks with Acrylate Links. *J. Am. Chem. Soc.* **138**, 10244-10251 (2016).

53 Castro-Gonzales, L., Kimmerle, K., Schippert, E. & Fickinger, D. Finding and Evaluating of Adequate Adsorbents for the Adsorption of CO_2 from Humid Gas Streams. *ChemistrySelect* **1**, 2834-2841 (2016).

54 Friebe, S., Diestel, L., Knebel, A., Wollbrink, A. & Caro, J. MOF-Based Mixed-Matrix Membranes in Gas Separation – Mystery and Reality. *Chem. Ing. Tech.* **88**, 1788-1797 (2016).

55 Batten, S. R., Chen, B. & Vittal, J. J. Coordination Polymers/MOFs: Structures, Properties and Applications. *ChemPlusChem* **81**, 669-670 (2016).

56 Maghsoudi, H. Comparative study of adsorbents performance in ethylene/ethane separation. *Adsorption* **22**, 1-8 (2016).

57 Zhu, H., Wang, L., Jie, X., Liu, D. & Cao, Y. Improved Interfacial Affinity and CO_2 Separation Performance of Asymmetric Mixed Matrix Membranes by Incorporating Postmodified MIL-53(Al). *ACS Appl. Mater. Interfaces* **8**, 22696-22704 (2016).

58 Chakraborty, A., Achari, A., Eswaramoorthy, M. & Maji, T. K. MOF-aminoclay composites for superior CO_2 capture, separation and enhanced catalytic activity in chemical fixation of CO_2. *Chem. Commun.* (2016).

59 Ibrahim, A. & Lin, Y. S. Pervaporation Separation of Organic Mixtures by MOF-5 Membranes. *Ind. Eng. Chem. Res.* **55**, 8652-8658 (2016).

60 Liu, S., Pan, J., Ma, Y., Qiu, F., Niu, X., Zhang, T. & Yang, L. Three-in-one strategy for selective adsorption and effective separation of cis-diol containing luteolin from peanut shell coarse extract using PU/GO/BA-MOF composite. *Chem. Eng. J.* **306**, 655-666 (2016).

61 Pullen, S. & Ott, S. Photochemical Hydrogen Production with Metal–Organic Frameworks. *Top. Catal.* **59**, 1712-1721 (2016).

62 Meyer, K., Bashir, S., Llorca, J., Idriss, H., Ranocchiari, M. & van Bokhoven, J. A. Photocatalyzed Hydrogen Evolution from Water by a Composite Catalyst of NH_2-MIL-125(Ti) and Surface Nickel(II) Species. *Chem. – Eur. J.* **22**, 13894-13899 (2016).

63 Gao, C.-Y., Tian, H.-R., Ai, J., Li, L.-J., Dang, S., Lan, Y.-Q. & Sun, Z.-M. A microporous Cu-MOF with optimized open metal sites and pore spaces for high gas storage and active chemical fixation of CO_2. *Chem. Commun.* (2016).

64 Li, J., Gao, H., Tan, L., Luan, Y. & Yang, M. Superparamagnetic core-shell metal-organic framework $Fe_3O_4/Cu_3(BTC)_2$ microspheres and their catalytic activities for the aerobic oxidation of alcohols and olefins. *Eur. J. Inorg. Chem.*, n/a-n/a (2016).

65 D, A. R., Kim, H. K., Kim, Y., Lee, S., Choi, J., Islam, M. J., Kumar, D. P. & Kim, T. Multicomponent Transition Metal Phosphides Derived from Layered Double Hydroxide Double-Shelled Nanocages as an Efficient Non-precious Co-catalyst for Hydrogen Production. *Journal of Materials Chemistry A* (2016).

66 Liu, S., Chen, J., Bao, X., Li, T., Ling, Y., Li, C., Wu, C. & Zhao, Y. Metal–Organic-Framework-Templated Polyelectrolyte Nanocapsules for the Encapsulation and Delivery of Small-Molecule–Polymer Conjugates. *Chem. – Asian J.* **11**, 1811-1820 (2016).

67 Simon-Yarza, T., Baati, T., Neffati, F., Njim, L., Couvreur, P., Serre, C., Gref, R., Najjar, M. F., Zakhama, A. & Horcajada, P. In vivo behavior of MIL-100 nanoparticles at early times after intravenous administration. *Int. J. Pharm.* **511**, 1042-1047 (2016).

68 Lin, X.-M., Niu, J.-L., Lin, J., Hu, L., Zhang, G. & Cai, Y.-P. A luminescent Tb(III)-MOF based on pyridine-3, 5-dicarboxylic acid for detection of nitroaromatic explosives. *Inorg. Chem. Commun.* **72**, 69-72 (2016).

69 Zhang, H., Fan, R., Chen, W., Fan, J., Dong, Y., Song, Y., Du, X., Wang, P. & Yang, Y. 3D Lanthanide Metal–Organic Frameworks Based on Mono-, Tri-, and Heterometallic Tetranuclear Clusters as Highly Selective and Sensitive Luminescent Sensor for Fe^{3+} and Cu^{2+} Ions. *Cryst. Growth Des.* **16**, 5429-5440 (2016).

70 Mahato, P., Yanai, N., Sindoro, M., Granick, S. & Kimizuka, N. Preorganized Chromophores Facilitate Triplet Energy Migration, Annihilation and Upconverted Singlet Energy Collection. *J. Am. Chem. Soc.* **138**, 6541-6549 (2016).

71 Maza, W. A. & Morris, A. J. Metal Organic Framework Solar Cells: A New Class of Sensitized Light Harvesting Devices. *Meeting Abstracts* **MA2015-02**, 1697 (2015).

72 He, H., Ma, E., Cui, Y., Yu, J., Yang, Y., Song, T., Wu, C.-D., Chen, X., Chen, B. & Qian, G. Polarized three-photon-pumped laser in a single MOF microcrystal. *Nat Commun* **7**, 11087 (2016).

73 Peng, T., Xu, T., Wang, X., Liu, Z., Dai, S., Liu, S., Zhao, Z. & Pan, Z. Simulation and fabrication of micro-structured optical fibers with extruded tubes. *Optik - International Journal for Light and Electron Optics* **127**, 8240-8247 (2016).

74 Biswas, P., Adhikary, P., Biswas, A. & Ghosh, S. N. Formation and stability analysis of parabolic pulses through specialty microstructured optical fibers at 2.1 μm. *Opt. Commun.* **377**, 120-127 (2016).

75 Dhara, B., Nagarkar, S. S., Kumar, J., Kumar, V., Jha, P. K., Ghosh, S. K., Nair, S. & Ballav, N. Increase in Electrical Conductivity of MOF to Billion-Fold upon Filling the Nanochannels with Conducting Polymer. *J. Phys. Chem. Lett.* **7**, 2945-2950 (2016).

76 Chakravarty, C., Mandal, B. & Sarkar, P. Coronene-based Metal-Organic Framework: A Theoretical Exploration. *Phys. Chem. Chem. Phys.* (2016).

77 Li, H., Eddaoudi, M., Groy, T. L. & Yaghi, O. M. Establishing Microporosity in Open Metal−Organic Frameworks: Gas Sorption Isotherms for Zn(BDC) (BDC = 1,4-Benzenedicarboxylate). *J. Am. Chem. Soc.* **120**, 8571-8572 (1998).

78 Clark, J. *Mercedes-Benz F125! research vehicle technology*, Retrieved Aug 11, 2016, from http://www.emercedesbenz.com/autos/mercedes-benz/concept-vehicles/mercedes-benz-f125-research-vehicle-technology/

79 Peplow, M. Materials science: The hole story. *Nature* **520**, 148-150 (2015).

80 Cenergy. *ANG Press Releases*, Retrieved Aug 12, 2016, from http://cenergysolutions.com/about-us/cng-news/ang-press-releases/

81 Konstas, K., Osl, T., Yang, Y., Batten, M., Burke, N., Hill, A. J. & Hill, M. R. Methane storage in metal organic frameworks. *J. Mater. Chem.* **22**, 16698-16708 (2012).

82 Kondo, M., Yoshitomi, T., Matsuzaka, H., Kitagawa, S. & Seki, K. Three-Dimensional Framework with Channeling Cavities for Small Molecules: $\{[M_2(4,4'\text{-bpy})_3(NO_3)_4]\cdot xH_2O\}n$ (M □ Co, Ni, Zn). *Angew. Chem. Int. Ed. Engl.* **36**, 1725-1727 (1997).

83 Ma, S., Sun, D., Simmons, J. M., Collier, C. D., Yuan, D. & Zhou, H.-C. Metal-Organic Framework from an Anthracene Derivative Containing Nanoscopic Cages Exhibiting High Methane Uptake. *J. Am. Chem. Soc.* **130**, 1012-1016 (2007).

84 Wu, H., Zhou, W. & Yildirim, T. High-Capacity Methane Storage in Metal−Organic Frameworks M_2(dhtp): The Important Role of Open Metal Sites. *J. Am. Chem. Soc.* **131**, 4995-5000 (2009).

85 Wilmer, C. E., Farha, O. K., Yildirim, T., Eryazici, I., Krungleviciute, V., Sarjeant, A. A., Snurr, R. Q. & Hupp, J. T. Gram-scale, high-yield synthesis of a robust metal-organic framework for storing methane and other gases. *Energy Environ. Sci.* **6**, 1158-1163 (2013).

86 Mason, J. A., Veenstra, M. & Long, J. R. Evaluating metal-organic frameworks for natural gas storage. *Chem. Sci.* **5**, 32-51 (2014).

87 Peng, Y., Krungleviciute, V., Eryazici, I., Hupp, J. T., Farha, O. K. & Yildirim, T. Methane Storage in Metal–Organic Frameworks: Current Records, Surprise Findings, and Challenges. *J. Am. Chem. Soc.* **135**, 11887-11894 (2013).

88 Centre, J. R. *CO_2 time series 1990-2014 per region/country*. Retrieved from http://edgar.jrc.ec.europa.eu/overview.php?v=CO2ts1990-2014&sort=des9

89 Sumida, K., Rogow, D. L., Mason, J. A., McDonald, T. M., Bloch, E. D., Herm, Z. R., Bae, T.-H. & Long, J. R. Carbon Dioxide Capture in Metal–Organic Frameworks. *Chem. Rev.* **112**, 724-781 (2012).

90 McDonald, T. M., Mason, J. A., Kong, X., Bloch, E. D., Gygi, D., Dani, A., Crocella, V., Giordanino, F., Odoh, S. O., Drisdell, W. S., Vlaisavljevich, B., Dzubak, A. L., Poloni, R., Schnell, S. K., Planas, N., Lee, K., Pascal, T., Wan, L. F., Prendergast, D., Neaton, J. B., Smit, B., Kortright, J. B., Gagliardi, L., Bordiga, S., Reimer, J. A. & Long, J. R. Cooperative insertion of CO_2 in diamine-appended metal-organic frameworks. *Nature* **519**, 303-308 (2015).

91 Caskey, S. R., Wong-Foy, A. G. & Matzger, A. J. Dramatic Tuning of Carbon Dioxide Uptake via Metal Substitution in a Coordination Polymer with Cylindrical Pores. *J. Am. Chem. Soc.* **130**, 10870-10871 (2008).

92 Wade, C. R. & Dinca, M. Investigation of the synthesis, activation, and isosteric heats of CO_2 adsorption of the isostructural series of metal-organic frameworks $M_3(BTC)_2$ (M = Cr, Fe, Ni, Cu, Mo, Ru). *Dalton Trans.* **41**, 7931-7938 (2012).

93 Li, T., Sullivan, J. E. & Rosi, N. L. Design and Preparation of a Core–Shell Metal–Organic Framework for Selective CO_2 Capture. *J. Am. Chem. Soc.* **135**, 9984-9987 (2013).

94 Yang, S., Sun, J., Ramirez-Cuesta, A. J., Callear, S. K., DavidWilliam, I. F., Anderson, D. P., Newby, R., Blake, A. J., Parker, J. E., Tang, C. C. & Schröder, M. Selectivity and direct visualization of carbon dioxide and sulfur dioxide in a decorated porous host. *Nat Chem* **4**, 887-894 (2012).

95 Nath, I., Chakraborty, J. & Verpoort, F. Metal organic frameworks mimicking natural enzymes: a structural and functional analogy. *Chem. Soc. Rev.* **45**, 4127-4170 (2016).

96 Lewis, N. S. & Nocera, D. G. Powering the planet: Chemical challenges in solar energy utilization. *Proc. Natl. Acad. Sci.* **103**, 15729-15735 (2006).

97 Lomoth, R. & Ott, S. Introducing a dark reaction to photochemistry: photocatalytic hydrogen from [FeFe] hydrogenase active site model complexes. *Dalton Trans.*, 9952-9959 (2009).

98 Pullen, S., Fei, H., Orthaber, A., Cohen, S. M. & Ott, S. Enhanced Photochemical Hydrogen Production by a Molecular Diiron Catalyst Incorporated into a Metal–Organic Framework. *J. Am. Chem. Soc.* **135**, 16997-17003 (2013).

99 Aresta, M. *Carbon dioxide as chemical feedstock.* (John Wiley & Sons, 2010).

100 Horiuchi, Y., Toyao, T., Saito, M., Mochizuki, K., Iwata, M., Higashimura, H., Anpo, M. & Matsuoka, M. Visible-Light-Promoted Photocatalytic Hydrogen Production by Using an Amino-Functionalized Ti(IV) Metal–Organic Framework. *J. Phys. Chem. C* **116**, 20848-20853 (2012).

101 Hanson, J. R. *Protecting Groups in Organic Synthesis: Postgraduate Chemistry Series*. (Wiley, 1999).

102 Deshpande, R. K., Minnaar, J. L. & Telfer, S. G. Thermolabile Groups in Metal–Organic Frameworks: Suppression of Network Interpenetration, Post-Synthetic Cavity Expansion, and Protection of Reactive Functional Groups. *Angew. Chem., Int. Ed.* **49**, 4598-4602 (2010).

103 Lun, D. J., Waterhouse, G. I. N. & Telfer, S. G. A General Thermolabile Protecting Group Strategy for Organocatalytic Metal−Organic Frameworks. *J. Am. Chem. Soc.* **133**, 5806-5809 (2011).

104 Gupta, A. S., Deshpande, R. K., Liu, L., Waterhouse, G. I. N. & Telfer, S. G. Porosity in metal-organic frameworks following thermolytic postsynthetic deprotection: gas sorption, dye uptake and covalent derivatisation. *CrystEngComm* **14**, 5701-5704 (2012).

105 Petersen, S. Niedermolekulare Umsetzungsprodukte aliphatischer Diisocyanate 5. Mitteilung über Polyurethane). *Justus Liebigs Ann. Chem.* **562**, 205-228 (1949).

106 Wicks, D. A. & Wicks Jr, Z. W. Blocked isocyanates III: Part A. Mechanisms and chemistry. *Prog. Org. Coat.* **36**, 148-172 (1999).

107 Chmielewski, M. K. Protecting of a Thermolabile Protecting Group: "Click-Clack" Approach. *Org. Lett.* **11**, 3742-3745 (2009).

108 Ratajczak, T. & Chmielewski, M. K. Oxidation of H-Phosphonates with Iodine by Intramolecular Support of a 2-Pyridyl Thermolabile Protecting Group. *J. Org. Chem.* **77**, 7866-7872 (2012).

109 Chmielewski, M. K. Novel thermolabile protecting groups with higher stability at ambient temperature. *Tetrahedron Lett.* **53**, 666-669 (2012).

110 Witkowska, A., Krygier, D., Brzezinska, J. & Chmielewski, M. K. Modulating the Stability of 2-Pyridinyl Thermolabile Hydroxyl Protecting Groups via the "Chemical Switch" Approach. *J. Org. Chem.* **80**, 12129-12136 (2015).

111 Brzezinska, J., Witkowska, A., Bałabańska, S. & Chmielewski, M. K. 2-Pyridinyl-N-(2,4-difluorobenzyl)aminoethyl Group As Thermocontrolled Implement for Protection of Carboxylic Acids. *Org. Lett.* **18**, 3230-3233 (2016).

112 Kaczyński, T. P., Manszewski, T. & Chmielewski, M. K. Stereoselective P-Cyclisation and -Diastereoisomeric Purification of 5-Phenyl-3-(pyridin-2-yl)-1,3,2-oxazaphospholidine Formed from a Thermolabile Protecting Group. *Eur. J. Org. Chem.* **2016**, 2522-2527 (2016).

113 Koukhareva, I. & Lebedev, A. 3′-Protected 2′-Deoxynucleoside 5′-Triphosphates as a Tool for Heat-Triggered Activation of Polymerase Chain Reaction. *Anal. Chem.* **81**, 4955-4962 (2009).

114 Wicks, D. A. & Wicks Jr, Z. W. Blocked isocyanates III: Part B: Uses and applications of blocked isocyanates. *Prog. Org. Coat.* **41**, 1-83 (2001).

115 Brinkman, L. F. (1989). U.S. Patent No. US4868298 A. Washington, DC: U.S. Patent and Trademark Office.

116 Gras, R. & Wolf, E. (1998). U.S. Patent No. US5719240 A. Washington, DC: U.S. Patent and Trademark Office.

117 Gras, R., Weiss, J. V., Wolf, E., & Schmitt, F. (1999). U.S. Patent No. US5859164 A. Washington, DC: U.S. Patent and Trademark Office.

118 Fleming, K. E. & Pietrasiewicz, J. S. (1988). U.S. Patent No. US4769413 A. Washington, DC: U.S. Patent and Trademark Office.

119 Carson, D.W., Schmitt, R.J., Seneker, C.A., Van Kuren, T.A., &Wallace, D.R. (1988). U.S. Patent No. US4720405 A. Washington, DC: U.S. Patent and Trademark Office.

120 Venham, L.D., Salek, M.M., & Potter, T.A. (1993). U.S. Patent No. US5232988 A. Washington, DC: U.S. Patent and Trademark Office.

121 Briggs, R.L. & Knight, M. (1994). U.S. Patent No. US5281443 A. Washington, DC: U.S. Patent and Trademark Office.

122 Rost, S. Coatings for Solderable Wires for the Modern Electric Industry. *Macromol. Mater. Eng.* **293**, 373-386 (2008).

123 Farber, B.M. & Harbison, W.C. (1994). U.S. Patent No. US5316791 A. Washington, DC: U.S. Patent and Trademark Office.

124 Hartz, R. E. Reaction during cure of a blocked isocyanate–epoxy resin adhesive. *J. Appl. Polym. Sci.* **19**, 735-746 (1975).

125 Bandlish, B.K. (1989). U.S. Patent No. US4847319 A. Washington, DC: U.S. Patent and Trademark Office.

126 Guise, G., Jackson, M. & Maclaren, J. The reaction of isocyanates with bisulphite salts. *Aust. J. Chem.* **25**, 2583-2595 (1972).

127 Sankar, S. S., Lonikar, S. V., Gilbert, R. D., Fornes, R. E. & Stejskal, E. O. Solid-state cpmas ^{13}C-NMR studies of the reaction of an epoxy resin with masked isocyanates. *J. Polym. Sci., Part B : Polym. Phys.* **28**, 293-302 (1990).

128 Fracaroli, A. M., Furukawa, H., Suzuki, M., Dodd, M., Okajima, S., Gándara, F., Reimer, J. A. & Yaghi, O. M. Metal–Organic Frameworks with Precisely Designed Interior for Carbon Dioxide Capture in the Presence of Water. *J. Am. Chem. Soc.* **136**, 8863-8866 (2014).

129 Fracaroli, A. M., Siman, P., Nagib, D. A., Suzuki, M., Furukawa, H., Toste, F. D. & Yaghi, O. M. Seven Post-synthetic Covalent Reactions in Tandem Leading to Enzyme-like Complexity within Metal–Organic Framework Crystals. *J. Am. Chem. Soc.* **138**, 8352-8355 (2016).

130 Wu, P., He, C., Wang, J., Peng, X., Li, X., An, Y. & Duan, C. Photoactive Chiral Metal–Organic Frameworks for Light-Driven Asymmetric α-Alkylation of Aldehydes. *J. Am. Chem. Soc.* **134**, 14991-14999 (2012).

131 Sun, F., Yin, Z., Wang, Q.-Q., Sun, D., Zeng, M.-H. & Kurmoo, M. Tandem Postsynthetic Modification of a Metal–Organic Framework by Thermal Elimination and Subsequent Bromination: Effects on Absorption Properties and Photoluminescence. *Angew. Chem., Int. Ed.* **52**, 4538-4543 (2013).

132 Sartor, M., Stein, T., Hoffmann, F. & Fröba, M. A New Set of Isoreticular, Homochiral Metal–Organic Frameworks with ucp Topology. *Chem. Mater.* **28**, 519-528 (2016).

133 Ganguly, S., Pachfule, P., Bala, S., Goswami, A., Bhattacharya, S. & Mondal, R. Azide-Functionalized Lanthanide-Based Metal–Organic Frameworks Showing Selective CO_2 Gas Adsorption and Postsynthetic Cavity Expansion. *Inorg. Chem.* **52**, 3588-3590 (2013).

134 Nguyen, H. G. T., Weston, M. H., Sarjeant, A. A., Gardner, D. M., An, Z., Carmieli, R., Wasielewski, M. R., Farha, O. K., Hupp, J. T. & Nguyen, S. T. Design, Synthesis, Characterization, and Catalytic Properties of a Large-Pore Metal-Organic Framework Possessing Single-Site Vanadyl(monocatecholate) Moieties. *Cryst. Growth Des.* **13**, 3528-3534 (2013).

135 Han, Q., He, C., Zhao, M., Qi, B., Niu, J. & Duan, C. Engineering Chiral Polyoxometalate Hybrid Metal–Organic Frameworks for Asymmetric Dihydroxylation of Olefins. *J. Am. Chem. Soc.* **135**, 10186-10189 (2013).

136 Li, B., Zhang, Y., Ma, D., Li, L., Li, G., Li, G., Shi, Z. & Feng, S. A strategy toward constructing a bifunctionalized MOF catalyst: post-synthetic modification of MOFs on organic ligands and coordinatively unsaturated metal sites. *Chem. Commun.* **48**, 6151-6153 (2012).

137 Helten, S., Sahoo, B., Müller, P., Janßen-Müller, D., Klein, N., Grünker, R., Bon, V., Glorius, F., Kaskel, S. & Senkovska, I. Functional group tolerance in BTB-based metal–organic frameworks (BTB – benzene-1,3,5-tribenzoate). *Microporous Mesoporous Mater.* **216**, 42-50 (2015).

138 Walton, K. S. & Snurr, R. Q. Applicability of the BET Method for Determining Surface Areas of Microporous Metal−Organic Frameworks. *J. Am. Chem. Soc.* **129**, 8552-8556 (2007).

139 Sabo, M., Henschel, A., Frode, H., Klemm, E. & Kaskel, S. Solution infiltration of palladium into MOF-5: synthesis, physisorption and catalytic properties. *J. Mater. Chem.* **17**, 3827-3832 (2007).

140 Song, J., Zhang, Z., Hu, S., Wu, T., Jiang, T. & Han, B. MOF-5/n-Bu_4NBr: an efficient catalyst system for the synthesis of cyclic carbonates from epoxides and CO_2 under mild conditions. *Green Chem.* **11**, 1031-1036 (2009).

141 Gao, S., Zhao, N., Shu, M. & Che, S. Palladium nanoparticles supported on MOF-5: A highly active catalyst for a ligand- and copper-free Sonogashira coupling reaction. *Applied Catalysis A: General* **388**, 196-201 (2010).

142 Müller, M., Hermes, S., Kähler, K., van den Berg, M. W. E., Muhler, M. & Fischer, R. A. Loading of MOF-5 with Cu and ZnO Nanoparticles by Gas-Phase Infiltration with Organometallic Precursors: Properties of Cu/ZnO@MOF-5 as Catalyst for Methanol Synthesis. *Chem. Mater.* **20**, 4576-4587 (2008).

143 Perez, E. V., Balkus Jr, K. J., Ferraris, J. P. & Musselman, I. H. Mixed-matrix membranes containing MOF-5 for gas separations. *J. Membr. Sci.* **328**, 165-173 (2009).

144 Rowsell, J. L. C., Millward, A. R., Park, K. S. & Yaghi, O. M. Hydrogen Sorption in Functionalized Metal−Organic Frameworks. *J. Am. Chem. Soc.* **126**, 5666-5667 (2004).

145 Yang, S. J., Choi, J. Y., Chae, H. K., Cho, J. H., Nahm, K. S. & Park, C. R. Preparation and Enhanced Hydrostability and Hydrogen Storage Capacity of CNT@MOF-5 Hybrid Composite. *Chem. Mater.* **21**, 1893-1897 (2009).

146 Civalleri, B., Napoli, F., Noel, Y., Roetti, C. & Dovesi, R. Ab-initio prediction of materials properties with CRYSTAL: MOF-5 as a case study. *CrystEngComm* **8**, 364-371 (2006).

147 Hermes, S., Witte, T., Hikov, T., Zacher, D., Bahnmüller, S., Langstein, G., Huber, K. & Fischer, R. A. Trapping Metal-Organic Framework Nanocrystals: An in-Situ Time-Resolved Light Scattering Study on the Crystal Growth of MOF-5 in Solution. *J. Am. Chem. Soc.* **129**, 5324-5325 (2007).

148 Frost, H., Düren, T. & Snurr, R. Q. Effects of Surface Area, Free Volume, and Heat of Adsorption on Hydrogen Uptake in Metal−Organic Frameworks. *J. Phys. Chem. B* **110**, 9565-9570 (2006).

149 Deng, H., Doonan, C. J., Furukawa, H., Ferreira, R. B., Towne, J., Knobler, C. B., Wang, B. & Yaghi, O. M. Multiple Functional Groups of Varying Ratios in Metal-Organic Frameworks. *Science* **327**, 846-850 (2010).

150 Goswami, S., Mahapatra, A. K. & Mukherjee, R. Molecular recognition of xanthine alkaloids: First synthetic receptors for theobromine and a series of new receptors for caffeine. *J. Chem. Soc., Perkin Trans. 1*, 2717-2726 (2001).

151 Khan, G. S., Dickson, B. D. & Barker, D. Synthesis of benzoic acids and polybenzamides containing tertiary alkylamino functionality. *Tetrahedron* **68**, 1790-1801 (2012).

152 Volkringer, C. & Cohen, S. M. Generating Reactive MILs: Isocyanate- and Isothiocyanate-Bearing MILs through Postsynthetic Modification. *Angew. Chem., Int. Ed.* **49**, 4644-4648 (2010).

153 Ahnfeldt, T., Gunzelmann, D., Loiseau, T., Hirsemann, D., Senker, J., Férey, G. & Stock, N. Synthesis and Modification of a Functionalized 3D Open-Framework Structure with MIL-53 Topology. *Inorg. Chem.* **48**, 3057-3064 (2009).

154 Millward, A. R. & Yaghi, O. M. Metal−Organic Frameworks with Exceptionally High Capacity for Storage of Carbon Dioxide at Room Temperature. *J. Am. Chem. Soc.* **127**, 17998-17999 (2005).

155 Rowsell, J. L. C. & Yaghi, O. M. Effects of Functionalization, Catenation, and Variation of the Metal Oxide and Organic Linking Units on the Low-Pressure Hydrogen Adsorption Properties of Metal−Organic Frameworks. *J. Am. Chem. Soc.* **128**, 1304-1315 (2006).

156 Saha, D., Bao, Z., Jia, F. & Deng, S. Adsorption of CO_2, CH_4, N_2O, and N_2 on MOF-5, MOF-177, and Zeolite 5A. *Environ. Sci. Technol.* **44**, 1820-1826 (2010).

157 Mu, B. & Walton, K. S. Adsorption equilibrium of methane and carbon dioxide on porous metal-organic framework Zn-BTB. *Adsorption* **17**, 777-782 (2011).

158 Rigaku (1998). PROCESS-AUTO. Rigaku Corporation, Tokyo, Japan.

159 Sheldrick, G. A short history of SHELX. *Acta Crystallographica Section A* **64**, 112-122 (2008).

160 Dassault Systèmes BIOVIA, D. S. M. E., Release 2017, San Diego: Dassault Systèmes, 2016.

161 2DP (Rigaku, 2011).

162 Schoedel, A., Boyette, W., Wojtas, L., Eddaoudi, M. & Zaworotko, M. J. A Family of Porous Lonsdaleite-e Networks Obtained through Pillaring of Decorated Kagomé Lattice Sheets. *J. Am. Chem. Soc.* **135**, 14016-14019 (2013).

163 *Trihexagonal tiling*, Retrieved July 1, 2016, from https://en.wikipedia.org/wiki/Trihexagonal_tiling

164 Schoedel, A., Wojtas, L., Kelley, S. P., Rogers, R. D., Eddaoudi, M. & Zaworotko, M. J. Network Diversity through Decoration of Trigonal-Prismatic Nodes: Two-Step Crystal Engineering of Cationic Metal–Organic Materials. *Angew. Chem., Int. Ed.* **50**, 11421-11424 (2011).

165 Schoedel, A., Cairns, A. J., Belmabkhout, Y., Wojtas, L., Mohamed, M., Zhang, Z., Proserpio, D. M., Eddaoudi, M. & Zaworotko, M. J. The asc Trinodal Platform: Two-Step Assembly of Triangular, Tetrahedral, and Trigonal-Prismatic Molecular Building Blocks. *Angew. Chem., Int. Ed.* **52**, 2902-2905 (2013).

166 *Kathleen Lonsdale*, Retrieved Jul 9, 2016, from https://en.wikipedia.org/wiki/Kathleen_Lonsdale

167 *Lonsdaleite*, Retrieved July 9, 2016, from https://en.wikipedia.org/wiki/Lonsdaleite

168 Kim, H., Sun, Y., Kim, Y., Kajiwara, T., Yamashita, M. & Kim, K. Metal-organic frameworks with rare topologies: lonsdaleite-type metal formates and their magnetic properties. *CrystEngComm* **13**, 2197-2200 (2011).

169 Patil, K. M., Dickinson, M. E., Tremlett, T., Moratti, S. C. & Hanton, L. R. Synthesis of Diamondoid and Lonsdaleite Networks from the Same Ag(I)–Ligand Combination, with Lonsdaleite the Softer Network. *Cryst. Growth Des.* **16**, 1038-1046 (2016).

170 Murphy, D. L., Malachowski, M. R., Campana, C. F. & Cohen, S. M. A chiral, heterometallic metal-organic framework derived from a tris(chelate) coordination complex. *Chem. Commun.*, 5506-5508 (2005).

171 Halper, S. R., Do, L., Stork, J. R. & Cohen, S. M. Topological Control in Heterometallic Metal−Organic Frameworks by Anion Templating and Metalloligand Design. *J. Am. Chem. Soc.* **128**, 15255-15268 (2006).

172 Chandler, B. D., Yu, J. O., Cramb, D. T. & Shimizu, G. K. H. Series of Lanthanide-Alkali Metal-Organic Frameworks Exhibiting Luminescence and Permanent Microporosity. *Chem. Mater.* **19**, 4467-4473 (2007).

173 Zhang, S., Han, L., Li, L., Cheng, J., Yuan, D. & Luo, J. A Highly Symmetric Metal–Organic Framework Based on a Propeller-Like Ru-Organic Metalloligand for Photocatalysis and Explosives Detection. *Cryst. Growth Des.* **13**, 5466-5472 (2013).

174 Marmier, M., Wise, M. D., Holstein, J. J., Pattison, P., Schenk, K., Solari, E., Scopelliti, R. & Severin, K. Carboxylic Acid Functionalized Clathrochelate Complexes: Large, Robust, and Easy-to-Access Metalloligands. *Inorg. Chem.* **55**, 4006-4015 (2016).

175 Spek, A. Single-crystal structure validation with the program PLATON. *J. Appl. Crystallogr.* **36**, 7-13 (2003).

176 Farha, O. K. & Hupp, J. T. Rational Design, Synthesis, Purification, and Activation of Metal−Organic Framework Materials. *Acc. Chem. Res.* **43**, 1166-1175 (2010).

177 Dybtsev, D. N., Chun, H., Yoon, S. H., Kim, D. & Kim, K. Microporous Manganese Formate: A Simple Metal−Organic Porous Material with High Framework Stability and Highly Selective Gas Sorption Properties. *J. Am. Chem. Soc.* **126**, 32-33 (2004).

178 Alexander, R., Kralert, P. G. & Kagi, R. I. Proceedings of the 15th International Meeting on Organic Geochemistry Kinetics and mechanism of the thermal decomposition of esters in sediments. *Org. Geochem.* **19**, 133-140 (1992).

179 Dau, P. V., Kim, M., Garibay, S. J., Münch, F. H. L., Moore, C. E. & Cohen, S. M. Single-Atom Ligand Changes Affect Breathing in an Extended Metal − Organic Framework. *Inorg. Chem.* **51**, 5671-5676 (2012).

180 Pichon, A., Fierro, C. M., Nieuwenhuyzen, M. & James, S. L. A pillared-grid MOF with large pores based on the $Cu_2(O_2CR)_4$ paddle-wheel. *CrystEngComm* **9**, 449-451 (2007).

181 Seo, J., Matsuda, R., Sakamoto, H., Bonneau, C. & Kitagawa, S. A Pillared-Layer Coordination Polymer with a Rotatable Pillar Acting as a Molecular Gate for Guest Molecules. *J. Am. Chem. Soc.* **131**, 12792-12800 (2009).

182 Gao, C., Liu, S., Xie, L., Sun, C., Cao, J., Ren, Y., Feng, D. & Su, Z. Rational design microporous pillared-layer frameworks: syntheses, structures and gas sorption properties. *CrystEngComm* **11**, 177-182 (2009).

183 Yin, Z., Wang, Q.-X. & Zeng, M.-H. Iodine Release and Recovery, Influence of Polyiodide Anions on Electrical Conductivity and Nonlinear Optical Activity in an

Interdigitated and Interpenetrated Bipillared-Bilayer Metal–Organic Framework. *J. Am. Chem. Soc.* **134**, 4857-4863 (2012).

184 Meng, X., Zhong, R.-L., Song, X.-Z., Song, S.-Y., Hao, Z.-M., Zhu, M., Zhao, S.-N. & Zhang, H.-J. A stable, pillar-layer metal-organic framework containing uncoordinated carboxyl groups for separation of transition metal ions. *Chem. Commun.* **50**, 6406-6408 (2014).

185 Wang, H.-N., Jiang, S.-Q., Lu, Q.-Y., Zhou, Z.-Y., Zhuo, S.-P., Shan, G.-G. & Su, Z.-M. A pillar-layer MOF for detection of small molecule acetone and metal ions in dilute solution. *RSC Advances* **5**, 48881-48884 (2015).

186 Wang, Q., Zhang, J., Zhuang, C.-F., Tang, Y. & Su, C.-Y. Guest Inclusion and Interpenetration Tuning of Cd(II)/Mn(II) Coordination Grid Networks Assembled from a Rigid Linear Diimidazole Schiff Base Ligand. *Inorg. Chem.* **48**, 287-295 (2009).

187 Bureekaew, S., Sato, H., Matsuda, R., Kubota, Y., Hirose, R., Kim, J., Kato, K., Takata, M. & Kitagawa, S. Control of Interpenetration for Tuning Structural Flexibility Influences Sorption Properties. *Angew. Chem.* **122**, 7826-7830 (2010).

188 Jiang, H.-L., Makal, T. A. & Zhou, H.-C. Interpenetration control in metal–organic frameworks for functional applications. *Coord. Chem. Rev.* **257**, 2232-2249 (2013).

189 Ferguson, A., Liu, L., Tapperwijn, S. J., Perl, D., Coudert, F.-X., Van Cleuvenbergen, S., Verbiest, T., van der Veen, M. A. & Telfer, S. G. Controlled partial interpenetration in metal–organic frameworks. *Nat Chem* **8**, 250-257 (2016).

190 Yang, J.-X., Qin, Y.-Y., Cheng, J.-K. & Yao, Y.-G. Tuning Different Kinds of Entangled Networks by Varying N-Donor Ligands: From Self-Penetrating to Multi-interpenetrating. *Cryst. Growth Des.* **14**, 1047-1056 (2014).

191 Liu, L. & Telfer, S. G. Systematic Ligand Modulation Enhances the Moisture Stability and Gas Sorption Characteristics of Quaternary Metal–Organic Frameworks. *J. Am. Chem. Soc.* (2015).

192 Lee, S. J., Doussot, C., Baux, A., Liu, L., Jameson, G. B., Richardson, C., Pak, J. J., Trousselet, F., Coudert, F.-X. & Telfer, S. G. Multicomponent Metal–Organic Frameworks as Defect-Tolerant Materials. *Chem. Mater.* **28**, 368-375 (2016).

193 Thompson, A. E., Hughes, G., Batsanov, A. S., Bryce, M. R., Parry, P. R. & Tarbit, B. Palladium-Catalyzed Cross-Coupling Reactions of Pyridylboronic Acids with Heteroaryl Halides Bearing a Primary Amine Group: Synthesis of Highly Substituted Bipyridines and Pyrazinopyridines. *J. Org. Chem.* **70**, 388-390 (2005).

194 Veerakumar, P., Velayudham, M., Lu, K.-L. & Rajagopal, S. Silica-supported PEI capped nanopalladium as potential catalyst in Suzuki, Heck and Sonogashira coupling reactions. *Applied Catalysis A: General* **455**, 247-260 (2013).

195 Zhang, L., Jian, Y., Wang, J., He, C., Li, X., Liu, T. & Duan, C. Post-modification of a MOF through a fluorescent-labeling technology for the selective sensing and adsorption of Ag^+ in aqueous solution. *Dalton Trans.* **41**, 10153-10155 (2012).

196 Kumar, K. S., Iqbal, J. & Pal, M. Amberlyst-15: a mild, efficient and reusable heterogeneous catalyst for N-tert-butoxycarbonylation of amines. *Tetrahedron Lett.* **50**, 6244-6246 (2009).

197 Chen, B., Eddaoudi, M., Hyde, S. T., O'Keeffe, M. & Yaghi, O. M. Interwoven Metal-Organic Framework on a Periodic Minimal Surface with Extra-Large Pores. *Science* **291**, 1021-1023 (2001).

198 Han, D., Jiang, F.-L., Wu, M.-Y., Chen, L., Chen, Q.-H. & Hong, M.-C. A non-interpenetrated porous metal-organic framework with high gas-uptake capacity. *Chem. Commun.* **47**, 9861-9863 (2011).

199 Ito, H., Ueda, M. & England, W. P. Thermal and acid-catalyzed deesterification and rearrangement of poly(2-cyclopropyl-2-propyl 4-vinylbenzoate) and their application to lithographic imaging. *Macromolecules* **23**, 2589-2598 (1990).

200 Zhang, W., Huang, H., Zhong, C. & Liu, D. Cooperative effect of temperature and linker functionality on CO_2 capture from industrial gas mixtures in metal-organic frameworks: a combined experimental and molecular simulation study. *Phys. Chem. Chem. Phys.* **14**, 2317-2325 (2012).

201 Park, I. (2001.May 20-25, 2001). *Adsorption Hysteresis Dynamics.* Paper presented at Seventh International Conference on Fundamentals of Adsorption, Nagasaki, Japan.

202 Senkovska, I., Hoffmann, F., Fröba, M., Getzschmann, J., Böhlmann, W. & Kaskel, S. New highly porous aluminium based metal-organic frameworks: Al(OH)(ndc) (ndc = 2,6-naphthalene dicarboxylate) and Al(OH)(bpdc) (bpdc = 4,4′-biphenyl dicarboxylate). *Microporous Mesoporous Mater.* **122**, 93-98 (2009).

203 Klein, N., Senkovska, I., Gedrich, K., Stoeck, U., Henschel, A., Mueller, U. & Kaskel, S. A Mesoporous Metal–Organic Framework. *Angew. Chem., Int. Ed.* **48**, 9954-9957 (2009).

204 Gedrich, K., Senkovska, I., Baburin, I. A., Mueller, U., Trapp, O. & Kaskel, S. New Chiral and Flexible Metal−Organic Framework with a Bifunctional Spiro Linker and Zn_4O-Nodes. *Inorg. Chem.* **49**, 4440-4446 (2010).

205 Klein, N., Herzog, C., Sabo, M., Senkovska, I., Getzschmann, J., Paasch, S., Lohe, M. R., Brunner, E. & Kaskel, S. Monitoring adsorption-induced switching by 129Xe NMR spectroscopy in a new metal-organic framework $Ni_2(2,6\text{-ndc})_2(\text{dabco})$. *Phys. Chem. Chem. Phys.* **12**, 11778-11784 (2010).

206 Gedrich, K., Senkovska, I., Klein, N., Stoeck, U., Henschel, A., Lohe, M. R., Baburin, I. A., Mueller, U. & Kaskel, S. A Highly Porous Metal–Organic Framework with Open Nickel Sites. *Angew. Chem., Int. Ed.* **49**, 8489-8492 (2010).

207 Grünker, R., Senkovska, I., Biedermann, R., Klein, N., Klausch, A., Baburin, I. A., Mueller, U. & Kaskel, S. Topological Diversity, Adsorption and Fluorescence Properties of MOFs Based on a Tetracarboxylate Ligand. *Eur. J. Inorg. Chem.* **2010**, 3835-3841 (2010).

208 O'Keeffe, M., Eddaoudi, M., Li, H., Reineke, T. & Yaghi, O. M. Frameworks for Extended Solids: Geometrical Design Principles. *J. Solid State Chem.* **152**, 3-20 (2000).

209 Fei, H., Cahill, J. F., Prather, K. A. & Cohen, S. M. Tandem Postsynthetic Metal Ion and Ligand Exchange in Zeolitic Imidazolate Frameworks. *Inorg. Chem.* **52**, 4011-4016 (2013).

210 Li, T., Kozlowski, M. T., Doud, E. A., Blakely, M. N. & Rosi, N. L. Stepwise Ligand Exchange for the Preparation of a Family of Mesoporous MOFs. *J. Am. Chem. Soc.* **135**, 11688-11691 (2013).

211 Yao, Q., Sun, J., Li, K., Su, J., Peskov, M. V. & Zou, X. A series of isostructural mesoporous metal-organic frameworks obtained by ion-exchange induced single-crystal to single-crystal transformation. *Dalton Trans.* **41**, 3953-3955 (2012).

212 Bosch, M., Zhang, M. & Zhou, H.-C. Increasing the Stability of Metal-Organic Frameworks. *Adv. Chem.* **2014**, 8 (2014).

213 Willis, R., Benin, A., Low, J. J., Venimadhavan, G., Faheem, S. & Lesch, D. (2008). *Carbon Dioxide Separation with Novel Metal Organic Frameworks.* Retrieved from https://www.researchgate.net/publication/228376266_Carbon_Dioxide_Separation_with_Novel_Microporous_Metal_Organic_Frameworks

214 Li, B., Zhang, Z., Li, Y., Yao, K., Zhu, Y., Deng, Z., Yang, F., Zhou, X., Li, G., Wu, H., Nijem, N., Chabal, Y. J., Lai, Z., Han, Y., Shi, Z., Feng, S. & Li, J. Enhanced Binding Affinity, Remarkable Selectivity, and High Capacity of CO_2 by Dual Functionalization of a rht-Type Metal–Organic Framework. *Angew. Chem., Int. Ed.* **51**, 1412-1415 (2012).

215 Britt, D., Furukawa, H., Wang, B., Glover, T. G. & Yaghi, O. M. Highly efficient separation of carbon dioxide by a metal-organic framework replete with open metal sites. *Proc. Natl. Acad. Sci.* **106**, 20637-20640 (2009).

216 Braglia, L., Borfecchia, E., Lomachenko, K. A., Øien, S., Lillerud, K. P. & Lamberti, C. XAS on Rh and Ir metal sites in post synthetically functionalized UiO-67 Zirconium MOFs. *J. Phys. : Conf. Ser.* **712**, 012053 (2016).

217 Beaucage, S. L., Wilk, A., & Grajkoski, A. (2004). U.S. Patent No. US6762298 B2. Washington, DC: U.S. Patent and Trademark Office. US Patent & Trademark Office

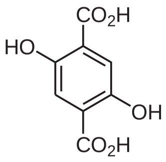

2,5-dihydroxo-1,4-bdc

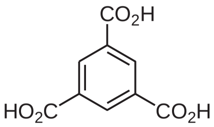

btc

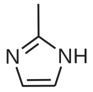

2-methylimidazole

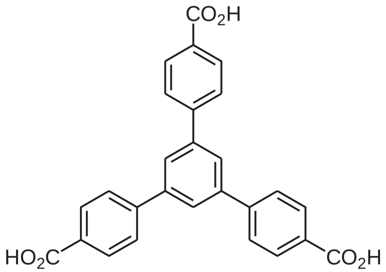

btb

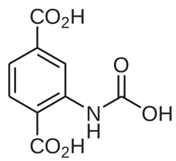

1,4-bdc-NHCO$_2$H

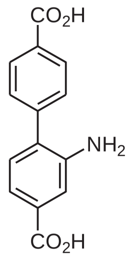

bpdc-NH$_2$

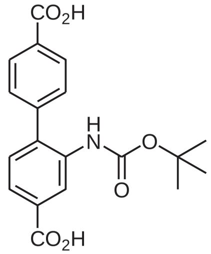

bpdc-NHBoc

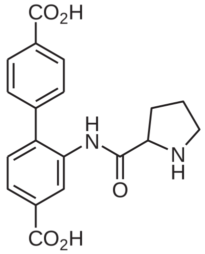

bpdc-Pro

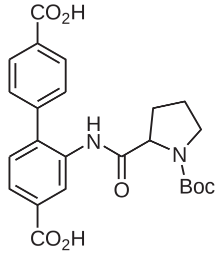

bpdc-Pro-Boc

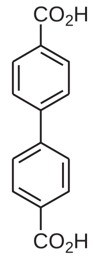

bpdc

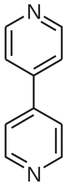

bpy

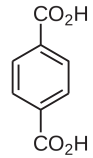

1,4-bdc

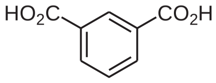

1,3-bdc

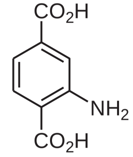

1,4-bdc-NH$_2$

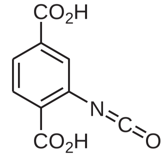

1,4-bdc-NCO

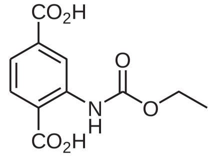

1,4-bdc-NHCOOEt

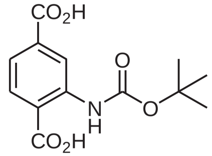

1,4-bdc-NHBoc

MOF-5-NHCOOEt = $[Zn_4O(1,4\text{-bdc-NHCOOEt})_3]$ **MOF-5-NHBoc** = $[Zn_4O(1,4\text{-bdc-NHBoc})_3]$

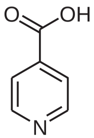

isonicotinic acid (isonic)

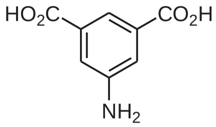

1,3-bdc-NH$_2$

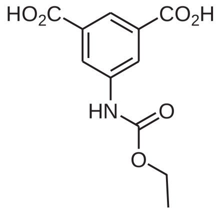

1,3-bdc-NHCOOEt

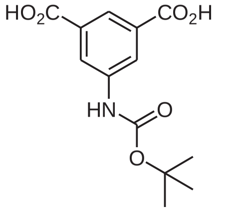

1,3-bdc-NHBoc

Ion-e-NHCOOEt = $[Zn_6(1,3\text{-bdc-NHCOOEt})_6[Cr_3O(\text{isonic})_6(H_2O)_2(OH)]$

Ion-e-NHBoc = $[Zn_6(1,3\text{-bdc-NHBoc})_6[Cr_3O(\text{isonic})_6(H_2O)_2(OH)]$

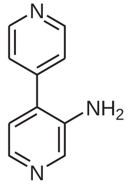

bpy-NH$_2$

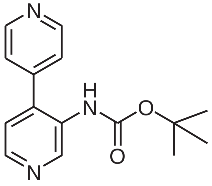

bpy-NHBoc

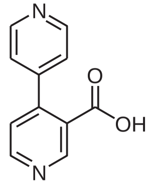

bpy-CO$_2$H

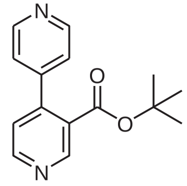

bpy-TBE

MUF20Aβ = $[Zn_2(\text{bpdc})_2(\text{bpy-NHBoc})]$
MUF20Aβ' = $[Zn_2(\text{bpdc})_2(\text{bpy-NH}_2)]$

MUF20Aγ =$[Zn_2(\text{bpdc})_2(\text{bpy-TBE})]$
Zn-DUT-23-TBE =$[Zn_2(\text{btb})_{4/3}(\text{bpy-TBE})]$
Cu-DUT-23-TBE =$[Cu_2(\text{btb})_{4/3}(\text{bpy-TBE})]$

Fold-out Reference Sheet

Abbreviations

BET	Brunauer-Emmett-Teller
DEF	*N*,*N*-diethylformamide
DMF	*N*,*N*-dimethylformamide
DUT	Dresden University of Technology
HKUST	Hong Kong University of Science and Technology
IRMOF	isoreticular metal-organic framework
IUPAC	International Union of Pure and Applied Chemistry
Lon-e	tp-PMBB-1-lon-e ($[Zn_6(1,3\text{-bdc})_6[Cr_3O(\text{isonicotinate})_6(H_2O)_2(OH)]]$)
MIL	Matérial Institut Lavoisier
MOF	metal-organic framework
MUF	Massey University framework
NMR	nuclear magnetic resonance
PCN	porous coordination network
PCP	porous coordination polymer
PSE	post-synthetic exchange
PSM	post-synthetic modification
PXRD	powder x-ray diffraction
SBU	secondary building unit
SXRD	single crystal x-ray diffraction
STP	standard temperature and pressure
SUMOF	Stockholm University metal-organic framework
TGA	Thermogravimetric analysis
TPG	Thermolabile Protecting Group
UiO	University of Oslo